



HAL
open science

Manipulation of Interactions in Quantum Gases : a theoretical approach

David Papoular

► **To cite this version:**

David Papoular. Manipulation of Interactions in Quantum Gases : a theoretical approach. Other [cond-mat.other]. Université Paris Sud - Paris XI, 2011. English. NNT : 2011PA112104 . tel-00624682

HAL Id: tel-00624682

<https://theses.hal.science/tel-00624682>

Submitted on 22 Sep 2011

HAL is a multi-disciplinary open access archive for the deposit and dissemination of scientific research documents, whether they are published or not. The documents may come from teaching and research institutions in France or abroad, or from public or private research centers.

L'archive ouverte pluridisciplinaire **HAL**, est destinée au dépôt et à la diffusion de documents scientifiques de niveau recherche, publiés ou non, émanant des établissements d'enseignement et de recherche français ou étrangers, des laboratoires publics ou privés.

Université Paris–Sud — U.F.R. des Sciences — Orsay

Thèse de doctorat

discipline: Physique

présentée par David PAPOULAR

pour obtenir le grade de docteur de l'Université Paris–Sud

Manipulation des Interactions dans les Gaz Quantiques: Approche théorique

soutenue le 11 juillet 2011 devant le Jury composé de

MM. J. DALIBARD
O. DULIEU
R. KAISER
G. SHLYAPNIKOV Directeur de thèse
S. STRINGARI Rapporteur
E. TRIZAC
J. WALRAVEN Rapporteur



Abstract

The interparticle interactions in ultracold atomic gases can be tuned using Fano–Feshbach scattering resonances, which occur in low–energy collisions between two atoms. These resonances are usually obtained using an external static magnetic field. They turn ultracold atomic gases into an experimental playground for the investigation of novel phases in which Quantum Physics plays a key role. The work presented in this memoir is part of the theoretical effort towards the search for yet unexplored quantum phases.

This manuscript is organised in two parts. The first one is devoted to composite bosons formed in a 2D heteronuclear Fermi gas. We characterise the zero–temperature phase diagram and show the gas–crystal phase transition in this system. Our results are promising in view of future experiments with the ${}^6\text{Li}$ – ${}^{40}\text{K}$ mixture.

In the second part, we propose an alternative to static–field Fano–Feshbach resonances. The idea is to achieve the coupling by using a resonant microwave magnetic field. Our scheme applies to any atomic species whose ground state is split by the hyperfine interaction. It does not require the use of a static magnetic field. First, these resonances are presented using a simple two–channel model. We then characterise them numerically using our own full–fledged implementation of the coupled–channel approach. Our results yield optimistic prospects for the observation of microwave–induced Fano–Feshbach resonances with the bosonic alkali atoms ${}^{23}\text{Na}$, ${}^{41}\text{K}$, ${}^{87}\text{Rb}$, and ${}^{133}\text{Cs}$.

Keywords: cold atoms, quantum gases, Feshbach resonance, cold molecules, quantum phase transition, microwave–dressed atoms, cold collisions, coupled–channel method.

Résumé

Les interactions entre particules dans les gaz quantiques ultrafroids peuvent être contrôlées à l’aide de résonances de Fano–Feshbach. Ces résonances de diffusion se produisent lors de collisions à basse énergie entre deux atomes et sont généralement obtenues à l’aide d’un champ magnétique statique externe. Elles font des gaz atomiques ultrafroids un terrain d’exploration pour la recherche de nouvelles phases dans lesquelles la physique quantique joue un rôle clef. Le travail présenté dans ce mémoire s’inscrit dans le cadre de la recherche de telles phases.

Ce manuscrit comporte deux parties. La première est consacrée à l’étude de bosons composites obtenus dans des gaz de Fermi hétéronucléaires 2D. Nous étudions le diagramme de phase de ce système à $T = 0$ et nous mettons en évidence une transition de phase gaz–cristal. Nos résultats sont prometteurs en vue d’expériences futures avec le mélange ${}^6\text{Li}$ – ${}^{40}\text{K}$.

Dans la seconde partie, nous proposons un nouveau type de résonance de Fano–Feshbach. Le couplage à l’origine de cette résonance est obtenu à l’aide d’un champ magnétique micro–onde. Notre méthode s’applique à n’importe quelle espèce atomique dont l’état fondamental est clivé par l’interaction hyperfine. Elle ne nécessite pas l’utilisation d’un champ magnétique statique. Nous décrivons d’abord ces résonances à l’aide d’un modèle simple à deux niveaux. Ensuite, nous les caractérisons numériquement à l’aide de notre propre programme implémentant l’approche multi–canaux des collisions atomiques. Nos résultats ouvrent des perspectives optimistes en vue de l’observation des résonances de Feshbach induites par un champ micro–onde avec les atomes alcalins bosoniques suivants : ${}^{23}\text{Na}$, ${}^{41}\text{K}$, ${}^{87}\text{Rb}$ et ${}^{133}\text{Cs}$.

Mots–clefs : atomes froids, gaz quantiques, résonance de Feshbach, molécules froides, transition de phase quantique, collisions froides, description multi–canaux des collisions atomiques.

*How much better it is to get wisdom than gold,
and to get understanding rather to be chosen than silver.*

Proverbs 16:16

In loving memory
of my grandfather Jules Salfati.

Contents

Foreword	1
I. A two-dimensional crystal of composite bosons	5
1. Introduction	7
1.1. Bosonic dimers obtained in a bipartite Fermi gas	7
1.2. Effective interaction between heteronuclear composite bosons	9
1.3. Zero-temperature phase diagram of a 2D system of composite bosons . .	10
1.4. Outline of the following chapters	11
2. Simple approaches to the crystal-gas phase diagram	13
2.1. The phase diagram in the harmonic approximation	13
2.2. Hard-core boson approximation for low densities	20
3. Born-Oppenheimer potentials for the interaction between composite bosons	23
4. Decay processes for composite bosons	29
4.1. Collisional relaxation into deeply bound states	29
4.2. Formation of trimer bound states	30
5. Suggestion for a new experiment	33
6. Article 1: Crystalline Phase of Strongly Interacting Fermi Mixtures	35
7. Conclusion and outlook	41
Bibliography	43
II. Microwave-induced Fano-Feshbach resonances	47
8. Introduction	49
8.1. Static-field Fano-Feshbach resonances	51
8.2. Previous work on alternative Feshbach resonances	52
8.3. Outline of the following chapters	53

9. An overview of microwave–induced Feshbach resonances	55
9.1. One single square well	55
9.2. The two–square–well model for microwave–induced Feshbach resonances	58
10. The Two–Atom Hamiltonian	67
10.1. A single atom in a magnetic field	67
10.2. Two atoms in a magnetic field	69
10.3. Block–matrix structure of the two–atom Hamiltonian	73
11. Characterising the resonances	81
11.1. The two–subspace approach	82
11.2. The coupled–channel approach	89
11.3. Experimental prospects	98
11.4. Comparison with RF–induced Feshbach resonances	99
12. The numerical calculation of two–atom wavefunctions	111
12.1. The multi–channel scattering state wavefunction	112
12.2. The Accumulated–Phase approach	115
12.3. The relaxation method	119
12.4. An approach based on the shooting method	121
12.5. Summary	126
13. Article 2: Microwave–Induced Fano–Feshbach resonances	129
14. Static–Field Feshbach resonances	135
14.1. Two atoms in a static magnetic field	135
14.2. Recovering known Feshbach resonance results	136
14.3. Low static–field resonances in Cesium	138
15. Towards an experimental observation of our predictions	145
15.1. Two atoms in a linearly–polarised magnetic field	145
15.2. In the absence of a static magnetic field	147
15.3. In the presence of a static magnetic field	154
16. Conclusion and outlook	157
Bibliography	161
Acknowledgements	167

Foreword

The achievement of Bose–Einstein condensation [1–3] has stimulated considerable developments in atomic Physics. Ultracold atoms have found applications in metrology [4]. They are used in high–precision experiments with the aim of determining physical constants [5] or testing the validity of fundamental theories [6]. Ultracold gases provide promising building blocks for quantum information processing [7]. They can be cooled down to quantum degeneracy and used to simulate condensed–matter systems [8] or to model systems for the investigation of problems arising in astrophysics [9]. Collateral work [10] has even lead to improved medical imaging methods.

A fundamental feature of ultracold atomic gases is that the interparticle interactions in the gas can be tailored at will. The manipulation of the interactions is performed using scattering resonances that occur in low–energy collisions between two atoms [11]. These Fano–Feshbach resonances are usually obtained using an external static magnetic field [12]. They have turned ultracold atomic gases into an experimental playground for the investigation of novel phases of matter in which Quantum Physics plays a key role. Bose–Einstein condensation stands among these new phases, and so do spinor condensates [13] and the Mott–insulating phase [14]. Furthermore, effective dimensionality can also be tuned by using a tight optical confinement of the gas in one or two directions. This has allowed the investigation of the 1D Tonks–Girardeau gas [15, 16] and the 2D Berezinskii–Kousterlitz–Thouless transition [17].

The work presented in this memoir is part of the theoretical effort underlying the search for yet unexplored quantum phases. It is organised in two parts:

- The shorter first part illustrates how the manipulation of atomic interactions can be applied to the search for new quantum phases. We focus on the crystalline phase of a two–dimensional assembly of composite bosons formed in an ultracold heteronuclear Fermi gas [18] and characterise the zero–temperature crystal–gas phase diagram of this system [19]. Our results are promising in view of a possible observation of this crystalline phase in a mixture of ${}^6\text{Li}$ and ${}^{40}\text{K}$ atoms.
- In the longer second part, the object of our analysis is the actual manipulation of interactions in ultracold gases. We propose an alternative to static–field Fano–Feshbach resonances. In our case, the coupling is achieved using a resonant microwave magnetic field [20]. This scheme is reminiscent of optical Feshbach resonances [21]. It applies to any atomic species whose ground state is split by the hyperfine interaction. The microwave–induced resonances that we discuss in this

manuscript are present even when no static-field Feshbach resonances are accessible. They do not require the presence of a static magnetic field component, which will be an asset in the investigation of new phases in spinor Bose-Einstein condensates [22]. Our results yield optimistic prospects for experiments with ^{23}Na , ^{41}K , ^{87}Rb , and ^{133}Cs .

References

- [1] M. H. Anderson et al. “Observation of Bose-Einstein Condensation in a Dilute Atomic Vapor”. In: *Science* 269.5221 (1995), pp. 198–201. DOI: 10.1126/science.269.5221.198.
- [2] C. C. Bradley et al. “Evidence of Bose-Einstein Condensation in an Atomic Gas with Attractive Interactions”. In: *Phys. Rev. Lett.* 75.9 (Aug. 1995), pp. 1687–1690. DOI: 10.1103/PhysRevLett.75.1687.
- [3] Kendall B. Davis et al. “Evaporative Cooling of Sodium Atoms”. In: *Phys. Rev. Lett.* 74.26 (June 1995), pp. 5202–5205. DOI: 10.1103/PhysRevLett.74.5202.
- [4] S. Bize et al. “Cold atom clocks and applications”. In: *Journal of Physics B: Atomic, Molecular and Optical Physics* 38.9 (2005), S449. DOI: 10.1088/0953-4075/38/9/002.
- [5] F. Biraben. “Spectroscopy of atomic hydrogen”. In: *The European Physical Journal-Special Topics* 172.1 (2009), pp. 109–119. DOI: 10.1140/epjst/e2009-01045-3.
- [6] Keng-Yeow Chung et al. “Atom interferometry tests of local Lorentz invariance in gravity and electrodynamics”. In: *Phys. Rev. D* 80.1 (July 2009), p. 016002. DOI: 10.1103/PhysRevD.80.016002.
- [7] J.J. García-Ripoll, P. Zoller, and J.I. Cirac. “Quantum information processing with cold atoms and trapped ions”. In: *Journal of Physics B: Atomic, Molecular and Optical Physics* 38 (2005), S567. DOI: 10.1088/0953-4075/38/9/008.
- [8] A. Georges. “Condensed-matter Physics with light and atoms”. In: *Proceedings of the International School of Physics “Enrico Fermi,” Course CLXIV, Varenna, 2006*. IOS Press, 2008.
- [9] Andrew G. Truscott et al. “Observation of Fermi Pressure in a Gas of Trapped Atoms”. In: *Science* 291.5513 (2001), pp. 2570–2572. DOI: 10.1126/science.1059318.
- [10] Michèle Leduc and Pierre Jean Nacher. “Polarized Helium to Image the Lung”. In: *AIP Conference Proceedings* 770.1 (2005). Ed. by Luis Gustavo Marcassa, Kristian Helmerson, and Vanderlei Salvador Bagnato, pp. 381–389. DOI: 10.1063/1.1928872.
- [11] Cheng Chin et al. “Feshbach resonances in ultracold gases”. In: *Rev. Mod. Phys.* 82.2 (Apr. 2010), pp. 1225–1286. DOI: 10.1103/RevModPhys.82.1225.

- [12] S. Inouye et al. “Observation of Feshbach resonances in a Bose–Einstein condensate”. In: *Nature* 392.6672 (1998), pp. 151–154. ISSN: 0028-0836. DOI: 10.1038/32354.
- [13] J. Stenger et al. “Spin domains in ground-state Bose-Einstein condensates”. In: *Nature* 396 (1998), p. 345. DOI: 10.1038/24567.
- [14] M. Greiner et al. “Quantum phase transition from a superfluid to a Mott insulator in a gas of ultracold atoms”. In: *Nature* 415 (2002), p. 39. DOI: 10.1038/415039a.
- [15] Toshiya Kinoshita, Trevor Wenger, and David S. Weiss. “Observation of a One-Dimensional Tonks-Girardeau Gas”. In: *Science* 305.5687 (2004), pp. 1125–1128. DOI: 10.1126/science.1100700.
- [16] B. Paredes et al. “Tonks-Girardeau gas of ultracold atoms in an optical lattice”. In: *Nature* 429 (2004), p. 277. DOI: 10.1038/nature02530.
- [17] Z. Hadzibabic et al. “Berezinskii-Kosterlitz-Thouless crossover in a trapped atomic gas”. In: *Nature* 441 (2006), p. 1118. DOI: 10.1038/nature04851.
- [18] D. S. Petrov, C. Salomon, and G. V. Shlyapnikov. “Molecular regimes in ultracold Fermi gases”. In: *Cold Molecules: Theory, Experiment, Applications*. CRC Press, 2009. Chap. 9. ISBN: 978-1-4200-5903-8.
- [19] D. S. Petrov et al. “Crystalline Phase of Strongly Interacting Fermi Mixtures”. In: *Phys. Rev. Lett.* 99.13 (Sept. 2007), p. 130407. DOI: 10.1103/PhysRevLett.99.130407.
- [20] D. J. Papoular, G. V. Shlyapnikov, and J. Dalibard. “Microwave-induced Fano-Feshbach resonances”. In: *Phys. Rev. A* 81.4 (Apr. 2010), p. 041603. DOI: 10.1103/PhysRevA.81.041603.
- [21] P. O. Fedichev et al. “Influence of Nearly Resonant Light on the Scattering Length in Low-Temperature Atomic Gases”. In: *Phys. Rev. Lett.* 77.14 (Sept. 1996), pp. 2913–2916. DOI: 10.1103/PhysRevLett.77.2913.
- [22] Tin-Lun Ho. “Spinor Bose Condensates in Optical Traps”. In: *Phys. Rev. Lett.* 81.4 (July 1998), pp. 742–745. DOI: 10.1103/PhysRevLett.81.742.

Part I.

A two-dimensional crystal of composite bosons

1. Introduction

The first part of the present manuscript focuses on the zero-temperature phase diagram of a two-dimensional system of composite bosons formed in a heteronuclear fermionic mixture with equal densities of the two species.

We consider an ultracold gas of fermionic atoms. In order to avoid a suppression of the atomic interactions due to the Pauli principle, we consider a bipartite mixture, *i.e.* a gas in which two types of atoms are present. These atoms may all belong to the same atomic species, part of them being in a different internal state than the others. Alternately, two different species of fermions, such as Lithium 6 and Potassium 40, may be present in the mixture.

Assuming that the gas is cold enough for s -wave collisions to be dominant [1], the nature (repulsive or attractive) and strength of the interaction between two distinguishable atoms are encoded in a single real parameter, the scattering length a . This interaction is represented by the following pseudopotential [2]:

$$U_{\text{pseudo}}(r) = \frac{4\pi\hbar^2}{m} a \delta(r) \quad , \quad (1.1)$$

where r is the interatomic distance.

The interatomic interactions in the ultracold gas can be tuned using a Fano-Feshbach resonance. These resonances will be described in detail in Part II (in particular, see Chapter 8), and we only briefly mention them here. Such a resonance is usually obtained using a static magnetic field [3]. It occurs for a fixed value B_{res} of the magnetic field. For fields B close to B_{res} , the scattering length diverges hyperbolically (see Fig. 1.1), which makes it possible to set the scattering length to the desired value and sign by tuning the magnetic field B .

1.1. Bosonic dimers obtained in a bipartite Fermi gas

The initial interest in bipartite fermionic mixtures has stemmed from the BEC-BCS crossover [4, 5]. For negative scattering lengths ($a < 0$, right-hand half of Fig. 1.1), fermions belonging to different components and with opposite momenta on the Fermi surface form correlated pairs, and at sufficiently low temperatures the system is superfluid [6]. By contrast, for positive scattering lengths ($a > 0$, left-hand half of Fig. 1.1), one has bosonic dimers representing weakly bound states of fermionic atoms of different components. Such dimers have been observed in homonuclear Fermi gases [7-9] and, more recently, in heteronuclear mixtures (see Fig. 1.2 and [10, 11]). These dimers are

1. Introduction

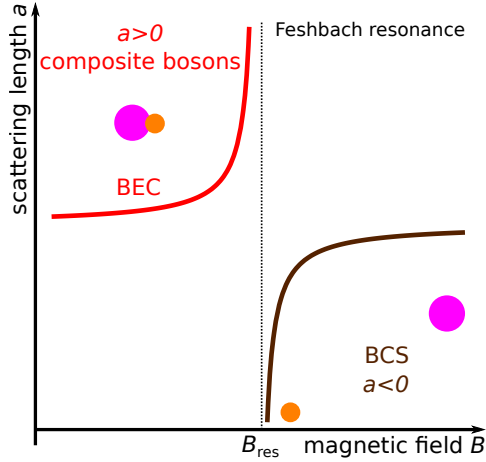


Figure 1.1. Feshbach resonance, BEC and BCS regimes. The heteronuclear molecules (composite bosons) are obtained on the BEC side of the resonance.

weakly bound composite bosons, and Bose–Einstein condensates of homonuclear Li_2 and K_2 dimers have been obtained in a number of experiments [12–14].

We focus on the case of positive scattering lengths a and further assume that a is much larger than the characteristic range R_e of the interatomic interaction potential. The diatomic molecules obtained in this situation (in either homonuclear or heteronuclear Fermi mixtures) exhibit two key features:

- They are the largest diatomic molecules obtained so far. Their size, which is of the order of a , has reached thousands of angstroms in current experiments. Accordingly, they are very weakly bound (their binding energy is $\lesssim 10 \mu\text{K}$).
- They are very stable with respect to collisional relaxation. Their lifetime can be of the order of seconds for typical densities (about $10^{13} \text{ atoms/cm}^3$).

1.1.1. Collisional relaxation

The long lifetime of these dimers is specific to composite bosons made up of fermions. It is due to the suppression of collisional relaxation caused by the Pauli principle.

The physics is the simplest in the case of homonuclear dimers [15, 16]. In order for a weakly bound dimer to relax to a deeply bound state (whose size is of the order of R_e), at least three fermions should approach each other at a distance $\sim R_e$. Among these three atoms, two are in the same quantum state. Recalling that the size of the dimers

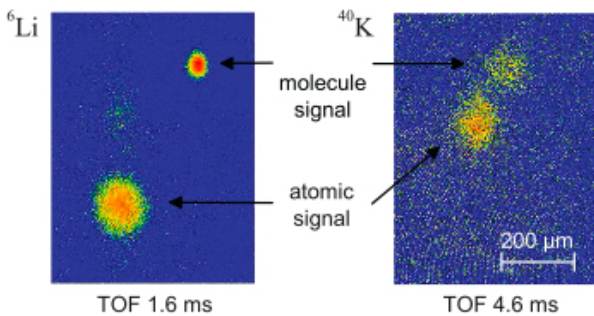


Figure 1.2. Absorption images of a heteronuclear mixture of ^6Li and ^{40}K in which molecules have been obtained by sweeping the magnetic field from the ($a < 0$) side to the ($a > 0$) side of a Feshbach resonance, after separation under the action of a magnetic field during time of flight (TOF). (Reproduced from [10].)

is $\sim a$, the typical momentum of the atoms is $k \sim 1/a$, and this three-body encounter is Pauli-suppressed by a factor of $(k R_e)^s \sim (R_e/a)^s \ll 1$, where s is of the order of 2.

In the case of heteronuclear dimers, the situation is more involved. The weakly bound heteronuclear molecules can decay towards lower-energy states through two main channels [17]: (i) the relaxation into deeply bound dimer states and (ii) the formation of trimer states.

The relaxation into deeply bound dimer states can occur in dimer-dimer collisions when one heavy and two light fermions¹ are within a distance $\sim R_e$ from each other. The relaxation rate acquires a dependence on the ratio M/m of the heavy to light fermionic masses [18], but the suppression of collisional relaxation still holds.

The formation of a trimer state requires two heavy and one light atoms to come at a distance $R \lesssim a$ from each other. At such distances the light fermion mediates an effective interaction between the two dimers which is attractive [17]. This attractive interaction is proportional to $-1/(mR^2)$, and it competes with the Pauli repulsion, which manifests itself through a centrifugal barrier which is proportional to $1/(MR^2)$. The physics thus depends on the value of the mass ratio M/m . For mass ratios $M/m \sim 1$, the Pauli repulsion is dominant and the trimer states do not exist. For mass ratios $M/m > 13.6$, the attractive interaction dominates, and Efimov trimers can appear [19]. These trimers cannot be described using the scattering length alone, and an additional three-body parameter must be introduced.

Besides the Efimov trimers, one light and two heavy atoms may form “universal” trimer states, which are well described in the zero-range approximation without introducing the three-body parameter [20]. They exist for the orbital angular momentum $\ell = 1$ and mass ratios below the critical value $M/m < 13.6$, where the Efimov effect is absent. One such state emerges for $M/m \approx 8.1$. These universal trimer states also exist above the critical mass ratio, but the trimer formation at such mass ratios is dominated by the formation of smaller- ℓ Efimov trimers.

1.2. Effective interaction between heteronuclear composite bosons

We now concentrate on the case of bosonic dimers obtained in a Fermi mixture containing two types of atoms, chosen such that the ratio M/m of the heavy to light fermion masses is large. These dimers interact with one another via an exchange interaction mediated by the light fermions [18, 19]. This interaction has been studied theoretically in two situations:

1. The motion of the heavy atoms is two-dimensional, whereas that of the light atoms is three-dimensional (abbreviated to 2×3 in [17]).

¹Experiments involving composite bosons are likely to be performed in the presence of an optical lattice (see Section 5). The relaxation process involving one light and two heavy fermions is heavily suppressed due to the presence of the lattice, as it requires the heavy fermions to occupy the same lattice site.

1. Introduction

2. The motion of both the heavy and light atoms is two-dimensional (abbreviated to 2×2 in [17]).

In *dilute systems* (*i.e.* if the mean intermolecular spacing R exceeds the scattering length a of the interatomic interaction), this interaction can be modelled by an effective pair potential. The detailed expression for the effective potential depends on the considered situation (2×3 or 2×2), but in both cases the interaction between the dimers is repulsive².

Analytical expressions for this effective potential have been obtained in both situations [17, 18] using the Born–Oppenheimer approximation. A detailed derivation of these expressions is given in Chapter 3. In the 2×3 case, the effective potential $U_{3D}(R)$ is given by:

$$U_{3D}(R) = 4 |\varepsilon_0| (1 - (2\kappa_0 R)^{-1}) \frac{\exp(-2\kappa_0 R)}{\kappa_0 R} \quad , \quad (1.2)$$

where the composite-boson molecular size κ_0^{-1} is related to the binding energy $|\varepsilon_0|$ of a single dimer:

$$|\varepsilon_0| = \frac{\hbar^2 \kappa_0^2}{2m} \quad , \quad (1.3)$$

with m being the mass of the light fermion. In the 2×3 case the molecular size $\kappa_0^{-1} = a$.

In the 2×2 case the effective potential $U_{2D}(R)$ reads:

$$U_{2D}(R) = 4 |\varepsilon_0| [\kappa_0 R K_0(\kappa_0 R) K_1(\kappa_0 R) - K_0^2(\kappa_0 R)] \quad , \quad (1.4)$$

where K_0 and K_1 are modified Bessel functions [21]. In this regime, achieved by confining the light-atom motion to zero-point oscillations with amplitude l_0 , the weakly-bound molecular states exist at a negative a . For $|a| \ll l_0$, the molecular size is given by $\kappa_0^{-1} = \sqrt{\pi} l_0 \exp(-\sqrt{\pi/2} l_0/a)$ [17, 22].

The potentials $U_{3D}(r)$ and $U_{2D}(r)$ are shown on Fig. 1.3. The range of these potentials is given by the molecular size κ_0^{-1} . Therefore, the dimer–dimer interaction can be made relatively long-ranged by selecting a value for a which does not greatly exceed the mean intermolecular separation.

1.3. Zero-temperature phase diagram of a 2D system of composite bosons

The interaction between the dimers described above is *repulsive*, and it can be made *long-range*³. These are two indications that the 2D system of composite bosons may exhibit a crystalline phase. Indeed, a triangular crystalline lattice maximises distances

²This is in contrast to the attractive effective interaction mediated by one light atom between two heavy atoms at a distance $R \lesssim a$: see Section 1.1.1.

³The crystalline phase is also predicted to exist for very low two-dimensional densities n . In this limit, the mean distance between molecules greatly exceeds the size of the molecule, and the system behaves like a set of 2D hard-core bosons: see Section 2.2.

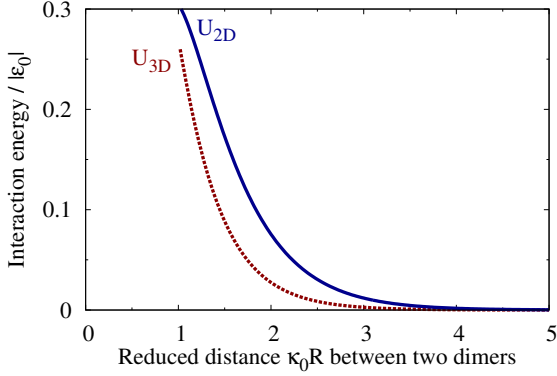


Figure 1.3. Interaction potentials between two composite bosons, for three-dimensional (dashed red) and two-dimensional (solid blue) motion of light atoms. Distances are expressed in units of the composite-boson molecular size κ_0^{-1} , and energies in units of the binding energy $|\varepsilon_0|$ of a single molecule.

between neighbouring atoms, and it is likely to minimise the total interaction energy, thus leading to classical equilibrium.

From the point of view of quantum mechanics, the phase (gaseous or crystalline) of the system in its ground state is dictated by a competition between two effects: *(i)* the repulsive interaction between pairs of dimers, and *(ii)* the kinetic energy of the dimers. The first of these effects yields a contribution to the total energy, which is proportional to $1/m$ (through the factor $|\varepsilon_0|$ in Eqs. (1.2) and (1.4)), whereas the contribution of the kinetic energy is proportional to the inverse total mass of a dimer, which is close to $1/M$ for large mass ratios. Therefore, the relative importance of these two effects can be tuned by varying the ratio M/m of the masses of the heavy and light atoms. Furthermore, interaction effects become more important if the two-dimensional density n of the dimers increases.

The arguments above suggest an exploration of the phase diagram of the system at zero temperature, by varying both the density n and the mass ratio M/m . We report such an exploration in [17]. The phase diagram of the system is calculated for various densities and mass ratios by Quantum Monte Carlo. A zero-temperature crystal-gas phase transition occurs both in the 2×3 and 2×2 situations. The system is found to be in the gaseous phase for low densities and mass ratios, where zero-point vibrations dominate over the interaction energy. It is in the crystalline phase for high densities and mass ratios, where interactions are dominant. The transition lines are obtained via DMC calculations [23]. We also calculate them using two simpler methods, described in detail in Chapter 2, whose results are in good agreement with the Quantum Monte Carlo predictions.

1.4. Outline of the following chapters

The present part of this manuscript is organised in five chapters.

- In Chapter 2, we present two simple approaches to the calculation of the composite-boson phase diagram. The approximate results which they yield for the crystal-gas transition line are in good agreement with the Quantum Monte Carlo results.

1. *Introduction*

- Chapter 3 is devoted to the derivation of the analytical expressions (1.2) and (1.4) for the effective interaction between composite bosons.
- In Chapter 4, we evaluate the decay rates of weakly bound composite bosons into deeply bound states and trimer states.
- Chapter 5 briefly sketches an experimental proposal for the observation of the crystalline phase of composite bosons.
- Chapter 6 reproduces our published article [17].

2. Simple approaches to the crystal–gas phase diagram

We consider a two–dimensional assembly of composite bosons obtained in an ultracold mixture of two different fermionic atoms. Throughout this chapter, we assume that the 2D density is sufficiently low for these composite bosons to be considered as basic entities interacting via an effective pair potential which is repulsive (see Chapter 1 and [17]).

The nature of the ground state of such a system results from the competition between two effects: *(i)* the zero–point kinetic energy, and *(ii)* the repulsive interaction between composite bosons. If the zero–point vibrations are dominant, the ground state is gaseous. On the other hand, if the interaction energy dominates, the ground state is crystalline. The numerical analysis of the system, using Diffusion Monte Carlo [23], has revealed [17] that the system should undergo a crystal–gas phase transition. The stable phase at $T = 0$ K depends on two parameters:

- the 2D density n , and
- the ratio M/m of the heavy (M) to light (m) fermion masses in the mixture.

In this chapter, we present two approximate methods which allow for simple calculations of the phase diagram of the system, with little or no input from the QMC results for this diagram. The first approach is based on a harmonic approximation to the crystal Hamiltonian, and it relies on the Lindemann criterion to predict the critical mass ratio as a function of the density. This approach is valid for all values of the parameters M/m and n for which the composite nature of the molecules does not come into play. The second method, which does not involve the Lindemann criterion, is only applicable for very low densities. In this limit, the composite bosons are modelled by hard disks, and for a given mass ratio the critical density can be deduced from accurate numerical analyses of the fluid–crystal phase transition in hard–disk systems.

Both approximate approaches are in good agreement with the more accurate Quantum Monte Carlo results.

2.1. The phase diagram in the harmonic approximation

2.1.1. Hamiltonian of the crystal

We consider a two–dimensional assembly of N composite bosons at an ultracold temperature. More precisely, we assume that $T = 0$.

2. Simple approaches to the crystal–gas phase diagram

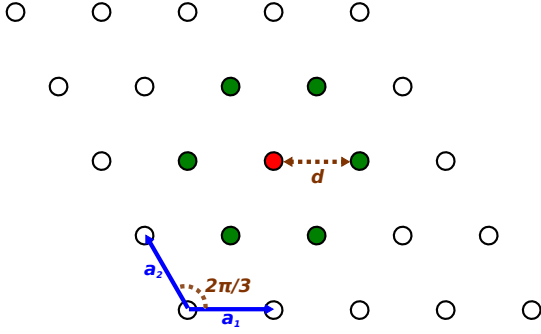


Figure 2.1. Triangular lattice spanned by the two (direct–lattice) vectors \mathbf{a}_1 and \mathbf{a}_2 . Any given atom (red) has six nearest neighbours (green).

Additionally, we assume that the system of composite bosons is in the crystalline phase. The effective interaction between composite bosons is repulsive, therefore the energy of the system decreases when the distance between nearest neighbours increases. Among all two–dimensional Bravais lattices, the triangular lattice¹ is the one which, for a given density, achieves the greatest distance between nearest neighbours [24]. It is therefore reasonable to assume that the system will crystallise into such a lattice. This hypothesis has been confirmed by the results of Quantum Monte Carlo simulations [17].

The triangular lattice (see Fig. 2.1) is spanned by two vectors \mathbf{a}_1 and \mathbf{a}_2 such that:

$$(\widehat{\mathbf{a}_1, \mathbf{a}_2}) = \frac{2\pi}{3} \quad \text{and} \quad |\mathbf{a}_1| = |\mathbf{a}_2| = d \quad , \quad (2.1)$$

where the lattice parameter d determines the distance between nearest–neighbour lattice sites. In the crystalline phase, the classical equilibrium positions of the particles² are the lattice sites \mathbf{r}_n , defined by:

$$\mathbf{r}_n = n_1 \mathbf{a}_1 + n_2 \mathbf{a}_2 \quad , \quad (2.2)$$

where $n = (n_1, n_2)$ is a double integer index spanning the whole lattice. However, the atoms are not fixed at their equilibrium positions, even at $T = 0$, due to quantum zero–point vibrations. Let \mathbf{u}_n be the displacement of particle n from the corresponding lattice site. The position of this particle is then $\mathbf{R}_n = \mathbf{r}_n + \mathbf{u}_n$.

Assuming that the mean distance between composite bosons is larger than the size of a single composite boson (determined by the fermion–fermion s –wave scattering length a), two composite bosons experience a mutual interaction which can be modelled by an effective potential $U_{\text{eff}}(R)$ (the detailed nature of this interaction depends on whether the motion of the light fermions is two– or three–dimensional, but it is isotropic and repulsive in both cases). The total Hamiltonian of the system of N composite bosons in its crystalline phase then reads:

$$H = \sum_n \frac{\mathbf{P}_n^2}{2M} + V_{\text{int}}((\mathbf{u}_n)) \quad , \quad (2.3)$$

¹We use the term “triangular lattice” as a synonym for “2D hexagonal Bravais lattice”.

²Throughout this chapter, the term “particle” refers to a composite boson.

where M is the mass of the heavier atomic species³, and the total interaction energy $V_{\text{int}}(\mathbf{u}_n)$ is given by:

$$V_{\text{int}}(\mathbf{u}_n) = \frac{1}{2} \sum_{i \neq j} U_{\text{eff}}(|(\mathbf{r}_i - \mathbf{r}_j) + (\mathbf{u}_i - \mathbf{u}_j)|) \quad . \quad (2.4)$$

2.1.2. Harmonic crystal dynamics

We are interested in the ground state properties of the N -particle system described by the Hamiltonian (2.3). This ground state has been numerically studied by Quantum Monte Carlo methods [17]. In this Section, we introduce a harmonic approximation to the N -particle Hamiltonian, which will be used to derive an approximate phase diagram of the system (see Section 2.1.4) with minimal input from the Monte Carlo results.

If the system is in its crystalline phase, the amplitude of the displacement \mathbf{u}_n of particle n from the corresponding lattice site n is characterised by the root-mean-square (RMS) displacement l_n :

$$l_n^2 = \langle \Omega | \mathbf{u}_n^2 | \Omega \rangle \quad , \quad (2.5)$$

where $|\Omega\rangle$ is the exact N -particle ground state of the Hamiltonian H . The discrete translational invariance of the crystal lattice implies that the RMS displacement is the same for all particles in the crystal, *i.e.* $l_n = l$. Deeply in the crystalline domain of the phase diagram, the RMS displacement l is small compared to the characteristic lengthscale R_{eff} of the effective interaction $U_{\text{eff}}(R)$ (*i.e.* $l/R_{\text{eff}} \ll 1$), and we expand the total interaction energy V_{int} as:

$$V_{\text{int}} = V_{\text{int}}^{(0)} + V_{\text{int}}^{(1)}(\mathbf{u}_n) + V_{\text{int}}^{(2)}(\mathbf{u}_n) + \dots \quad . \quad (2.6)$$

In Eq. (2.6) we have the following terms:

- The term $V_{\text{int}}^{(0)}$ is the value of the interaction energy for all particles fixed at their classical equilibrium positions \mathbf{r}_n . It is a constant number and has no incidence on the dynamics of the crystal. It will be dropped in subsequent calculations.
- The term $V_{\text{int}}^{(1)}(\mathbf{u}_n)$ is the contribution to V_{int} which is linear in the displacements (\mathbf{u}_n) . The expansion is performed around the classical equilibrium state of the system, which minimises the total interaction energy $V_{\text{int}}(\mathbf{u}_n)$. Therefore, this term vanishes.
- The term $V_{\text{int}}^{(2)}(\mathbf{u}_n)$ is the contribution to V_{int} which is quadratic in the displacements (\mathbf{u}_n) .

³The total mass of a composite boson is $(M + m)$, where M and m are the masses of the heavier and lighter atoms, respectively. However, the phase transition occurs for mass ratios $M/m > 100$ (see Fig. 2.3), and the lighter mass m can thus be neglected in the kinetic energy part of Eq. (2.3).

2. Simple approaches to the crystal–gas phase diagram

The harmonic approximation, used throughout this section, consists in neglecting all terms containing products of three or more displacement operators. We have thus replaced the original Hamiltonian H by the approximate Hamiltonian H_{harm} given by:

$$H_{\text{harm}} = \sum_n \frac{\mathbf{P}_n^2}{2M} + V_{\text{int}}^{(2)}(\mathbf{u}_n) \quad . \quad (2.7)$$

The Hamiltonian H_{harm} can be diagonalised in terms of phonons, each of which is the quantum equivalent of a classical vibrational mode of the system.

Classical crystal vibrations

We first briefly introduce classical vibrational modes of the crystal [24, 25].

Each classical vibrational mode is characterised by (i) its wavevector \mathbf{k} , and (ii) its polarisation index $p = 1$ or 2 . These two attributes can be condensed into a single multi-index $\kappa = (\mathbf{k}, p)$. The classical vibrational mode κ corresponds to the following lattice wave:

$$\mathbf{u}_n = A \mathbf{e}_\kappa \exp(i(\mathbf{k} \cdot \mathbf{r}_n - \omega_\kappa t)) \quad , \quad (2.8)$$

where A is an arbitrary amplitude, the unit vector \mathbf{e}_κ gives the polarisation, and ω_κ is the frequency of the mode.

For a crystal which comprises N particles, there are $2N$ independent vibrational modes. In order to characterise these modes, we write the quadratic part of the interaction energy as:

$$V_{\text{int}}^{(2)} = \frac{1}{2} \sum_{pq} {}^t\mathbf{u}_p \Lambda_{pq} \mathbf{u}_q \quad , \quad (2.9)$$

where ${}^t\mathbf{u}_p$ is the (real) transpose of \mathbf{u}_p , and the (Λ_{pq}) 's are 2×2 real symmetric matrices given by:

$$\Lambda_{pq}^{ij} = \left. \frac{\partial^2 U^{\text{tot}}(\mathbf{u}_n)}{\partial u_p^i \partial u_q^j} \right|_{(\mathbf{u}_n=\mathbf{0})} \quad . \quad (2.10)$$

The discrete translational invariance of the crystal lattice implies that $\Lambda_{pq} = \Lambda(\mathbf{r}_p - \mathbf{r}_q)$. We now introduce the momentum–space dynamical matrix $\Lambda(\mathbf{k})$ defined as [24]:

$$\Lambda(\mathbf{k}) = \sum_p \Lambda(\mathbf{r}_p) e^{-i\mathbf{k} \cdot \mathbf{r}_p} = -2 \sum_p \Lambda_{0p} \sin^2 \left(\frac{1}{2} \mathbf{k} \cdot \mathbf{r}_p \right) \quad , \quad (2.11)$$

where the second equality follows from the invariance of the crystal lattice under spatial inversion. The classical vibrational modes of the crystal lattice are completely determined by the eigenelements of the dynamical matrices $\Lambda(\tilde{\mathbf{k}})$ [24]. For a given wavevector \mathbf{k} , $\tilde{\Lambda}(\mathbf{k})$ is a 2×2 real symmetric matrix whose eigenvalues are $M\omega_{\mathbf{k},1}^2$ and $M\omega_{\mathbf{k},2}^2$, where $\omega_{\mathbf{k},1}$ and $\omega_{\mathbf{k},2}$ are the frequencies of the two vibrational modes with wavevector \mathbf{k} . The corresponding (unit–normalised and orthogonal) eigenvectors $\mathbf{e}_{\mathbf{k},1}$ and $\mathbf{e}_{\mathbf{k},2}$ are the polarisations of these vibrational modes.

Quantum crystal vibrations

We now return to quantum mechanics and introduce the phonon annihilation (a_κ) and creation (a_κ^\dagger) operators defined by the following relations [26]:

$$\begin{cases} \mathbf{u}_n = \frac{1}{\sqrt{2N}} \sum_{\kappa} \left(\frac{\hbar}{M\omega_\kappa} \right)^{1/2} (a_\kappa \mathbf{e}_\kappa e^{i\mathbf{k}\cdot\mathbf{r}_n} + a_\kappa^\dagger \mathbf{e}_\kappa^* e^{-i\mathbf{k}\cdot\mathbf{r}_n}) \\ \mathbf{P}_n = \frac{i}{\sqrt{2N}} \sum_{\kappa} (M\hbar\omega_\kappa)^{1/2} (-a_\kappa \mathbf{e}_\kappa e^{i\mathbf{k}\cdot\mathbf{r}_n} + a_\kappa^\dagger \mathbf{e}_\kappa^* e^{-i\mathbf{k}\cdot\mathbf{r}_n}) \end{cases} \quad (2.12)$$

The operators a_κ^\dagger and a_κ are the creation and annihilation operators for a phonon in the mode related to the lattice wave of Eq. (2.8). They satisfy the bosonic commutation rules $[a_\kappa, a_{\kappa'}^\dagger] = \delta_{\kappa, \kappa'}$ and $[a_\kappa, a_{\kappa'}] = [a_\kappa^\dagger, a_{\kappa'}^\dagger] = 0$, where $\delta_{\kappa, \kappa'}$ is the Krönecker symbol. In terms of these operators, the Hamiltonian (2.7) reduces to that of $2N$ independent harmonic oscillators indexed by κ :

$$H_{\text{harm}} = \sum_{\kappa} \hbar\omega_\kappa \left(a_\kappa^\dagger a_\kappa + \frac{1}{2} \right) \quad , \quad (2.13)$$

The ground state $|0\rangle$ of the Hamiltonian H_{harm} , corresponding to the absence of any phonon excitation, is an approximation to the N -particle ground state $|\Omega\rangle$ of the complete Hamiltonian H of Eq. (2.3). This approximate ground state can be used to evaluate the RMS displacement l_0 of a particle in the crystal around its lattice site:

$$l_0^2 = \frac{1}{2N} \sum_{\kappa} \frac{\hbar}{M\omega_\kappa} \quad . \quad (2.14)$$

As expected from the discrete translational invariance of the system, the RMS displacement l_0 is the same for all particles in the crystal. It depends both on the distance d between neighbouring lattice sites and on the mass ratio M/m . The dependence on the mass ratio can be made explicit. Recalling that the effective potential $U_{\text{eff}}(R)$ is proportional to⁴ $1/m$ and that the $M\omega_\kappa^2$ are the eigenvalues of the matrix $\Lambda(\mathbf{k})$, we find that the frequency ω_κ is proportional to $(Mm)^{-1/2}$. Equation (2.14) then shows that l_0 is proportional to $(M/m)^{-1/4}$.

2.1.3. The specific case of the triangular lattice

In this Section, we apply the general formalism summarised in Section 2.1.4 to the specific case of the 2D triangular lattice. We obtain an analytical expression for the two branches of the phonon dispersion relation in the nearest-neighbour approximation and compare these analytical results to numerical calculations including five rings of neighbours.

⁴The effective interaction $U_{\text{eff}}(R)$ between two composite bosons is mediated by the lighter fermions: see Chapter 1.

2. Simple approaches to the crystal–gas phase diagram

We express the displacement vectors (\mathbf{u}_n) in an orthonormal basis ($\mathbf{e}_x, \mathbf{e}_y$) with $\mathbf{e}_x = \mathbf{a}_1/d$. Equation (2.10) yields the following expression for Λ_{0p} , where $p = (p_1, p_2)$ is a double integer index:

$$\Lambda_{0p} = -\frac{1}{4} \frac{d^2}{r_p^2} \begin{bmatrix} (2p_1 - p_2)^2 U''(r_p) + 3p_2^2 \frac{U'(r_p)}{r_p} & \sqrt{3} p_2 (2p_1 - p_2) (U''(r_p) - \frac{U'(r_p)}{r_p}) \\ \sqrt{3} p_2 (2p_1 - p_2) (U''(r_p) - \frac{U'(r_p)}{r_p}) & 3p_2^2 U''(r_p) + (2p_1 - p_2)^2 \frac{U'(r_p)}{r_p} \end{bmatrix}. \quad (2.15)$$

We assume that the range R_{eff} of the effective potential $U_{\text{eff}}(R)$ is significantly smaller than the distance d between nearest–neighbour lattice sites. Therefore, we calculate the dynamical matrices $\Lambda(\mathbf{k})$ in the nearest–neighbour approximation. Equation (2.16) yields:

$$\Lambda(\mathbf{k}) = \begin{bmatrix} 4U''(d)s_1^2 + (U''(d) + 3\frac{U'(d)}{d})(s_2^2 + s_3^2) & \sqrt{3}(U''(d) - \frac{U'(d)}{d})(s_3^2 - s_2^2) \\ \sqrt{3}(U''(d) - \frac{U'(d)}{d})(s_3^2 - s_2^2) & 4\frac{U'(d)}{d} + (3U''(d) + \frac{U'(d)}{d})(s_2^2 + s_3^2) \end{bmatrix}, \quad (2.16)$$

where $s_1 = \sin(\frac{1}{2}\mathbf{k} \cdot \mathbf{a}_1)$, $s_2 = \sin(\frac{1}{2}\mathbf{k} \cdot \mathbf{a}_2)$, and $s_3 = \sin(\frac{1}{2}\mathbf{k} \cdot (\mathbf{a}_1 + \mathbf{a}_2))$. Equation (2.16) yields the following analytical expression for the two branches of the dispersion relation, which are obtained as the two eigenvalues of $\Lambda(\mathbf{k})$:

$$m\omega_{1,2}^2(\mathbf{k}) = 2 \left(U''(d) + \frac{U'(d)}{d} \right) (s_1^2 + s_2^2 + s_3^2) \pm 2 \left(U''(d) - \frac{U'(d)}{d} \right) s_0^2, \quad (2.17)$$

where $s_0^2 = \sqrt{(s_1^2 + s_2^2 + s_3^2)^2 - 3(s_1^2 s_2^2 + s_2^2 s_3^2 + s_3^2 s_1^2)}$. Equation 2.17 is symmetrical in s_1, s_2 , and s_3 , and is thus compatible with the six–fold symmetry of the two–dimensional hexagonal lattice.

The wavevectors \mathbf{k} are conveniently described in the reciprocal lattice basis ($\mathbf{a}_1^*, \mathbf{a}_2^*$) defined by $\mathbf{a}_i^* \cdot \mathbf{a}_j = 2\pi \cdot \delta_{ij}$. The reciprocal lattice of a hexagonal lattice is also a hexagonal lattice (see Fig. 2.2(right)):

$$|\mathbf{a}_1^*| = |\mathbf{a}_2^*| = \frac{2\pi}{d} \frac{2}{\sqrt{3}} \quad \text{and} \quad \widehat{(\mathbf{a}_1^*, \mathbf{a}_2^*)} = \frac{\pi}{3}. \quad (2.18)$$

The two branches $\omega_{1,2}^2(\mathbf{k})$ of the dispersion relation are represented in Figure 2.2(right) in the case of the pair potential characterising the interaction between two composite bosons in the fully two–dimensional situation (see Chapter 1), for wavevectors \mathbf{k} whose tips lie on the high–symmetry axes of the Brillouin zone[27]. The analytical results obtained in the nearest–neighbour approximation (Equation 2.17) are compared to numerical calculations taking into account five rings of neighbours on a finite–sized hexagonal lattice with 100 independent particles in both the \mathbf{a}_1 and \mathbf{a}_2 directions. Both calculations have been performed for the lattice parameter $\kappa_0 d = 2.0$ ($1/\kappa_0$ being the composite–boson molecular size). For this lattice parameter, the two branches $\omega_{1,2}^2(\mathbf{k})$ of the dispersion relation are positive for all wavevectors in the Brillouin zone, which ensures that the triangular lattice of composite bosons is stable with respect to harmonic lattice vibrations.

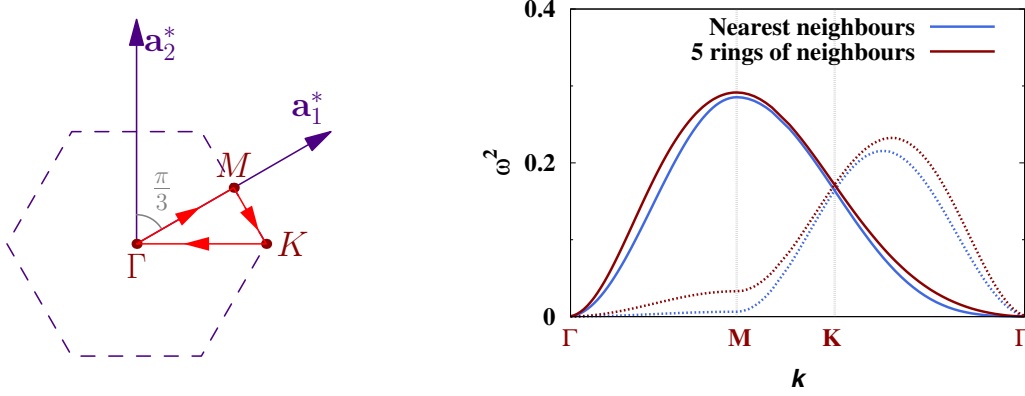


Figure 2.2. **Left:** Brillouin zone of the two-dimensional hexagonal Bravais lattice, with the high-symmetry points $\Gamma(0,0)$, $M(\frac{1}{2},0)$, and $K(\frac{1}{3},\frac{1}{3})$. **Right:** the two branches $\omega_{1,2}^2(\mathbf{k})$ of the dispersion relation for the hexagonal lattice, for wavevectors \mathbf{k} with origin Γ and whose tips lie on the Γ - M - K - Γ path represented in red on the diagram on the left. The pair potential is the one characterising the interaction of two composite bosons in the purely two-dimensional case. The blue graphs correspond to the analytical result in the nearest-neighbour approximation; the red graphs are numerical results taking into account five rings of neighbours. The lattice spacing is $\kappa_0 d = 2.0$, and the squared angular frequencies ω^2 are expressed in units of $(\hbar\kappa_0^2/m)^2$, where $1/\kappa_0$ is the composite-boson molecular size.

2.1.4. Calculation of the phase diagram using the Lindemann criterion

We now use the dispersion relation derived in Section 2.1.3 to obtain an approximate crystal-gas phase diagram of the system of N composite bosons.

For that purpose, we apply the phenomenological Lindemann criterion [25, 28]. We assume at first that the system is in the crystalline phase. Combining Eq. (2.14) with the analytical expression for the two branches of the dispersion relation (Eq. (2.17)), we numerically evaluate the RMS displacement l_0 of a given particle around the corresponding lattice site. The Lindemann criterion states that the crystalline phase is stable as long as $l_0 < \gamma d$, where γ is a constant number which is of the order of 0.2. On the other hand, if $l_0 > \gamma d$, the crystalline phase is unstable, and the ground state of the system corresponds to a gaseous phase.

The value of the Lindemann parameter γ can be extracted from the Quantum Monte Carlo results [17]. This parameter is weakly dependent on the considered scenario (see Chapter 1): $\gamma = 0.23$ if both the heavy and the light atomic motions are two-dimensional, and $\gamma = 0.24$ if the motion of the heavy atoms is two-dimensional whereas that of the light atoms is three-dimensional.

Assuming that the value of the parameter γ is known, the Lindemann criterion, applied within the framework of the harmonic approximation presented in Sections 2.1.2 and 2.1.3, provides a simple approach to the calculation of the phase diagram. For a given two-dimensional density $n = 2/[\sqrt{3}(\kappa_0 d)^2]$, we calculate the RMS displacement l_0^{ref} for

2. Simple approaches to the crystal–gas phase diagram

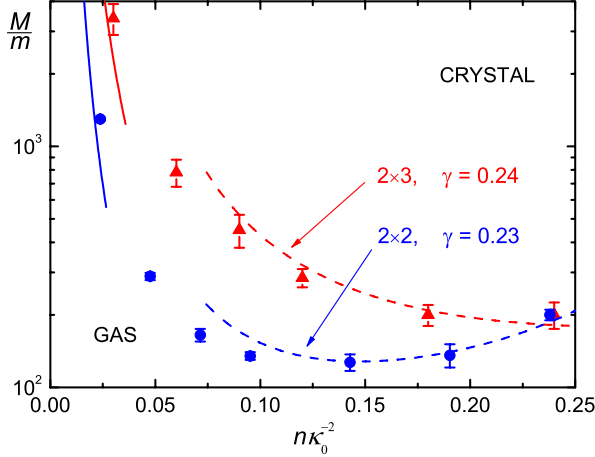


Figure 2.3. Zero-temperature gas–crystal phase diagram of a 2D system of composite bosons, for 3D (red) and 2D (blue) motion of light atoms. The varied parameters are the reduced density $n\kappa_0^{-2}$ (horizontal axis) and the mass ratio M/m (vertical axis). The triangles and circles are the DMC results, the dashed curves show the results of the harmonic approach, and the solid curves show the low-density hard-disk limit. (Reproduced from [17].)

the reference mass ratio $M/m = 1$. The RMS displacement at an arbitrary mass ratio m/M is then given by $l_0 = l_0^{\text{ref}} (M/m)^{-1/4}$ (see Section 2.1.2), and the Lindemann criterion therefore predicts that the crystal–gas phase transition occurs for the following critical mass ratio:

$$\left(\frac{M}{m}\right)_{\text{crit}} = \left(\frac{l_0^{\text{ref}}}{\gamma d}\right)^4. \quad (2.19)$$

The predicted crystal–gas phase diagram is represented in Fig. 2.3, where the results of Eq. (2.19) are seen to be in good agreement with the more accurate Quantum Monte Carlo results [17].

2.2. Hard-core boson approximation for low densities

In this section, we focus on the low-density part of the phase diagram, in which the typical value of the distance between two dimers is much larger than the range R_{eff} of the effective interaction potential $U_{\text{eff}}(R)$. In this limit, and at low enough temperatures, the details of the interaction potential no longer matter, and the low-energy scattering properties of this potential are encoded in the corresponding s -wave scattering length. This scattering length is a two-body parameter which can be extracted from the asymptotic behaviour of the zero-energy scattering wavefunction characterising the relative motion of two colliding particles. In the case of a two-dimensional s -wave collision, the large- R behaviour of this scattering wavefunction reads:

$$\Psi(R) \underset{R \rightarrow \infty}{=} C \ln(R/a_{2D}) \quad , \quad (2.20)$$

where C is an arbitrary constant, and a_{2D} is the sought two-dimensional s -wave scattering length.

In the present case, the considered collision involves two composite bosons. The relative motion of these particles is governed by the Hamiltonian $h = \mathbf{P}^2/M + U_{\text{eff}}(R)$, where \mathbf{R} is the relative position of the two particles, \mathbf{P} is its conjugate momentum, $R = |\mathbf{R}|$, and the reduced mass of two particles of mass M is $M/2$. The effective

interaction $U_{\text{eff}}(R)$ is proportional to $1/m$, whereas the kinetic term is proportional to $1/M$, therefore a_{2D} is a function of the mass ratio M/m .

In the low-density limit, the potential may be replaced by any other potential which has the same two-dimensional scattering length. The crystal-fluid phase diagram of a two-dimensional assembly of hard disks at zero temperature has been studied numerically using Quantum Monte Carlo methods [29]. Therefore, we replace the effective potential $U_{\text{eff}}(R)$ by a hard-disk potential $U_{\text{HD}}(R)$, characterised by the hard-disk diameter D :

$$U_{\text{HD}}(R) = \begin{cases} +\infty & \text{for } R < D/2, \\ 0 & \text{for } R > D/2. \end{cases} \quad (2.21)$$

The scattering length characterising the s -wave collision between two hard disks of radius D is given by⁵ $a_{\text{HD}} = D$. Therefore, for a given mass ratio M/m , the hard-disk radius is chosen to be equal to the ‘physical’ scattering length $a_{2D}(M/m)$.

The Quantum Monte Carlo analysis reported in [29] shows that a two-dimensional system of N bosonic hard disks of radius D undergoes a crystal-fluid phase transition at the critical density $n_{\text{HD}}^{\text{crit}} = 0.33/D^2$. For densities $n_{\text{HD}} < n_{\text{HD}}^{\text{crit}}$, the ground state of the system exhibits no crystalline order, whereas for $n_{\text{HD}} > n_{\text{HD}}^{\text{crit}}$ the ground state is a crystal (even though in the classical picture separated hard disks do not interact at all).

The numerical results for bosonic hard-disk systems yield a simple way to evaluate the low-density part of the phase diagram of our system of composite bosons. For a given mass ratio M/m (chosen large, so that the phase transition occurs at low density: see Fig. 2.3), we calculate the scattering length $a_{2D}(M/m)$ characterising the low-density and low-temperature scattering by the effective potential $U_{\text{eff}}(R)$. Replacing this effective potential by the hard-disk potential $U_{\text{HD}}(R)$, and choosing the radius $D = a_{2D}(M/m)$ so as to leave the scattering length unchanged, the critical density for the crystal-gas phase transition is thus close to $n^{\text{crit}}(M/m) = 0.33/a_{2D}^2(M/m)$.

The results of this approximate low-density approach are compared in Fig. 2.3 to the more accurate Quantum Monte Carlo results, and a good agreement can be observed between the two approaches for densities $n\kappa_0^{-2} < 0.25$.

⁵The centres of the two hard disks can never come any closer than $2 \times D/2 = D$. Combining the asymptotic behaviour of Eq. (2.20), which is exact for $R \geq D$, with the hard-disk condition $\Psi(D) = 0$, one obtains $a_{\text{HD}} = D$.

3. Born–Oppenheimer potentials for the interaction between composite bosons

The object of this chapter is the derivation of the analytical expressions (1.2) and (1.4) for the potentials characterising the effective interaction between two composite bosons in the 2×3 and 2×2 situations, respectively [17]. This derivation hinges on two approximations: (i) the zero–range approximation for the interatomic interaction, and (ii) the Born–Oppenheimer approach, assuming that the motion of the heavy atoms is much slower than that of the light atoms.

The zero–range approximation

As a first step, we consider the interaction between one heavy atom and one light atom. We assume that the scattering length a characterising this interaction is much larger than the range R_e of the interaction potential. Under this assumption, the detailed nature of the atomic interaction is no longer important, and it can be taken into account through the boundary condition for the wavefunction at vanishing interparticle distances. In the case of a 3D s -wave interaction between two atoms, this boundary condition reads [30]:

$$\lim_{r \rightarrow 0} \frac{(r\psi_{3D})'}{r\psi_{3D}} = -\frac{1}{a_{3D}} \quad , \quad (3.1)$$

where $a = a_{3D}$ is the 3D scattering length, r is the interatomic distance, the (s -wave) wavefunction $\psi(r)$ describes the relative motion of the two atoms, and C is an unknown constant. This boundary condition can be rewritten as:

$$\psi_{3D}(r) = C \left(\frac{1}{r} - \frac{1}{a_{3D}} \right) \quad \text{for } R_e \ll r \quad , \quad (3.2)$$

which is the familiar condition that the radial wavefunction be proportional to $(r - a_{3D})$ for $R_e \ll r$. In the 2D case, the corresponding condition reads:

$$\psi_{2D}(r) = C \ln \left(\frac{r}{a_{2D}} \right) \quad \text{for } R_e \ll r \quad , \quad (3.3)$$

where ψ_{2D} is the wavefunction describing the 2D relative motion and a_{2D} is the 2D analog of the scattering length.

3. Born–Oppenheimer potentials for the interaction between composite bosons

We now state the Bethe–Peierls boundary conditions (Eqs. 3.2 and 3.3) in a way that does not depend on dimensionality (3D or 2D). For that purpose, we introduce the free–particle Green’s function $G_\kappa(r)$ for the bound–state energy¹ $\varepsilon = -\hbar^2\kappa^2/2m$, which satisfies the following differential equation:

$$(-\Delta + \kappa^2)G_\kappa(\mathbf{r}) = \delta(\mathbf{r}) \quad . \quad (3.4)$$

In the 3D case, it is given by:

$$G_\kappa^{3D}(r) = \frac{e^{-\kappa r}}{4\pi r} \quad , \quad (3.5)$$

whereas in the 2D case it reads:

$$G_\kappa^{2D}(r) = \frac{K_0(\kappa r)}{2\pi} \quad , \quad (3.6)$$

where $K_0(x)$ is the modified Bessel’s function which decays exponentially for large x [21]. Introducing $\kappa_0 = 1/a$, where $a = a_{3D}$ or a_{2D} depending on the considered case, Eqs. 3.2 and (3.3) both reduce to the condition:

$$\psi(r) = C G_{\kappa_0}(r) \quad \text{for } R_e \ll r \quad . \quad (3.7)$$

The Born–Oppenheimer wavefunction

We now consider a system of N heavy atoms and N light atoms. We use the Born–Oppenheimer approach [31], taking advantage of the motion of the N heavy atoms being much slower than that of the N light atoms. We thus wish to describe the system assuming that the heavy atoms are fixed at their positions $\{\mathbf{R}_i\}_{1 \leq i \leq N}$.

Furthermore, we neglect the interaction between the identical light fermions (which is zero in the zero–range approximation because of the Pauli principle). Hence, we wish to calculate the wavefunction $\Psi(\{\mathbf{R}_i\}, \mathbf{r})$ of a single light fermion in the presence of N fixed heavy atoms. Note that the vectors $\{\mathbf{R}_i\}$ belong to the 2D plane of the heavy atoms, whereas the vector \mathbf{r} , giving the position of the light fermion, can be 3D or 2D depending on the considered situation (2×3 or 2×2 : see Chapter 1).

More precisely, we wish to calculate the N lowest eigenvalues of the Hamiltonian for a single light fermion whose motion is free everywhere except at the positions of the heavy atoms, where the Bethe–Peierls condition (3.7) is applied. The sum of these N energies will provide the Born–Oppenheimer potential describing the effective interaction between the molecules.

We seek the wavefunction of a single light fermion in the form

$$\Psi(\{\mathbf{R}_i\}, \mathbf{r}) = \sum_{i=1}^N C_i G_\kappa(\mathbf{r} - \mathbf{R}_i) \quad , \quad (3.8)$$

¹The mass m of a light atom is very close the reduced mass $Mm/(M + m)$ of one light atom and one heavy atom.

which describes free motion everywhere except at the singular points \mathbf{R}_i . The energy of the state $\Psi(\{\mathbf{R}_i\}, \mathbf{r})$ is $\varepsilon = -\hbar^2 \kappa^2 / 2m$. The Green's functions G_κ are given by Eq. (3.5) or by Eq. (3.6) depending on whether the motion of the light atoms is 3D or 2D, and are calculated for the energy ε .

The coefficients C_i appearing in Eq. (3.8) are determined by applying the Bethe–Peierls boundary condition at the N heavy atom positions $\{\mathbf{R}_i\}$:

$$\Psi(\{\mathbf{R}_i\}, \mathbf{r}) \underset{\mathbf{r} \rightarrow \mathbf{R}_i}{=} C_i G_{\kappa_0}(\mathbf{r} - \mathbf{R}_i) \quad . \quad (3.9)$$

The coefficient of G_{κ_0} on the right–hand side of Eq. (3.9) is C_i in order to ensure that both sides of the equality have the same irregular parts. These N boundary conditions yield a system of N linear equations for the coefficients $\{C_i\}_{1 \leq i \leq N}$, which we write as

$$A \mathbf{C} = 0 \quad . \quad (3.10)$$

In Eq. (3.10), \mathbf{C} is the N –component vector (C_1, \dots, C_N) , and A is an $N \times N$ real symmetric matrix depending on κ and $\{\mathbf{R}_i\}$, whose coefficients A_{ij} are given by:

$$A_{ij} = \lambda(\kappa) \delta_{ij} + G_\kappa(R_{ij}) (1 - \delta_{ij}) \quad , \quad (3.11)$$

where $R_{ij} = |\mathbf{R}_i - \mathbf{R}_j|$ and

$$\lambda(\kappa) = \lim_{r \rightarrow 0} [G_\kappa(r) - G_{\kappa_0}(r)] \quad . \quad (3.12)$$

The linear system (3.10) has non–zero solutions if

$$\det(A(\kappa, \{\mathbf{R}_i\})) = 0 \quad , \quad (3.13)$$

which is a polynomial equation whose N roots $(\kappa_i)_{1 \leq i \leq N}$ yield the sought N energies $\varepsilon_i = -\hbar^2 \kappa_i^2 / 2m$.

Calculation of the total energy

For infinitely large separations R_{ij} between heavy atoms, all off–diagonal elements in A vanish, and Eq. (3.13) yields an N –fold degenerate ground state whose energy is $-\hbar^2 \kappa_0^2 / 2m$. We now consider finite, albeit large, values of $\{R_{ij}\}$. More precisely, we assume that the following parameter remains small:

$$\xi = \frac{G_{\kappa_0}(\tilde{R})}{\kappa_0 \lambda'_\kappa(\kappa_0)} \ll 1 \quad , \quad (3.14)$$

where \tilde{R} is a typical value for the $\{R_{ij}\}$ and $\lambda'_\kappa(\kappa_0) = d\lambda/d\kappa$, taken at $\kappa = \kappa_0$.

Calculation of the determinant

We now calculate the determinant appearing in Eq. (3.13) to second order in ξ . The parameter ξ being small entails that $\lambda'_\kappa(\kappa_0)$ is large and, hence, that $\kappa(\lambda)$ is a slowly-varying function for small values of λ . We expand $\kappa(\lambda)$ to second order in λ :

$$\kappa(\lambda) = \kappa_0 + \kappa'_\lambda \lambda + \frac{1}{2} \kappa''_{\lambda\lambda} \lambda^2 \quad , \quad (3.15)$$

where $\kappa'_\lambda = \partial\kappa/\partial\lambda$ and $\kappa''_{\lambda\lambda} = \partial^2\kappa/\partial\lambda^2$, all derivatives being taken at $\lambda = 0$. We also expand $G_\kappa(R_{ij})$ to first order in λ :

$$G_\kappa(R_{ij}) = G_{\kappa_0}(R_{ij}) + \kappa'_\lambda \lambda \frac{\partial G_{\kappa_0}(R_{ij})}{\partial\kappa} \quad . \quad (3.16)$$

We introduce the $N \times N$ symmetric matrix K such that:

$$A = \lambda (\mathbb{1} + K) \quad , \quad (3.17)$$

The matrix elements K_{ij} depend on λ and are all of order ξ :

$$K_{ij}(\lambda) = \frac{1}{\lambda} \left[G_{\kappa_0}(R_{ij}) + \kappa'_\lambda \lambda \frac{\partial G_{\kappa_0}(R_{ij})}{\partial\kappa} \Big|_{\kappa=\kappa_0} \right] (1 - \delta_{ij}) \quad . \quad (3.18)$$

We calculate the determinant $\det(A)$ through the identity²:

$$\det(A) = \exp[\text{Tr}(\ln A)] \quad , \quad (3.19)$$

where $\text{Tr}(M)$ denotes the trace of the square matrix M . Noting that $\text{Tr}(K) = 0$, Eqs. (3.17), (3.18), and (3.19) yield the following expansion for $\det(A)$ up to second order in ξ :

$$\begin{aligned} \det(A) = \lambda^N & \left(1 - \frac{1}{2} \kappa'^2_\lambda \sum_{i \neq j} \left[\frac{\partial G_{\kappa_0}(R_{ij})}{\partial\kappa} \right]^2 \right) \\ & - \lambda^{N-1} \frac{1}{2} \kappa'_\lambda \sum_{i \neq j} \frac{\partial G_{\kappa_0}^2(R_{ij})}{\partial\kappa} - \lambda^{N-2} \frac{1}{2} \sum_{i \neq j} G_{\kappa_0}^2(R_{ij}) + \dots \quad (3.20) \end{aligned}$$

Calculation of the total energy

The N roots λ_i of the polynomial (3.20) yield the N sought bound–state energies ε_i . The total energy of N light fermions in the presence of the N fixed heavy fermions is $E = \sum_{i=1}^N \varepsilon_i$, which, using Eq. (3.15), is given by:

$$E = -\frac{\hbar^2}{2m} \left[N\kappa_0^2 + 2\kappa_0\kappa'_\lambda \sum_{i=1}^N \lambda_i + (\kappa\kappa'_\lambda)'_\lambda \sum_{i=1}^N \lambda_i^2 \right] \quad , \quad (3.21)$$

²Equation (3.19) holds for any positive–definite symmetric matrix.

where $(\kappa\kappa'_\lambda)'_\lambda = \kappa_0\kappa''_{\lambda\lambda} + \kappa'^2_\lambda$. The quantities $\sum_{i=1}^N \lambda_i$ and $\sum_{i=1}^N \lambda_i^2$ are symmetric functions of the roots $\{\lambda_i\}$ of the polynomial (3.20). Hence, they can be expressed in terms of the coefficients of this polynomial. Up to second order in ξ , we find:

$$\sum_{i=1}^N \lambda_i = \frac{1}{2}\kappa'_\lambda \sum_{i \neq j} \frac{\partial G^2_{\kappa_0}(R_{ij})}{\partial \kappa} \quad , \quad (3.22)$$

$$\sum_{i=1}^N \lambda_i^2 = \sum_{i \neq j} G^2_{\kappa_0}(R_{ij}) \quad . \quad (3.23)$$

Finally, substituting Eqs. (3.22) and (3.23) into Eq. (3.21), the total energy E reduces to:

$$E(\{\mathbf{R}_i\}) = -N \varepsilon_0 + \frac{1}{2} \sum_{i \neq j} U(R_{ij}) \quad , \quad (3.24)$$

where $\varepsilon_0 = -\hbar^2\kappa_0^2/2m$ and the function $U(R)$ is given by:

$$U(R) = -\frac{\hbar^2}{m} \left[\kappa_0(\kappa'_\lambda)^2 \frac{\partial G^2_{\kappa_0}(R)}{\partial \kappa} + (\kappa\kappa'_\lambda)'_\lambda G^2_{\kappa_0}(R) \right] \quad . \quad (3.25)$$

Analytical expressions for the effective potentials

We have calculated the total energy $E(\{\mathbf{R}_i\})$ of N light atoms as a function of the positions $\{\mathbf{R}_i\}$ of the heavy atoms. In the Born–Oppenheimer approach [31], the total energy of the light atoms gives the effective potential energy for the heavy atoms. Therefore, Eq. (3.25) gives the total effective potential for a system of N composite bosons. Dropping the constant energy offset $(-N \varepsilon_0)$, the structure of this equation shows that the composite bosons interact via the *effective pair potential* $U(R)$. We now derive analytical expressions for this effective potential in the 2×3 and 2×2 situations.

If the motion of the light atoms is 3D (2×3 situation), the Green's function G^3_κ is given by Eq. (3.5). Equation (3.12) then leads to $\lambda_{3D}(\kappa) = (\kappa_0 - \kappa)/4\pi$. The effective potential reads:

$$U_{3D}(R) = 4|\varepsilon_0| (1 - (2\kappa_0 R)^{-1}) \frac{\exp(-2\kappa_0 R)}{\kappa_0 R} \quad , \quad (1.2)$$

and the corresponding validity criterion, given by Eq. (3.14), is $\exp(-\kappa_0 R)/(\kappa_0 R) \ll 1$.

If the motion of the light atoms is 2D (2×2 situation), the Green's function G^2_κ is given by Eq. (3.6). In this case, $\lambda_{2D}(\kappa) = \ln(\kappa_0/\kappa)/2\pi$. The effective potential is given by:

$$U_{2D}(R) = 4|\varepsilon_0| \left[\kappa_0 R K_0(\kappa_0 R) K_1(\kappa_0 R) - K_0^2(\kappa_0 R) \right] \quad , \quad (1.4)$$

and the validity criterion is $K(\kappa_0 r) \ll 1$.

Both criteria are well satisfied for $\kappa_0 R \geq 2$.

4. Decay processes for composite bosons

The gaseous and solid phases of weakly bound molecules are actually metastable. The main decay channels are the relaxation of molecules into deep bound states and the formation of trimer states by one light and two heavy atoms (see Section 1.1.1 and [17]).

In order to achieve the large mass ratios $M/m > 100$ required for the realisation of the crystalline phase, one should put heavy atoms in an optical lattice, where for a small filling factor they acquire a large effective mass M_* . The crystalline phase then emerges as a superlattice.

In this chapter, we focus on the stability of the dimers in an optical lattice, and we evaluate the relaxation rates for the two main decay processes.

4.1. Collisional relaxation into deeply bound states

Let m be the mass of the light atoms, and M_* the effective mass of the heavy fermions in an optical lattice. For a large effective mass ratio M_*/m , the relaxation into deeply bound states occurs when a molecule is approached by another light atom¹ and both light-heavy separations are of the order of the size of a deep bound state. This size is determined by the range R_e of the interatomic interaction, which satisfies $R_e \ll \kappa_0^{-1}$, where κ_0^{-1} is the molecular size (see Section 1.2) and \tilde{R} is a typical value for the distances $\{R_{ij}\}$ between the heavy atoms. The released binding energy is taken by outgoing particles which escape from the sample. The rate of this process is not influenced by the optical lattice.

We estimate this rate in the solid phase and near the gas-solid transition to the leading order in $(\kappa_0 \tilde{R})^{-1}$. At light-heavy separations $r_{1,2} \ll \kappa_0^{-1}$ the initial-state wavefunction for a single heavy atom (position \mathbf{R}) and two light atoms (positions \mathbf{r}_1 and \mathbf{r}_2) reads:

$$\tilde{\Psi}(\mathbf{R}, \mathbf{r}_1, \mathbf{r}_2) = B(\kappa_0^{-1}, \tilde{R}) \psi(\mathbf{r}_1, \mathbf{r}_2) \quad . \quad (4.1)$$

We write the wavefunction (4.1) as an antisymmetrized product of wavefunctions of the form $C_i G_\kappa(\mathbf{r}_i - \mathbf{R})$, where G_κ is the free-particle Green's function, given by Eq. (3.5) or by Eq. (3.6) depending on whether the motion of the light atoms is 3D (2×3 case) or 2D (2×2 case). For the 2×3 case ($\kappa_0^{-1} = a$), we find

$$B \approx (1/\tilde{R}a^2) \exp(-\tilde{R}/a) \quad . \quad (4.2)$$

¹The relaxation involving one light and two heavy atoms is strongly suppressed, as it requires the heavy atoms to approach each other and get to the same lattice site.

4. Decay processes for composite bosons

The quantity $W = B^2 R_e^6$ is the probability of having both light atoms at distances $\sim R_e$ from a heavy atom, and the relaxation rate is $\nu_{3D} \propto W$. As the short-range physics is characterised by the energy scale \hbar^2/mR_e^2 , we restore the dimensions and write:

$$\nu_{3D} = C(\hbar/m)(R_e/a)^4(1/\tilde{R}^2) \exp(-2\tilde{R}/a), \quad (4.3)$$

where the typical distance \tilde{R} is linked to the 2D density by $\tilde{R}^{-2} \approx n$. The coefficient C depends on a particular system and is ~ 1 within an order of magnitude. The relaxation rate ν_{3D} is generally rather low. For the ^{40}K - ^6Li mixture, where $R_e \approx 50 \text{ \AA}$, even at $na^2 = 0.24$ (see Fig. 1) the relaxation time exceeds 10s for the density $n = 10^9 \text{ cm}^{-2}$ and the scattering length $a = 1600 \text{ \AA}$. In the 2×2 case, for the same n and κ_0^{-1} the probability W is smaller and the relaxation is slower.

4.2. Formation of trimer bound states

The formation of trimer bound states by one light and two heavy atoms occurs when two molecules approach each other at distances $R \lesssim \kappa_0^{-1}$. It is accompanied by a release of the second light atom.

4.2.1. Born–Oppenheimer wavefunction for a trimer

The existence of the trimer states is seen considering a light atom (position \mathbf{r}) interacting with two heavy ones (positions \mathbf{R}_1 and \mathbf{R}_2). We use the Born–Oppenheimer approximation, assuming as a first step that the heavy atoms are fixed. We seek the wavefunction of this system in the form:

$$\Psi_{\text{trimer}}(\{\mathbf{R}_1, \mathbf{R}_2\}, \mathbf{r}) = C_1 G_\kappa(\mathbf{r} - \mathbf{R}_1) + C_2 G_\kappa(\mathbf{r} - \mathbf{R}_2) \quad , \quad (4.4)$$

where $G_\kappa(\mathbf{r})$ is the (3D or 2D) free-particle Green’s function. Applying the Bethe–Peierls boundary condition (3.7) at each of the two heavy-atom positions, we obtain a second-order polynomial condition on κ (see Eq. (3.13)), whose roots yield the energies $-\hbar^2\kappa^2/2m$ of the possible states Ψ_{trimer} . The lowest-energy solution is the gerade state ($C_1 = C_2$). In the Born–Oppenheimer approach, its energy $\varepsilon_+(R)$ introduces an effective attractive potential acting on the heavy atoms, and the trimer states are bound states of two heavy atoms in this potential.

4.2.2. Trimer formation in an optical lattice

In an optical lattice, the trimers are eigenstates of the Hamiltonian

$$H_0 = -\frac{\hbar^2}{2M_*} \sum_{i=1,2} \Delta_{\mathbf{R}_i} + \varepsilon_+(R_{12}) \quad . \quad (4.5)$$

In a deep lattice, one can neglect all higher bands and regard \mathbf{R}_i as discrete lattice coordinates and Δ as the lattice Laplacian. Then, the fermionic nature of the heavy atoms prohibits them to be in the same lattice site.

For a very large effective mass ratio M_*/m , the kinetic energy term in H_0 can be neglected, and the lowest trimer state has the energy

$$\varepsilon_{\text{tr}} \approx \varepsilon_+(L) \quad , \quad (4.6)$$

where L is the spatial period of the lattice. It consists of a pair of heavy atoms localized at neighbouring sites and a light atom in the gerade state. Higher trimer states are formed by heavy atoms localized in sites separated by distances $R > L$. This picture breaks down at large R , where the spacing between trimer levels is comparable with the tunneling energy \hbar^2/M_*L^2 and the heavy atoms are delocalized.

The scale of energies in a many-body system of composite bosons is much smaller than $|\varepsilon_0|$. Thus, the formation of trimers in molecule-molecule ‘‘collisions’’ is energetically allowed only if the trimer binding energy is $\varepsilon_{\text{tr}} < 2\varepsilon_0$. Since the lowest trimer energy in the optical lattice is $\varepsilon_+(L)$, the trimer formation requires the condition $\varepsilon_+(L) \lesssim 2\varepsilon_0$, which is equivalent to $\kappa_0^{-1} \gtrsim 1.6L$ in the 2×3 case and $\kappa_0^{-1} \gtrsim 1.25L$ in the 2×2 case. This means that for a sufficiently small molecular size κ_0^{-1} , or for a sufficiently large lattice period L , the formation of trimers is forbidden. At a larger molecular size or smaller L the trimer formation is possible.

4.2.3. Rate of formation of trimers in an optical lattice

We now assume that κ_0^{-1}/L is large enough for the formation of trimers to be energetically allowed, and we calculate the rate of trimer formation.

For that purpose, we consider the interaction between two molecules as a reduced three-body problem, accounting for the fact that one of the light atoms is in the gerade state and the other one in the ungerade state ($C_1 = -C_2$). The gerade light atom is integrated out and is substituted by the effective potential $\varepsilon_+(R)$. For the ungerade state the adiabaticity breaks down at inter-heavy separations $R \lesssim \kappa_0^{-1}$, and the ungerade light atom is treated explicitly.

The wavefunction of the reduced 3-body problem satisfies the Schrödinger equation

$$\left[H_0 - \frac{\hbar^2 \nabla_{\mathbf{r}}^2}{2m} - E \right] \psi(\{\mathbf{R}\}, \mathbf{r}) = 0 \quad , \quad (4.7)$$

where the energy E is close to $2\varepsilon_0$, $\{\mathbf{R}\}$ denotes the set $\{\mathbf{R}_1, \mathbf{R}_2\}$, and \mathbf{r} is the coordinate of the ungerade light atom. The interaction between this atom and the heavy ones is replaced by the Bethe–Peierls boundary condition (3.7) on ψ . The three-body problem can then be solved by encoding the information on the wavefunction ψ in an auxiliary function $f(\{\tilde{\mathbf{R}}\})$ [32] and representing the solution of Eq. (4.7) in the form:

$$\psi = \sum_{\{\tilde{\mathbf{R}}\}, \nu} \chi_{\nu}(\{\mathbf{R}\}) \chi_{\nu}^*(\{\tilde{\mathbf{R}}\}) f(\{\tilde{\mathbf{R}}\}) F_{\kappa_{\nu}}(\mathbf{r}, \{\tilde{\mathbf{R}}\}) \quad , \quad (4.8)$$

where $\chi_{\nu}(\{\mathbf{R}\})$ is an eigenfunction of H_0 with energy ε_{ν} , $F_{\kappa_{\nu}}(\mathbf{r}, \{\tilde{\mathbf{R}}\}) = G_{\kappa_{\nu}}(\mathbf{r} - \tilde{\mathbf{R}}_1) - G_{\kappa_{\nu}}(\mathbf{r} - \tilde{\mathbf{R}}_2)$, and $\kappa_{\nu} = \sqrt{2m(\varepsilon_{\nu} - E)/\hbar^2}$. For $\varepsilon_{\nu} < E$, the

4. Decay processes for composite bosons

trimer formation in the state ν is possible. This is consistent with an imaginary value for κ_ν and the Green function G_{κ_ν} describing an outgoing wave of the light atom and trimer.

We derive an equation for the function f in a deep lattice, where the tunneling energy $\hbar^2/M_*L^2 \ll |\varepsilon_0|$. Then the main contribution to the sum in Eq. (4.8) comes from the states ν for which $|\varepsilon_\nu - \varepsilon_+(R_{12})| \lesssim \hbar^2/M_*L^2$. The sum is calculated by expanding κ_ν around $\kappa(R_{12}) = \sqrt{2m(\varepsilon_+(R_{12}) - E)/\hbar^2}$ up to first order in $(\varepsilon_\nu - \varepsilon_+(R_{12}))/\varepsilon_0$ and using the equation $(H_0 - \varepsilon_\nu)\chi_\nu = 0$. The equation for f is then obtained by taking the limit $\mathbf{r} \rightarrow \mathbf{R}_1$ in the resulting expression for ψ and comparing it with the boundary condition (3.7). This yields

$$\left[-\frac{\hbar^2}{2M_*} \sum_{i=1,2} \Delta_{\mathbf{R}_i} + U_{\text{eff}}(R_{12}) \right] f(\mathbf{R}_1, \mathbf{R}_2) = 0 \quad , \quad (4.9)$$

where the effective potential $U_{\text{eff}}(R_{12})$ is given by

$$U_{\text{eff}}(R) = \frac{\hbar^2 \kappa(R)}{m} \frac{\lambda(\kappa(R)) - G_{\kappa(R)}(R)}{(\partial/\partial \kappa)[\lambda(\kappa(R)) - G_{\kappa(R)}(R)]} \quad , \quad (4.10)$$

and

$$\lambda(\kappa) = \lim_{r \rightarrow 0} [G_\kappa(r) - G_{\kappa_0}(r)] \quad . \quad (3.12)$$

At large distances one has $U_{\text{eff}} \approx U(R) + 2\varepsilon_0 - E$, and for smaller R where $\varepsilon_+(R) < E$, the potential U_{eff} acquires an imaginary part accounting for the decay of molecules into trimers. The number of trimer states that can be formed grows with the molecular size. It eventually becomes independent of L , and so does the loss rate.

In this limit, we solve Eq. (4.9) for two molecules with zero total momentum under the condition that $f(\mathbf{R}_1, \mathbf{R}_2)$ is maximal for $|\mathbf{R}_1 - \mathbf{R}_2| = \tilde{R} \approx n^{-1/2}$. We thus obtain E as a function of the density and mass ratio, and its imaginary part gives the loss rate ν for the many body system. Numerical analysis for $0.06 < n\kappa_0^{-2} < 0.4$ and $50 < M_*/m < 2000$ is well fitted by

$$\nu \approx (D\hbar n/M_*)(n\kappa_0^{-2}) \exp(-J\sqrt{M_*/m}) \quad , \quad (4.11)$$

with $D = 7$ and $J = 0.95 - 1.4(n\kappa_0^{-2})$ for the 2×3 case, and $D = 10^2$, $J = 1.45 - 2.8(n\kappa_0^{-2})$ in the 2×2 case. One can suppress ν by increasing M_*/m , whereas for $M_*/m \lesssim 100$ the trimers can be formed on a time scale $\tau \lesssim 1$ s.

5. Suggestion for a new experiment

In real experiments the ultracold mixture of fermionic atoms is in a trapping potential created, for example, by an optical dipole trap [10, 33]: a red-detuned Gaussian laser beam is added to the setup, and in order to minimise their total energy, neutral atoms are attracted towards the focal point of the laser beam (solid red lines on Fig. 5.1).

The fermionic atoms are to be trapped, in the quantum degenerate regime, in the presence of a static magnetic field tuned close to an interspecies Feshbach resonance (in the case of a mixture of ${}^6\text{Li}$ and ${}^{40}\text{K}$, such a resonance occurs, for instance, for the magnetic field $B_{\text{res}} = 159.5 \text{ G}$ [34]). Molecules can be created on the BEC side of the resonance (see Fig. 1.1) either by directly cooling the gas at a positive value of the interatomic scattering length a , or by first cooling the gas on the BCS side and then sweeping the magnetic field adiabatically through the resonance [10].

The two-dimensional regime for the heavy atoms is to be reached by loading the heavy atoms into an optical lattice (see Fig. 5.1). In the 2×3 situation, the light atoms are present in the system because they take part in bound dimers involving the heavy atoms. In order to achieve the 2×2 situation, an additional optical lattice, constraining the motion of the light atoms to a 2D plane, is added to the setup.

The exploration of the full zero-temperature phase diagram reported in [17] requires both the 2D density n and the mass ratio M/m to be varied. The density n can be tuned by changing the number of trapped molecules: indeed, the 2D planes generated by the optical lattice have a finite area S , and the density is thus $\propto N/S$.

The ratio M/m of the bare atomic masses is a fixed number. Furthermore, in the case of a ${}^6\text{Li}$ - ${}^{40}\text{K}$ mixture, the bare mass ratio $M/m = 6.7$ is too low for crystallisation to be observed: the crystalline phase is only expected for mass ratios $M/m \gtrsim 100$ (see Fig. 2.3 and [17]). The large mass ratios required for the observation of the crystalline order can be obtained using an additional optical lattice, represented by green horizontal wave on Fig. 5.1). Assuming that the filling factor for the heavy atoms is small, this optical lattice conveys an effective mass M_* to the heavy atoms, which can be made very large. The predicted crystalline phase should then appear as a superlattice. No interplay is expected between the crystal lattice and the underlying optical lattice [19].

An optical lattice with a spatial period of 250 nm, inducing an effective mass $M^* = 20 M$ for ${}^{40}\text{K}$ atoms, should allow the crystalline phase to develop as a superlattice. Using an interspecies Feshbach resonance [34], the scattering length can be tuned to

5. Suggestion for a new experiment

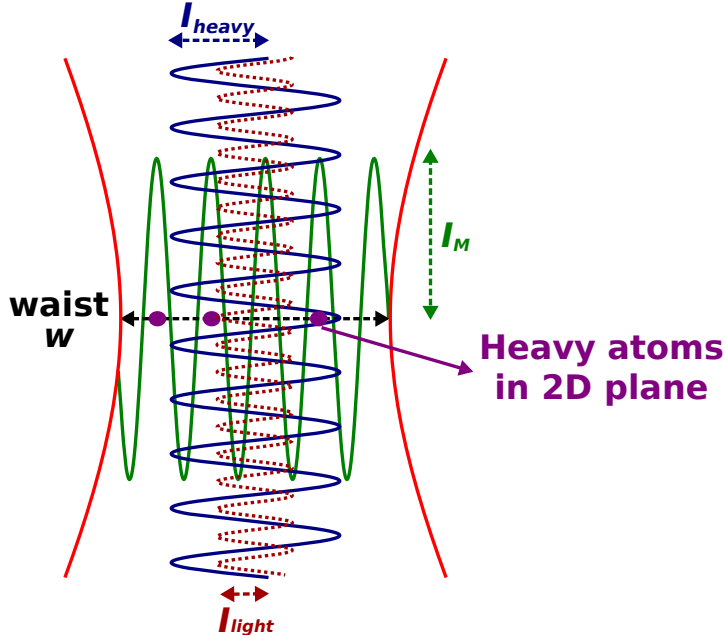


Figure 5.1. Projected experimental setup. The heavy atoms (purple) are trapped within a 2D plane by an optical lattice (I_{heavy} , blue wave). In order to achieve the 2×2 situation, an additional optical lattice is added to the setup in order to constrain the motion of the light atoms to a 2D plane (I_{light} , dashed red wave) The horizontal optical lattice (green) conveys a tunable effective mass to the heavy atoms.

$a = 500$ nm, corresponding to the binding energy $\hbar^2/(ma^2) = 300$ nK, and lower temperatures are experimentally accessible in heteronuclear Fermi gases. With these parameters, crystallisation is predicted to occur for densities of the order of 10^7 atoms/cm², which are experimentally accessible as well.

The lifetime of composite bosons is determined by the rates of decay through the relaxation to deeply bound states and the formation of trimers (see Section 1.1.1). For the values of the experimental parameters chosen above, this lifetime is expected to be of the order of a few seconds [17].

6. Article 1: Crystalline Phase of Strongly Interacting Fermi Mixtures

Crystalline Phase of Strongly Interacting Fermi Mixtures

D. S. Petrov,^{1,2} G. E. Astrakharchik,³ D. J. Papoular,¹ C. Salomon,⁴ and G. V. Shlyapnikov^{1,5}

¹Laboratoire de Physique Théorique et Modèles Statistiques, CNRS, Université Paris Sud, 91405 Orsay, France

²Russian Research Center Kurchatov Institute, Kurchatov Square, 123182 Moscow, Russia

³Departament de Física i Enginyeria Nuclear, Campus Nord B4-B5, Universitat Politècnica de Catalunya, E-08034 Barcelona, Spain

⁴Laboratoire Kastler Brossel, CNRS, Ecole Normale Supérieure, 24 rue Lhomond, 75231 Paris, France

⁵Van der Waals-Zeeman Institute, University of Amsterdam, Valckenierstraat 65/67, 1018 XE Amsterdam, The Netherlands

(Received 24 June 2007; published 28 September 2007)

We show that the system of weakly bound molecules of heavy and light fermionic atoms is characterized by a long-range intermolecular repulsion and can undergo a gas-crystal quantum transition if the mass ratio exceeds a critical value. For the critical mass ratio above 100 obtained in our calculations, this crystalline order can be observed as a superlattice in an optical lattice for heavy atoms with a small filling factor. We also find that this novel system is sufficiently stable with respect to molecular relaxation into deep bound states and to the process of trimer formation.

DOI: 10.1103/PhysRevLett.99.130407

PACS numbers: 05.30.Fk, 03.75.Ss

The use of Feshbach resonances for tuning the interaction in two-component ultracold Fermi gases of ^6Li or ^{40}K has led to remarkable developments, such as the observation of superfluid behavior in the strongly interacting regime through vortex formation [1], and Bose-Einstein condensation of weakly bound molecules of fermionic atoms on the positive side of the resonance (the atom-atom scattering length $a > 0$) [2]. Being highly excited, these extremely large diatomic molecules are remarkably stable with respect to collisional relaxation into deep bound states, which is a consequence of the Pauli exclusion principle for identical fermionic atoms [3].

Currently, a new generation of experiments is being set up for studying mixtures of different fermionic atoms, with the idea of revealing the influence of the mass difference on superfluid properties and finding novel types of superfluid pairing. Weakly bound heteronuclear molecules on the positive side of the resonance are unique objects [4,5], which should manifest collisional stability and can pave a way to creating ultracold dipolar gases.

So far it was believed that dilute Fermi mixtures should be in the gas phase, like Fermi gases of atoms in two different internal states. In this Letter we find that the system of molecules of heavy (mass M) and light (mass m) fermions can undergo a phase transition to a crystalline phase. This is due to a repulsive intermolecular potential originating from the exchange of light fermions and inversely proportional to m . As the kinetic energy of the molecules has a prefactor $1/M$, above a certain mass ratio M/m the system can crystallize.

We show that the interaction potential in a sufficiently dilute system of molecules is equal to the sum of their pair interactions and then analyze the case where the motion of heavy atoms is confined to two dimensions, whereas the light fermions can be either 2D or 3D [6]. We calculate the zero-temperature gas-crystal transition line using the diffusion Monte Carlo (DMC) method and draw the phase

diagram in terms of the mass ratio and density. This phase transition resembles the one for the flux lattice melting in superconductors, where the flux lines are mapped onto a system of bosons interacting via a 2D Yukawa potential [7]. In this case the Monte Carlo studies [8,9] identified the first order liquid-crystal transition at zero and finite temperatures. Aside from the difference in the interaction potentials, a distinguished feature of our system is related to its stability. The molecules can undergo collisional relaxation into deep bound states, or form weakly bound trimers. We analyze resulting limitations on the lifetime of the system.

We first derive the Born-Oppenheimer interaction potential in the system of N molecules. In this approach the state of light atoms adiabatically adjusts itself to the set of heavy-atom coordinates $\{\mathbf{R}\} = \{\mathbf{R}_1, \dots, \mathbf{R}_N\}$ and one calculates the wave function and energy of light fermions in the field of fixed heavy atoms. Omitting the interaction between light (identical) fermions, it is sufficient to find N lowest single-particle eigenstates, and the sum of their energies will give the interaction potential for the molecules. For the interaction between light and heavy atoms we use the Bethe-Peierls approach [10] assuming that the motion of light atoms is free everywhere except for their vanishing distances from heavy atoms.

The wave function of a single light atom then reads

$$\Psi(\{\mathbf{R}\}, \mathbf{r}) = \sum_{i=1}^N C_i G_\kappa(\mathbf{r} - \mathbf{R}_i), \quad (1)$$

where \mathbf{r} is its coordinate, and the Green function G_κ satisfies the equation $(-\nabla_{\mathbf{r}}^2 + \kappa^2)G_\kappa(\mathbf{r}) = \delta(\mathbf{r})$. The energy of the state (1) equals $\epsilon = -\hbar^2 \kappa^2 / 2m$, and here we only search for negative single-particle energies (see below). The dependence of the coefficients C_i and κ on $\{\mathbf{R}\}$ is obtained using the Bethe-Peierls boundary condition:

$$\Psi(\{\mathbf{R}\}, \mathbf{r}) \propto G_{\kappa_0}(\mathbf{r} - \mathbf{R}_i); \quad \mathbf{r} \rightarrow \mathbf{R}_i. \quad (2)$$

Up to a normalization constant, G_{κ_0} is the wave function of a bound state of a single molecule with energy $\epsilon_0 = -\hbar^2 \kappa_0^2/2m$ and molecular size κ_0^{-1} . From Eqs. (1) and (2) one gets a set of N equations: $\sum_j A_{ij} C_j = 0$, where $A_{ij} = \lambda(\kappa) \delta_{ij} + G_{\kappa}(R_{ij})(1 - \delta_{ij})$, $R_{ij} = |\mathbf{R}_i - \mathbf{R}_j|$, and $\lambda(\kappa) = \lim_{r \rightarrow 0} [G_{\kappa}(r) - G_{\kappa_0}(r)]$. The single-particle energy levels are determined by the equation

$$\det[A_{ij}(\kappa, \{\mathbf{R}\})] = 0. \quad (3)$$

For $R_{ij} \rightarrow \infty$, Eq. (3) gives an N -fold degenerate ground state with $\kappa = \kappa_0$. At finite large R_{ij} , the levels split into a narrow band. Given a small parameter

$$\xi = G_{\kappa_0}(\tilde{R})/\kappa_0 |\lambda'_{\kappa}(\kappa_0)| \ll 1, \quad (4)$$

where \tilde{R} is a characteristic distance at which heavy atoms can approach each other, the bandwidth is $\Delta \epsilon \approx 4|\epsilon_0| \xi \ll |\epsilon_0|$. It is important for the adiabatic approximation that all lowest N eigenstates have negative energies and are separated from the continuum by a gap $\sim |\epsilon_0|$.

We now calculate the single-particle energies up to second order in ξ . To this order we write $\kappa(\lambda) \approx \kappa_0 + \kappa'_{\lambda} \lambda + \kappa''_{\lambda\lambda} \lambda^2/2$ and turn from $A_{ij}(\kappa)$ to $A_{ij}(\lambda)$:

$$A_{ij} = \lambda \delta_{ij} + [G_{\kappa_0}(R_{ij}) + \kappa'_{\lambda} \lambda \partial G_{\kappa_0}(R_{ij})/\partial \kappa](1 - \delta_{ij}), \quad (5)$$

where all derivatives are taken at $\lambda = 0$. Using A_{ij} (5) in Eq. (3) gives a polynomial of degree N in λ . Its roots λ_i give the light-atom energy spectrum $\epsilon_i = -\hbar^2 \kappa^2(\lambda_i)/2m$. The total energy $E = \sum_{i=1}^N \epsilon_i$ is then given by

$$E = -(\hbar^2/2m) \left[N \kappa_0^2 + 2 \kappa_0 \kappa'_{\lambda} \sum_{i=1}^N \lambda_i + (\kappa \kappa'_{\lambda})'_{\lambda} \sum_{i=1}^N \lambda_i^2 \right]. \quad (6)$$

Keeping only the terms up to second order in ξ and using basic properties of determinants and polynomial roots we find that the first order terms vanish, and the energy reads $E = N \epsilon_0 + \frac{1}{2} \sum_{i \neq j} U(R_{ij})$, where

$$U(R) = -\frac{\hbar^2}{m} \left[\kappa_0 (\kappa'_{\lambda})^2 \frac{\partial G_{\kappa_0}^2(R)}{\partial \kappa} + (\kappa \kappa'_{\lambda})'_{\lambda} G_{\kappa_0}^2(R) \right]. \quad (7)$$

Thus, up to second order in ξ the interaction in the system of N molecules is the sum of binary potentials (7).

If the motion of light atoms is 3D, the Green function is $G_{\kappa}(R) = (1/4\pi R) \exp(-\kappa R)$, and $\lambda(\kappa) = (\kappa_0 - \kappa)/4\pi$, with the molecular size κ_0^{-1} equal to the 3D scattering length a . Equation (7) then gives a repulsive potential

$$U_{3D}(R) = 4|\epsilon_0| [1 - (2\kappa_0 R)^{-1}] \exp(-2\kappa_0 R)/\kappa_0 R, \quad (8)$$

and the criterion (4) reads $(1/\kappa_0 R) \exp(-\kappa_0 R) \ll 1$. For the 2D motion of light atoms we have $G_{\kappa}(R) = (1/2\pi) K_0(\kappa R)$ and $\lambda(\kappa) = -(1/2\pi) \ln(\kappa/\kappa_0)$, where K_0 is the decaying Bessel function, and κ_0^{-1} follows from [6]. This leads to a repulsive intermolecular potential

$$U_{2D}(R) = 4|\epsilon_0| [\kappa_0 R K_0(\kappa_0 R) K_1(\kappa_0 R) - K_0^2(\kappa_0 R)], \quad (9)$$

with the validity criterion $K_0(\kappa_0 R) \ll 1$. In both cases, which we denote 2×3 and 2×2 for brevity, the validity criteria are well satisfied already for $\kappa_0 R \approx 2$.

The Hamiltonian of the many-body system reads

$$H = -(\hbar^2/2M) \sum_i \Delta_{\mathbf{R}_i} + \frac{1}{2} \sum_{i \neq j} U(R_{ij}), \quad (10)$$

and the state of the system is determined by two parameters: the mass ratio M/m and the rescaled 2D density $n \kappa_0^{-2}$. At a large M/m , the potential repulsion dominates over the kinetic energy and one expects a crystalline ground state. For separations $R_{ij} < \kappa_0^{-1}$ the adiabatic approximation breaks down. However, the interaction potential $U(R)$ is strongly repulsive at larger distances. Hence, even for an average separation between heavy atoms \tilde{R} close to $2/\kappa_0$, they approach each other at distances smaller than κ_0^{-1} with a small tunneling probability $P \propto \exp(-\beta \sqrt{M/m}) \ll 1$, where $\beta \sim 1$. We extended $U(R)$ to $R \lesssim \kappa_0^{-1}$ in a way providing a proper molecule-molecule scattering phase shift in vacuum and checked that the phase diagram for the many-body system is not sensitive to the choice of this extension.

Using the DMC method [11] we solved the many-body problem at zero temperature. For each phase, gaseous and solid, the state with a minimum energy was obtained in a statistically exact way. The lowest of the two energies corresponds to the ground state, the other phase being metastable. The phase diagram is displayed in Fig. 1. The guiding wave function was taken in the Nosanow-Jastrow form [12]. Simulations were performed with 30 particles and showed that the solid phase is a 2D triangular lattice. For the largest density we checked that using more particles has little effect on the results.

For both 2×3 and 2×2 cases the (Lindemann) ratio γ of the rms displacement of molecules to \tilde{R} on the transition

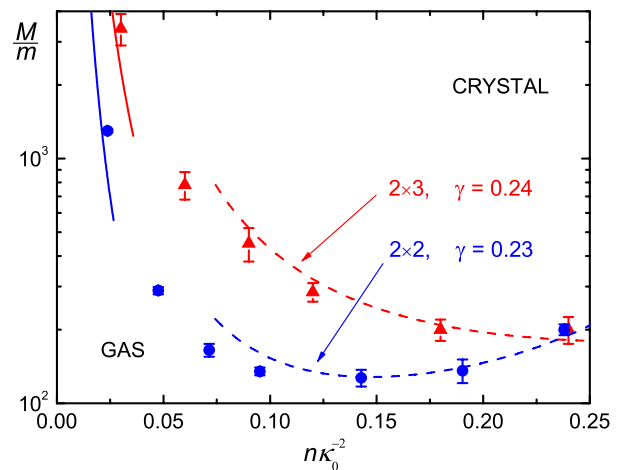


FIG. 1 (color online). DMC gas-crystal transition lines for 3D (triangles) and 2D (circles) motion of light atoms. Solid curves show the low-density hard-disk limit, and dashed curves the results of the harmonic approach (see text).

lines ranges from 0.23 to 0.27. At low densities n the de Broglie wavelength of molecules is $\Lambda \sim \gamma\bar{R} \gg \kappa_0^{-1}$, and $U(R)$ can be approximated by a hard-disk potential with the diameter equal to the 2D scattering length. Then, using the DMC results for hard-disk bosons [13], we obtain the transition lines shown by solid curves in Fig. 1. At larger n , we have $\Lambda < \kappa_0^{-1}$ and use the harmonic expansion of $U(R)$ around equilibrium positions in the crystal, calculate the Lindemann ratio, and select γ for the best fit to the DMC data points (dashed curves in Fig. 1).

The mass ratio above 100, required for the observation of the crystalline order (see Fig. 1), can be achieved in an optical lattice with a small filling factor for heavy atoms. Their effective mass in the lattice M_* can be made very large, and the discussed solid phase should appear as a superlattice. There is no interplay between the superlattice order and the shape of the underlying optical lattice, in contrast to the recently studied solid and supersolid phases in a triangular lattice with the filling factor of order one [14]. Our superlattice remains compressible and supports two branches of phonons.

The gaseous and solid phases of weakly bound molecules are actually metastable. The main decay channels are the relaxation of molecules into deep bound states and the formation of trimer states by one light and two heavy atoms. A detailed analysis of scattering properties of these molecules will be given elsewhere, and here we focus on their stability in an optical lattice.

For a large effective mass ratio M_*/m , the relaxation into deep states occurs when a molecule is approached by another light atom and both light-heavy separations are of the order of the size of a deep state, $R_e \ll \kappa_0^{-1}$ [15]. The released binding energy is taken by outgoing particles which escape from the sample. The rate of this process is not influenced by the optical lattice.

We estimate this rate in the solid phase and near the gas-solid transition to the leading order in $(\kappa_0\bar{R})^{-1}$. At light-heavy separations $r_{1,2} \ll \kappa_0^{-1}$ the initial-state wave function reads $\tilde{\Psi} = B(\kappa_0^{-1}, \bar{R})\psi(\mathbf{r}_1, \mathbf{r}_2)$. Writing it as an antisymmetrized product of wave functions (1), for the 2×3 case ($\kappa_0^{-1} = a$) we find $B \approx (1/\bar{R}a^2)\exp(-\bar{R}/a)$. The quantity $W = B^2R_e^6$ is the probability of having both light atoms at distances $\sim R_e$ from a heavy atom, and the relaxation rate is $\nu_{3D} \propto W$. As the short-range physics is characterized by the energy scale \hbar^2/mR_e^2 , we restore the dimensions and write

$$\nu_{3D} = C(\hbar/m)(R_e/a)^4(1/\bar{R}^2)\exp(-2\bar{R}/a), \quad (11)$$

where $\bar{R}^{-2} \approx n$. The coefficient C depends on a particular system and is ~ 1 within an order of magnitude. The relaxation rate ν_{3D} is generally rather low. For the K-Li mixture where $R_e \approx 50 \text{ \AA}$, even at $na^2 = 0.24$ (see Fig. 1) the relaxation time exceeds 10 s for $n = 10^9 \text{ cm}^{-2}$ and $a = 1600 \text{ \AA}$. In the 2×2 case, for the same n and κ_0^{-1} the probability W is smaller and the relaxation is slower.

The formation of trimer bound states by one light and two heavy atoms occurs when two molecules approach each other at distances $R \lesssim \kappa_0^{-1}$. It is accompanied by a release of the second light atom. The existence of the trimer states is seen considering a light atom interacting with two heavy ones. The lowest energy solution of Eq. (3) for $N = 2$ is the gerade state ($C_1 = C_2$). Its energy $\epsilon_+(R)$ introduces an effective attractive potential acting on the heavy atoms, and the trimer states are bound states of two heavy atoms in this potential.

In an optical lattice the trimers are eigenstates of the Hamiltonian $H_0 = -(\hbar^2/2M_*)\sum_{i=1,2}\Delta_{\mathbf{R}_i} + \epsilon_+(R_{12})$. In a deep lattice one can neglect all higher bands and regard \mathbf{R}_i as discrete lattice coordinates and Δ as the lattice Laplacian. Then, the fermionic nature of the heavy atoms prohibits them to be in the same lattice site. For a very large mass ratio M_*/m the kinetic energy term in H_0 can be neglected, and the lowest trimer state has energy $\epsilon_{\text{tr}} \approx \epsilon_+(L)$, where L is the lattice period. It consists of a pair of heavy atoms localized at neighboring sites and a light atom in the gerade state. Higher trimer states are formed by heavy atoms localized in sites separated by distances $R > L$. This picture breaks down at large R , where the spacing between trimer levels is comparable with the tunneling energy \hbar^2/M_*L^2 and the heavy atoms are delocalized.

In the many-body molecular system the scale of energies in Eq. (10) is much smaller than $|\epsilon_0|$. Thus, the formation of trimers in molecule-molecule ‘‘collisions’’ is energetically allowed only if the trimer binding energy is $\epsilon_{\text{tr}} < 2\epsilon_0$. Since the lowest trimer energy in the optical lattice is $\epsilon_+(L)$, the trimer formation requires the condition $\epsilon_+(L) \lesssim 2\epsilon_0$, which is equivalent to $\kappa_0^{-1} \gtrsim 1.6L$ in the 2×3 case and $\kappa_0^{-1} \gtrsim 1.25L$ in the 2×2 case. This means that for a sufficiently small molecular size or large lattice period L the formation of trimers is forbidden.

At a larger molecular size or smaller L the trimer formation is possible. For finding the rate we consider the interaction between two molecules as a reduced 3-body problem, accounting for the fact that one of the light atoms is in the gerade and the other one in the ungerade state ($C_1 = -C_2$). The gerade light atom is integrated out and is substituted by the effective potential $\epsilon_+(R)$. For the ungerade state the adiabaticity breaks down at interheavy separations $R \lesssim \kappa_0^{-1}$, and the ungerade light atom is treated explicitly. The wave function of the reduced 3-body problem satisfies the Schrödinger equation

$$[H_0 - \hbar^2\nabla_{\mathbf{r}}^2/2m - E]\psi(\{\mathbf{R}\}, \mathbf{r}) = 0, \quad (12)$$

where the energy E is close to $2\epsilon_0$, $\{\mathbf{R}\}$ denotes the set $\{\mathbf{R}_1, \mathbf{R}_2\}$, and \mathbf{r} is the coordinate of the ungerade atom. The interaction between this atom and the heavy ones is replaced by the boundary condition (2) on ψ . The 3-body problem can then be solved by encoding the information on the wave function ψ in an auxiliary function $f(\{\tilde{\mathbf{R}}\})$ [16] and representing the solution of Eq. (12) in the form

$$\psi = \sum_{\{\tilde{\mathbf{R}}\}, \nu} \chi_{\nu}(\{\mathbf{R}\}) \chi_{\nu}^*(\{\tilde{\mathbf{R}}\}) f(\{\tilde{\mathbf{R}}\}) F_{\kappa_{\nu}}(\mathbf{r}, \{\tilde{\mathbf{R}}\}), \quad (13)$$

where $\chi_{\nu}(\{\mathbf{R}\})$ is an eigenfunction of H_0 with energy ϵ_{ν} , and $F_{\kappa_{\nu}}(\mathbf{r}, \{\tilde{\mathbf{R}}\}) = G_{\kappa_{\nu}}(\mathbf{r} - \tilde{\mathbf{R}}_1) - G_{\kappa_{\nu}}(\mathbf{r} - \tilde{\mathbf{R}}_2)$ with $\kappa_{\nu} = \sqrt{2m(\epsilon_{\nu} - E)/\hbar^2}$. For $\epsilon_{\nu} < E$ the trimer formation in the state ν is possible. This is consistent with imaginary κ_{ν} and the Green function $G_{\kappa_{\nu}}$ describing an outgoing wave of the light atom and trimer.

We derive an equation for the function f in a deep lattice, where the tunneling energy $\hbar^2/M_*L^2 \ll |\epsilon_0|$. Then the main contribution to the sum in Eq. (13) comes from the states ν for which $|\epsilon_{\nu} - \epsilon_+(R_{12})| \lesssim \hbar^2/M_*L^2$. The sum is calculated by expanding κ_{ν} around $\kappa(R_{12}) = \sqrt{2m(\epsilon_+(R_{12}) - E)/\hbar^2}$ up to first order in $[\epsilon_{\nu} - \epsilon_+(R_{12})]/\epsilon_0$ and using the equation $(H_0 - \epsilon_{\nu})\chi_{\nu} = 0$. The equation for f is then obtained by taking the limit $\mathbf{r} \rightarrow \mathbf{R}_1$ in the resulting expression for ψ and comparing it with the boundary condition (2). This yields

$$\left[-(\hbar^2/2M_*) \sum_{i=1,2} \Delta_{\mathbf{R}_i} + U_{\text{eff}}(R_{12}) \right] f(\mathbf{R}_1, \mathbf{R}_2) = 0, \quad (14)$$

where the effective potential $U_{\text{eff}}(R_{12})$ is given by

$$U_{\text{eff}}(R) = \frac{\hbar^2 \kappa(R)}{m} \frac{\lambda(\kappa(R)) - G_{\kappa(R)}(R)}{(\partial/\partial \kappa)[\lambda(\kappa(R)) - G_{\kappa(R)}(R)]}. \quad (15)$$

At large distances one has $U_{\text{eff}} \approx U(R) + 2\epsilon_0 - E$, and for smaller R where $\epsilon_+(R) < E$, the potential U_{eff} acquires an imaginary part accounting for the decay of molecules into trimers. The number of trimer states that can be formed grows with the molecular size. Eventually it becomes independent of L and so does the loss rate.

In this limit, we solve Eq. (14) for two molecules with zero total momentum under the condition that $f(\mathbf{R}_1, \mathbf{R}_2)$ is maximal for $|\mathbf{R}_1 - \mathbf{R}_2| = \bar{R} \approx n^{-1/2}$. We thus obtain E as a function of the density and mass ratio, and its imaginary part gives the loss rate ν for the many-body system. Numerical analysis for $0.06 < n\kappa_0^{-2} < 0.4$ and $50 < M_*/m < 2000$ is well fitted by $\nu \approx (D\hbar n/M_*)(n\kappa_0^{-2}) \times \exp(-J\sqrt{M_*/m})$, with $D = 7$ and $J = 0.95-1.4(n\kappa_0^{-2})$ for the 2×3 case, and $D = 10^2$, $J = 1.45-2.8(n\kappa_0^{-2})$ in the 2×2 case. One can suppress ν by increasing M_*/m , whereas for $M_*/m \lesssim 100$ the trimers can be formed on a time scale $\tau \lesssim 1$ s.

In conclusion, we have shown that the system of weakly bound molecules of heavy and light fermionic atoms can undergo a gas-crystal quantum transition. The necessary mass ratio is above 100 and the observation of such crystalline order requires an optical lattice for heavy atoms, where it appears as a superlattice. A promising candidate is the ${}^6\text{Li}$ - ${}^{40}\text{K}$ mixture as the Li atom may tunnel freely in a lattice while localizing the heavy K atoms to reach high

mass ratios. A lattice with period 250 nm and K effective mass $M^* = 20M$ provide a tunneling rate $\sim 10^3 \text{ s}^{-1}$ sufficiently fast to let the crystal form. Near a Feshbach resonance, a value $a = 500$ nm gives a binding energy 300 nK, and lower temperatures should be reached in the gas. The parameters $n\kappa_0^{-2}$ of Fig. 1 are then obtained at 2D densities in the range $10^7-10^8 \text{ cm}^{-2}$ easily reachable in experiments. For $n = 10^8 \text{ cm}^{-2}$ the rate of the trimer formation is of the order of seconds, and these peculiar bound states can be detected optically.

This work was supported by the IFRAF Institute, by ANR (Grants No. 05-BLAN-0205, No. 05-NANO-008-02, and No. 06-NANO-014), by the Dutch Foundation FOM, by the Russian Foundation for Fundamental Research, and by the National Science Foundation (Grant No. PHY05-51164). LKB is a research unit No. 8552 of CNRS, ENS, and University of Pierre et Marie Curie. LPTMS is a research unit No. 8626 of CNRS and University Paris-Sud.

- [1] M. W. Zwierlein *et al.*, Nature (London) **435**, 1047 (2005).
- [2] M. Greiner *et al.*, Nature (London) **426**, 537 (2003); S. Jochim *et al.*, Science **302**, 2101 (2003); M. W. Zwierlein *et al.*, Phys. Rev. Lett. **91**, 250401 (2003); T. Bourdel *et al.*, *ibid.* **93**, 050401 (2004); G. B. Partridge *et al.*, *ibid.* **95**, 020404 (2005).
- [3] D. S. Petrov, C. Salomon, and G. V. Shlyapnikov, Phys. Rev. Lett. **93**, 090404 (2004); Phys. Rev. A **71**, 012708 (2005).
- [4] D. S. Petrov, C. Salomon, and G. V. Shlyapnikov, J. Phys. B **38**, S645 (2005).
- [5] C. Ospelkaus *et al.*, Phys. Rev. Lett. **97**, 120402 (2006).
- [6] In the 2D regime achieved by confining the light-atom motion to zero point oscillations with amplitude l_0 , the weakly bound molecular states exist at a negative a satisfying the condition $|a| \ll l_0$. See D. S. Petrov and G. V. Shlyapnikov, Phys. Rev. A **64**, 012706 (2001).
- [7] D. R. Nelson and H. S. Seung, Phys. Rev. B **39**, 9153 (1989).
- [8] W. R. Magro and D. M. Ceperley, Phys. Rev. B **48**, 411 (1993).
- [9] H. Nordborg and G. Blatter, Phys. Rev. Lett. **79**, 1925 (1997).
- [10] H. Bethe and R. Peierls, Proc. R. Soc. A **148**, 146 (1935).
- [11] For a general reference on the DMC method, see, e.g., J. Boronat and J. Casulleras, Phys. Rev. B **49**, 8920 (1994).
- [12] G. E. Astrakharchik *et al.*, Phys. Rev. Lett. **98**, 060405 (2007).
- [13] L. King, Phys. Rev. B **42**, 8426 (1990).
- [14] S. Wessel and M. Troyer, Phys. Rev. Lett. **95**, 127205 (2005); D. Heidarian and K. Damle, *ibid.* **95**, 127206 (2005); R. G. Melko *et al.*, *ibid.* **95**, 127207 (2005).
- [15] The relaxation involving one light and two heavy atoms is strongly suppressed as it requires the heavy atoms to approach each other and get to the same lattice site.
- [16] D. S. Petrov, Phys. Rev. A **67**, 010703(R) (2003).

7. Conclusion and outlook

The subject of the first part of the present manuscript has been the calculation of the zero-temperature phase diagram of a two-dimensional system of composite bosons formed in an ultracold mixture containing two different types of fermionic atoms. This system has been predicted to undergo a zero-temperature crystal-gas phase transition [17], due to the competition between the zero-point kinetic energy of the molecules and the repulsive interaction between them due to an exchange of light fermions.

The phase diagram of the system has been accurately calculated using the Diffusion Monte Carlo method. We have presented two simple approaches which allow an approximate calculation of this phase diagram (see Chapter 2). The results of these two approaches are in good agreement with the accurate DMC results reported in [17]. Our first approach relies on a harmonic approximation for the total interaction energy in the crystal phase, and the crystal-gas transition line is determined using the phenomenological Lindemann criterion. Our second approach, which does not rely on the Lindemann criterion, is applicable for very low densities. In this limit, the system behaves like a set of 2D hard-core bosons, and the existing prediction [29] for the phase transition in this simpler system can be used.

Prospects for theoretical extensions of this work include the development of a convenient method to distinguish between the crystal and gas phases in experiments. For example, low-energy vibrational modes of the system can be excited using a rotating anisotropic potential. The calculation of the low-energy spectrum for the crystal phase, and its comparison to the corresponding spectrum for molecular Bose-Einstein condensates in the usual gaseous phase, may yield such a method.

Another planned extension on the theory side deals with the behaviour of the system at high densities. The increasing high-density part of the dashed blue line in the crystal-gas phase diagram (Fig. 2.3) suggests that the crystal of composite bosons will melt for higher densities in the 2×2 case. This quantum melting has yet to be confirmed and understood. The beginning of an explanation, in terms of a classical harmonic stability analysis of the 2D triangular lattice, is presented in [35].

The study of heteronuclear fermionic mixtures presented in this part of the manuscript also yields interesting experimental prospects.

First, the phase diagram that we discussed is promising for the observation of the zero-temperature crystal-gas phase transition (see Chapter 5). Such an experiment could be performed, for instance, using heteronuclear Fermi mixture containing equal numbers of ^6Li and ^{40}K atoms. In order to achieve the large mass ratios required to observe crystallisation, an optical lattice can be used to endow the ^{40}K atoms with a

7. Conclusion and outlook

heavier effective mass, while the ${}^6\text{Li}$ atoms tunnel freely through the lattice. An optical lattice with a spatial period of 250 nm, inducing an effective mass $M^* = 20M$ for ${}^{40}\text{K}$ atoms, should allow the crystalline phase to develop as a superlattice. Using an interspecies Feshbach resonance [34], the scattering length can be tuned to $a = 500$ nm, corresponding to the binding energy $\hbar^2/(ma^2) = 300$ nK, and lower temperatures are experimentally accessible in heteronuclear Fermi gases. With these parameters, crystallisation is predicted to occur for densities of the order of 10^7 atoms/cm², which are experimentally accessible as well.

Another interesting prospect is the transfer of the (highly excited) composite bosons obtained on the BEC side of the Feshbach resonance to their ground state. Similar experiments have already been performed with molecules consisting of bosonic atoms (${}^{85}\text{Rb}{}^{133}\text{Cs}$ [36, 37], ${}^{87}\text{Rb}_2$ [38], and ${}^7\text{Li}{}^{133}\text{Cs}$ [39, 40]) and with fermionic ${}^{40}\text{K}{}^{87}\text{Rb}$ molecules [41, 42]. Heteronuclear molecules in their ground state have a large electric dipole moment (0.6 Debye for ${}^{40}\text{K}{}^{87}\text{Rb}$). The dipolar gases thus obtained exhibit anisotropic long-range dipole-dipole interactions [43]. These long-range interactions will strongly affect the physics of Bose-Einstein condensation. The realisation of ground-state composite bosons in the quantum degenerate regime will allow for an experimental exploration of the predicted novel phases [44].

Finally, the collisional stability of weakly-bound heteronuclear molecules (see Section 1.1.1 and [18, 45]) involves few-body effects such as the formation of Efimov trimers. (see *e.g.* [46] for evidence of the Efimov effect through the measurement of the rate of three-body recombination in an ultracold atomic gas). Heteronuclear Fermi mixtures offer a promising alternative system for the experimental investigation of these few-body effects.

Bibliography

- [1] J. Dalibard. “Collisional dynamics of ultracold atomic gases”. In: *Proceedings of the International School of Physics Enrico Fermi, Course CXL: Bose – Einstein condensation in gases*. Societa Italiana di Fisica, 1998. Chap. Collisional dynamics of ultracold atomic gases.
- [2] C. Pethick and H. Smith. *Bose-Einstein condensation in dilute gases*. Cambridge University Press, 2002. ISBN: 0521665809.
- [3] Cheng Chin et al. “Feshbach resonances in ultracold gases”. In: *Rev. Mod. Phys.* 82.2 (Apr. 2010), pp. 1225–1286. DOI: 10.1103/RevModPhys.82.1225.
- [4] Stefano Giorgini, Lev P. Pitaevskii, and Sandro Stringari. “Theory of ultracold atomic Fermi gases”. In: *Rev. Mod. Phys.* 80.4 (Oct. 2008), pp. 1215–1274. DOI: 10.1103/RevModPhys.80.1215.
- [5] Immanuel Bloch, Jean Dalibard, and Wilhelm Zwerger. “Many-body physics with ultracold gases”. In: *Rev. Mod. Phys.* 80.3 (July 2008), pp. 885–964. DOI: 10.1103/RevModPhys.80.885.
- [6] E.M. Lifshitz and L.P. Pitaevskii. *Statistical Physics, Part II*. Pergamon Press, 1980.
- [7] C. A. Regal et al. “Creation of ultracold molecules from a Fermi gas of atoms”. In: *Nature* 424 (2003), p. 47. DOI: 10.1038/nature01738.
- [8] J. Cubizolles et al. “Production of Long-Lived Ultracold Li_2 Molecules from a Fermi Gas”. In: *Phys. Rev. Lett.* 91.24 (Dec. 2003), p. 240401. DOI: 10.1103/PhysRevLett.91.240401.
- [9] S. Jochim et al. “Pure Gas of Optically Trapped Molecules Created from Fermionic Atoms”. In: *Phys. Rev. Lett.* 91.24 (Dec. 2003), p. 240402. DOI: 10.1103/PhysRevLett.91.240402.
- [10] A.-C. Voigt et al. “Ultracold Heteronuclear Fermi-Fermi Molecules”. In: *Phys. Rev. Lett.* 102.2 (Jan. 2009), p. 020405. DOI: 10.1103/PhysRevLett.102.020405.
- [11] F. M. Spiegelhalder et al. “All-optical production of a degenerate mixture of 6Li and ^{40}K and creation of heteronuclear molecules”. In: *Phys. Rev. A* 81.4 (Apr. 2010), p. 043637. DOI: 10.1103/PhysRevA.81.043637.
- [12] M. Greiner, C. Regal, and D. S. Jin. “Emergence of a molecular Bose-Einstein condensate from a Fermi gas”. In: *Nature* 426 (2003). DOI: 10.1038/nature02199.
- [13] S. Jochim et al. “Bose-Einstein Condensation of Molecules”. In: *Science* 302.5653 (2003), pp. 2101–2103. DOI: 10.1126/science.1093280.

Bibliography

- [14] M. W. Zwierlein et al. “Observation of Bose-Einstein Condensation of Molecules”. In: *Phys. Rev. Lett.* 91.25 (Dec. 2003), p. 250401. DOI: 10.1103/PhysRevLett.91.250401.
- [15] D. S. Petrov, C. Salomon, and G. V. Shlyapnikov. “Weakly Bound Dimers of Fermionic Atoms”. In: *Phys. Rev. Lett.* 93.9 (Aug. 2004), p. 090404. DOI: 10.1103/PhysRevLett.93.090404.
- [16] D. S. Petrov, C. Salomon, and G. V. Shlyapnikov. “Scattering properties of weakly bound dimers of fermionic atoms”. In: *Phys. Rev. A* 71.1 (Jan. 2005), p. 012708. DOI: 10.1103/PhysRevA.71.012708.
- [17] D. S. Petrov et al. “Crystalline Phase of Strongly Interacting Fermi Mixtures”. In: *Phys. Rev. Lett.* 99.13 (Sept. 2007), p. 130407. DOI: 10.1103/PhysRevLett.99.130407.
- [18] D. S. Petrov, C. Salomon, and G. V. Shlyapnikov. “Diatomic Molecules in Ultracold Fermi Gases — Novel Composite Bosons”. In: *Journal of Physics B* 38 (2005). DOI: 10.1088/0953-4075/38/9/014.
- [19] D. S. Petrov, C. Salomon, and G. V. Shlyapnikov. “Molecular regimes in ultracold Fermi gases”. In: *Cold Molecules: Theory, Experiment, Applications*. CRC Press, 2009. Chap. 9. ISBN: 978-1-4200-5903-8.
- [20] O I Kartavtsev and A V Malykh. “Low-energy three-body dynamics in binary quantum gases”. In: *Journal of Physics B: Atomic, Molecular and Optical Physics* 40.7 (2007), p. 1429. DOI: 10.1088/0953-4075/40/7/011.
- [21] M. Abramowitz and I.A. Stegun. *Handbook of mathematical functions with formulas, graphs, and mathematical tables*. Dover publications, 1964.
- [22] D. S. Petrov and G. V. Shlyapnikov. “Interatomic collisions in a tightly confined Bose gas”. In: *Phys. Rev. A* 64.1 (June 2001), p. 012706. DOI: 10.1103/PhysRevA.64.012706.
- [23] J. Boronat and J. Casulleras. “Monte Carlo analysis of an interatomic potential for He”. In: *Phys. Rev. B* 49.13 (Apr. 1994), pp. 8920–8930. DOI: 10.1103/PhysRevB.49.8920.
- [24] N. W. Ashcroft and N. D. Mermin. *Solid State Physics*. Holt, Rinehart, and Winston, 1976.
- [25] J. M. Ziman. *Principles of the Theory of Solids*. 2nd ed. Cambridge University Press, 1972.
- [26] L. D. Landau and E. M. Lifshitz. *Statistical Physics, Part I*. 3rd ed. Pergamon Press, 1980.
- [27] C. Kittel and C. Fong. *Quantum theory of solids*. Vol. 316. Wiley New York, 1987. ISBN: 0471624128.
- [28] F. A. Lindemann. “The calculation of molecular vibration frequencies”. In: *Physik. Z* 11 (1910), pp. 609–612.

- [29] Lei Xing. “Monte Carlo simulations of a two-dimensional hard-disk boson system”. In: *Phys. Rev. B* 42.13 (Nov. 1990), pp. 8426–8430. DOI: 10.1103/PhysRevB.42.8426.
- [30] H. Bethe and R. Peierls. “Quantum theory of the dipton”. In: *Proceedings of the Royal Society of London. Series A-Mathematical and Physical Sciences* 148.863 (1935), p. 146.
- [31] C. Cohen-Tannoudji et al. *Quantum Mechanics. Vols. 1 and 2*. Wiley Interscience, 1977.
- [32] D. S. Petrov. “Three-body problem in Fermi gases with short-range interparticle interaction”. In: *Phys. Rev. A* 67.1 (Jan. 2003), p. 010703. DOI: 10.1103/PhysRevA.67.010703.
- [33] Steven Chu et al. “Experimental Observation of Optically Trapped Atoms”. In: *Phys. Rev. Lett.* 57.3 (July 1986), pp. 314–317. DOI: 10.1103/PhysRevLett.57.314.
- [34] E. Wille et al. “Exploring an Ultracold Fermi-Fermi Mixture: Interspecies Feshbach Resonances and Scattering Properties of ${}^6\text{Li}$ and ${}^{40}\text{K}$ ”. In: *Phys. Rev. Lett.* 100.5 (Feb. 2008), p. 053201. DOI: 10.1103/PhysRevLett.100.053201.
- [35] D. J. Papoular. “Harmonic Stability Analysis of the 2D Square and Hexagonal Bravais Lattices for a Finite-Ranged Repulsive Pair Potential. Consequence for a 2D System of Ultracold Composite Bosons”. In: *ArXiv e-prints* (June 2008). arXiv:0806.4325.
- [36] Andrew J. Kerman et al. “Production and State-Selective Detection of Ultracold RbCs Molecules”. In: *Phys. Rev. Lett.* 92.15 (Apr. 2004), p. 153001. DOI: 10.1103/PhysRevLett.92.153001.
- [37] Jeremy M. Sage et al. “Optical Production of Ultracold Polar Molecules”. In: *Phys. Rev. Lett.* 94.20 (May 2005), p. 203001. DOI: 10.1103/PhysRevLett.94.203001.
- [38] K. Winkler et al. “Coherent Optical Transfer of Feshbach Molecules to a Lower Vibrational State”. In: *Phys. Rev. Lett.* 98.4 (Jan. 2007), p. 043201. DOI: 10.1103/PhysRevLett.98.043201.
- [39] J. Deiglmayr et al. “Formation of Ultracold Polar Molecules in the Rovibrational Ground State”. In: *Phys. Rev. Lett.* 101.13 (Sept. 2008), p. 133004. DOI: 10.1103/PhysRevLett.101.133004.
- [40] J. Deiglmayr et al. “Permanent dipole moment of LiCs in the ground state”. In: *Phys. Rev. A* 82.3 (Sept. 2010), p. 032503. DOI: 10.1103/PhysRevA.82.032503.
- [41] K.-K. Ni et al. “A High Phase-Space-Density Gas of Polar Molecules”. In: *Science* 322.5899 (2008), pp. 231–235. DOI: 10.1126/science.1163861.
- [42] S. Ospelkaus et al. “Controlling the Hyperfine State of Rovibronic Ground-State Polar Molecules”. In: *Phys. Rev. Lett.* 104.3 (Jan. 2010), p. 030402. DOI: 10.1103/PhysRevLett.104.030402.

Bibliography

- [43] K.-K. Ni et al. “Dipolar collisions of polar molecules in the quantum regime”. In: *Nature* 464 (2010), p. 1324. DOI: 10.1038/nature08953.
- [44] L. Santos and T. Pfau. “Spin-3 Chromium Bose-Einstein Condensates”. In: *Phys. Rev. Lett.* 96.19 (May 2006), p. 190404. DOI: 10.1103/PhysRevLett.96.190404.
- [45] B. Marcelis et al. “Collisional properties of weakly bound heteronuclear dimers”. In: *Phys. Rev. A* 77.3 (Mar. 2008), p. 032707. DOI: 10.1103/PhysRevA.77.032707.
- [46] T. Kraemer et al. “Evidence for Efimov quantum states in an ultracold gas of caesium atoms”. In: *Nature* 440 (2006), p. 315. DOI: 10.1038/nature04626.

Part II.

Microwave–Induced Fano–Feshbach Resonances

8. Introduction

The second part of this manuscript presents a new scheme we have developed for the manipulation of interactions in ultracold atomic gases using microwave magnetic fields.

The possibility to tailor the nature (repulsive or attractive) and the strength of atomic interactions is a key feature of ultracold atomic systems, making them a versatile experimental playground for the exploration of a vast range of collective quantum phenomena [1, 2]. Let us illustrate this statement with three examples where the manipulation of interactions plays an important role.

We first consider an ultracold gas of bosonic atoms in a trap, cooled down below the critical Bose–Einstein condensation temperature. The stability of the condensate in the trap depends on the nature of the atomic interaction [3, 4]. Repulsive atomic interactions favour large condensate sizes and compete against the confinement due to the trapping potential: hence, repulsive interactions lead to stable Bose–Einstein condensates, such as the one observed with Rubidium 87 in 1995 (see Fig. 8.1(left) and [5]). On the other hand, if the atomic interactions are attractive, the gas tends to increase its density at the centre of the trap: the atomic interactions no longer compensate the confinement due to the trap, and, for large enough atom numbers, the Bose–Einstein condensate implodes. Changing the nature of the atomic interaction makes it possible to go from one regime to the other. For example, starting from a condensed gas of Rubidium 85 atoms, in which condensates are naturally stable, Cornell and Wieman [6] have made the atomic interaction attractive using a Fano–Feshbach resonance [7] and witnessed the implosion of the Bose–Einstein condensate (see Fig. 8.1(right)).

Next, we turn to quantum–degenerate Fermi gases. In order to avoid a suppression

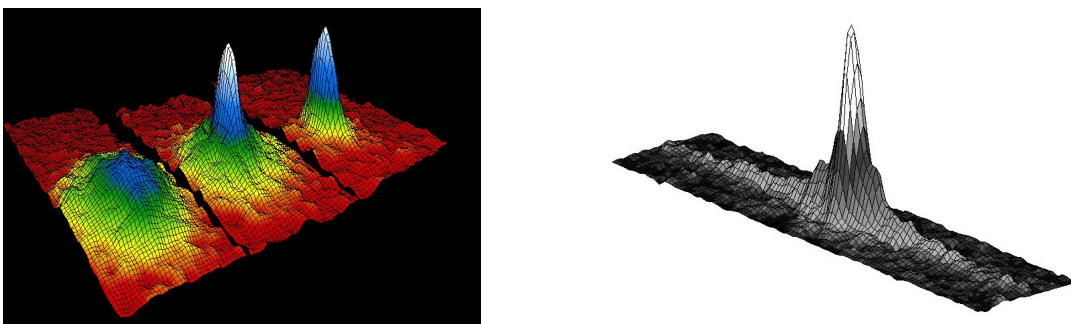


Figure 8.1. **Left:** Stable Bose–Einstein condensate in an ultracold gas of Rubidium 87 atoms. **Right:** Remaining atoms in the trap after a ‘burst’ in an unstable condensate of Rubidium 85 atoms in which the scattering length has been tuned to a negative value. (Reproduced from [5] and [6], respectively).

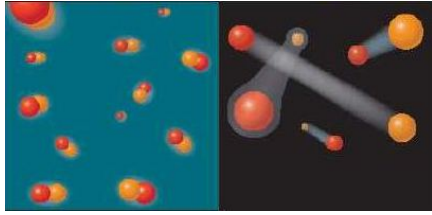


Figure 8.2. Illustration of the two different regimes expected in an ultracold Fermi gas. For strong attractive interactions ($a < 0$, right), the system is in the BCS regime, and its ground state is made up of long-ranged Cooper pairs. For strong repulsive interactions ($a > 0$, left), diatomic (bosonic) molecules appear, and the ground state is a BEC of these molecules.

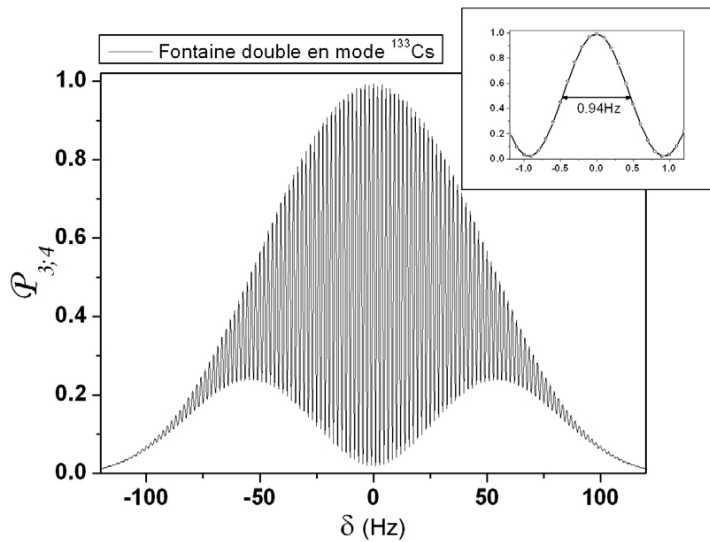


Figure 8.3. Ramsey fringes obtained with the SYRTE Cesium fountain clock, which allows frequency measurements with an accuracy $\approx 10^{-16}$. (Reproduced from [12]).

of the atomic interaction due to the Pauli principle, we assume that the gas contains two different types of atoms: the mixture contains either a single atomic species present in two different internal states [8] or two different atomic species [2]. The ground state of such a system once again depends on the nature of the interaction [9]: for strong attractive interactions, the ground state comprises long-ranged diatomic Cooper pairs, whereas for strong repulsive interactions, diatomic molecules appear (see Fig. 8.2). Fano-Feshbach resonances have been used to explore the crossover between these two different regimes [9].

Our third example is related to metrology. Atomic clocks use ultracold atomic interferometry to provide the most accurate time and frequency measurements to date, with uncertainty estimates as low as a few 10^{-16} [10]. In Cesium atomic fountain clocks, oscillations between two different hyperfine atomic states are probed with a microwave magnetic field whose frequency is tuned close to the atomic transition frequency, using Ramsey interferometry (see Fig. 8.3). However, atomic interactions in the clock cause the atomic transition frequency to be shifted away from the single-atom hyperfine transition frequency by a small amount called the clock shift [11]. This clock shift is highly sensitive to the interaction parameters, and it is one of the most important limitations on the accuracy of the clocks. A precise control over the atomic interactions would allow smaller fluctuations of the clock shift, thus leading to improved clock accuracies.

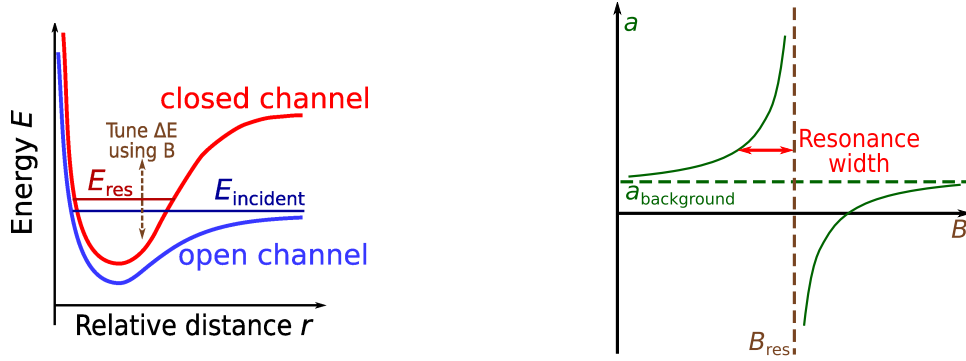


Figure 8.4. Fano–Feshbach resonance induced by a static magnetic field (in the absence of inelastic processes). **Left:** The static magnetic field couples the incident scattering state in the open channel to a bound state of the two atoms in the closed channel; the scattering resonance occurs for magnetic fields such that the scattering state and the bound state have neighbouring energies. **Right:** Illustration of the parameters characterising a Feshbach resonance: the background scattering length a_{bg} , the resonance width ΔB , and the resonance position B_{res} .

8.1. Static-field Fano–Feshbach resonances

The manipulation of atomic interactions is presently performed in ultracold atomic experiments through the use of Fano–Feshbach resonances. These scattering resonances typically occur in the presence of a static magnetic field (see [1, 7] for a review of the theory and experimental applications of static-field Feshbach resonances).

We now give a simplified physical picture for Feshbach resonances occurring in static magnetic fields (see the left-hand part of Fig. 8.4). These resonances are due to the dependence of the magnetic moment of a given atom on its internal state. Let us consider a pair of atoms colliding at very low energies, in a given two-atom internal state, which is represented in blue on Fig. 8.4. We assume that another two-atom internal state is accessible to the atom pair, and we consider a bound dimer state relating to this internal state, represented in red. The blue and red two-atom states relate to different internal states, hence, their magnetic moments are different. Therefore, it is possible to tune the difference in energies between the blue and red two-atom states by adding a static magnetic field. For values of the magnetic field for which the blue and red two-atom states have similar energies, a scattering resonance occurs.

This scattering resonance causes a divergence in the scattering length $a(B_{\text{stat}})$, which exhibits the following behaviour in the vicinity of the resonance:

$$a(B_{\text{stat}}) = a_{\text{bg}} \left(1 - \frac{\Delta B}{B_{\text{stat}} - B_{\text{res}}} \right), \quad (8.1)$$

where B_{stat} is the amplitude of the static magnetic field. In Eq. (8.1), B_{res} is the value of the static magnetic field at which the resonance occurs, the background scattering length a_{bg} is the value of the scattering length for values of B_{stat} that are sufficiently far from B_{res} , and the resonance width ΔB gives the range of values of B_{stat} around B_{res} for which the scattering length a is substantially affected by the resonance. The

resonance parameters B_{res} , a_{bg} and ΔB are illustrated on the right-hand part of Fig. 8.4. Tuning the static magnetic field close to the resonant value B_{res} therefore makes it possible to set the scattering length to an arbitrary value and sign. Positive scattering lengths correspond to an effective atomic interaction which is repulsive, whereas negative scattering lengths correspond to attractive interactions [13].

Fano–Feshbach resonances in static magnetic fields have proved to be an invaluable tool [1, 2, 9] to manipulate the interaction properties of a number of atomic species, such as Lithium, Potassium, or Cesium. In order for a Feshbach resonance to be a convenient experimental tool, it has to be broad enough ($\Delta B \gtrsim 10 \text{ G}$), so that the scattering length can be tuned to the desired value with sufficient accuracy despite the presence of small stray magnetic fields. Broad Feshbach resonances are available for all three atoms listed above (see [7] for a list of available Feshbach resonances: all three atoms listed above exhibit resonances whose widths satisfy $|\Delta B| > 50 \text{ G}$).

However, broad static-field resonances are not available for all atomic species. Furthermore, these resonances often occur for large magnetic fields. For example, all known Feshbach resonances in ^{23}Na occur for magnetic fields larger than 850 G and their widths are smaller than 1.5 G [14]. The observation of resonances in ^{87}Rb is even more involved, as the broadest available resonance is less than 200 mG wide and occurs for a magnetic field larger than 1000 G [15]. These resonances in Sodium and Rubidium have been observed; however, their observation requires elaborate experimental setups involving large coils and highly stabilised currents, and they are thus more difficult to use as a tool in more complex experiments. The manipulation of interactions in atoms such as ^{87}Rb and ^{23}Na thus calls for other experimental schemes.

8.2. Previous work on alternative Feshbach resonances

Alternative schemes causing Feshbach resonances have already been considered, based on the use of electromagnetic fields that are not pure static magnetic fields:

- **Marinescu and You** ([16], November 1998) have suggested using *DC electric fields*;
- Our scheme is especially reminiscent of the *optically-induced Feshbach resonances*, first proposed by **Fedichev, Kagan, Shlyapnikov and Walraven** ([17], September 1996). These resonances are due to a coupling between the scattering state and the resonant bound state caused by an *oscillating electric field* whose frequency is in the optical range. They have been experimentally demonstrated in [18, 19]. However, the lifetimes of the atomic samples undergoing optically-induced Feshbach resonances are severely limited by the losses due to spontaneous emission through the resonant bound state, which is an electronically-excited dimer.
- **Moerdijk, Verhaar, and Nagtegaal** ([20], June 1996) have considered Sodium atoms in the lower hyperfine manifold ($f_1 = 1, f_2 = 1$), trapped in a static mag-

netic field, and suggested using a *radio-frequency* magnetic field whose frequency is tuned close to the single-atom Zeeman splitting to induce scattering resonances. A detailed analysis of their scheme is presented in Section 11.4, where we emphasize the similarities and differences between their RF-induced resonances and the microwave-induced resonances that we describe in our own published work [21].

8.3. Outline of the following chapters

In the present part of this manuscript, we describe an alternative to static-field Fano-Feshbach resonances where the incident scattering state is resonantly coupled by a microwave magnetic field to a bound state corresponding to a different two-atom internal state. All states taking part in the resonance belong to the electronic ground level of the atoms. The microwave magnetic field amplitude is kept fixed, and the resonance is reached by tuning the microwave frequency.

These microwave-induced resonances occur even in the absence of a static magnetic field. Their characteristics are not directly related to those of the resonances induced by static fields. Their widths are proportional to the squared amplitude of the oscillating magnetic field.

For the sake of simplicity, we focus on the case of bosonic alkali atoms, but neither of these assumptions is essential. We study the microwave-induced resonances occurring with ${}^7\text{Li}$, ${}^{23}\text{Na}$, ${}^{41}\text{K}$, ${}^{87}\text{Rb}$, and ${}^{133}\text{Cs}$. Except for ${}^7\text{Li}$ (for which a broad static-field resonance is already available [22]), our results yield optimistic prospects for experiments with all of these atoms.

The present part of this manuscript is organised in seven chapters.

- Chapter 9 is introductory. It provides an overview of our analysis of the microwave-induced Feshbach resonances, based on a simple model involving two coupled square wells. It briefly presents many of the concepts used and described in depth in later chapters.
- Chapter 10 introduces the Hamiltonian we have used to describe collisions between two alkali atoms in the presence of an oscillating magnetic field. We analyse its simple block structure, exploited in all subsequent chapters.
- Chapter 11 contains a detailed description of the approaches we have used to characterise the microwave-induced Feshbach resonances, based on the resonances we have analysed in [21].
- In Chapter 12, we present our own implementations of the numerical methods we have used to calculate the multi-channel wavefunctions characterising the two atoms in the presence of static and oscillating magnetic fields.
- Chapter 13 reproduces our published article [21].

8. Introduction

- Chapter 14 is devoted to *static-field* Feshbach resonances. We have numerically reproduced Feshbach resonances observed in ^{133}Cs for very small magnetic fields (SYRTE–Observatoire de Paris), which to our knowledge had remained unexplained. We interpret these measurements as *s*-wave resonances involving the weakest-bound triplet dimer state in ^{133}Cs .
- In Chapter 15, we present numerical results for microwave-induced Feshbach resonances involving experimental parameters accessible in a Cesium fountain clock. These realistic parameters lead to calculations involving a larger number of coupled channels, and inelastic processes are accounted for.

9. An overview of microwave–induced Feshbach resonances

This chapter initiates our analysis of scattering resonances occurring in ultracold atomic systems. We focus on a low–energy collision between two atoms occurring in the presence of a microwave magnetic field. Our goal is to justify that, for an appropriate choice of the microwave frequency, a scattering resonance occurs, which can be used to tune the interaction within the ultracold gas. This goal is achieved in Chapter 13, where our published results [21] are presented.

An accurate description of these microwave–induced Feshbach resonance requires elaborate numerical coupled–channel calculations involving a precise description of the atomic interaction. These numerical calculations will be presented in later chapters. In this preliminary chapter, we give a simplified analysis of these resonances. This analysis is based on the two–square–well model: the interaction between two atoms, in the presence of an oscillating magnetic field, is represented by two coupled square wells.

We start with a brief review the scattering properties of a single square–well potential. Then, we show that a suitable choice of two square–well potentials can be used to model the interaction between two atoms, reproducing the key physical parameters involved in a microwave–induced resonance. The two–square–well model yields an exact analytical expression for the scattering length a as a function of the magnetic field amplitude and frequency: we use this expression to derive approximate values for the characteristics of microwave–induced resonances. These approximate values are in good agreement with the accurate results presented in later chapters.

Our presentation of the two–square–well model will lead us to introduce many of the concepts involved in the description of scattering resonances. In this preliminary chapter, we only briefly describe these concepts, and refer to the relevant sections in later chapters where they are described in greater detail.

9.1. One single square well

We consider two identical alkali atoms in their ground state, ignoring — as a first step — their internal state structure¹. Their mutual interaction can be modelled by a centrally–symmetric ‘electronic’ potential $V(r)$ [23]. This potential will be described in detail in Chapter 10. In this introductory chapter, we simply highlight its three key properties:

- For large interatomic distances ($r \gtrsim$ a few tens of a_0 , where $a_0 = 53$ nm is the Bohr

¹This internal state structure will be taken into account starting from Section 9.2

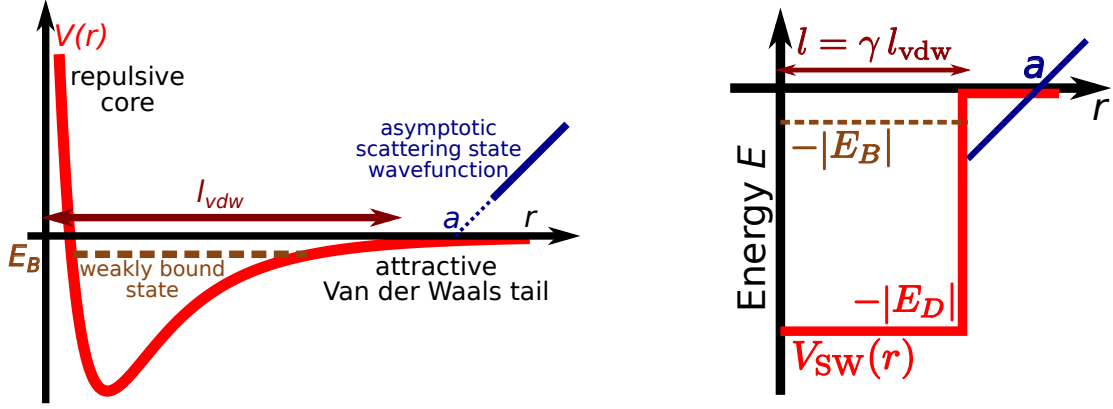


Figure 9.1. **Left:** sketch of the ‘physical’ electronic potential characterising the interaction between two identical ground-state alkali atoms. **Right:** simplified isotropic square-well potential mimicking the scattering properties of the ‘physical’ potential.

radius), the potential $V(r)$ describes an attractive Van-der-Waals interaction of the form $V(r) = -C_6/r^6$;

- The potential has a repulsive inner core (for $r \lesssim 10 a_0$) owing to the Pauli repulsion between the electrons for atoms that are close together.
- For all atomic species considered in this work (${}^7\text{Li}$, ${}^{23}\text{Na}$, ${}^{41}\text{K}$, ${}^{87}\text{Rb}$, and ${}^{133}\text{Cs}$), the ground-state electronic potentials exhibit a minimum for interatomic distances of the order of $10 a_0$.

The typical shape of such a potential is sketched on the left-hand part of Fig. 9.1.

9.1.1. A simple model for the interaction between two atoms

Figure 9.1(left) shows that the ‘physical’ interaction potential $V(r)$ is essentially an isotropic potential well. The simplified model presented in this chapter replaces the ‘physical’ potential by a simpler one which has similar scattering properties as far as ultracold collisions are concerned. We choose to work with the isotropic square-well potential $V_{SW}(r)$ represented on the right-hand part of Fig. 9.1.

The isotropic square well of Fig. 9.1(right) is fully characterised by two parameters: its width l and its depth $|E_D|$. The range of the ‘physical’ potential $V(r)$ is determined by the Van-der-Waals length l_{vdw} associated with the long-range behaviour of the potential $V(r)$ (for large r , $V(r) \approx -C_6/r^6$, and the Van der Waals length is $l_{vdw} = (m C_6/\hbar^2)^{1/2} / 2$ [24]), therefore we choose the width to be close to l_{vdw} : $l = \gamma l_{vdw}$, where γ is a positive number of order 1. For a given width l , the depth $|E_D|$ of the well determines the value of the scattering length a associated with the potential well, the number of bound states supported by the well, and the energy of the weakest bound state.

9.1.2. Scattering length and bound state energies of a square well

The scattering properties and the bound-state structure of the isotropic square-well potential are well known [25]. Let us briefly review the key results of this standard problem. These results are relevant to the study of scattering resonances for two reasons: (i) they provide a simple example of a scattering resonance, and (ii) they shed light on the link between the value of the scattering length and the binding energy of the weakest-bound state.

We consider a collision between two identical atoms whose mutual interaction is described by the potential V_{SW} . The Hamiltonian describing the relative motion of the two particles reads:

$$H_{\text{SW}} = \frac{\mathbf{p}^2}{2m_r} + V_{\text{SW}}(r) \quad , \quad (9.1)$$

where $m_r = m/2$ is the reduced mass, \mathbf{r} is the relative position and \mathbf{p} is its conjugate momentum. The spherical symmetry of the potential $V_{\text{SW}}(r)$ makes it possible to seek eigenstates of H_{SW} having a definite value of the angular momentum $\ell^2 = \ell(\ell + 1)$. We shall focus on the s -wave interaction ($\ell = 0$), which dominates the ultracold regime [26], and which is described by the following radial Hamiltonian deduced from Eq. (9.1):

$$H_{\text{SW}} = \frac{p_r^2}{2m_r} + V_{\text{SW}}(r) \quad , \quad (9.2)$$

where p_r is the radial component of the relative momentum operator \mathbf{p} . In particular, the ultracold scattering properties of H_{SW} are encoded in the s -wave scattering length a associated with H_{SW} . This scattering length is given, in terms of the well width l and the well depth $|E_D|$, by:

$$1 - \frac{a}{l} = \frac{\tan(k_D l)}{k_D l} \quad , \quad (9.3)$$

where $k_D l = (|E_D|/E_l)^{1/2}$ and $E_l = \hbar^2/(2m_r l^2)$. The (possibly many) bound state energies, measured from the threshold energy of the square well, are the $E_B = -E_l (\kappa l)^2$, where (κ, k) are solutions of the following two coupled equations:

$$\begin{cases} (k_D l)^2 = (\kappa l)^2 + (k l)^2 \\ \kappa l = -k l / \tan(k l) \end{cases} \quad (9.4)$$

The scattering length a and the bound state energies E_B are plotted on Fig. 9.2 as a function of the parameter $k_D l = (|E_D|/E_l)^{1/2}$. If the well depth E_D is chosen such that $(2n_B - 1)\frac{\pi}{2} < k_D l < (2n_B + 1)\frac{\pi}{2}$ (where n_B is an integer), the square well supports exactly n_B bound states. Furthermore, the scattering length diverges each time a new bound state appears in the well, *i.e.* for all values of E_D such that $k_D l = (2n_B + 1)\frac{\pi}{2}$. These well-known divergences in the scattering length are the signature of zero-energy scattering resonances.

The comparison between the top and bottom parts of Fig. 9.2 also reveals a strong connection between the value of the scattering length and the position of the highest-energy bound state supported by the potential well. For depths $|E_D|$ such that a/l is

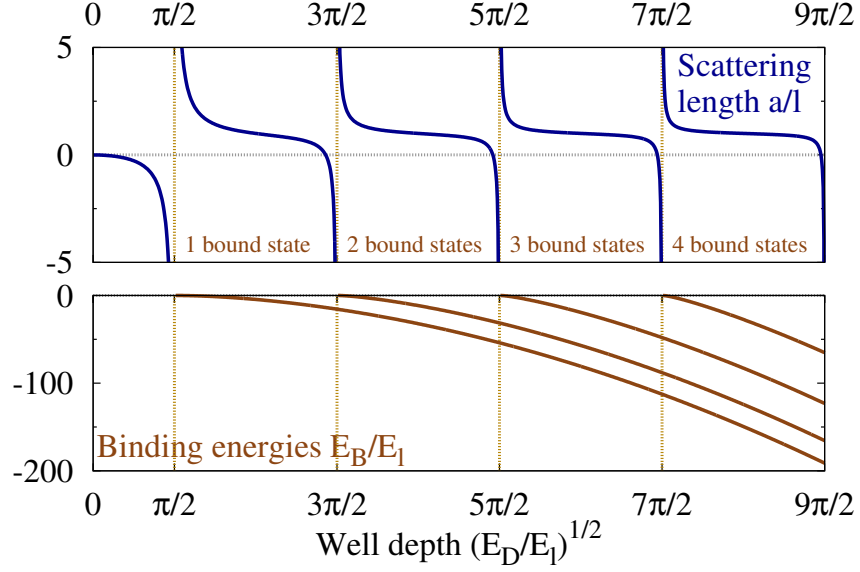


Figure 9.2. Scattering length (top) and bound state energies (bottom) for a single isotropic square well, as a function of the parameter $k_D l = (|E_D|/E_l)^{1/2}$. Scattering lengths are measured in units of the well width l and energies in units of $E_l = \hbar^2/2m_r l^2$.

negative (such as for $k_D l < \pi/2$, *i.e.* very shallow wells), the potential supports no weakly bound state. If the depth of the potential is increased, the scattering length remains negative, and it becomes arbitrarily large as one approaches the scattering resonance at $k_D = (2n_B + 1)\frac{\pi}{2}$. Immediately after the resonance, a/l is positive, and the well supports a very weakly bound state. A subsequent increase in the well depth causes a to decrease and the highest-energy bound state to become deeper bound.

We have rigorously justified the connection between the value of a and the presence (or absence) of a weakly bound state only in the specific case of the isotropic square-well potential of Fig. 9.1(right). However, it remains valid for the ‘physical’ interaction potential $V(r)$ (see *e.g.* [27, 28]). We will refer to this connection in the following chapters. For example, the triplet scattering length for ${}^7\text{Li}$ being negative ($a_T = -28 a_0$) indicates that the triplet potential for Lithium does not support a weakly-bound molecular state (see Section 11.1.4). Similarly, the triplet scattering length for ${}^{133}\text{Cs}$ being positive and large ($a_T = 24 l_{\text{vdw}}$) is a strong indication that the triplet potential for Cesium supports a very weakly bound molecular state (see Section 11.2.4).

9.2. The two-square-well model for microwave-induced Feshbach resonances

We now account for the internal-state structure of the two atoms. We introduce the two-square-well model on the particular example of the microwave-induced resonance

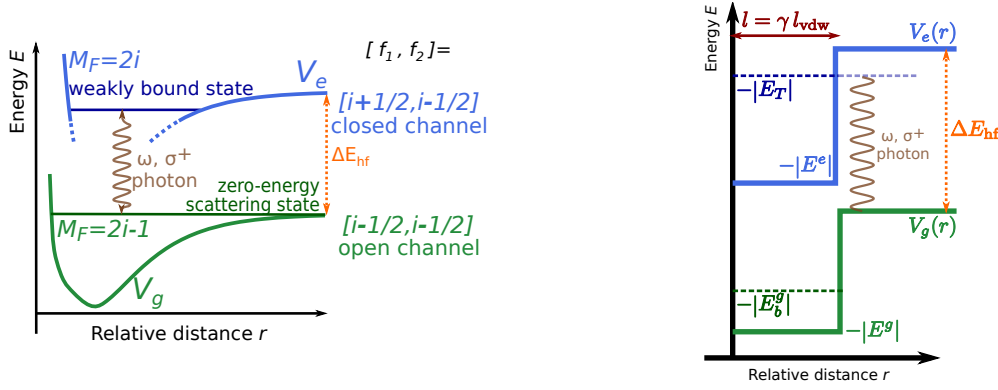


Figure 9.3. The two-square-well model for microwave-induced Feshbach resonances: the two ‘physical’ potentials (left) are replaced by two isotropic square-well potentials (right). The nuclear spin i , the hyperfine quantum numbers f_1 , f_2 , and the two-atom spin projection M_F labelling the potential curves will be introduced in Chapter 9.

involving the ($M_F = 2i - 1$) and ($M_F = 2i$) internal-state subspaces, which are coupled by a σ^+ -polarised magnetic field; the definitions of the relevant internal-state subspaces are deferred to Chapter 9, and the resonance described in this section is characterised in greater detail in Chapter 10.

We consider a low-energy collision between two identical alkali atoms, both of which are in their ground hyperfine state, in the presence of an oscillating magnetic field. The frequency of the oscillating field is tuned close to the hyperfine transition frequency for a single atom. One of the atoms may absorb a photon, which causes the atom pair to transit to the upper hyperfine state. We call $|g\rangle$ (“ground”) the lower-energy two-atom internal state, and $|e\rangle$ (“excited”) the higher-energy two-atom internal state: the energies of these two states differ by the hyperfine transition energy ΔE_{hf} . The interaction between the two atoms depends on the two-atom internal state, and we thus introduce two *different* electronic potentials V_g and V_e , modelling the interatomic interaction in the states $|g\rangle$ and $|e\rangle$, respectively². These two potentials, coupled by the oscillating magnetic field, are represented on the left-hand part of Fig. 9.3.

We assume that the excited-state potential curve V_e supports a weakly-bound dimer state with the binding energy $|E_T|$. If the frequency $\omega/2\pi$ of the oscillating magnetic field is tuned close to the energy difference $\hbar\omega_{\text{res}}^0 = \Delta E_{\text{hf}} - |E_T|$ between the threshold energy of the potential well V_g and the energy of the bound state in V_e (see Fig. 9.3(left)), a scattering resonance occurs. This resonance causes a hyperbolic divergence in the scattering length $a(\omega)$ characterising ultracold collisions between two atoms in the state $|g\rangle$ (see Chapter 11). For frequencies close to the resonant frequency ω_{res} ,

$$a(\omega) = a_{\text{bg}} \left(1 + \frac{\Delta\omega}{\omega - \omega_{\text{res}}} \right), \quad (9.5)$$

where a_{bg} is the background scattering length and $\Delta\omega$ is the resonance width (see Fig. 11.2).

²A more accurate description of the atomic interaction will be introduced in Section 10.2.

We will show in Section 11.1.2 that the resonance width $\Delta\omega$ is proportional to B_{osc}^2 , where B_{osc} is the amplitude of the oscillating magnetic field. The coupling between the two channels $|g\rangle$ and $|e\rangle$ causes the resonance frequency ω_{res} to be slightly shifted away from ω_{res}^0 (see [1] and Section 11.1):

$$\omega_{\text{res}} = \omega_{\text{res}}^0 + \alpha B_{\text{osc}}^2 \quad . \quad (9.6)$$

The main goal of the present work is to characterise the microwave-induced Feshbach resonances described by Eqs. (9.5) and (9.6), *i.e.* to evaluate the resonance width $\Delta\omega$ and the resonance shift α for given choices of the two-atom states $|g\rangle$ and $|e\rangle$ and of the resonant bound state $|E_T\rangle$. An accurate characterisation of these resonances will be presented in Chapter 11. These accurate results are obtained through complex numerical calculations based on the coupled-channel approach (see Chapter 12). In this section, we present a simplified approach based on the square-well potentials introduced in Section 9.1. This simple model can be solved analytically (see Section 9.2.5) and yields numerical results for the resonance characteristics (see Section 9.2.6) which are in good agreement with the full-fledged coupled-channel results of Chapter 11 (see Table 11.2).

Analyses of Feshbach resonances in terms of two coupled square wells have previously been reported [29]. The two-square-well model presented in this chapter has been developed independently, within the context of microwave-induced resonances (rather than resonances induced by static fields [7]); it is not equivalent³ to the one presented in [29].

9.2.1. Choice of the square wells modelling the atomic interaction

Our simple model is based on replacing each of the potential well V_g and V_e of the left-hand side of Fig. 9.3 by the isotropic square-well potentials shown on the right-hand side of this figure. In order to define these two wells, four parameters have to be specified: the two well widths l_g and l_e , and the two well depths $|E_g|$ and $|E_e|$.

The ‘physical’ electronic potentials V_g and V_e have the same spatial range, determined by the Van-der-Waals length l_{vdw} which is the same for $|g\rangle$ and $|e\rangle$ [24]. Consequently, we choose the two square wells to have the same width $l = l_g = l_e = \gamma l_{\text{vdw}}$, where γ is a positive number of order 1.

The resonance we are describing occurs in the ultracold regime, where the scattering properties of the potentials V_g and V_e are encapsulated in the corresponding scattering lengths a_g and a_e . Therefore, we require the two square wells of Fig. 9.3(right) to have the same scattering lengths as the corresponding original potentials.

The strength of the coupling between the incoming scattering state in the potential V_g and the resonant bound state in the potential V_e is determined by the overlap between the two corresponding wavefunctions (see Section 11.1.2). This overlap depends on the

³For instance, the model described in [29] uses a closed-channel square well which is infinite for $r > l$, whereas both of our wells are finite for all values of $r > 0$. Furthermore, they choose the width of both square wells to be equal to the Van-der-Waals length l_{vdw} , whereas our square-well width is an adjustable parameter which we tune to reproduce the binding energy of the closed-channel bound state: see Section 9.2.1.

binding energy of the resonant bound state: a weakly bound state has a large spatial extent, leading to a large overlap and a strong coupling to the scattering state; a deeply bound state has a small spatial extent, and its coupling to the scattering state is thus much smaller (see Section 11.1.4). Hence, we wish the square-well potential representing V_e to support a bound state which has the same binding energy $|E_T|$ as the resonant bound state in V_e .

We call $|\varphi_g^{\text{scat}}\rangle$ the threshold-energy scattering state wavefunction in the square-well potential representing V_g , and $|\varphi_e^{\text{bound}}\rangle$ the wavefunction of the bound state having the energy $-|E_T|$ in the square-well potential representing V_e . The overlap $F = \langle \varphi_e^{\text{bound}} | \varphi_g^{\text{scat}} \rangle$ between these two wavefunctions is the sum of two contributions: $F = F_{<} + F_{>}$, where $F_{<}$ corresponds to the inner $r < l$ region in which the square wells are non-zero, and $F_{>}$ corresponds to the outer region ($r > l$) where both square well potentials vanish. Let us assume at first that one of the two well depths is much larger than the other: we take $|E_g| \gg |E_e|$ (but the argument also holds in the opposite limit). In this case, the kinetic energy available in the $r < l$ region is much larger for an atom pair in the state $|g\rangle$ than it is for an atom pair in the state $|e\rangle$. Therefore, in the region $r < l$, the wavefunction $\varphi_g(r)$ oscillates much faster than $\varphi_e(r)$ does: these fast oscillations average $F_{<}$ to zero. This is not the expected behaviour for the inner part of the overlap, where the oscillations occur in phase and build up a non-vanishing contribution to the total overlap (see the multi-channel numerical results for the overlaps, represented on Figs. 11.5). In order to avoid this non-physical averaging, the depths $|E_g|$ and $|E_e|$ should have the same orders of magnitude, *i.e.* the two square-well potentials should support the same number of bound states⁴ $n_B = n_B^g = n_B^e$.

To sum up, the four square well parameters l_g, l_e, E_g and E_e are chosen to satisfy the following four conditions:

1. The two square-well potentials have the same width l , which is of the order of, but not equal to, the Van-der-Waals length of the original potentials;
2. The square-well potentials have the same scattering lengths a_g and a_e as the original potentials V_g and V_e ;
3. The highest-energy bound state of the square-well potential representing V_e has the same binding energy as the resonant bound state in V_e ;
4. The two square-well potentials support the same number of bound states.

The parameters a_g, a_e, l , and n_B defining the two square-well potentials of our simplified model are collected in Table 9.1 for all considered alkali atoms. For the sake of simplicity, we choose the smallest number of bound states n_B for which the four conditions stated above can be simultaneously satisfied ($n_B = 1$ or 2 for all considered atomic species). We have checked that using a larger number of bound states $n_B^g = n_B^e$ does not substantially modify the results obtained with this model. On the contrary, choosing a

⁴Figure 9.2 shows that the depth of a square-well potential supporting n_B bound states roughly behaves as $|E_D| \approx E_l \pi^2 n_B^2$.

	⁷ Li	²³ Na	⁴¹ K	⁸⁷ Rb	¹³³ Cs
Scattering lengths for the wells V_g and V_e					
a_g (a_0)	5.0	55	64	100	-2500
a_e (a_0)	-28	65	60	99	2400
Energy of resonant state					
$ E_T /\hbar$ (MHz)	12000	200	140	25	$5 \cdot 10^{-3}$
Parameters of the two-square-well model					
l/l_{vdw}	0.77	1.2	0.77	1.01	2.3
$n_B^g = n_B^e$	1	2	2	2	2

Table 9.1. Parameters for the two-square well model: scattering lengths a_g and a_e (measured in units of the Bohr radius $a_0 = 52.9 \cdot 10^{-12}$ m), width l , and number of bound states $n_B^g = n_B^e$ in the two wells.

different number of bound states in the two wells leads to results that are farther away from the accurate coupled-channel results of Table 11.2.

The specific case of Cesium 133

In the particular case of ¹³³Cs, the resonant bound state is so weakly bound ($|E_T| = h \cdot 5 \text{ kHz} = 2 \cdot 10^{-3} E_{\text{vdw}}$, where $E_{\text{vdw}} = \hbar^2/2m_r l_{\text{vdw}}^2$ is the Van-der-Waals energy [24]) that its binding energy is completely determined by the scattering length of the corresponding potential [1]: $|E_T| = \hbar^2/2m_r a_e^2$, where $a_e = 2400 a_0$. Hence, the quantities a_e and $|E_T|$ contain equivalent information. When defining the square-well potentials mimicking V_g and V_e for Cesium, we enforce the conditions 1, 2, and 4 above, but we do *not* apply the condition 3 on the energy $|E_T| = h \cdot 5 \text{ kHz}$ of the *weakest* bound state. Instead, we require the square-well potential representing V_e to have two bound states, and choose the square-well parameters such that the deeper bound state has the same binding energy as the *second-highest* bound state of V_e , namely $h \cdot 110 \text{ MHz}$.

9.2.2. The Hamiltonian of the two-square-well model

We now include a constant coupling between the two channels $|g\rangle$ and $|e\rangle$, which models the coupling of the microwave magnetic field to the total electronic spin of the atom pair. More specifically, we consider the following two-channel radial Hamiltonian, which describes the relative motion of the atom pair in the presence of an oscillating magnetic field of amplitude B_{osc} :

$$H = \frac{p_r^2}{2m_r} \mathbb{1} + \begin{pmatrix} V_g(r) & 0 \\ 0 & V_e(r) \end{pmatrix} + \begin{pmatrix} 0 & 0 \\ 0 & -\hbar\delta \end{pmatrix} + \begin{pmatrix} 0 & \frac{\hbar\Omega_1}{2} \\ \frac{\hbar\Omega_1}{2} & 0 \end{pmatrix}. \quad (9.7)$$

In Eq. (9.7), the operator $p_r^2/2m_r \mathbb{1}$ is the kinetic energy of the reduced particle, the second term is an r -dependent diagonal matrix which models the electronic interaction V_{el} (see Section 10.2.4), and the third term includes the detuning $\hbar\delta = \hbar\omega - \Delta E_{\text{hf}}$ of

the microwave frequency $\omega/2\pi$ with respect to the single-atom hyperfine splitting ΔE_{hf} . The last term is a constant symmetric matrix which only has off-diagonal elements and models the coupling of the two channels due to the *magnetic dipole coupling* between the microwave magnetic field and the total electronic spin S . The strength Ω_1 of the coupling between the channels $|g\rangle$ and $|e\rangle$ relates to the amplitude B_{osc} of the oscillating magnetic field through:

$$\frac{\hbar\Omega_1}{2} = \mu_B B_{\text{osc}} \quad , \quad (9.8)$$

where we have assumed that the g -factor of the resonant bound state is $g = 1$.

The Hamiltonian (9.7) is the simplified version, within the framework of the two-square-well model, of the two-atom Hamiltonian (10.13) presented in Chapter 10 and used in all subsequent chapters. The two Hamiltonians have a similar structure, and the terms appearing in them are discussed in greater detail in Section 10.2.2.

9.2.3. The microwave-dressed two-atom states

In this section, we briefly present the microwave-dressed two-atom states. These dressed states are the stationary states of a pair of atoms that are infinitely far away from each other.

We first introduce the total potential $V_{\text{tot}}(r)$, which is the 2×2 operator defined by:

$$V_{\text{tot}}(r) = \begin{pmatrix} V_g(r) & 0 \\ 0 & V_e(r) \end{pmatrix} + \begin{pmatrix} 0 & 0 \\ 0 & -\hbar\delta \end{pmatrix} + \begin{pmatrix} 0 & \frac{\hbar\Omega_1}{2} \\ \frac{\hbar\Omega_1}{2} & 0 \end{pmatrix} \quad , \quad (9.9)$$

so that the Hamiltonian (9.7) reads $H = \frac{p^2}{2m_r} \mathbb{1} + V_{\text{tot}}(r)$.

For $r > l$, both of the square-well potentials $V_g(r)$ and $V_e(r)$ vanish. The matrix $V_{\text{tot}}(r)$ does not vanish, but it reduces to a constant matrix V_∞ :

$$V_\infty = V_{\text{tot}}(r > l) = \begin{pmatrix} 0 & \frac{\hbar\Omega_1}{2} \\ \frac{\hbar\Omega_1}{2} & -\delta \end{pmatrix} \quad . \quad (9.10)$$

The matrix V_∞ is real and symmetric, therefore it has two orthogonal eigenvectors $|\tilde{g}\rangle$ and $|\tilde{e}\rangle$, which are the microwave-dressed (two-atom) internal states [30]. The coupling terms $\hbar\Omega_1/2$, modelling the magnetic dipole interaction between the atom pair and the oscillating magnetic field, do not depend on r : their presence causes the dressed states to differ from the ‘bare’ two-atom states $|g\rangle$ and $|e\rangle$.

Note that the dressed states $|\tilde{g}\rangle$ and $|\tilde{e}\rangle$, as well as the corresponding dressed energies $E_{\tilde{g}}$ and $E_{\tilde{e}}$, depend both on the coupling strength Ω_1 and on the detuning δ .

We assume $E_{\tilde{g}} < E_{\tilde{e}}$. The dressed-state energy splitting $\hbar\Omega = E_{\tilde{e}} - E_{\tilde{g}}$ is given by (see Fig. 11.7):

$$\Omega = (\Omega_1^2 + \delta^2)^{1/2} \quad . \quad (9.11)$$

A more detailed presentation of the microwave-dressed two-atom states will be given in Section 11.2.2.

9.2.4. The two-channel scattering state

We are interested in the scattering length $a(\delta, \Omega_1)$, associated with collisions between atoms which are asymptotically all in the lowest-energy dressed state $|\tilde{g}\rangle$, for given values of the detuning δ and the coupling strength Ω_1 . We thus solve for the zero-energy stationary scattering state $|\Psi_0\rangle$ of the Hamiltonian (9.7). The state $|\Psi_0\rangle$ is a *two-channel* wavefunction, in the sense that it has two r -dependent components $\langle g|\Psi_0(r)\rangle$ and $\langle e|\Psi_0(r)\rangle$. It depends on the detuning δ and on the coupling strength Ω_1 . It is defined by the stationary Schrödinger equation:

$$H|\Psi_0\rangle = E_{\tilde{g}}|\Psi_0\rangle \quad , \quad (9.12)$$

along with the asymptotic behaviour (exact for $r > l$):

$$|\Psi_0\rangle \underset{r>l}{=} \left(1 - \frac{a}{r}\right)|\tilde{g}\rangle + f_{\tilde{e}\tilde{g}} \frac{e^{-\kappa r}}{r} |\tilde{e}\rangle \quad . \quad (9.13)$$

Note that the asymptotic behaviour of Eq. (9.13) is expressed in the dressed-state basis $\{|\tilde{g}\rangle, |\tilde{e}\rangle\}$ (rather than in the bare-state basis $\{|g\rangle, |e\rangle\}$). The constant κ characterises the decay of the closed-channel component $\langle \tilde{g}|\Psi_0(r)\rangle$:

$$\kappa l = (\hbar\Omega/E_l)^{1/2} \quad . \quad (9.14)$$

A lengthier discussion of multi-channel wavefunctions, open and closed channels, and boundary conditions will be given in Section 12.1.3.

9.2.5. Analytical expression for the scattering length

The scattering length a and the scattering amplitude $f_{\tilde{e}\tilde{g}}$ appearing in Eq. (9.13) are unknown *a priori*: they are determined from the large- r behaviour of the wavefunction components $\langle \tilde{g}|\Psi_0(r)\rangle$ and $\langle \tilde{e}|\Psi_0(r)\rangle$, respectively.

The two-square-well model allows for an exact calculation of the scattering length a . It can be expressed analytically in terms of the well depths $|E_g|$ and $|E_e|$, the coupling strength Ω_1 , and the detuning δ :

$$\frac{a}{l} = 1 - \frac{(\kappa l) u_1 u_2 + \sin^2 \Psi u_1 + \cos^2 \Psi u_2}{1 + (\kappa l) (\cos^2 \Psi u_1 + \sin^2 \Psi u_2)} \quad . \quad (9.15)$$

The auxiliary parameters appearing in Eq. (9.15) are defined below:

$$u_1 = \frac{\tan(k_1 l)}{k_1 l} \quad \text{and} \quad u_2 = \frac{\tan(k_2 l)}{k_2 l} \quad , \quad (9.16)$$

$$\cos(2\Psi) = \frac{\delta}{\Omega} \frac{\hbar\delta + |E_e| - |E_g|}{\hbar\chi} + \frac{\Omega_1}{\Omega} \frac{\Omega_1}{\chi} \quad , \quad (9.17)$$

$$\hbar\chi = ((|E_e| - |E_g| + \hbar\delta)^2 + (\hbar\Omega_1)^2)^{1/2} \quad , \quad (9.18)$$

$$k_1 l = \left(\frac{|E_e| + |E_g| - \hbar\Omega - \hbar\chi}{2E_l} \right)^{1/2} \quad \text{and} \quad k_2 l = \left(\frac{|E_e| + |E_g| - \hbar\Omega + \hbar\chi}{2E_l} \right)^{1/2} \quad . \quad (9.19)$$

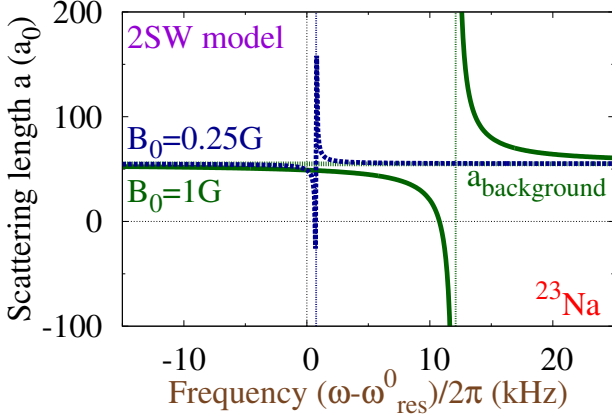


Figure 9.4. Scattering length $a(\omega)$ for ^{23}Na in the vicinity of the microwave-induced resonance which occurs for detunings close to $\delta_{\text{res}}^0/2\pi = 200$ MHz, calculated using the two-square-well approach for $B_{\text{osc}} = 0.25$ G and $B_{\text{osc}} = 1$ G. This graph, calculated from Eq. (9.15), is the two-square-well analog of the coupled-channel results presented on Fig. 11.8.

	^7Li	^{23}Na	^{41}K	^{87}Rb	^{133}Cs
Energy of resonant state and resonance frequency					
$ E_T /\hbar$ (MHz)	12000	200	140	25	$5 \cdot 10^{-3}$
$\omega_{\text{res}}^0/2\pi$ (GHz)	11	16	0.12	6.8	9.2
Results of the two-square-well model					
α (kHz/G ²)	0.34	12	32	163	$-900 \cdot 10^3$
$\Delta\omega_{2\text{SW}}/2\pi$ (Hz/G ²)	6.2	1300	222	100	$-3.3 \cdot 10^9$

Table 9.2. Characteristics of the microwave-induced Feshbach resonances in ^7Li , ^{23}Na , ^{41}K , ^{87}Rb , and ^{133}Cs involving the triplet bound states with energies E_T , calculated using the two-square-well method. The resonance width $\Delta\omega$ is proportional to B_0^2 , and it is given for $B_0 = 1$ G. The results for the resonance widths $\Delta\omega$ and shifts α are in good agreement with the coupled-channel results collected in Table 11.2.

9.2.6. Numerical results

We have numerically calculated the scattering length $a(\omega)$ given by Eq. (9.15), for magnetic field amplitudes B_{osc} of the order of 1 G and frequencies $\omega/2\pi$ close to the zero-field resonance frequency $\hbar\omega_{\text{res}}^0 = \Delta E_{\text{hf}} - |E_T|$, as illustrated on Fig. 9.4 in the particular case of ^{23}Na . Our numerical results confirm that the scattering length diverges hyperbolically for frequencies close to ω_{res}^0 , as expressed by Eq. (9.5). They also confirm that the resonance width $\Delta\omega$ and the shift on the resonance frequency ($\omega_{\text{res}} - \omega_{\text{res}}^0$) are both proportional to B_{osc}^2 .

Our results for the resonance characteristics $\Delta\omega$ and α are collected in Table 9.2. These results are in good agreement with the coupled-channel results of Table 11.2.

In this first chapter on scattering resonances, we have introduced the parameters involved in the description of microwave-induced Feshbach resonances: the background scattering length a_{bg} , the resonance width $\Delta\omega$, and the resonance frequency $\omega_{\text{res}}/2\pi$. We have presented a simple model for these resonances: the two-square well model. This

9. An overview of microwave-induced Feshbach resonances

model leads to an exact analytical expression of the scattering length a . We have used it to derive orders of magnitude of the resonance positions and shifts for the bosonic alkali atoms ^7Li , ^{23}Na , ^{41}K , ^{87}Rb , and ^{133}Cs .

We have also briefly presented the key concepts involved in the analysis of ultracold scattering resonances, among which the electronic interaction between two atoms, dressed two-atom states, and multi-channel scattering wavefunctions. All of these concepts will be described in greater detail in Chapters 10 and 11.

Starting from Chapter 10, we relinquish the two-square-well model of the present chapter and turn towards more accurate approaches. These approaches are more involved as they require numerical coupled-channel calculations. Our accurate coupled-channel results are given at the end of Chapter 11 (in particular, see Table 11.2), and the numerical methods we have used to obtain them are presented in Chapter 12.

10. The Two–Atom Hamiltonian

In Chapter 9, we have presented a simple two–square–well model which provides orders of magnitude for the characteristics of microwave–induced Feshbach resonances. However, an accurate description of these resonances can only be obtained by accounting for the coupling between multiple two–atom internal states. The present chapter and the following one are devoted to the application of multi–channel scattering theory to the characterisation of Feshbach resonances.

This chapter introduces the model we have used to describe collisions between two alkali atoms in a magnetic field [20, 31]. The first section is introductory and briefly reviews the properties of a single alkali atom in a magnetic field. In the next section, we describe the Hamiltonian describing two atoms in the presence of a magnetic field which may have both static and oscillating components. The last section is devoted to the symmetries of the two–atom Hamiltonian. These symmetries yield a simple block–matrix structure, which will be exploited in all subsequent chapters to determine the scattering channels that are relevant for the description of a given resonance.

10.1. A single atom in a magnetic field

We start by describing the internal states of a single atom. For simplicity’s sake, we focus on the case of a bosonic alkali atom, such as Sodium 23 (^{23}Na), Rubidium 87 (^{87}Rb), or Cesium 133 (^{133}Cs). We describe the internal state of this alkali atom in terms of two spins¹: (*i*) a single electron spin \mathbf{s} , which models the internal state of the single valence electron, and (*ii*) the nuclear spin \mathbf{i} . The modulus of the electron spin satisfies $s = 1/2$. The quantum number i , which determines the modulus of the nuclear spin \mathbf{i} , is a characteristic of the considered atom, and it must be half–integer for bosonic alkalis: for ^{23}Na and ^{87}Rb , $i = 3/2$, whereas in the case of ^{133}Cs , $i = 7/2$ [32].

10.1.1. One atom in the absence of a magnetic field

In the absence of a magnetic field, the internal state of a single atom is governed by the following Hamiltonian, which describes the hyperfine coupling [33] between the electron and nuclear spins of a single atom:

$$v_{\text{hf}} = a_{\text{hf}} \mathbf{s} \cdot \mathbf{i} = \frac{1}{2} a_{\text{hf}} (\mathbf{f}^2 - \mathbf{s}^2 - \mathbf{i}^2) \quad , \quad (10.1)$$

¹Throughout this manuscript, lowercase letters denote single–atom quantities and operators. Their uppercase counterparts represent the corresponding two–atom quantities.

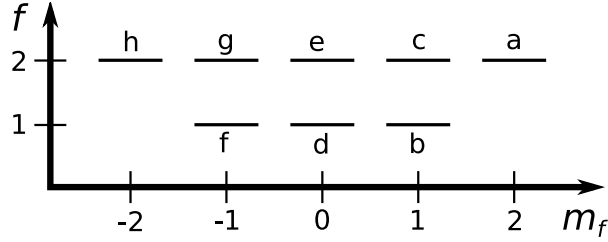


Figure 10.1. Single-atom hyperfine states for an alkali atom with nuclear spin $i = 3/2$, such as ^{23}Na or ^{87}Rb : there are 3 states with $f = f^- = 1$ and 5 states with $f = f^+ = 2$.

where the operator \mathbf{f} is the total single-atom spin: $\mathbf{f} = \mathbf{s} + \mathbf{i}$.

Equation (10.1) shows that the Hamiltonian v_{hf} conserves both hyperfine quantum numbers f and m_f , where m_f characterises the total spin projection f_z . Therefore, it is convenient to describe the internal states of a single atom using the hyperfine basis states $|f, m_f\rangle$. For an alkali atom, f can take two values: $f^- = i - 1/2$ and $f^+ = i + 1/2$. The internal-state subspace thus has dimension $(2f^- + 1) + (2f^+ + 1) = 4i + 2$. The single-atom hyperfine states are represented on Fig. 10.1 in the case of an atom with nuclear spin $i = 3/2$, for which the internal-state subspace has dimension 8. In the case of an atom with nuclear spin $i = 7/2$, the internal-state subspace has dimension 16. In the absence of a magnetic field, all hyperfine states $|f, m_f\rangle$ with the same quantum number f are degenerate.

10.1.2. One atom in a static magnetic field

If a static magnetic field \mathbf{B}_{stat} is added to the system, the Hamiltonian acquires a Zeeman term v_Z . Choosing the direction \mathbf{e}_z of the static magnetic field as the quantisation axis, the total single-atom Hamiltonian reads [33]

$$h_{\text{stat}} = v_{\text{hf}} + v_Z \quad , \quad (10.2)$$

where

$$v_Z = 2 \frac{\mu_B B_{\text{stat}}}{\hbar} s_z \quad , \quad (10.3)$$

μ_B is the Bohr magneton, and s_z is the projection along \mathbf{e}_z of the electron-spin operator. The Hamiltonian h_{stat} conserves the spin projection m_f , but it no longer conserves f .

10.1.3. One atom in an oscillating magnetic field

We now add to the system an oscillating magnetic field \mathbf{B}_{osc} , whose frequency $\omega/2\pi$ is tuned close to the hyperfine transition frequency of the considered atoms, *i.e.* in the microwave range. We still assume the presence of a static magnetic field \mathbf{B}_{stat} , whose direction determines the quantisation axis \mathbf{e}_z .

We use a quantum description for the oscillating field, and we assume that all of its photons are in the same mode. We call a^\dagger the creation operator for a photon in the

relevant mode, and $\boldsymbol{\varepsilon}$ its polarisation. The magnetic field operator is then given by [30]:

$$\mathbf{B}_{\text{osc}} = \frac{b_0}{\sqrt{2}}(\boldsymbol{\varepsilon}a + \boldsymbol{\varepsilon}^*a^\dagger) \quad , \quad (10.4)$$

where b_0 is related to the magnetic field amplitude $B_{\text{osc}} = b_0\sqrt{N}$, and N is the total number of photons, which we assume to be $\gg 1$.

The magnetic field and the atom are coupled via the magnetic dipole coupling term:

$$w = -\mathbf{m} \cdot \mathbf{B}_{\text{osc}} \quad , \quad (10.5)$$

where $\mathbf{m} = -2\mu_B \mathbf{s}/\hbar$ is the total magnetic dipole operator for the atom [33], assuming that the valence electron has zero orbital angular momentum ($\mathbf{l} = 0$).

We focus on the case of a σ^+ -polarised magnetic field about the quantisation axis \mathbf{e}_z : $\boldsymbol{\varepsilon} = \frac{\mathbf{e}_x + i\mathbf{e}_y}{\sqrt{2}}$. Equations (10.4) and (10.5) then yield²:

$$w = w_1 (s^+ a + s^- a^\dagger) \quad , \quad (10.6)$$

where

$$w_1 = \frac{\mu_B b_0}{\hbar} \quad , \quad (10.7)$$

and $s^\pm = s_x \pm is_y$ are the ladder operators for the electron spin.

Including both the static field \mathbf{B}_{stat} and the oscillating field \mathbf{B}_{osc} , the total single-atom internal-state Hamiltonian reads:

$$h = v_{\text{hf}} + v_Z + \hbar\omega a^\dagger a + w \quad . \quad (10.8)$$

The Hamiltonian h conserves none of the quantum numbers f , m_f , and N (only the sum $(m_f + N)$ of the atomic spin and the photon number is conserved). The stationary states of the Hamiltonian h are thus dressed states of the joint system “single atom and oscillating magnetic field”, which can be expressed as linear combinations of basis states of the form $|f, m_f, N\rangle$.

10.2. Two atoms in a magnetic field

In Section 10.1, we described the internal-state subspace for a single atom in the presence of a magnetic field. However, the resonances we wish to describe involve a collision between two atoms. In this section, we introduce the complete two-atom Hamiltonian, which takes into account both the internal-state and magnetic terms described in Section 10.1, and the coupling between the spatial dynamics and the internal degrees of freedom of the atoms.

²Strictly speaking, the magnetic field also couples to the nuclear spin \mathbf{i} . However, this coupling is very weak, as the nuclear gyromagnetic ratios g_i are about 1000 times smaller than that of the electron ($g_s = 2$). This coupling is included in our numerical calculations, but we omit it in Eqs. (10.3) and (10.5) for the sake of clarity.

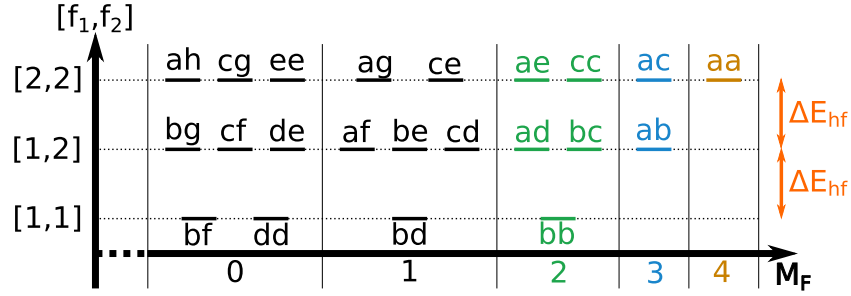


Figure 10.2. Two-atom basis states $|\{f_1, m_1, f_2, m_2\}^+\rangle$ for an alkali atom with nuclear spin $3/2$. The single-atom states carry the labels a, \dots, h defined on Fig. 10.1. The subspaces characterised by opposite values of M_F have similar structures, therefore only the positive- M_F subspaces are represented.

10.2.1. The two-atom internal states

We consider two bosonic alkali atoms in the presence of the oscillating magnetic field described above. The internal-state subspace is spanned by basis vectors of the form $|\{f_1, m_1, f_2, m_2\}^+, N\rangle$, where the superscript $+$ denotes bosonic symmetry, and f_j and m_j , $j = 1$ or 2 , determine the total spin modulus (f_j^2) and projection (f_{jz}) for each of the two atoms. Disregarding the photon quantum number N , there are 36 different two-atom internal states if the nuclear spin is $i = 3/2$, and 124 two-atom states if $i = 7/2$. The two-atom internal states for atoms with $i = 3/2$ are represented on Fig. 10.2, where they are sorted by total spin projections $M_F = m_1 + m_2$ and by the single-atom hyperfine quantum numbers $[f_1, f_2]$.

10.2.2. The two-atom Hamiltonian

The Hamiltonian describing the relative motion of the two atoms in the presence of the static and oscillating magnetic fields reads [20, 31]:

$$H = \frac{\mathbf{p}^2}{2m_r} \mathbb{1} + V_{\text{el}}(r) + V_{\text{hf}} + V_Z + \hbar\omega a^\dagger a + W \quad . \quad (10.9)$$

The Hamiltonian (10.9) contains the following terms:

- The first term, $\mathbf{p}^2/2m_r$, is the kinetic energy of the reduced particle, whose momentum is \mathbf{p} and whose (reduced) mass is $m_r = m/2$, where m is the mass of a single atom. The identity operator $\mathbb{1}$ stresses that this term does not act on the internal states of the atom pair.
- The operator $V_{\text{el}}(r)$ is the electron-interaction term. It is spherically symmetric ($r = |\mathbf{r}|$), and it couples the motion of the atom pair to its internal states. It will be described in more detail in Section 10.2.4.

- The operator V_{hf} is the hyperfine interaction term. It is the sum of the hyperfine interactions $v_{\text{hf}}^{(j)}$ for the two atoms, hence it reads:

$$V_{\text{hf}} = a_{\text{hf}} (\mathbf{s}_1 \cdot \mathbf{i}_1 + \mathbf{s}_2 \cdot \mathbf{i}_2) \quad , \quad (10.10)$$

where \mathbf{s}_j and \mathbf{i}_j are respectively the electron and nuclear spin for the atom j .

- The operator V_Z is the Zeeman term, which describes the coupling between the static magnetic field \mathbf{B}_{stat} and the electronic spins. It is the sum of the single-atom Zeeman terms $v_Z^{(j)}$:

$$V_Z = 2 \frac{\mu_B B_{\text{stat}}}{\hbar} S_z \quad , \quad (10.11)$$

where S_z is the projection along \mathbf{e}_z of the total electron spin $\mathbf{S} = \mathbf{s}_1 + \mathbf{s}_2$.

- The term $\hbar\omega a^\dagger a$ gives the bare photon energies.
- The final term, W , is the magnetic dipole term coupling the atomic internal states to the oscillating magnetic field. It is the sum of the two single-atom coupling terms $w^{(j)}$. Assuming that \mathbf{B}_{osc} is σ^+ -polarised, it reads:

$$W = w_1 (S^+ a + S^- a^\dagger) \quad , \quad (10.12)$$

where w_1 is defined by Eq. (10.7) and $S^\pm = S_x \pm iS_y$ are the ladder operators of the total electron spin \mathbf{S} .

Neglected terms

We have neglected one contribution to the two-atom Hamiltonian (10.9): the weak spin-dependent interaction $V_{\text{ss}}(r)$. This interaction consists of two parts: (i) the spin-spin dipole interaction [34], and (ii) the second-order spin-orbit interaction [35]. These two parts are both anisotropic, and hence the operator $V_{\text{ss}}(r)$ couples different partial waves. This spin-dependent coupling causes weak inelastic relaxation and gives rise to small resonance strengths [7, 36]. We neglect it in our numerical calculations. In Section 11.4, we discuss its role in RF-induced Feshbach resonances [20].

10.2.3. Restriction to s -wave collisions

The spherical symmetry of the electron-interaction term $V_{\text{el}}(r)$ makes it possible to seek eigenstates of H which have a definite quantum number ℓ , characterising the modulus of the angular momentum ℓ of the reduced particle. We focus on s -wave collisions ($\ell = 0$), which yield the dominant contribution in the ultracold regime³ [26]. Therefore,

³Collisions in other partial waves $\ell > 0$ involve an additional term in the radial Hamiltonian H : the centrifugal barrier $\frac{\ell(\ell+1)}{2m_r r^2}$. For low incident energies, this barrier prevents the incident particles from coming close enough (small r) to be scattered by the remaining terms in the Hamiltonian.

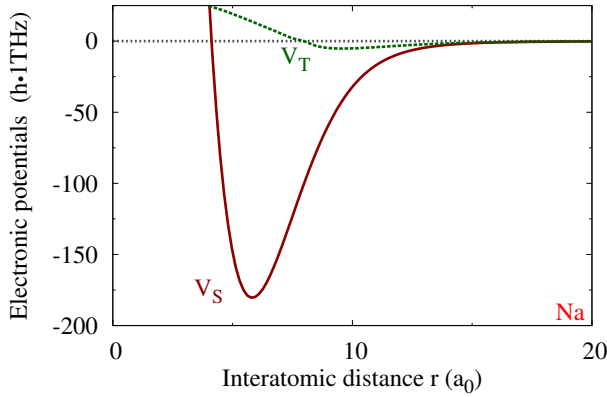


Figure 10.3. Electronic potentials $V_S(r)$ and $V_T(r)$ characterising the interaction between two ^{23}Na atoms ($a_0 = 52.9 \cdot 10^{-12} \text{ m}$ is the Bohr radius).

Eq. (10.9) reduces to the following radial Hamiltonian for the relative motion of the two atoms:

$$H = \frac{p_r^2}{2m_r} \mathbb{1} + V_{\text{el}}(r) + V_{\text{hf}} + V_Z + \hbar\omega a^\dagger a + W \quad , \quad (10.13)$$

where p_r is the radial component of the momentum \mathbf{p} of the reduced particle.

10.2.4. The electronic interaction term

The interaction between the two atoms is modelled by a potential operator $V_{\text{el}}(r)$, which depends on the interatomic distance $r = |\mathbf{r}|$ and on the two-electron spin state: the two spin-1/2 electrons can combine to form either a singlet state (total electron spin $S = 0$) or a triplet state ($S = 1$). The operator $V_{\text{el}}(r)$ can be expressed as [31]:

$$V_{\text{el}}(r) = V_S(r) P_S + V_T(r) P_T \quad , \quad (10.14)$$

where $V_S(r)$ and $V_T(r)$ are the singlet and triplet electronic interaction potentials, and P_S and P_T are the projectors onto the electron-singlet and triplet subspaces.

The operator V_{el} depends on r and thus couples the spatial motion of the atoms to their internal states. Furthermore, the basis states $|\{f_1, m_1, f_2, m_2\}^+, N\rangle$ do not all have a well-defined total electron spin S (see Section 10.3.3), therefore V_{el} causes couplings between these states.

For a given atomic species, the electronic interaction potentials $V_S(r)$ and $V_T(r)$ which appear in Eq. (10.14) share the same dispersive behaviour for large r (van der Waals interaction), characterised by a power-law decay to zero of the form $-C_6/r^6$. For smaller values of r , V_S and V_T differ because of the exchange interaction V_{exch} , defined by

$$V_{\text{exch}}(r) = (V_T - V_S)/2 \quad , \quad (10.15)$$

which decays exponentially for large r (see Eq. (12.12)). The electronic potentials are represented on Fig. 10.3 in the case of ^{23}Na .



Figure 10.4. Illustration of the spin recoupling phenomenon. For large interatomic separations, the electron spin of each atom couples to the corresponding nuclear spin. For small interatomic separations, the two electron spins couple together.

10.2.5. The spin–recoupling phenomenon

The spin–recoupling phenomenon [1] is a dynamical change in the coupling scheme for the four spins (two electron spins \mathbf{s}_j , two nuclear spins \mathbf{i}_j) involved in the collision between two atoms. Its qualitative description can be directly read off the Hamiltonian (10.9). It is due to a competition between two terms in the Hamiltonian: (i) the hyperfine interaction V_{hf} , given by Eq. (10.10), and (ii) the exchange interaction V_{exch} , given by Eq. (10.15). For large interatomic separations ($r \gg 30 a_0$), V_{hf} dominates over V_{exch} ($|V_T(r) - V_S(r)| \ll a_{\text{hf}}$), and the electron and nuclear spin of each atom couple together. On the contrary, for small interatomic separations ($r \ll 20 a_0$), the exchange interaction dominates over the hyperfine interaction: $|V_T(r) - V_S(r)| \gg a_{\text{hf}}$: The electronic interaction tends to separate electronic singlet and triplet states, therefore the two electrons couple together. This effect is schematically depicted on Fig. 10.4.

10.3. Block–matrix structure of the two–atom Hamiltonian

The mathematical property underlying the spin–recoupling phenomenon is that the hyperfine term V_{hf} and the electron interaction V_{el} do not commute [1]. Furthermore, the magnetic dipole coupling W commutes with neither of these two operators. Hence, there is no basis which diagonalises the complete Hamiltonian H of Eq. (10.13). Instead, there are bases which separately diagonalise each term of this Hamiltonian. In this section, we describe two bases for the internal–state subspace, in which the Hamiltonian has a simple block–matrix structure.

10.3.1. Relevance of the quantum numbers F and M_F

As a first step, we assume that both the static and oscillating magnetic field are turned off: $B_{\text{stat}} = B_{\text{osc}} = 0$. The two–atom Hamiltonian H of Eq. (10.13) reduces to:

$$H_0 = \frac{p_r^2}{2m_r} \mathbb{1} + V_{\text{el}}(r) + V_{\text{hf}} \quad . \quad (10.16)$$

The two atoms carry a total of four spins: two electron spins \mathbf{s}_j and two nuclear spins

\mathbf{i}_j . The addition of these four spins yields the total two-atom spin \mathbf{F} :

$$\mathbf{F} = \mathbf{s}_1 + \mathbf{i}_1 + \mathbf{s}_2 + \mathbf{i}_2 \quad . \quad (10.17)$$

The Hamiltonian H_0 commutes with the total spin \mathbf{F}^2 and its projection F_z along the quantisation axis \mathbf{e}_z :

- The kinetic energy term is rotationally invariant.
- The single-atom spins \mathbf{s}_j and \mathbf{i}_j are vector operators⁴, and the scalar products $\mathbf{s}_j \cdot \mathbf{i}_j$ are thus scalar operators, hence they commute with \mathbf{F}^2 and F_z . Therefore, so does V_{hf} .
- The electron interaction can be rewritten as [37]:

$$V_{\text{el}}(r) = \left(\frac{1}{4}V_S(r) + \frac{3}{4}V_T(r) \right) + (V_T(r) - V_S(r)) \frac{\mathbf{s}_1 \cdot \mathbf{s}_2}{\hbar^2} \quad . \quad (10.18)$$

The operator $\mathbf{s}_1 \cdot \mathbf{s}_2$ is a scalar operator, and $V_S(r)$ and $V_T(r)$ depend only on r , therefore V_{el} is rotationally invariant.

It is therefore relevant to use internal-state basis vectors which have well-defined quantum number F and M_F , which characterise the modulus of \mathbf{F} and its projection F_z , respectively.

In the presence of static and oscillating magnetic fields, the quantum numbers F and M_F are no longer conserved. However, we show below that the Hamiltonian H does have a simple block-matrix structure in bases involving these quantum numbers.

10.3.2. Two bases for two spin-coupling modes

We focus on the subspace characterised by given values of the quantum numbers F and M_F . There are two distinct bases⁵ spanning this subspace, corresponding to the two coupling modes represented on Fig. 10.4:

1. The two electron spins couple together ($\mathbf{S} = \mathbf{s}_1 + \mathbf{s}_2$) and the two nuclear spins couple together ($\mathbf{I} = \mathbf{i}_1 + \mathbf{i}_2$), then \mathbf{F} results from the addition of \mathbf{S} and \mathbf{I} . This coupling mode results in the ‘*molecular*’ basis:

$$\mathbf{e}_M = (|S, I, F, M_F\rangle) \quad , \quad (10.19)$$

and corresponds to the left-hand part of Fig. 10.4.

2. The two spins on each atom couple together ($\mathbf{f}_j = \mathbf{s}_j + \mathbf{i}_j$), then \mathbf{F} results from the addition of \mathbf{f}_1 and \mathbf{f}_2 . This coupling mode results in the ‘*atomic*’ basis:

$$\mathbf{e}_A = (|\{f_1, f_2\}^{\varepsilon_f}, F, M_F\rangle) \quad , \quad (10.20)$$

and corresponds to the right-hand part of Fig. 10.4.

⁴Each of these four operators \mathbf{V} satisfies the characteristic commutation relations $[F_i, V_j] = i \sum_k \varepsilon_{ijk} V_k$, where ε_{ijk} is the antisymmetric unit tensor.

⁵For a given (F, M_F) subspace, the ‘frame transformation’ linking the basis states in \mathbf{e}_A to those in \mathbf{e}_M is conveniently expressed in terms of Wigner 9j coefficients.

Consequences of bosonic symmetry The basis states in ϵ_M and ϵ_A are all either symmetric or antisymmetric under the exchange of the two atoms. In order to enforce bosonic symmetry, the ‘molecular’ basis ϵ_M only contains states with $(S + I)$ even. In the case of the ‘atomic’ basis ϵ_A , the (anti-)symmetric two-atom states of Eq. (10.20) are defined by:

$$|\{f_1, f_2\}^{\varepsilon_f}, F, M_F\rangle = \frac{1}{\sqrt{2(1 + \delta_{f_1, f_2})}} (|f_1, f_2, F, M_F\rangle + \varepsilon_f |f_2, f_1, F, M_F\rangle) \quad (10.21)$$

Bosonic symmetry requires that ϵ_A only contain states such that $\varepsilon_f = (-1)^{f_1 + f_2 - F}$.

10.3.3. Analysis of the subspaces characterised by (F, M_F)

Let us consider an internal-state subspace characterised by given quantum numbers (F, M_F) . The addition rules for angular momenta and the symmetry properties described in Section 10.3.2 constrain the dimension and electron-spin properties of this subspace.

If F is odd ($F = 2i, 2i - 2, \dots$, or 1):

The (F, M_F) subspace has dimension 1. It is spanned by the single internal-state vector $|\{f^+, f^-\}^+, F, M_F\rangle = |S = 1, I = F, F, M_F\rangle$, which is electronic-triplet.

If F is even ($F = 2i + 1, 2i - 1, \dots$, or 0):

The (F, M_F) subspace has dimension 3. It is spanned by three ‘atomic’ basis states:

$|\{f^+, f^+\}, F, M_F\rangle$, $|\{f^+, f^-\}^-, F, M_F\rangle$, and $|\{f^-, f^-\}, F, M_F\rangle$,

or, equivalently, by three ‘molecular’ basis states:

$|S = 1, I = F + 1, F, M_F\rangle$, $|S = 0, I = F, F, M_F\rangle$, and $|S = 1, I = F - 1, F, M_F\rangle$.

It has no well-defined total electronic spin S .

The $(F \text{ even}, M_F)$ block is affected by a finite-size effect for $F = 2i + 1$. In this case, the first two ‘molecular-basis’ states do not exist: the $(F = 2i + 1, M_F)$ subspace has dimension 1 and is electronic-triplet.

Other finite-size effects affect other $(F \text{ even}, M_F)$ blocks, but for simplicity’s sake we shall not describe them here⁶.

10.3.4. Ordering of the basis states in ϵ_A and ϵ_M

Bringing together the ‘molecular’ basis states spanning the (F, M_F) subspaces as described above, we obtain the complete ‘molecular’ basis ϵ_M , which spans all internal states accessible to the atom pair. We order these basis states by values of M_F , decreasing from $M_F = 2i + 1$ to $M_F = -(2i + 1)$. Within each subspace characterised by a given value of M_F , we order the states as shown in Table 10.1:

⁶However, they are accounted for in all of our results.

10. The Two-Atom Hamiltonian

- we sort the states by decreasing values of F , from $F = 2i + 1$ to $|M_F|$;
- Within each (F, M_F) subspace that is not one-dimensional, we sort them by decreasing values of I .

Similarly, we construct the complete ‘atomic’ basis \mathbf{e}_A by collecting the basis states for all (F, M_F) subspaces. We order them by decreasing values of M_F ; within a given M_F subspace, we order them as shown in Table 10.2:

- We sort the states by decreasing values of F .
- Within each (F, M_F) subspace that is not one-dimensional, we sort them by decreasing values of $(f_1 + f_2)$.

10.3.5. Block-matrix structure in the ‘molecular’ basis \mathbf{e}_M

Restriction of the Hamiltonian to a stable $(M_F + N)$ subspace

The operators V_{el} , V_{hf} and V_Z all commute with F_z , and do not act on the photon number. The photon energy term $\hbar\omega a^\dagger a$ commutes with the photon number operator $a^\dagger a$, and does not act on the atomic spins. In the case of a σ^+ -polarised oscillating magnetic field \mathbf{B}_{osc} , the coupling term W^{σ^+} commutes neither with F_z nor with $a^\dagger a$. However, a direct calculation yields

$$\left[W^{\sigma^+}, \frac{F_z}{\hbar} + a^\dagger a \right] = 0 \quad , \quad (10.22)$$

which can be seen as a consequence of the conservation of angular momentum for the system “two atoms in the presence of the magnetic field”. Therefore, for a given value of N_0 , the subspace spanned by all states $|S, I, F, M_F, N\rangle$, where N is the photon number and $M_F + N = N_0$, is stable under H . We choose $N_0 \gg 1$, its exact value being arbitrary: the physically meaningful parameter is the average magnetic field amplitude $B_{\text{osc}} = b_0 \sqrt{N_0}$, where b_0 has been introduced in Eq. (10.4).

We write $H = \frac{p_r^2}{2m_r} + V_{\text{tot}}(r)$, where the total matrix potential $V_{\text{tot}}(r)$ reads:

$$V_{\text{tot}}(r) = V_{\text{el}}(r) + V_{\text{hf}} + V_Z + \hbar\omega a^\dagger a + W \quad . \quad (10.23)$$

We are interested in a matrix representation of the restriction of $V_{\text{tot}}(r)$ to the stable subspace described above.

We find that this matrix has a simple ‘block’ structure in the ‘molecular’ basis \mathbf{e}_M described in Section 10.3.4. This block structure is represented on Fig. 10.5. The next few paragraphs focus on its derivation.

	$S = 1, I = 2i$	$S = 0, I = 2i - 1$	$S = 1, I = 2i - 2$	$S = 0, I = 2i - 3$	$S = 1, I = 2i - 4$
$F = 2i + 1$	$ 1, 2i, 2i + 1, M_F\rangle$				
$F = 2i$	$ 1, 2i, 2i, M_F\rangle$				
$F = 2i - 1$	$ 1, 2i, 2i - 1, M_F\rangle$	$ 0, 2i - 1, 2i - 1, M_F\rangle$	$ 1, 2i - 2, 2i - 1, M_F\rangle$		
$F = 2i - 2$			$ 1, 2i - 2, 2i - 2, M_F\rangle$		
$F = 2i - 3$			$ 1, 2i - 2, 2i - 3, M_F\rangle$	$ 0, 2i - 3, 2i - 3, M_F\rangle$	$ 1, 2i - 4, 2i - 3, M_F\rangle$
$F = 2i - 4$					\vdots

Table 10.1. ‘Molecular’ basis states $\{|S, I, F, M_F\rangle\}$ in a given M_F block. All states in a given line (resp. column) have the same value of F (resp. S and I). The states are ordered as shown in the table, read from left to right and from top to bottom. The electronic-triplet states ($S = 1$) are shown in green.

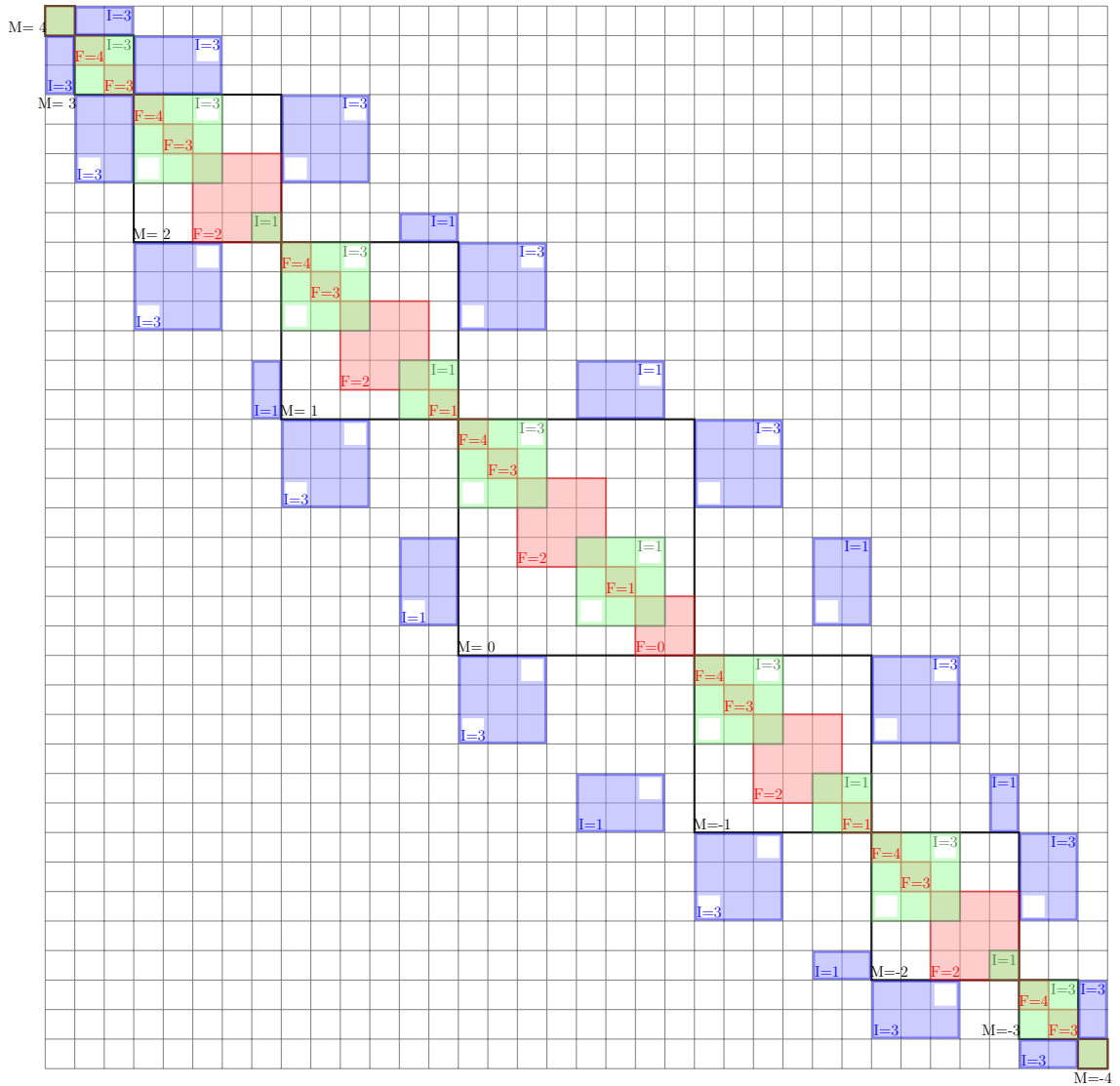


Figure 10.5. ‘Block-matrix’ structure, of the restriction of H to the stable subspace spanned by ‘molecular’ all states $|S, I, F, M_F, N\rangle$ such that $M_F + N = N_0$ (valid for a σ^+ -polarised magnetic field \mathbf{B}_{osc}), in the case of an alkali atom with nuclear spin $i = 3/2$ (such as ^{23}Na or ^{87}Rb). Each elementary square corresponds to one matrix element. The black blocks correspond to given values of M_F , decreasing from $M_F = 4$ to $M_F = -4$. The red blocks represent the contribution of $V_{\text{el}} + V_{\text{hf}}$ (given values of M_F and F), the green blocks correspond to V_Z (given values of M_F , S , and I), and the blue blocks correspond to W (given values of S and I , $\Delta M_F = \pm 1$). All matrix elements which are not filled in with colour are zero.

	$\{f^+, f^+\}$	$\{f^+, f^-\}^\pm$	$\{f^-, f^-\}$
$F = 2i + 1$	$ \{f^+, f^+\}, 2i + 1, M_F\rangle$		
$F = 2i$		$ \{f^+, f^-\}^+, 2i, M_F\rangle$	
$F = 2i - 1$	$ \{f^+, f^+\}, 2i - 1, M_F\rangle$	$ \{f^+, f^-\}^-, 2i - 1, M_F\rangle$	$ \{f^-, f^-\}, 2i - 1, M_F\rangle$
$F = 2i - 2$		$ \{f^+, f^-\}^+, 2i - 2, M_F\rangle$	
$F = 2i - 3$	$ \{f^+, f^+\}, 2i - 3, M_F\rangle$	$ \{f^+, f^-\}^-, 2i - 3, M_F\rangle$	$ \{f^-, f^-\}, 2i - 3, M_F\rangle$
$F = 2i - 4$		\vdots	

Table 10.2. ‘Atomic’ basis states $|\{f_1, f_2\}^\epsilon, F, M_F\rangle$ in a given M_F block. All states on a given line (resp. column) have the same quantum number F (resp. $\{f_1, f_2\}^\epsilon$). The states are ordered as shown in the Table, read from left to right and from top to bottom. The electronic-triplet states ($S = 1$) are shown in green.

Contribution of the rotationally invariant terms

We have shown in Section 10.3.1 that the operators V_{el} and V_{hf} are rotationally invariant. Furthermore, the photon-energy term $\hbar\omega a^\dagger a$ does not act on the atomic spins.

These three terms conserve F , M_F , and N . Therefore, they can only mix the states that appear in a given line of Table 10.1. Hence, they contribute the red blocks of Fig. 10.5, each of which corresponds to a subspace characterised by given values of F and M_F .

To be more specific:

- The operator $\hbar\omega a^\dagger a$ only contributes diagonal matrix elements, which, within each M_F subspace, are all equal to $(N_0 - M_F)\hbar\omega$;
- The expression (10.14) for the electronic interaction V_{el} shows that it is diagonal in the ‘molecular’ basis ϵ_{M} . For a given value of r , it contributes $V_T(r)$ along each triplet state (typeset in green in Table 10.1), and $V_S(r)$ along each singlet state;
- The hyperfine term V_{hf} is *not diagonal* in the basis ϵ_{M} (although it is diagonal in the basis ϵ_{A}).

Contribution of the Zeeman term

The Zeeman term V_Z breaks rotational invariance, as it singles out the direction \mathbf{e}_z of the static magnetic field: it does not conserve the total spin modulus F .

The expression (10.11) for V_Z shows that it is proportional to S_z , which is the projection along z of the total electronic spin operator \mathbf{S} . This implies that V_Z conserves the quantum numbers S , I , and M_F . Additionally, S_z , and hence V_Z , give zero when applied to any singlet state. These remarks show that V_Z can only mix triplet states which belong to a given column of Table 10.1. Hence, it contributes the green blocks of Fig. 10.5, each of which corresponds to a subspace characterised by $S = 1$ and given values of I and M_F .

Furthermore, \mathbf{S} is a vector operator, therefore V_Z obeys the vector selection rule [37] on the quantum number F : it can have non-zero matrix elements only in between states whose quantum numbers F_1 and F_2 satisfy $|F_1 - F_2| \leq 1$. The green-block matrix elements which do not satisfy this criterion are zero, and are shown in white on Fig. 10.5.

Contribution of the magnetic dipole coupling term

The magnetic dipole coupling term W does not conserve F , M_F , or N .

As pointed out in Section 10.3.5, W conserves the sum ($M_F + N$). Furthermore, it is a sum of two terms which involve S^+ and S^- (see Eq. (10.12)). Hence, it conserves the quantum numbers S and I , and it gives zero when acting on any singlet state.

The operators S^\pm have non-zero matrix elements only in between states whose quantum numbers M_{F1} and M_{F2} satisfy $|M_{F1} - M_{F2}| = 1$. Therefore, W connects a given triplet column of Table 10.1, belonging to a subspace with given M_F , to the corresponding column of Table 10.1 in the subspaces having the total spin projections $M_F + 1$ and $M_F - 1$. It contributes the blue blocks on Fig. 10.5.

Finally, the S^\pm are the ladder operators for the vector operator \mathbf{S} , therefore W obeys the vector selection rule on F . The blue-block matrix elements which do not satisfy this criterion are zero, and are shown in white on Fig. 10.5.

11. Characterising the resonances

We consider a collision between two bosonic alkali atoms, in the presence of an oscillating magnetic field. If this collision occurs at sufficiently low energy, it is fully characterised by the corresponding scattering length a [1, 26]. We assume that both atoms are asymptotically in their lowest-energy hyperfine state. The oscillating magnetic field acts on the internal atomic states, and it may cause a coupling to a weakly-bound dimer state relating to different internal states. If the microwave frequency ω approaches the energy difference between the incident scattering state and a weakly-bound dimer state (see Fig. 11.1), the pair of atoms undergoes virtual spin-flip transitions which cause a resonant variation of the scattering length with ω .

In this chapter we show that, for low-enough amplitudes B_{osc} of the *oscillating* magnetic field, these resonances yield a hyperbolic divergence in the scattering length as a function of the microwave frequency ω (see [21], reproduced in Chapter 13):

$$a(\omega) = a_{\text{bg}} \left(1 + \frac{\Delta\omega}{\omega - \omega_{\text{res}}} \right) \quad , \quad (11.1)$$

where ω_{res} is the resonant frequency, $\Delta\omega$ is the resonance width, and a_{bg} is the background scattering length (*i.e.* the value of the scattering length for frequencies ω which are far from ω_{res} ; see Fig. 11.2). We show that the resonant frequency ω_{res} is close to the hyperfine transition frequency $\Delta E_{\text{hf}}/\hbar$, and that the resonance width $\Delta\omega$ scales with the squared amplitude B_{osc}^2 of the oscillating magnetic field.

We describe two approaches we have used to characterise microwave-induced resonances. We illustrate these approaches on the specific case of the microwave-induced

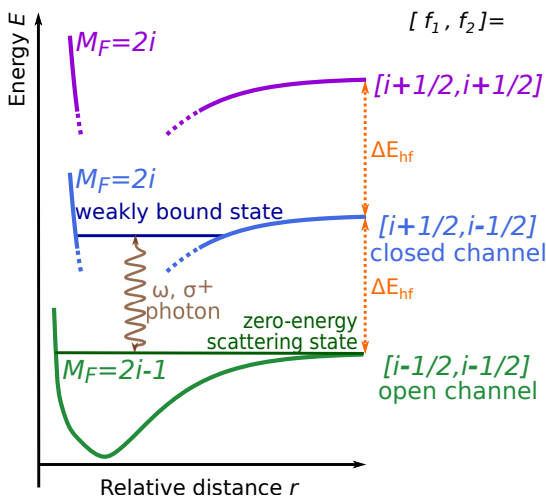


Figure 11.1. Fano–Feshbach resonance in a collision between two atoms, induced by an oscillating magnetic field.

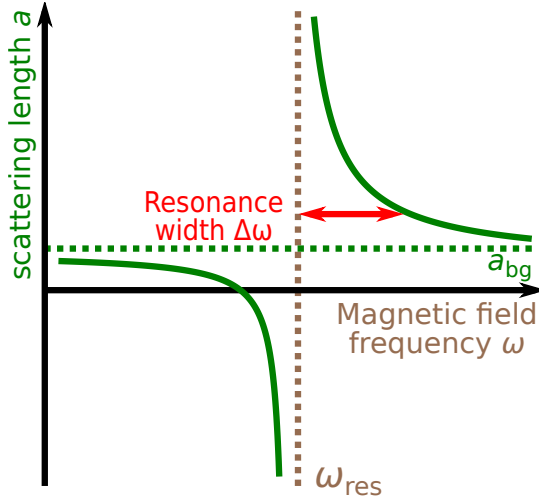


Figure 11.2. Definitions of the resonance frequency ω_{res} , the resonance width $\Delta\omega$, and the background scattering length a_{bg} , for a hyperbolic microwave-induced resonance.

resonance studied in the published article of Chapter 13. We calculate the resonance frequencies and widths for the bosonic alkalis ${}^7\text{Li}$, ${}^{23}\text{Na}$, ${}^{41}\text{K}$, ${}^{87}\text{Rb}$, and ${}^{133}\text{Cs}$. Our results yield optimistic prospects for an experimental observation of these resonances using the four latter species.

11.1. The two-subspace approach

11.1.1. Reduction to a two-subspace problem

We consider a collision involving a pair of atoms whose asymptotic state is $|f^-, m_f = i - 1/2; f^-, m_f = i - 1/2\rangle$ (this is the state labelled ‘bb’ on Fig. 10.2). This two-atom state carries the quantum numbers $\{f^-, f^-\}$ and the two-atom total spin projection $M_F = 2i - 1$. An inspection of Table 10.2 shows that it has a well-defined quantum number $F = 2i - 1$. In terms of the molecular basis ϵ_M , it belongs to the three-dimensional block characterised by $F = M_F = 2i - 1$, and Table 10.1 shows that it does not have well defined electronic and nuclear spins.

Throughout this chapter, we assume that no static magnetic field is present: $B_{\text{stat}} = 0$ and, hence, the Zeeman term $V_Z = 0$. The coupling between the atom pair and the oscillating magnetic field is described by the magnetic dipole coupling term $W = w_1(S^+a + S^-a^\dagger)$ of Eq. (10.12). The atom pair can either...

- *absorb* a photon, in which case its total spin projection M_F *increases* by 1, or
- *emit* a photon, in which case its total spin projection M_F *decreases* by 1.

The conservation of energy, applied to the system “atom pair and electromagnetic field”, requires the emission of a photon by the atom pair to be accompanied by a decrease in the energy of the pair. This is not possible in the present case as both atoms are asymptotically in the lowest-energy hyperfine state f^- . Therefore, the atom pair can only absorb a photon. This process corresponds to a direct coupling of the ($F = M_F =$

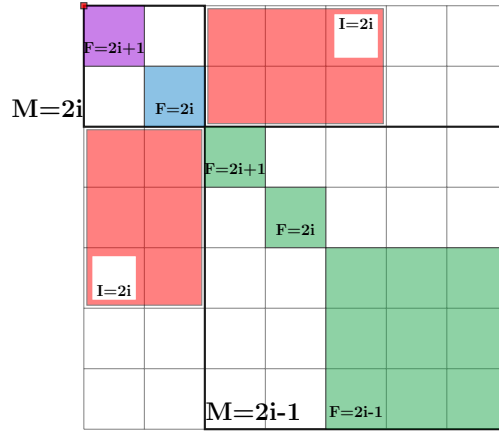


Figure 11.3. Block-matrix representation, in the ‘molecular’ basis ϵ_M , of the restriction of H to the subspaces $M_F = 2i - 1$ and $M_F = 2i$. The diagonal purple ($M_F = 2i$, $F = 2i + 1$), blue ($M_F = 2i$, $F = 2i$), and green ($F = M_F = 2i - 1$) blocks represent the contribution of V_{hf} and V_{el} , and respectively correspond to the purple, blue, and green potentials of Fig. 11.1. The red off-diagonal blocks ($S = 1$, $I = 2i$) represent the coupling term W . The asymptotic state of the atom pair belongs to the three-dimensional $F = M_F = 2i - 1$ subspace (green 3×3 block).

$2i - 1$) subspace to the ($F = M_F = 2i$) subspace. The block-matrix structure of the Hamiltonian H (Eq. (10.13)), restricted to these two subspaces, is shown on Fig. 11.3.

The vector selection rules enforced on W (see Section 10.3.5) imply that this operator has no non-zero matrix element linking the subspaces ($F = M_F = 2i - 1$) and ($F = 2i + 1$, $M_F = 2i$). Therefore, the ($F = M_F = 2i - 1$) subspace is directly coupled by W to only one subspace, characterised by $F = M_F = 2i$. This makes it possible to restrict the Hamiltonian to the four-dimensional subspace spanned by the ($F = M_F = 2i - 1$) and ($F = M_F = 2i$) blocks. The resulting 4×4 Hamiltonian, whose block structure is represented on Fig. 11.4, has a two-subspace structure:

- The ($F = M_F = 2i - 1$) subspace (dimension 3), which contains the asymptotic state of the atom pair, is the open subspace;
- The ($F = M_F = 2i$) subspace (dimension 1) is the closed subspace;
- The coupling is due to the magnetic dipole coupling operator W .

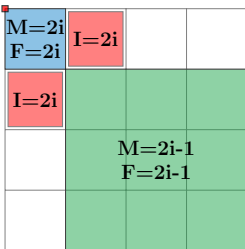


Figure 11.4. Block structure of the Hamiltonian H , restricted to the subspace spanned by the ($F = M_F = 2i - 1$) block (green) and the ($F = M_F = 2i$) block (blue) (basis ϵ_M). This Hamiltonian has a two-subspace structure, where the green block is the open subspace, the blue block is the closed subspace, and the coupling (red blocks) is due to the magnetic dipole coupling W .

11. Characterising the resonances

We call H_0 the ‘bare’ Hamiltonian describing the two atoms in the absence of any magnetic field ($B_{\text{stat}} = B_{\text{osc}} = 0$):

$$H_0 = \frac{p_r^2}{2m_r} \mathbb{1} + V_{\text{el}} + V_{\text{hf}} \quad . \quad (11.2)$$

The results of Section 10.3.5 show that the subspaces ($F = M_F = 2i - 1$) and ($F = M_F = 2i$) are both stable under H_0 . We introduce the restrictions H_{op} and H_{cl} of H_0 to these two subspaces. Tables 10.1 and 10.2 show that the ($F = M_F = 2i$) subspace is one-dimensional, and that it is spanned by the electronic-triplet state

$$|\eta_1\rangle = |\{f^+, f^-\}^-, F = 2i, M_F = 2i\rangle = |S = 1, I = 2i, F = 2i, M_F = 2i\rangle \quad . \quad (11.3)$$

We also introduce the 1×3 coupling operator \hat{W} defined by:

$$\hat{W} = \frac{\mu_B B_{\text{osc}}}{\hbar} \langle \eta_1 | S^+ | \zeta_1 \rangle \begin{pmatrix} 1 & 0 & 0 \end{pmatrix} \quad , \quad (11.4)$$

where $|\zeta_1\rangle = |S = 1, I = 2i, F = 2i - 1, M_F = 2i - 1\rangle$ is the only state in the basis \mathfrak{e}_M which is directly connected to $\langle \eta_1 |$ by S^+ . Assuming that the electromagnetic field initially contains N photons (with $N \gg 1$), the two-subspace Hamiltonian of Fig. 11.4 reads:

$$H_{2\text{sub}} = \begin{pmatrix} H_{\text{cl}} + (N - 1)\hbar\omega & \hat{W} \\ \hat{W}^\dagger & H_{\text{op}} + N\hbar\omega \end{pmatrix} \quad , \quad (11.5)$$

where we have used the fact that the atom pair must absorb a photon to transit from the open subspace to the closed subspace. Next, we note (see Table 10.1) that the closed subspace is spanned by a single electronic-triplet state. Introducing the single-atom hyperfine splitting ΔE_{hf} , the detuning $\hbar\delta = \hbar\omega - \Delta E_{\text{hf}}$ of the microwave frequency with respect to ΔE_{hf} , and the energy $E_{\{f^-, f^-\}}$ of two atoms in their ground hyperfine state (in the absence of any magnetic field), the two-subspace Hamiltonian reduces to:

$$H_{2\text{sub}} = (N\hbar\omega + E_{\{f^-, f^-\}}) \mathbb{1} + \begin{pmatrix} H_T - \hbar\delta & \hat{W} \\ \hat{W}^\dagger & H_{\text{op}} - E_{\{f^-, f^-\}} \end{pmatrix} \quad , \quad (11.6)$$

where

$$H_T = \frac{p_r^2}{2m_r} + V_T(r) \quad (11.7)$$

is the (single-channel) triplet Hamiltonian.

An approximation for the resonance frequency ω_{res} can be read off Equation (11.6): the resonance occurs for frequencies close to the frequency ω_{res}^0 for which the (diagonal) open-subspace and closed-subspace components of $H_{2\text{sub}}$ are equal. We recall that the atom pair collides with the energy $E_{\{f^-, f^-\}}$, which is the scattering threshold of H_{op} . Furthermore, Table 10.2 shows that the closed-channel state carries the quantum numbers $\{f^+, f^-\}$, which correspond to the hyperfine energy $E_{\{f^+, f^-\}} = E_{\{f^-, f^-\}} + \Delta E_{\text{hf}}$. Calling $|E_T|$ the binding energy of the resonant (triplet) bound dimer state in the closed channel, we thus obtain:

$$\omega_{\text{res}}^0 = \Delta E_{\text{hf}} - |E_T| \quad . \quad (11.8)$$

11.1.2. Main results of the two-channel approach

We now apply the standard two-channel results to the Hamiltonian (11.6). Our goal is to extract from $H_{2\text{sub}}$ information concerning the resonance frequency ω_{res} and the corresponding resonance width $\Delta\omega$.

The Hamiltonian (11.6) differs from the standard two-channel Hamiltonian as the coupling operator \hat{W} is a constant with respect to r , and, hence, does not vanish for $r \rightarrow \infty$. This causes a difference Δ of the threshold scattering energy of $H_{2\text{sub}}$ with respect to that of $H_{\text{op}} + N\hbar\omega$. This difference in threshold energies is associated with single-atom dressed-state effects [20]. If the detuning $\hbar\delta = \hbar\omega - \Delta E_{\text{hf}}$ of the microwave frequency ω with respect to the single-atom hyperfine splitting ΔE_{hf} is greater than $\mu_B B_{\text{osc}}$, then $\hbar\Delta \sim \frac{(\mu_B B_{\text{osc}})^2}{\hbar\delta}$. The two-channel results are applicable to $H_{2\text{sub}}$ if $\Delta \ll |E_T|$ and can be neglected. Near the resonance, where $\delta \approx -|E_T|$ (see Eq. (11.8)), this condition requires $\mu_B B_{\text{osc}} \ll |E_T|$.

In the regime where Δ is negligible, the solution of the two-channel model within the single-resonance approximation [1] yields the expected hyperbolic divergence (11.1) for the scattering length $a(\omega)$ in the vicinity of the resonance. It predicts the resonance frequency:

$$\omega_{\text{res}} = \omega_{\text{res}}^0 + \alpha B_{\text{osc}}^2 \quad , \quad (11.9)$$

where ω_{res}^0 is defined by Eq. (11.8), and the additional term αB_{osc}^2 is a small shift on the resonance frequency, due to the coupling between the open and closed subspaces, which is proportional to the square of the magnetic field amplitude. The two-channel approach provides an expression for the coefficient α in terms of the bound-state wavefunction $|\varphi_T\rangle$ and the open-channel Green's function $G_{\text{op}}^+(E_{\{f^-, f^-\}})$; however, the shift αB_{osc}^2 is more easily obtained within the framework of the full coupled-channel approach described in Section 11.2, and we shall not discuss the two-channel result for the coefficient α .

The expression for the resonance width involves the bare open- and closed-channel wavefunctions. The open-channel wavefunction is the threshold-energy scattering state $|\Psi_{\mathbf{k}=\mathbf{0}}^{(2i-1)}\rangle$, in the presence of N photons. For large interatomic separations, this state corresponds to the two-particle state $|\{f^-, f^-\}, F = 2i - 1, M_F = 2i - 1\rangle$, in which both atoms have $f = m_f = i - 1/2$. The closed-channel wavefunction $|\Psi_0^{(2i)}\rangle = |\varphi_T, \eta_1\rangle$, where $|\eta_1\rangle$ is defined by Eq. (11.3) and $\varphi_T(r)$ is the wavefunction of the resonant weakly-bound (triplet) dimer state, in the presence of $N - 1$ photons.

The two-channel model predicts the following resonance width:

$$\hbar\Delta\omega = \frac{1}{2\pi} \frac{m_r}{a_{\text{bg}}\hbar^2} (\mu_B B_{\text{osc}})^2 \left| \langle \Psi_0^{(2i)} | S^+ | \Psi_{\mathbf{k}=\mathbf{0}}^{(2i-1)} \rangle \right|^2 \quad . \quad (11.10)$$

It is proportional to the squared amplitude B_{osc}^2 of the magnetic field, and to the spin-flip Franck-Condon factor characterising the strength of the coupling between the open and closed channels.

11. Characterising the resonances

	⁷ Li	²³ Na	⁴¹ K	⁸⁷ Rb	¹³³ Cs (1)	¹³³ Cs (2)
Binding energy of resonant triplet state and resonance frequency						
$ E_T /\hbar$ (MHz)	12000	200	140	25	$5 \cdot 10^{-3}$	110
$\omega_{\text{res}}^0/2\pi$ (GHz)	11	16	0.12	6.8	9.2	9.1
Two-subspace approach						
$\Delta\omega/2\pi$ (Hz/G ²)	6	1400	350	60	$-5.8 \cdot 10^9$	-4500

Table 11.1. Numerical values for the resonance widths $\Delta\omega$, obtained using the two-subspace method, for the bosonic alkalis ⁷Li, ²³Na, ⁴¹K, ⁸⁷Rb, ¹³³Cs. The binding energies $|E_T|$ of the resonant triplet bound states are also shown. For all atoms except Cesium, the considered bound state is the highest-energy bound state of the triplet potential. For Cesium, the columns labelled Cs(1) and Cs(2) respectively refer to the highest and second-highest triplet bound states.

11.1.3. Numerical results

The evaluation of the resonance widths given by Eq. (11.10) requires the numerical calculation of the wavefunctions $\varphi_T(r)$ (one channel) and $\Psi_{\mathbf{k}=0}^{(2i-1)}(r)$ (three channels). The methods used for these numerical calculations will be presented in Chapter 12. Our numerical results for the resonance widths, obtained within the two-subspace approach with the bosonic alkalis ⁷Li, ²³Na, ⁴¹K, ⁸⁷Rb, ¹³³Cs, are collected in Table 11.1.

We have restricted our analysis to *s*-wave collisions, therefore the open- and closed-channel wavefunctions can be expressed in terms of the corresponding radial wavefunctions $\mathbf{u}_{\mathbf{k}=0}^{(2i-1)}$ and $u_T(r)$:

$$\Psi_{\mathbf{k}=0}^{(2i-1)}(r) = \frac{Y_0^0}{r} \mathbf{u}_{\mathbf{k}=0}^{(2i-1)} \quad \text{and} \quad \varphi_T(r) = \frac{Y_0^0}{r} u_T(r) \quad , \quad (11.11)$$

with $Y_0^0 = 1/\sqrt{4\pi}$ being the spherical harmonic for $l = m = 0$. In terms of these radial wavefunctions, the overlap involved in the expression (11.10) for the resonance width reads:

$$\langle \Psi_0^{(2i)} | S^+ | \Psi_{\mathbf{k}=0}^{(2i-1)} \rangle = \langle \eta_1 | S^+ | \zeta_1 \rangle \int_0^\infty dr u_T(r) \langle \zeta_1 | \mathbf{u}_{\mathbf{k}=0}^{(2i-1)} \rangle(r) \quad . \quad (11.12)$$

The radial bound-state wavefunction $u_T(r)$, and the radial wavefunction component $\langle \zeta_1 | \mathbf{u}_{\mathbf{k}=0}^{(2i-1)} \rangle(r)$, are plotted on Figs. 11.5 for all five considered atoms. Both wavefunctions show oscillations for small values of r , for which the electronic potentials V_S and V_T are large and negative (see Fig. 10.3) and, hence, the kinetic energy is large. For large values of r , the zero-energy scattering state component $\langle \zeta_1 | \mathbf{u}_{\mathbf{k}=0}^{(2i-1)} \rangle(r)$ varies linearly with r , whereas the bound-state wavefunction $u_T(r)$ decays exponentially.

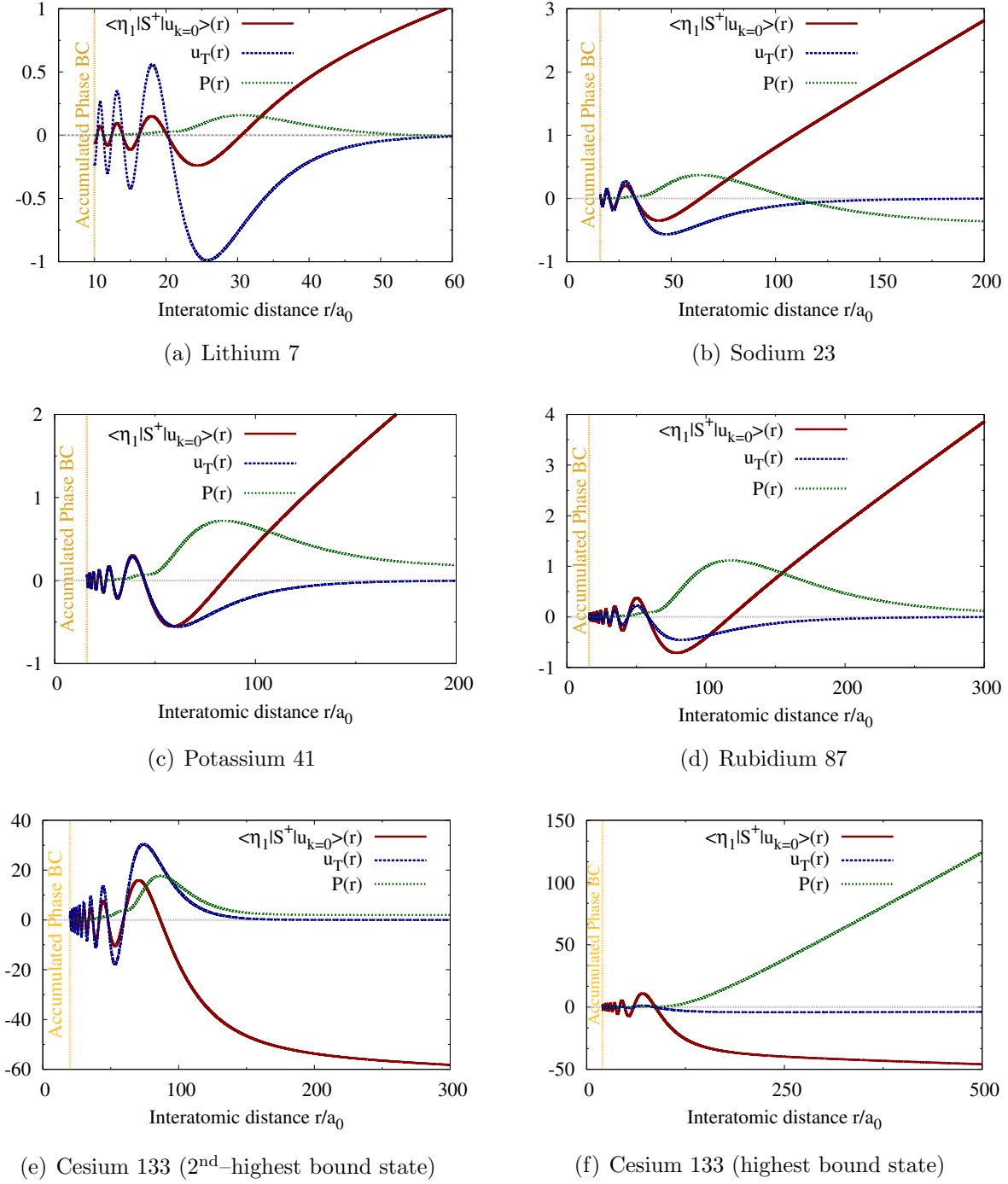


Figure 11.5. Radial wavefunctions (arbitrary units) versus the interatomic distance r (in units of the Bohr radius a_0), for the bosonic alkalis ${}^7\text{Li}$, ${}^{23}\text{Na}$, ${}^{41}\text{K}$, ${}^{87}\text{Rb}$, and ${}^{133}\text{Cs}$. Blue curve: radial wavefunction $u_T(r)$ of the last bound state of the Triplet Hamiltonian. Red curve: $\langle \zeta_1 | \mathbf{u}_{k=0}^{(2i-1)} \rangle(r)$. Green curve: partial overlap $P(r)$, defined by Eq. (11.13). An additional graph (Fig. 11.5(e)) is shown for ${}^{133}\text{Cs}$, illustrating the overlap obtained with the second-highest Triplet bound state.

11. Characterising the resonances

Figures 11.5 also show the dependence on r of the ‘partial’ overlap $P(r)$, defined by¹

$$P(r) = \int_{r_0}^r d\rho u_T(\rho) \langle \zeta_1 | \mathbf{u}_{\mathbf{k}=\mathbf{0}}^{(2i-1)} \rangle(\rho) \quad , \quad (11.13)$$

so that $\langle \Psi_0^{(2i)} | S^+ | \Psi_{\mathbf{k}=\mathbf{0}}^{(2i-1)} \rangle = \langle \eta_1 | S^+ | \zeta_1 \rangle P(r \rightarrow \infty)$. The plots of $P(r)$ show that, for all considered cases except the resonance in ^{133}Cs involving the highest triplet bound state of (Fig. 11.5(f)), the contribution to the overlap of the small- r region (where the wavefunctions oscillate) and the large- r region (where the wavefunctions reach their asymptotic behaviour) have opposite signs and comparable magnitudes: this leads to a reduction of the total overlap and, hence, to smaller resonance widths than could have been expected by neglecting the large- r wavefunction ‘tails’.

The resonance in ^{133}Cs involving the highest triplet bound state (see Fig. 11.5(f) and the column labelled $^{133}\text{Cs}(1)$ in Table 11.1) is particularly large. In this specific case, the resonant bound state is very weakly bound ($|E_T|/E_{\text{vdw}} \approx 2 \cdot 10^{-3}$, where the van-der-Waals energy E_{vdw} [24] is an energy scale associated with the large- r behaviour of the electron potentials) and thus has a very large spatial extent, determined by the scattering length $a_T = 2500 a_0$: in this particular case, the large- r contribution dominates, which leads to a very large resonance width compared to the results obtained with all other atoms (see Table 11.1). However, the two-channel result for this giant resonance is only applicable for magnetic fields which satisfy $\mu_B B_{\text{osc}} \lesssim |E_T|$ (*i.e.* $B_{\text{osc}} \lesssim 4 \text{ mG}$), above which dressed-state effects affect the shape of the resonance, as explained in Section 11.2.

To our knowledge, no experimental measurement of the weakly-bound state in ^{133}Cs has yet been published. The large value of the triplet scattering length ($a_T = 2500 a_0$) is a strong indication that it does exist (see Section 9.1.2). Furthermore, we interpret the Feshbach resonances occurring in ^{133}Cs for small static magnetic fields, analysed in Chapter 14, as experimental evidence of its existence.

11.1.4. Narrow resonances for Lithium and Rubidium

The numerical results for the resonance widths, collected in Table 11.1, show that microwave-induced Feshbach resonances are particularly narrow for ^7Li ($\Delta\omega = 6 \text{ Hz/G}^2$) and ^{87}Rb ($\Delta\omega = 60 \text{ Hz/G}^2$). The reasons behind such narrow resonances are different for the two atoms.

In the case of ^7Li , the triplet scattering length a_T , characterising collisions in the closed channel, is negative: $a_T = -28 a_0$ [38]. Thinking along the lines of bound states in a square-well potential (see Section 9.1.2), a negative scattering length is a good indication that the highest bound state is deeply bound. Indeed, the binding energy of the last triplet bound state is $|E_T| = h \cdot 12 \text{ GHz}$, whereas the corresponding binding

¹ In Eq. (11.13), the lower bound r_0 is the small non-zero value of r at which the accumulated-phase boundary condition is applied: see Chapter 12. The contribution to the overlap of the $0 < r < r_0$ region is neglected in the two-subspace approach; it is taken into account in the coupled-channel approach presented in Section 11.2.

energies for all other considered atoms are of the order of 100 MHz. The wavefunction $\Psi_0^{(2i)}(r)$ of this deeply-bound state has a very small spatial extent, hence its overlap with the open-channel wavefunction $\Psi_{\mathbf{k}=0}^{(2i-1)}$ is also small. In accordance with Eq. (11.10), this leads to a narrow resonance width.

In the case of ^{87}Rb , the narrowness of the resonance stems from the near-degeneracy of the singlet and triplet scattering lengths: $a_S = 90 a_0$ and $a_T = 99 a_0$ [39] differ by less than 10%. Therefore, the singlet and triplet Hamiltonians have very similar properties as far as ultracold collisions are concerned. In particular, the scattering-state wavefunction $\Psi_{\mathbf{k}=0}^{(2i-1)}$ and the bound-state wavefunction $\Psi_0^{(2i)}$ are almost eigenstates of the same Hamiltonian, and are therefore almost orthogonal. This leads to a small overlap for these two wavefunctions and, hence, to a narrow resonance width.

11.1.5. Limitations of the two-subspace approach

The two-subspace approach provides simple expressions for the resonance frequency (Eq. (11.9)) and width (Eq. (11.10)). It exhibits a simple scaling with B_{osc}^2 for both of these parameters.

However, this approach has one main limitation: it does not account for \hat{W} not going to zero for large values of r . The effect of such a ‘long-ranged’ coupling term can be neglected for small B_{osc} , but it affects the shape of the resonance for larger magnetic field amplitudes.

Furthermore, the two-subspace approach neglects a small contribution to the Franck-Condon factor of Eq. (11.10), coming from the small- r region (see footnote 1).

In the next section, we present a more elaborate approach which properly accounts for W not vanishing for large interatomic separations, and which does not require the small- r part of the wavefunctions to be neglected. This new approach confirms our two-channel results for small values of B_{osc} . It also allows for a straightforward calculation of the shift αB_{osc}^2 . Finally, it enables us to explore the behaviour of the resonance in ^{133}Cs involving the highest triplet bound state for magnetic fields larger than 5 mG.

11.2. The coupled-channel approach

In this section, we give up the simple scaling laws obtained with the two-subspace approach of Section 11.1.1, in favour of a more accurate and more general coupled-channel approach. *We assume, as in the previous section, that the magnetic field has no static component: $B_{\text{stat}} = 0$ and $V_Z = 0$.*

11.2.1. Hamiltonian for the coupled-channel approach

Within the framework of the two-subspace method of Section 11.1, we were only interested in internal states which were connected to each other, by the magnetic dipole coupling term W , via the absorption or emission of a single photon. However, the system we are considering actually contains two atoms, each of which can absorb a photon.

11. Characterising the resonances

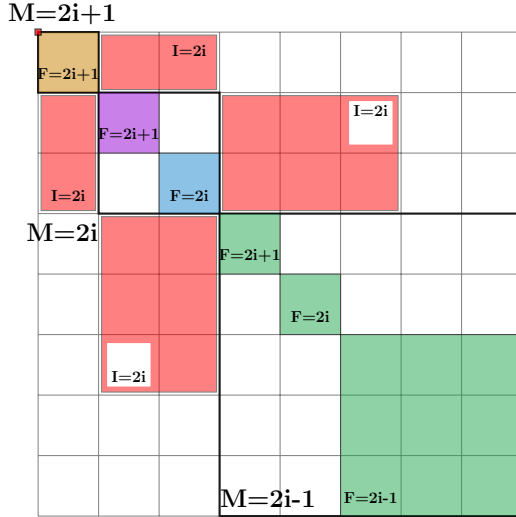


Figure 11.6. Block-structure of the two-atom Hamiltonian H , restricted to the subspace spanned by the $(M_F = 2i - 1)$ (green), $(M_F = 2i)$ (blue and purple), and $(M_F = 2i + 1)$ (orange) blocks, as used in the coupled-channel approach (8 coupled channels).

We assume, as we did in Section 11.1, that the asymptotic state of the atom pair relates² to both atoms having the quantum numbers $f = m_f = 2i - 1$, in the presence of N photons ($N \gg 1$). This asymptotic state belongs to the $(M_F = 2i - 1)$ subspace (dimension 5). In the case of a σ^+ -polarised magnetic field, this subspace is connected to the $(M_F = 2i)$ subspace through the absorption of a photon by one atom, and to the $(M_F = 2i + 1)$ subspace through the absorption of a photon by each of the two atoms. Therefore, we consider the restriction of the two-atom Hamiltonian H (Eq. (10.13)) to the eight-dimensional subspace spanned by the $(M_F = 2i - 1)$ block (dimension 5), the $(M_F = 2i)$ block (dimension 2), and the $(M_F = 2i + 1)$ block (dimension 1). This restricted Hamiltonian operates on an internal-state subspace whose dimension is $N_{\text{states}} = 5 + 2 + 1 = 8$. The block-structure, in the basis \mathbf{e}_M , of this eight-channel Hamiltonian is represented on Fig. 11.6.

11.2.2. Microwave-dressed two-atom states

We have already pointed out (see Section 11.1.2) that the magnetic dipole coupling W does not vanish for small r . The coupled-channel approach accounts for the ‘long-range’ nature of W through the use of microwave-dressed two-atom states, which we now present.

We first introduce the r -dependent potential part $V_{\text{tot}}(r)$ of the Hamiltonian H , which is the (matrix) operator defined by $H = \frac{p_r^2}{2m_r} + V_{\text{tot}}(r)$:

$$V_{\text{tot}}(r) = V_{\text{el}}(r) + V_{\text{hf}} + \hbar\omega a^\dagger a + W \quad . \quad (11.14)$$

The electronic interaction $V_{\text{el}}(r)$ decays as $-C_6/r^6$ for large r , therefore V_{tot} asymptotically reduces to an r -independent ($N_{\text{states}} \times N_{\text{states}}$) matrix V_∞ :

$$V_\infty = V_{\text{tot}}(r \rightarrow \infty) = V_{\text{hf}} + \hbar\omega a^\dagger a + W \quad . \quad (11.15)$$

²This assumption will be stated more accurately in Section 11.2.2.

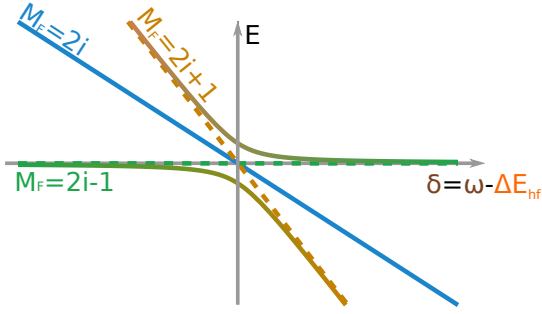


Figure 11.7. Dressed-state energies, for a given magnetic field amplitude $B_{\text{osc}} > 0$, as a function of the frequency detuning δ . The multiple-state structure of the $(M_F = 2i - 1)$ and $(M_F = 2i)$ subspaces is not represented.

The operator V_∞ is real and symmetric. Its eigenstates are the microwave-dressed two-atom states. We call

$$\mathbf{e}_D = \{|D_1\rangle, \dots, |D_{N_{\text{states}}}\rangle\} \quad (11.16)$$

the basis of eigenstates of V_∞ , ordered such that the corresponding eigenvalues satisfy $\varepsilon_1^D \leq \dots \leq \varepsilon_{N_{\text{states}}}^D$. Note that the dressed states $|D_n\rangle$ and the corresponding energies ε_n depend on the magnetic field amplitude B_{osc} as well as on the microwave frequency $\omega/2\pi$.

Had no approximation been performed on the Hamiltonian H , V_∞ could have been written as a sum of one-atom operators, and therefore the microwave-dressed states that we have just defined would have reduced to tensor products of two single-atom microwave-dressed states. However, for the calculations presented here, this factorisation is only approximate, as we have restricted H to the subspace spanned by the $N_{\text{states}} = 8$ internal states having $M_F = 2i - 1$, $2i$, or $2i + 1$ (see Section 11.2.1).

In the absence of the oscillating magnetic field ($B_{\text{osc}} = 0$), the basis states in \mathbf{e}_D coincide with those of the ‘atomic’ basis \mathbf{e}_A (although their ordering is not the same in \mathbf{e}_A and \mathbf{e}_D , as the states are not sorted by increasing energies in Table 10.2). For nonzero, albeit small³, values of B_{osc} , the basis states in \mathbf{e}_A and \mathbf{e}_D remain close to each other. For larger values of B_{osc} , the “dressed” states in \mathbf{e}_D are linear combinations of the “bare” states in \mathbf{e}_A , as illustrated on Fig. 11.7 [30].

The relevance of the dressed-state basis \mathbf{e}_D stems from the fact that, when projected into it, the N_{states} coupled components of a Schrödinger equation associated with H asymptotically decouple. Therefore, the eigenstates of H can be sought such that the asymptotic internal state of the atom pair is one of the microwave-dressed states in \mathbf{e}_D .

We wish to calculate the s -wave scattering length characterising the collision, in the presence of the oscillating magnetic field, between two atoms whose asymptotic two-atom internal state is $|D_1\rangle$ — we choose the lowest-energy dressed state so as to avoid inelastic processes causing losses into lower-energy channels [33]. This scattering length can be extracted from the asymptotic behaviour of the corresponding zero-energy scattering-state wavefunction. The sought N_{states} -component wavefunction $|\Psi\rangle$

³More precisely, the dressing of the atomic states by the microwave magnetic field is negligible if the Rabi frequency $\mu_B B_{\text{osc}}/\hbar$ is much smaller than the amplitude $|\delta|$ of the detuning of the microwave frequency with respect to the hyperfine transition frequency.

11. Characterising the resonances

satisfies both the stationary Schrödinger equation:

$$H|\Psi\rangle = \varepsilon_1^D|\Psi\rangle \quad (11.17)$$

and the large- r boundary conditions [37]:

$$\langle D_1 | \Psi(r) \rangle = \frac{r-a}{r} \quad (\text{entrance channel}) \quad (11.18a)$$

$$\langle D_p | \Psi(r) \rangle = A_p \frac{\exp(-\kappa_p r)}{r} \quad \text{for } 2 \leq p \leq N_{\text{states}} \quad (\text{closed channels}), \quad (11.18b)$$

where $\hbar\kappa_p = (2m_r(\varepsilon_N^D - \varepsilon_1^D))^{1/2}$ for all closed channels $p > 1$. In other words, for large interatomic separations r , the radial wavefunction reduces to the usual linear form $(r-a)$ in the entrance channel (where, asymptotically, no kinetic energy is present) and decays exponentially in all closed channels. In Eqs. (11.18), the real numbers A_p and the real scattering length a are initially unknown: their values are extracted from the asymptotic behaviour of the wavefunction $\Psi(r)$ after its numerical calculation.

In order to fully define the wavefunction $|\Psi\rangle$, an additional condition must be specified, which enforces that $\Psi(r)$ be regular at $r = 0$ [25]:

$$\lim_{r \rightarrow 0} (r \Psi(r)) = 0 \quad . \quad (11.19)$$

Technical difficulties, arising from the electronic potentials V_T and V_T being less well-known for small values of r , lead us to replace the condition (11.19) by the “accumulated-phase” boundary condition [31], applied at a non-zero minimal radius r_0 (see Chapter 12), but this more elaborate condition has a similar interpretation.

The Schrödinger equation (11.17), along with the boundary conditions for large r (Eqs. (11.18)) and small r (Eq. (11.19)), defines a two-point boundary-value problem which we solve numerically using the methods described in Chapter 12.

11.2.3. Results for small oscillating magnetic fields

For a given atomic species and a given value of the magnetic field amplitude B_{osc} , we solve the Schrödinger equation of Section 11.2.2 for various values of the microwave frequency ω close to the zero-field resonance frequency ω_{res}^0 . Figure 11.8 shows plots of the scattering length $a(\omega)$, calculated using this method, with ^{23}Na and the two magnetic field amplitudes $B_{\text{osc}} = 0.25 \text{ G}$ and $B_{\text{osc}} = 1 \text{ G}$. These plots confirm that the scattering length diverges hyperbolically near the resonance. They also confirm that the effect of increasing the magnetic field amplitude is two-fold, as predicted by the two-subspace approach in the small- B_{osc} regime: (i) the resonance width increases, and (ii) the resonance frequency is shifted away from ω_{res}^0 .

For each considered atomic species, we have checked that, in the small- B_{osc} regime, the resonance width $\Delta\omega$ and the frequency shift $(\omega_{\text{res}} - \omega_{\text{res}}^0)$ are proportional to B_{osc}^2 (see Figs. 11.9), as predicted by the two-subspace approach (Eqs. (11.9) and (11.10)).

The numerical results for this approach are summarised in Table 11.2. The results for the resonance widths are in very good agreement with the two-subspace results of Table 11.1. Furthermore, the results for the resonance widths and shifts are of the same order as those obtained with the two-square-well model of Chapter 9.

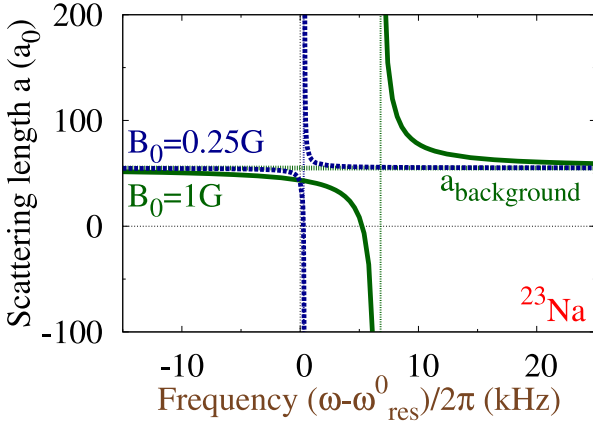


Figure 11.8. Scattering length $a(\omega)$ for Sodium atoms, near the resonance occurring at $\omega_{\text{res}}^0/2\pi = 1600$ MHz, for two values of the magnetic field amplitude: $B_{\text{osc}} = 0.25$ G (blue) and $B_{\text{osc}} = 1$ G (green).

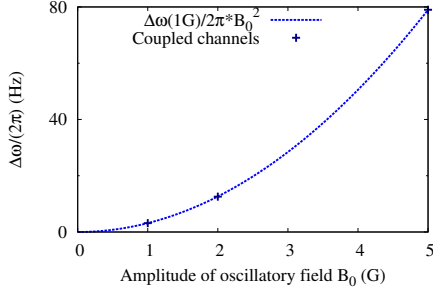
	⁷ Li	²³ Na	⁴¹ K	⁸⁷ Rb	¹³³ Cs (1)	¹³³ Cs (2)
Binding energy of resonant triplet state and resonance frequency						
$ E_T /h$ (MHz)	12000	200	140	25	$5 \cdot 10^{-3}$	110
$\omega_{\text{res}}^0/2\pi$ (GHz)	11	16	0.12	6.8	9.2	9.1
Full-fledged 8-channel numerics						
α (kHz/G ²)	0.33	6.8	21	120	$-830 \cdot 10^3$	30
$\Delta\omega_{8\text{ch}}/2\pi$ (Hz/G ²)	3.2	1400	350	60	$-5.8 \cdot 10^9$	-4800
Comparison with the two-square-well model						
$\beta = \frac{\Delta\omega_{8\text{ch}}}{\Delta\omega_{2\text{SW}}}$	0.97	1.1	1.6	0.60	1.7	n/a

Table 11.2. Characteristics of the microwave-induced Feshbach resonances in ⁷Li, ²³Na, ⁴¹K, ⁸⁷Rb, and ¹³³Cs involving the triplet bound states with energies E_T , calculated using the coupled-channel method. The resonance width $\Delta\omega$ is proportional to B_0^2 , and it is given for $B_0 = 1$ G.

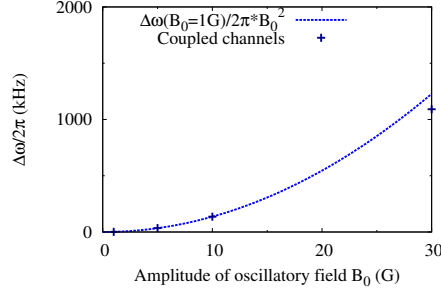
The column labelled “¹³³Cs (1)” relates to the resonance in Cesium involving the highest triplet bound state, whereas the column labelled “¹³³Cs (2)” relates to the resonance involving the second-highest triplet bound state.

The coupled-channel results of this Section are compared to the results of the two-square-well model presented in Table 9.2. The ratio $\beta = \frac{\Delta\omega_{8\text{ch}}}{\Delta\omega_{2\text{SW}}}$ of the resonance widths obtained with the two approaches depends on the considered resonance but always remains of order 1.

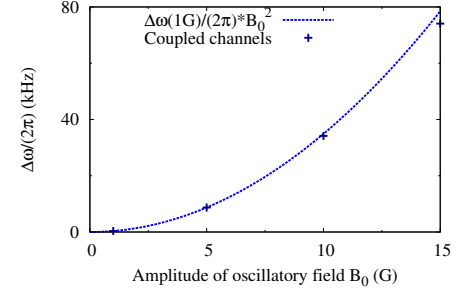
11. Characterising the resonances



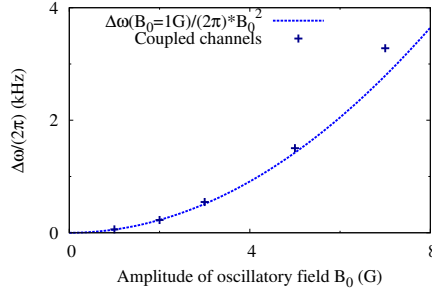
(a) Lithium 7, $\Delta\omega/2\pi = 3.2 \text{ Hz/G}^2$



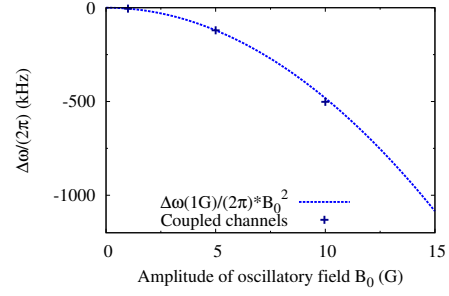
(b) Sodium 23, $\Delta\omega/2\pi = 1400 \text{ Hz/G}^2$



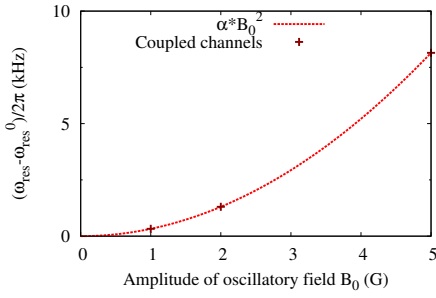
(c) Potassium 41, $\Delta\omega/2\pi = 350 \text{ Hz/G}^2$



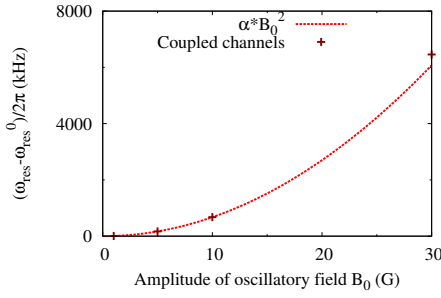
(d) Rubidium 87, $\Delta\omega/2\pi = 57 \text{ Hz/G}^2$



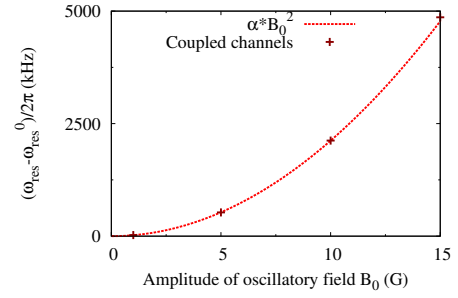
(e) Cesium 133, $\Delta\omega/2\pi = -4800 \text{ Hz/G}^2$



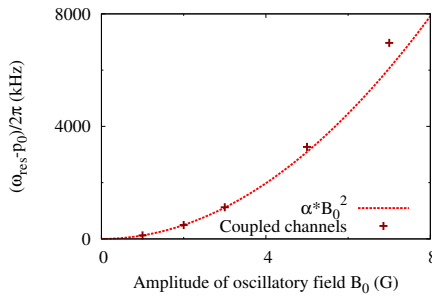
(f) Lithium 7, $\alpha = 0.33 \text{ kHz/G}^2$



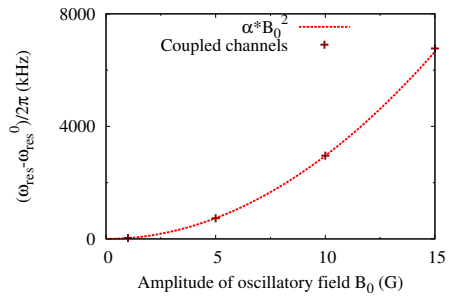
(g) Sodium 23, $\alpha = 6.8 \text{ kHz/G}^2$



(h) Potassium 41, $\alpha = 21 \text{ kHz/G}^2$



(i) Rubidium 87, $\alpha = 120 \text{ kHz/G}^2$



(j) Cesium 133, $\alpha = 30 \text{ kHz/G}^2$

Figure 11.9. Characterisation of the mw-induced resonances in ${}^7\text{Li}$, ${}^{23}\text{Na}$, ${}^{41}\text{K}$, ${}^{87}\text{Rb}$, and ${}^{133}\text{Cs}(2)$ using the coupled-channel method. Figures (a) to (e) show the resonance widths $\Delta\omega(B_{\text{osc}})/2\pi$ as a function of B_{osc} . Figures (f) to (j) show the shifts $(\omega_{\text{res}} - \omega_{\text{res}}^0)(B_{\text{osc}})/2\pi$ on the resonance frequencies. Both the widths and the shifts are proportional to B_{osc}^2 for small magnetic field amplitudes.

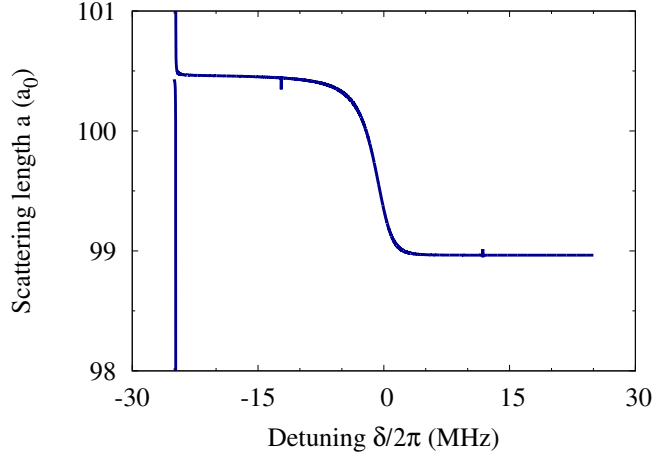


Figure 11.10. Scattering length $a(\omega)$, calculated using the full coupled-channel approach in the case of ^{87}Rb atoms with $B_{\text{osc}} = 1$ G. The first-order resonance (intersection *A* of Fig. 11.11) is visible at $\delta/2\pi = -25$ MHz. The two second-order resonances (intersections *B* and *D*) yield small features at $\delta/2\pi = -12.5$ MHz and $+13$ MHz.

A bird's-eye view of the dependence $a(\omega)$

The relevance of the coupled-channel approach is not limited to the vicinity of the zero-field resonance frequency ω_{res}^0 : it can be used to evaluate the scattering length a for any microwave frequency ω .

Figure 11.10 shows a plot of a as a function of the detuning δ (defined in Section 11.1.2), calculated for a collision involving two ^{87}Rb atoms. The plot explores a 50 MHz-wide range of detunings centred on zero. The main resonance is clearly visible near $\delta = -25$ MHz.

The plot reveals that the value of the background scattering length changes continuously from an asymptote which is $> 100 a_0$ for negative detunings to another which is $\approx 99 a_0$ for positive detunings. This is a dressed-state effect [30] which can be understood by examining the dressed-state energy-level diagram of Fig. 11.7, keeping in mind that, for large r , the colliding atoms are asymptotically the lowest-energy dressed state. For $\delta < 0$, this state is close to the $M_F = 2i - 1$ asymptote, and the background scattering length is $a_{F=M_F=2} = 100.5 a_0$, in agreement with the value observed on the $\delta < 0$ part of Fig. 11.10. On the other hand, for $\delta > 0$, the lowest-energy dressed state lies close to the $M_F = 2i + 1$ asymptote: the $(M_F = 2i + 1)$ subspace is purely electronic-triplet, therefore the background scattering length is $a_T = 99 a_0$, as confirmed by the $\delta > 0$ part of Fig. 11.10.

Two additional small features are visible on Fig. 11.10: one for $\delta \approx -12.5$ MHz and the other for $\delta \approx +12$ MHz. These are narrow second-order resonances, whose causes are explained on Fig. 11.11. The narrow resonance for $\delta < 0$ is due to the second-order coupling between the incident atoms in the $(M_F = 2i - 1)$ subspace, in the presence of N photons, and the triplet bound state in the $(M_F = 2i + 1)$ subspace, in the presence

11. Characterising the resonances

of $(N - 2)$ photons: it corresponds to the intersection B on Fig. 11.11. The narrow resonance for $\delta > 0$ is due to the second-order coupling between the incident atoms in the $(M_F = 2i + 1)$ subspace, in the presence of $(N - 2)$ photons, and the bound state in the $(M_F = 2i - 1)$ subspace, in the presence of N photons: it corresponds to the intersection D .

The intersection C does not yield a first-order resonance for positive detunings, because it corresponds to a coupling between the subspaces $(M_F = 2i)$ and $(M_F = 2i + 1)$. Both of these subspaces are purely electronic-triplet, therefore the spin-flip Franck-Condon factor involves an overlap between two wavefunctions which are eigenstates of the same Hamiltonian: these two wavefunctions are orthogonal, leading to a Franck-Condon factor which is zero and thus to a vanishing resonance width.

11.2.4. A giant resonance in Cesium

The coupled-channel approach allows us to explore the large- B_{osc} behaviour of the resonance in ^{133}Cs involving the highest triplet bound state ($|E_T| = h \cdot 5 \text{ kHz}$, columns labelled “Cs(1)” in Tables 11.1 and 11.2). In this particular case, Eqs. (11.9) and (11.10) are inapplicable for magnetic field amplitudes larger than $|E_T|/\mu_B = 4 \text{ mG}$.

Graphs of the scattering length $a(\delta)$, calculated using the coupled-channel method for various values of B_{osc} , are shown on Fig. 11.12. For small amplitudes ($B_{\text{osc}} = 0.1 \text{ mG}$ and 1 mG), the behaviour of $a(\delta)$ is similar to the one shown on Fig. 11.10 for ^{87}Rb : the main resonance at $\delta = h \cdot (-5) \text{ kHz}$, the ‘step’ corresponding to the change in background scattering lengths near $\delta = 0$, and the two narrow second-order resonances are all visible on the plot for $B_{\text{osc}} = 1 \text{ mG}$. For larger magnetic field amplitudes ($B_{\text{osc}} \geq 5 \text{ mG}$), the scattering length becomes very large for $\hbar\omega \approx \Delta E_{\text{hf}}$, but the resonance is no longer hyperbolic: the $\delta < 0$ asymptote corresponds to $a_{F=M_F=6} = -2500 a_0$, whereas for large $\delta > 0$ the scattering length goes to $a_T = +2500 a_0$. This ‘giant’ resonance has an approximate width of the order of 1 MHz for $B_{\text{osc}} = 1 \text{ G}$. Its non-standard shape results from the interplay between (i) the two-atom resonance and (ii) the (single-atom) dressed-state effect leading to different background scattering lengths for $\delta < 0$ and $\delta > 0$.

11.2.5. Applicability in more general situations

The coupled-channel approach has a wide applicability. We have used it to characterise the resonance involving the highest-energy triplet bound state in ^{133}Cs for more realistic experimental parameters, which lead to a greater number of coupled channels and require inelastic collisions to be accounted for: see Chapter 15. We have also used it to characterise *static-field* Feshbach resonances occurring in ^{133}Cs for very small magnetic field amplitudes: these static-field resonances are described in Chapter 14.

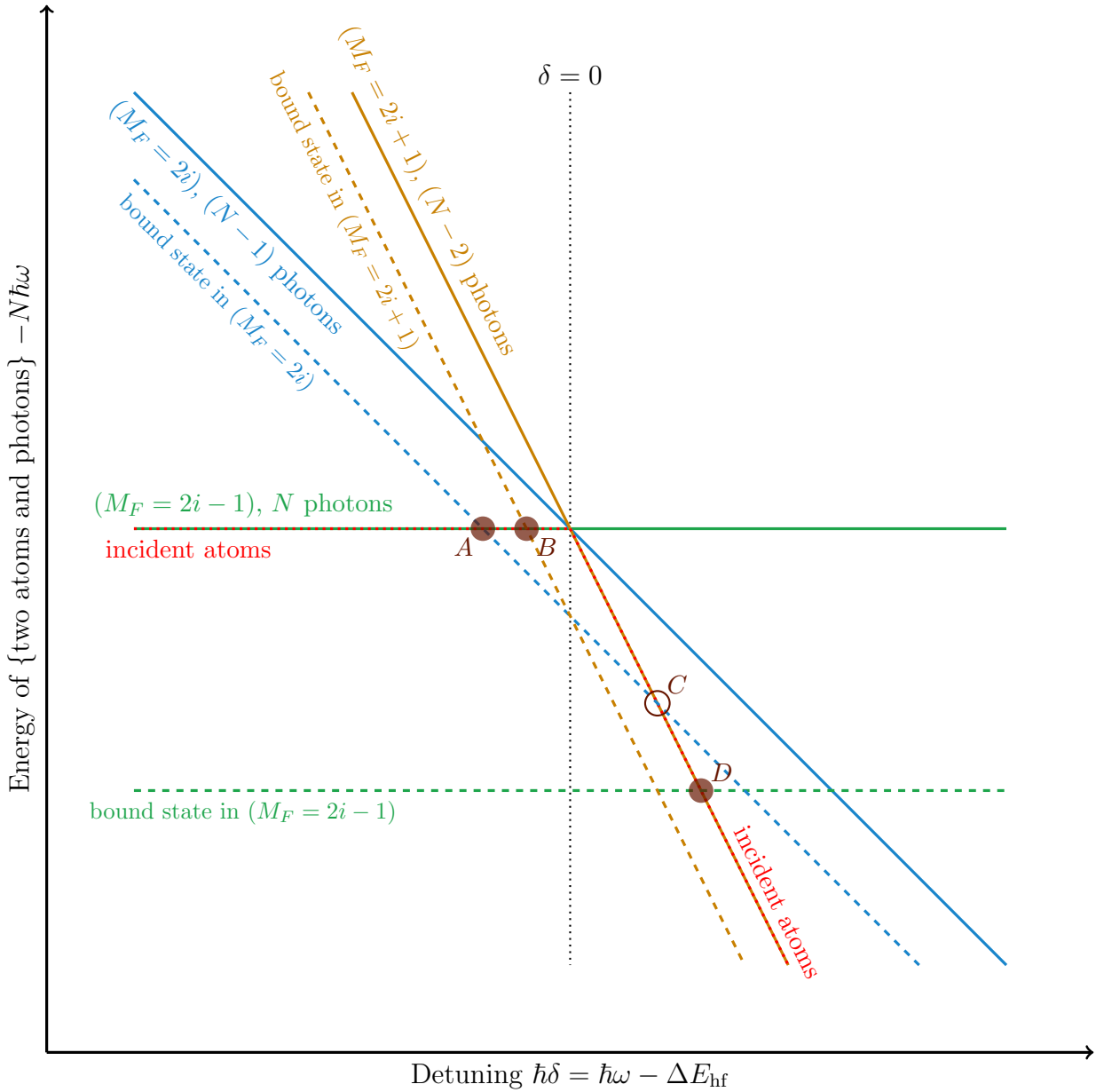


Figure 11.11. Asymptotic energy-level diagram for the atom pair in the presence of the electromagnetic field. The solid lines show the threshold energies of the $(M_F = 2i - 1)$ (N photons), $(M_F = 2i)$ ($N - 1$ photons), and $M_F = 2i + 1$ ($N - 2$ photons) subspaces. The dashed lines show the energies of the triplet bound state in each of these subspaces. The dotted red line shows the incident state of the two atoms (it is different for $\delta < 0$ and $\delta > 0$). The intersection A yields the main resonance. The intersections B ($\delta < 0$) and D ($\delta > 0$) yield narrow, second-order resonances. The resonance corresponding to intersection C is suppressed, because it corresponds to a connection between two purely electronic-triplet subspaces.

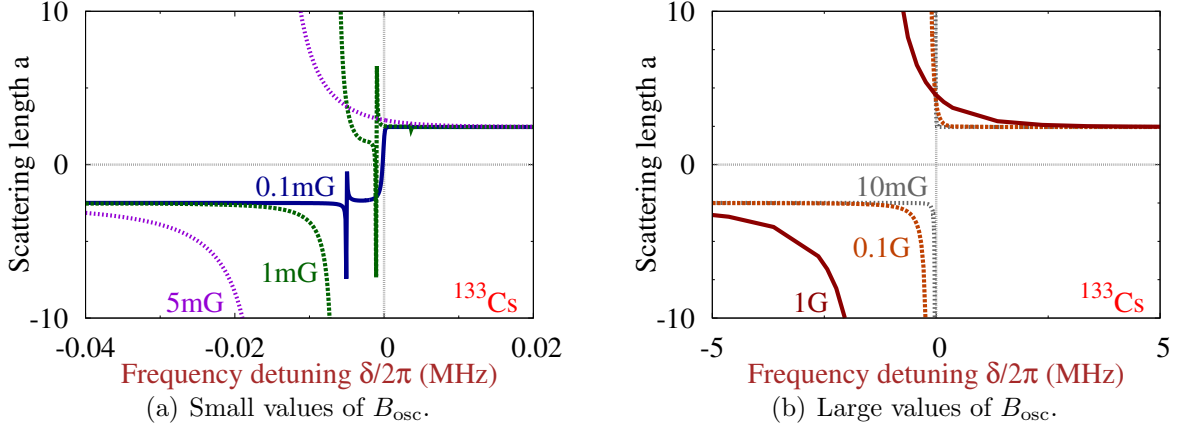


Figure 11.12. The “giant” resonance in Cesium, involving the highest triplet bound state ($|E_T| = h \cdot 5 \text{ kHz} = \mu_B \cdot 4 \text{ mG}$). The scattering length a is expressed in units of $1000 a_0$. For small magnetic field amplitudes ($B_{\text{osc}} \lesssim 5 \text{ mG}$), the resonance is hyperbolic, with $\Delta\omega \approx -5.8 \text{ GHz/G}^2$. For larger magnetic field amplitudes, the resonance is contaminated by single-atom dressed-state effects and is no longer hyperbolic. For $B_{\text{osc}} = 1 \text{ G}$, the non-hyperbolic resonance has an approximate width of the order of 1 MHz.

11.3. Experimental prospects

We wish to use the microwave-induced resonances characterised in this chapter as an experimental tool to manipulate the collisional properties of ultracold atoms. Ideally, they should enable experimentalists to tune a to any desired value and sign.

In order for this to be possible, the resonance width $\Delta\omega$ has to be larger than all experimental frequency broadenings. Two noteworthy sources of broadening are *(i)* stray static magnetic fields and *(ii)* the inhomogeneity of the microwave transition frequency due to atomic interactions [13].

The fluctuations in the ambient static magnetic field can be brought down to less than 1 mG using a standard magnetic field shield (advanced setups used in atomic clock experiments [40] lead to fluctuation amplitudes which are smaller than $1 \mu\text{G}$). Magnetic field fluctuations of 1 mG lead to a frequency broadening of the order of 1 kHz (within a factor of 2, depending on the Landé factors of the sublevels involved in the resonance).

The inhomogeneity of the mw transition is also expected to be of the order of 1 kHz.

Consequently, in order for a resonance to be experimentally relevant, its width has to be greater than 1 kHz. Recalling that the resonance width scales with B_{osc}^2 , the question amounts to which magnetic field amplitudes can be produced in the desired microwave frequency range. Using small resonant transmitting loop antennas in the near-field regime [41, 42], it is possible to reach amplitudes $B_{\text{osc}} \sim 10 \text{ G}$ using a reasonable incident electromagnetic power (below 10 W).

For the magnetic field amplitude $B_{\text{osc}} = 10 \text{ G}$, the widths of all identified resonances except the one involving ^7Li (see for instance Table 11.2) are much larger than 1 kHz. Our results thus yield optimistic prospects for an experiment with all considered species

except ${}^7\text{Li}$. The absence of a broad microwave-induced resonance for ${}^7\text{Li}$ is not a drastic issue, as a broad static-field Feshbach resonance is available for this atom [22].

Other experimental schemes are being considered for the observation of microwave-induced resonances. For example, the microwave magnetic field could also be ‘sprayed’ onto the atoms from the end of a waveguide connected to a powerful mw amplifier [43]. Alternatively, the experiment could be performed in a cavity which is reflective for mw fields but transparent in the optical domain [44]. The most promising scheme presently seems to be the observation of the large resonance in ${}^{133}\text{Cs}$ using an atomic fountain clock. The experimental parameters relevant for such an observation lead to a more involved theoretical description: a greater number of coupled channels is involved, and inelastic collisions must be taken into account. The results of this more elaborate calculation are presented in Chapter 15.

11.4. Comparison with RF-induced Feshbach resonances

To our present knowledge, the first published proposals for the manipulation of ultracold scattering properties using oscillating electromagnetic fields date back to 1996: (i) Moerdijk, Verhaar, and Nagtegaal reported a theoretical analysis of resonances induced by *radio-frequency magnetic fields* [20], and (ii) Fedichev *et al.* proposed using *optically-induced* Feshbach resonances [17].

In this section, we focus on the work reported in [20] by Moerdijk *et al.*. In the fourth section of that paper, the authors consider ${}^{23}\text{Na}$ atoms in a static magnetic trap. They assume that all of the atoms are in the ground hyperfine manifold ($f = i - 1/2 = 1$), and that the static magnetic field amplitude at the centre of the trap is zero. They study the effect of an additional radio-frequency magnetic field on atoms at the centre of the trap, and they focus on the RF frequency⁴ $\omega/2\pi = 7\text{ MHz}$. They perform coupled-channel calculations of the scattering matrix characterising a cold collision between two Sodium atoms which are asymptotically both in the state $|f = 1, m_f = -1\rangle$, for the fixed RF frequency $\omega/2\pi = 7\text{ MHz}$ and for Rabi frequencies $\omega_r/2\pi$ ranging from 0 to 700 MHz. They report a series of narrow scattering resonances (whose widths $\Delta\omega_r/2\pi$ are of the order of 100 Hz for temperatures of the order of $T = 3\ \mu\text{K}$) occurring for $\omega_r/2\pi \approx 60\text{ MHz}$, 200 MHz, . . . , and a broader resonance occurring for $\omega_r/2\pi = 255\text{ MHz}$ (whose width is $\Delta\omega_r/2\pi \approx 40\text{ kHz}$ at the same temperature). Their plot of the S -matrix element characterising collisions in the presence of the RF field is shown on Fig. 11.13.

To our knowledge, these resonances have not yet been observed experimentally. The broad resonance occurs for a Rabi frequency $\omega_r/2\pi$ which is 36 times larger than the RF frequency $\omega/2\pi = 7\text{ MHz}$. Its observation will require the use of RF amplitudes of the order of 500 G. In contrast, the microwave-induced resonance involving Sodium which we have characterised in Sections 11.1 and 11.2 have comparable widths for magnetic field amplitudes of the order of $B_{\text{osc}} = 5\text{ G}$, and it can be made even broader by increasing the oscillating magnetic field amplitude as its width is proportional to B_{osc}^2 (see Fig. 11.9(b)).

⁴The static magnetic field is zero, hence the detuning δ from the Zeeman splitting is equal to ω .

11. Characterising the resonances

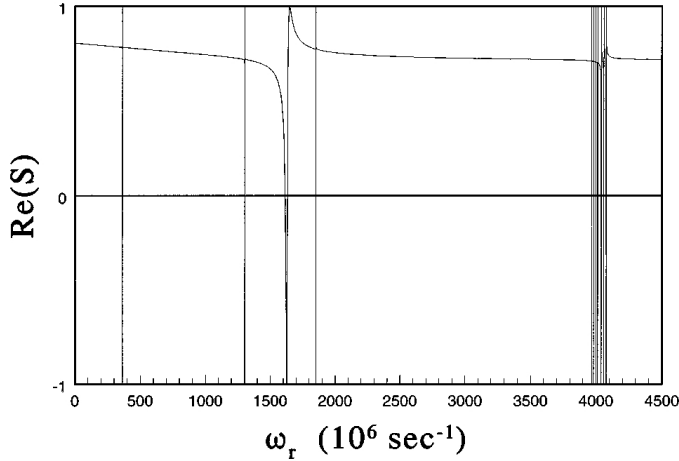


Figure 11.13. Real part of the S -matrix element characterising a collision between two Sodium atoms in the state $|f = 1, m_f = -1\rangle$ in the presence of a radiofrequency magnetic field, as a function of the Rabi frequency ω_r . No static field is present ($B_{\text{stat}} = 0$), the RF frequency is $\omega/2\pi = \delta/2\pi = 7$ MHz and the collision energy is $E/k_B = 100 \mu\text{K}$. (Reproduced from [20].)

This large discrepancy between the magnetic field amplitudes required to achieve the same resonance width is due to a difference in the nature of the coupling which causes the resonance. In the case of the resonances we have studied in Sections 11.1 and 11.2, the incident channel is coupled to the resonant two-atom bound state by the *magnetic dipole coupling* W . In contrast, we will show in Section 11.4.2 that the resonances reported in [20] cannot be due to the magnetic dipole coupling alone: this term affects the energies of the resonant states but it cannot cause a coupling between them. The coupling causing these latter resonances is provided by the weak *spin-dependent interaction* $V_{\text{ss}}(r)$ (see Section 10.2.2). They can therefore be seen as the oscillating-field equivalent of ‘narrow’ Feshbach resonances [1] (whereas the microwave-induced resonances we describe are analogous to ‘broad’ resonances as they do not involve V_{ss}).

11.4.1. Hamiltonian in the lower hyperfine manifold

In this section and in Section 11.4.2, we neglect the *spin-dependent interaction* V_{ss} , just like in Sections 11.1 and 11.2. The two-atom Hamiltonian thus conserves the spatial angular momentum ℓ (see Section 10.2). For the sake of clarity, we focus on s -wave collisions, but the argument holds for any (even) value of ℓ . The effect of the anisotropic coupling term V_{ss} will be considered in Section 11.4.3.

Following [20], we restrict our analysis to the lower hyperfine manifold. The nuclear spin of Sodium atoms is $i = 3/2$, therefore there are three single-atom states in this manifold: these are the $|f = 1, m_f\rangle$, with $m_f = +1, 0$, and -1 . We are considering s -wave collisions (*i.e.* the angular momentum is $\ell = 0$), for which the two-atom internal states should be symmetric, therefore the quantum number F , giving the total two-atom spin, may be either 0 or 2 (but not 1: see Section 10.3.2). Hence, the lower hyperfine manifold ($f_1 = 1, f_2 = 1$) comprises six two-atom states:

- 5 states having $F = 2$: the $|f_1 = 1, f_2 = 1, F = 2, M_F\rangle$, with $-2 \leq M_F \leq 2$;

- 1 state having $F = 0$: $|f_1 = 1, f_2 = 1, F = 0, M_F = 0\rangle$.

In order to determine the state of the system “two atoms in the presence of the radio-frequency magnetic field” completely, the quantum number N , giving the number of photons, has to be specified as well. For the sake of simplicity, we assume that the radio-frequency magnetic field is σ^- -polarised⁵⁶. In this context, the magnetic dipole coupling term is $W = W^{\sigma^-}$ and reads:

$$W^{\sigma^-} = w_1 (S^+ a^\dagger + S^- a) \quad , \quad (11.20)$$

where w_1 is defined by Eq. (10.7). The conservation of angular momentum implies that the quantum number $N_0 = -M_F + N$ is conserved (see Section 10.3.5). Therefore, we choose a value⁷ for N_0 and we restrict the Hamiltonian H of Eq. (10.13) to the six-dimensional stable subspace spanned by the states

$|f_1 = 1, f_2 = 1, F = 2, M_F, N = N_0 + M_F\rangle$ ($-2 \leq M_F \leq 2$) and
 $|f_1 = 1, f_2 = 1, F = 0, M_F = 0, N = N_0\rangle$.

Just like in Section 10.3.5, we write $H = \frac{p_r^2}{2m_r} + V_{\text{tot}}(r)$, where the total potential matrix $V_{\text{tot}}(r)$ reads:

$$V_{\text{tot}}(r) = V_{\text{el}}(r) + V_{\text{hf}} + V_Z + \hbar\omega a^\dagger a + W \quad . \quad (10.23)$$

We are interested in the block structure of the matrix representation of $V_{\text{tot}}(r)$ restricted to the stable subspace defined above.

- The electronic-interaction term V_{el} conserves both F and M_F , and it thus only contributes diagonal matrix elements.
- All of the six relevant states bear the hyperfine quantum numbers $f_1 = f_2 = 1$, therefore the hyperfine term V_{hf} only contributes a constant to the Hamiltonian ($V_{\text{hf}} = -\frac{5}{2} a_{\text{hf}} \mathbb{1}$).
- The photon-energy term $\hbar\omega a^\dagger a$ contributes the usual diagonal matrix elements.
- The Zeeman term V_Z obeys the vector selection rule on F (see Section 10.3.5), therefore it does not couple the ($F = 2$) subspace to the $F = 0$ state. Furthermore, it conserves the total spin projection M_F , therefore it only contributes diagonal matrix elements.
- The magnetic dipole coupling term W also obeys vector selection rules, hence, it does not couple the ($F = 2$) and ($F = 0$) subspaces. It contributes off-diagonal coupling terms within the ($F = 2$) subspace (represented in blue on Fig. 11.14).

⁵This assumption is not a requirement: any polarisation which is perpendicular to the quantisation axis can be seen as a linear combination of σ^+ and σ^- polarisations. In the context of the evaporative cooling of Sodium atoms mentioned in [20], the resonant term is the second one, because the low-field-seeking single-atom state $|f = 1, m_f = -1\rangle$ has a higher energy than the untrapped states $|f = 1, m_f = 0\rangle$ and $|f = 1, m_f = +1\rangle$ [45].

⁶This polarisation is defined by the vector $\mathbf{e}_{\sigma^-} = (\mathbf{e}_x - i\mathbf{e}_y)/\sqrt{2}$: see also Fig. 15.1.

⁷We choose $N_0 \gg 1$, its exact value being arbitrary: see Section 10.3.5.

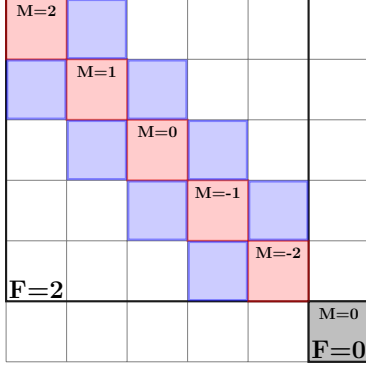


Figure 11.14. Block-matrix structure of the restriction of the radial two-atom Hamiltonian (Eq. 10.13) to the $(f_1 = 1, f_2 = 1)$ hyperfine manifold for two spin-3/2 alkali atoms such as ^{23}Na . More specifically, we consider the restriction of H to the stable six-dimensional subspace spanned by the states $|f_1 = 1, f_2 = 1, F = 2, M_F, N = N_0 - M_F\rangle$ and $|f_1 = 1, f_2 = 1, F = 0, M_F = 0, N = N_0\rangle$. The r -dependent part of the Hamiltonian is diagonal, and it is the same for all $(F = 2)$ states (red diagonal matrix elements). The off-diagonal blue blocks in the $(F = 2)$ subspace are due to the magnetic dipole coupling term W .

Finally, we point out an additional property of the (diagonal) matrix elements of V_{el} within the $(F = 2)$ subspace. These matrix elements are expressed in terms of the triplet and singlet electronic potentials as:

$$\begin{aligned}
 V_{\text{el}}^{F=2, M_F}(r) &= \langle f_1 = 1, f_2 = 1, F = 2, M_F | V_{\text{el}}(r) | f_1 = 1, f_2 = 1, F = 2, M_F \rangle = \\
 &V_T(r) \left[|\langle f_1 = 1, f_2 = 1, F = 2, M_F | S = 1, I = 3, F = 2, M_F \rangle|^2 \right. \\
 &\quad \left. + |\langle f_1 = 1, f_2 = 1, F = 2, M_F | S = 1, I = 1, F = 2, M_F \rangle|^2 \right] \quad (11.21) \\
 &+ V_S(r) |\langle f_1 = 1, f_2 = 1, F = 2, M_F | S = 0, I = 2, F = 2, M_F \rangle|^2
 \end{aligned}$$

The values of the scalar products $\langle f_1 = 1, f_2 = 1, F = 2, M_F | S, I, F = 2, M_F \rangle$ appearing on the right-hand side of Eq. (11.21) are independent of the total spin projection M_F [37]. Therefore, the (diagonal) matrix element $V_{\text{el}}^{F=2}(r)$ is the same for all of the $F = 2$ states⁸ $|f = 1, f = 1, F = 2, M_F\rangle$.

The block structure of the restriction of the Hamiltonian to the lower hyperfine manifold $(f_1 = 1, f_2 = 1)$ is illustrated on Fig. 11.14. The important properties of this block structure can be summarised as follows: (i) The $(F = 2)$ and $(F = 0)$ subspaces are uncoupled, and (ii) within the $F = 2$ subspace, the electronic interaction $V_{\text{el}}(r)$ is purely diagonal and does not depend on M_F ($V_{\text{el}}(r) = V_{\text{el}}^{F=2}(r) \mathbb{1}_{F=2}$).

11.4.2. Absence of resonances due to the magnetic dipole coupling

The goal of this section is to justify that the magnetic dipole coupling W alone cannot cause a resonance within the lower hyperfine manifold. As in Section 11.4.1, *the effect of the spin-dependent coupling term V_{ss} is neglected.*

Let us assume that a resonance caused by W occurs between the open channel $|\text{op}\rangle$ and the closed channel $|\text{cl}\rangle$. The two-subspace approach predicts that the resonance width $\Delta\omega$ is proportional to the strength of the coupling between the two channels (see

⁸This result is a consequence of the rotational invariance of the electronic interaction V_{el} . In particular, it implies that the scattering length $a(F = 2)$ does not depend on the total spin projection M_F [46].

Eq. (11.10) and [1]):

$$\Delta\omega \propto |\langle \Psi_{\text{cl}} | W | \Psi_{\text{op}} \rangle|^2 \quad , \quad (11.22)$$

where $|\Psi_{\text{op}}\rangle$ and $|\Psi_{\text{cl}}\rangle$ are the wavefunctions in the open and closed channels, respectively. The decoupling between the ($F = 0$) and ($F = 2$) subspaces, described in Section 11.4.1, makes it possible to choose open- and closed-channel wavefunctions which have a well-defined quantum number F .

If the wavefunctions $|\Psi_{\text{op}}\rangle$ and $|\Psi_{\text{cl}}\rangle$ correspond to *different values of F* (i.e. one of them has $F = 2$ and the other has $F = 0$), the matrix element on the right-hand side of Eq. (11.22) is zero because W does not connect the ($F = 2$) and ($F = 0$) subspaces.

We now assume that $|\Psi_{\text{op}}\rangle$ and $|\Psi_{\text{cl}}\rangle$ *bear the same quantum number F* . For the sake of definiteness, we take $F = 2$ (but the argument also holds for $F = 0$). The operator $V_{\text{el}}^{F=2}(r)$ not depending on the spin projection M_F makes it possible to choose open- and closed-channel wavefunctions of the form:

$$|\Psi_{\text{op}}(r)\rangle = \varphi_{\text{op}}^{F=2}(r) |\chi_{\text{op}}^{F=2}\rangle \quad \text{and} \quad |\Psi_{\text{cl}}(r)\rangle = \varphi_{\text{cl}}^{F=2}(r) |\chi_{\text{cl}}^{F=2}\rangle \quad , \quad (11.23)$$

where $|\chi_{\text{op}}^{F=2}\rangle$ and $|\chi_{\text{cl}}^{F=2}\rangle$ are two (RF-dressed) two-atom internal states belonging to the ($F = 2$) subspace, and the (single-channel) spatial wavefunctions $\varphi_{\text{op}}^{F=2}(r)$ and $\varphi_{\text{cl}}^{F=2}(r)$ are both eigenfunctions of the spatial Hamiltonian

$$H_{\text{spatial}}^{F=2} = p_r^2/2m_r + V_{\text{el}}^{F=2}(r) \quad . \quad (11.24)$$

The open-channel wavefunction is a scattering state of $H_{\text{spatial}}^{F=2}$, and the closed-channel wavefunction is a bound state of the same Hamiltonian. Two different eigenfunctions of the same (Hermitian) Hamiltonian are always orthogonal, hence $\langle \varphi_{\text{op}}^{F=2} | \varphi_{\text{cl}}^{F=2} \rangle = 0$. Thus, the resonance width is zero:

$$\Delta\omega \propto |\langle \chi_{\text{op}}^{F=2} | W | \chi_{\text{cl}}^{F=2} \rangle|^2 |\langle \varphi_{\text{op}}^{F=2} | \varphi_{\text{cl}}^{F=2} \rangle|^2 = 0 \quad , \quad (11.25)$$

which finishes the proof that the magnetic dipole coupling term W alone cannot cause any resonance within the ($f = 1, f = 1$) hyperfine manifold.

11.4.3. Resonances due to the spin-dependent interaction V_{ss}

We have justified in Section 11.4.2 that the magnetic dipole coupling W alone cannot cause resonances within the lower hyperfine manifold ($f_1 = 1, f_2 = 1$). We now justify that the resonances reported by Moerdijk *et al.* [20] are due to the spin-dependent interaction $V_{\text{ss}}(r)$ (see Section 10.2), and we identify the resonant two-atom states yielding the resonances visible on Fig. 11.13.

The complete two-atom Hamiltonian

The complete two-atom Hamiltonian, including $V_{\text{ss}}(r)$, reads:

$$H_{\text{complete}} = \frac{p_r^2}{2\mu} + \frac{\ell^2}{2\mu r^2} + V_{\text{tot}}(r) + V_{\text{ss}}(r) = H + V_{\text{ss}}(r) \quad , \quad (11.26)$$

11. Characterising the resonances

where ℓ is the angular momentum of the reduced particle, the operator $V_{\text{tot}}(r)$ is defined by Eq. (10.23), and H is the Hamiltonian introduced in Section 11.4.1. The spin-dependent interaction $V_{\text{ss}}(r)$ can be expressed as [47]:

$$V_{\text{ss}}(r) = f(r) [\mathbf{s}_1 \cdot \mathbf{s}_2 - 3(\mathbf{s}_1 \cdot \hat{\mathbf{r}})(\mathbf{s}_2 \cdot \hat{\mathbf{r}})] \quad . \quad (11.27)$$

It is anisotropic and, hence, couples partial waves with different angular momenta ℓ [7]; therefore, the centrifugal term $\ell^2/2\mu r^2$ is included in Eq. (11.26) and in H .

We apply the two-channel model to the Hamiltonian H_{complete} (see also Section 11.1 and [1]), considering H as the bare Hamiltonian and V_{ss} as the coupling operator.

Choice of the open- and closed-channel wavefunctions

The symmetry considerations presented in Sections 11.4.1 and 11.4.2 fully apply to the bare Hamiltonian H . Thus, the bare open- and closed-channel wavefunctions can be chosen within specific $(f_1 = f_2 = 1, F, N_0, \ell)$ subspaces, where the quantum number F gives the total (electronic and nuclear) two-atom spin, the integer N_0 specifies the RF-dressed manifold, and the partial-wave index ℓ determines the angular momentum of the reduced particle.

The incident state used in [20] describes a collision of two atoms which, for large separations, are both in an RF-dressed state relating to $|f = 1, m_f = -1\rangle$, with the incident energy $E_{\text{inc}} = k_B \cdot 100 \mu\text{K}$. This two-atom wavefunction has components with angular momenta $\ell = 0, 2, \dots$. We choose the open channel to be the component having the angular momentum ℓ^{op} , which is of the form:

$$|\Psi_{\text{op}}^{(F=2, N_0^{\text{op}}, \ell^{\text{op}})}(r)\rangle = \varphi_{\text{op}}^{(F=2, \ell^{\text{op}})}(r) |\chi_{\text{op}}^{(F=2, N_0^{\text{op}})}\rangle \quad , \quad (11.28)$$

where $|\chi_{\text{op}}^{(F=2, N_0^{\text{op}})}\rangle$ is an RF-dressed two-atom state belonging to the $(f_1 = f_2 = 1, F = 2, N_0^{\text{op}})$ subspace and the (single-channel) spatial wavefunction $\varphi_{\text{op}}^{(F=2, \ell^{\text{op}})}(r)$ is the scattering state of $H_{\text{spatial}}^{F=2, \ell^{\text{op}}}$ with the energy E_{inc} , the spatial Hamiltonian $H_{\text{spatial}}^{(F=2, \ell)}$ being defined by:

$$H_{\text{spatial}}^{(F=2, \ell)} = \frac{p_r^2}{2m_r} + \frac{\ell(\ell + 1)}{2m_r r^2} + V_{\text{el}}^{(F=2)}(r) \quad . \quad (11.29)$$

The closed-channel wavefunction may belong to any subspace $(f_1 = f_2 = 1, F, N_0^{\text{cl}}, \ell^{\text{cl}})$ which is coupled to the open-channel state by V_{ss} . In particular, the quantum number F must be 2 or 0, and the partial wave ℓ^{cl} must be even. According to [48], the two highest bound states of two Sodium atoms satisfying these conditions are $F = 2$ states:

- The state $|\nu = 15, \ell = 0, SI = (13), F = 2\rangle$ has the binding energy $h \cdot 90 \text{ MHz}$;
- The state $|\nu = 14, \ell = 4, SI = (13), F = 2\rangle$ has the binding energy $h \cdot 900 \text{ MHz}$.

Our aim is to show that the RF-induced resonances visible on Fig. 11.13 are due to these two weakly-bound states. For that purpose, we consider a closed-channel wavefunction of the form:

$$|\Psi_{\text{cl}}^{(F=2, N_0^{\text{cl}}, \ell^{\text{cl}})}(r)\rangle = \varphi_{\text{cl}}^{(F=2, \ell^{\text{cl}})}(r) |\chi_{\text{cl}}^{(F=2, N_0^{\text{cl}})}\rangle \quad , \quad (11.30)$$

where $|\chi_{\text{cl}}^{(F=2, N_0^{\text{cl}})}\rangle$ is an RF-dressed two-atom state in the ($f_1 = f_2 = 1, F = 2, N_0^{\text{cl}}, \ell^{\text{cl}}$) subspace (where $\ell^{\text{cl}} = 0$ or 2), and the (single-channel) spatial wavefunction $\varphi_{\text{cl}}^{(F=2, \ell^{\text{cl}})}(r)$ is a bound state of $H_{\text{spatial}}^{(F=2, \ell^{\text{cl}})}$.

RF-dressed energies of the open- and closed-channel wavefunctions

We now evaluate the ‘bare’⁹ energies of the open-channel state $|\Psi_{\text{op}}^{(F=2, N_0^{\text{op}}, \ell^{\text{op}})}\rangle$ and the closed-channel state $|\Psi_{\text{cl}}^{(F=2, N_0^{\text{cl}}, \ell^{\text{cl}})}\rangle$ as a function of the Rabi frequency ω_r .

Within a given ($f_1 = f_2 = 1, F = 2, N_0, \ell$) subspace, the ‘bare’ Hamiltonian H reads:

$$H = H_{\text{spatial}}^{(F=2, \ell)} + V_{\infty}^{(F=2, N_0)} \quad , \quad (11.31)$$

where $H_{\text{spatial}}^{(F=2, \ell)}$ is defined by Eq. (11.29), and $V_{\infty}^{(F=2, N_0)}$ is given by:

$$V_{\infty}^{(F=2, N_0)} = \left(-\frac{5}{2}a_{\text{hf}} + N_0 \hbar\omega\right) + \hbar\omega F_z + \frac{\mu_B B_{\text{osc}}}{\sqrt{N_0}}(S^+ a^\dagger + S^- a) \quad . \quad (11.32)$$

The operator $H_{\text{spatial}}^{(F=2, \ell)}$ only acts on the spatial part of the wavefunction, whereas the operator $V_{\infty}^{(F=2, N_0)}$ only acts on the internal-state part. Consequently, the energy of each of the two bare states (Eqs. (11.28) and (11.30)) is a sum of two terms, corresponding to the contributions of the spatial and internal-state parts of the wavefunction.

The contribution of the spatial part is an eigenvalue of $H_{\text{spatial}}^{(F=2, \ell)}$ and, hence, does not depend on the magnetic field amplitude.

The contribution of the internal-state part is an eigenvalue of $V_{\infty}^{(F=2, N_0)}$, which does depend on the magnetic field amplitude. We wish to express this dependence in terms of the Rabi frequency ω_r , defined by $\hbar\omega_r = -\sqrt{2}\mu_B B_{\text{osc}}/4$ [20]. The Wigner-Eckart theorem [25] shows that the restriction of the vector operator \mathbf{S} to the subspace ($f_1 = f_2 = 1, F = 2$) satisfies $\mathbf{S} = -\mathbf{F}/4$. The operator $V_{\infty}^{(F=2, N_0)}$ thus reduces to:

$$V_{\infty}^{F=2, N_0} = \left(-\frac{5}{2}a_{\text{hf}} + N_0 \hbar\omega\right) + \hbar\omega F_z + \frac{\hbar\omega_r}{\sqrt{2N_0}}(F^+ a^\dagger + S^- a) \quad . \quad (11.33)$$

The diagonalisation of this operator within the five-dimensional ($f_1 = f_2 = 1, F = 2, N_0, \ell$) subspace yields five RF-dressed states, whose energies are represented on Fig. 11.15 as a function of ω_r , for the fixed RF frequency $\omega/2\pi = 7$ MHz.

We first consider the open-channel wavefunction $|\Psi_{\text{op}}^{(F=2, N_0^{\text{op}}, \ell^{\text{op}})}\rangle$. Neglecting the small contribution¹⁰ due to the spatial component, its ‘bare’ energy is:

$$E_{\text{op}}(\omega_r) = E_{\text{op}}^{\text{int}}(\omega_r) \quad , \quad (11.34)$$

⁹These two states are eigenfunctions of the ‘bare’ Hamiltonian H , and their ‘bare’ energies are the corresponding eigenvalues of H .

¹⁰This contribution is of the order of $+h \cdot 2$ MHz for the parameters used in [20].

11. Characterising the resonances

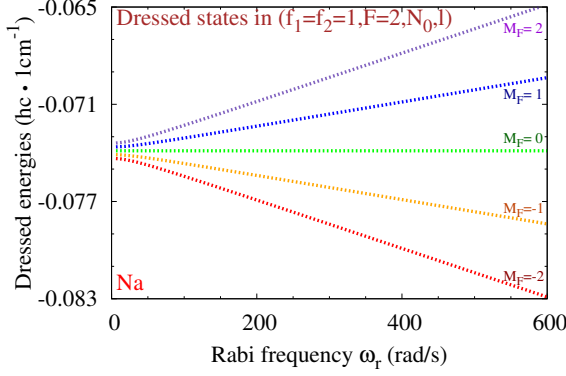


Figure 11.15. Energies of the five RF-dressed two-atom states in the $(f_1 = f_2 = 1, F = 2, N_0, \ell)$ subspace, calculated for the RF frequency $\omega/2\pi = 7$ MHz.

where the internal-state energy $E_{\text{op}}^{\text{int}}(\omega_r)$ is the eigenvalue of $V_{\infty}^{(F=2, N_0^{\text{op}})}$ corresponding to the eigenstate $|\chi_{\text{op}}^{(F=2, N_0^{\text{op}})}\rangle$.

We now turn to the bare energy of the closed-channel wavefunction $|\Psi_{\text{cl}}^{(F=2, N_0^{\text{cl}}, \ell^{\text{cl}})}(r)\rangle$:

$$E_{\text{cl}}(\omega_r) = -|E_b| + E_{\text{cl}}^{\text{int}}(\omega_r) \quad , \quad (11.35)$$

where $|E_b|$ is the binding energy of the bound state $\varphi_{\text{cl}}^{(F=2, \ell^{\text{cl}})}(r)$ of the spatial Hamiltonian $H_{\text{spatial}}^{(F=2, \ell^{\text{cl}})}$, and $E_{\text{cl}}^{\text{int}}(\omega_r)$ is the eigenvalue of $V_{\infty}^{(F=2, N_0^{\text{cl}})}$ corresponding to the eigenstate $|\chi_{\text{cl}}^{(F=2, N_0^{\text{cl}})}\rangle$. In Eq. (11.35), the separation between the spatial-state and internal-state contributions to the energy (E_b and $E_{\text{cl}}^{\text{int}}(\omega_r)$, respectively) is *not* a perturbative result: it stems from our restricting the analysis to a given $(f_1 = f_2 = 1, F = 2, \ell)$ subspace, within which the electronic interaction V_{el} does not couple the spatial motion of the atoms to their internal states (see Section 11.4.1).

Identification of the RF-induced resonances reported in [20]

A divergence on Fig. 11.13, occurring for a given Rabi frequency ω_r^{res} , can be explained in terms of a resonance between two ‘bare’ states $|\Psi_{\text{op}}\rangle$ and $|\Psi_{\text{cl}}\rangle$ if the corresponding ‘bare’ energies are equal for a Rabi frequency ω_r which is close to ω_r^{res} .

The entrance channel used in [20] is an RF-dressed scattering state relating, for small ω_r , to the bare two-atom state $|f_1 = f_2 = 1, F = 2, M_F = -2, N_0^{\text{op}} - 2\rangle$. The corresponding threshold energy is represented by the dashed red line on Figs. 11.15 and 11.16.

We first consider the bound state $|\nu = 15, \ell = 0, SI = (13), F = 2\rangle$, which has the binding energy $h \cdot 90$ MHz [48]. Within each $(f_1 = f_2 = 1, F = 2, \ell = 0, N_0)$ subspace, this level is split into five RF-dressed bound states. The left-hand part of Fig. 11.16 represents the dependence on ω_r of the energies of the five dressed bound states relating, for

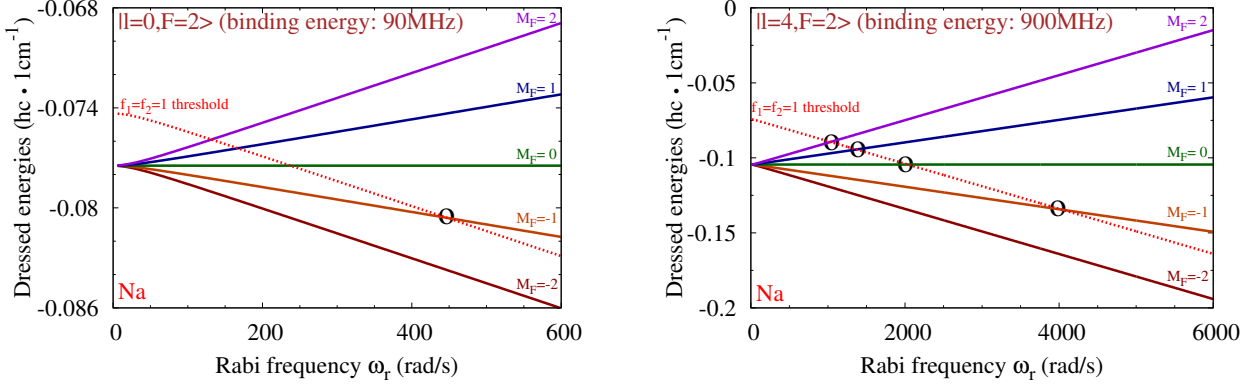


Figure 11.16. RF-dressed energies of two high-energy Sodium dimer states reported in [48], calculated within given ($f = 1, f = 1, F = 2, \ell$) subspaces for the fixed detuning $\delta/2\pi = 7$ MHz, as a function of the Rabi frequency ω_r . **Left:** RF-split energies of the bound state $|\nu = 15, \ell = 0, SI = (13), F = 2\rangle$ (binding energy: 90 MHz). **Right:** RF-split energies of the bound state $|\nu = 14, \ell = 4, SI = (13), F = 2\rangle$ (binding energy: 900 MHz). On both plots, the dashed red line represents the $|f_1 = f_2 = 1, F = 2, M_F = -2\rangle$ dissociation threshold, and the intersections mentioned in the text are circled in black.

small ω_r , to the bare states¹¹ $|f_1 = f_2 = 1, F = 2, M_F, \ell = 0, N = N_0^{\text{op}} - 2\rangle$, for $-2 \leq M_F \leq 2$. The dressed state relating to $(M_F = -1, N = N_0^{\text{op}} - 2)$ (solid orange line) has the same energy as the the open-channel state (dashed red line) for $\omega_r \approx 450 \cdot 10^6$ rad/s, which is close to the Rabi frequency $\omega_r \approx 375 \cdot 10^6$ rad/s of the first resonance observed on Fig. 11.13. Furthermore, the internal states $|f_1 = f_2 = 1, F = 2, M_F = -1, \ell^{\text{cl}} = 0, N = N_0^{\text{op}} - 2\rangle$ (closed channel) and $|f_1 = f_2 = 1, F = 2, M_F = -2, \ell^{\text{op}} = 2, m_\ell = 1, N = N_0^{\text{op}} - 2\rangle$ (open channel) are coupled together¹² by the spin-dependent interaction V_{ss} (the total spin projection $M_F + m_\ell$ and the photon number $N = N_0^{\text{op}} - 2$ are conserved, $|\ell^{\text{op}} - \ell^{\text{cl}}| \leq 2$, $|F^{\text{op}} - F^{\text{cl}}| \leq 2$, and $|M_F^{\text{op}} - M_F^{\text{cl}}| \leq 2$; see [7, 47]). Therefore, the resonance predicted for $\omega_r \approx 375 \cdot 10^6$ rad/s is due to a coupling of the $\ell^{\text{op}} = 2$ component of the incident scattering state, via V_{ss} , to the bound state $|\nu = 15, \ell^{\text{cl}} = 0, SI = (13), F = 2\rangle$.

We now consider the bound state $|\nu = 14, \ell = 4, SI = (13), F = 2\rangle$, which has the binding energy $h \cdot 900$ MHz [48]. This level is split into five RF-dressed bound states within each ($f_1 = f_2 = 1, F = 2, \ell = 4, SI = (13), N_0$) subspace. The right-hand part of Fig. 11.16 represents the dependence on ω_r of the energies of the five dressed bound states relating, for small ω_r , to the bare states $|f_1 = f_2 = 1, F = 2, M_F, \ell = 4, N = N_0^{\text{op}} - 2\rangle$, for $-2 \leq M_F \leq 2$. The energies of the four highest-energy dressed states cross the

¹¹ These five dressed states belong to five different dressed-state manifolds: the state bearing the quantum number M_F belongs to the $(N_0^{\text{cl}} = N_0^{\text{op}} - M_F - 2)$ manifold. The dressed-state energies do depend on N_0^{cl} through the photon-energy term $N_0^{\text{cl}} \hbar \omega$, but this dependence is weak, as $\omega/2\pi = 7$ MHz is small compared to the dressed-state splitting which is of the order of 100 MHz for $\omega_r = 500$ rad/s and increases for larger Rabi frequencies (see Figs. 11.16).

¹²The open-channel wavefunction cannot be chosen with $\ell^{\text{op}} = 0$ because V_{ss} conserves $(M_F + m_\ell)$.

11. Characterising the resonances

threshold energy once, for Rabi frequencies which are close to the resonant Rabi frequencies $\omega_r^{\text{res}} \approx 1300 \cdot 10^6 \text{ rad/s}$, $1600 \cdot 10^6 \text{ rad/s}$, $1850 \cdot 10^6 \text{ rad/s}$, and $4000 \cdot 10^6 \text{ rad/s}$ observed on Fig. 11.13.

The closed-channel internal states $|f_1 = f_2 = 1, F = 2, M_F^{\text{cl}}, \ell^{\text{cl}} = 4, m_\ell^{\text{cl}}, N = N_0^{\text{op}} - 2\rangle$ are coupled to the s -wave open-channel states $|f_1 = f_2 = 1, F = 2, M_F = -2, \ell^{\text{op}} = 0, N = N_0^{\text{op}} - 2\rangle$ (choose $M_F^{\text{cl}} + m_\ell^{\text{cl}} = -2$ in order to conserve the total angular momentum) to second order in V_{ss} . Thus, the four resonances mentioned above can be explained in terms of a second-order coupling via V_{ss} of the s -wave component of the incident scattering state to the bound state $|\nu = 14, \ell = 4, SI = (13), F = 2\rangle$ to second order in V_{ss} .

The resonance occurring for $\omega_r^{\text{res}} \approx 4000 \cdot 10^6 \text{ rad/s}$ has a multi-peaked structure, at least seven peaks being visible on Fig. 11.15. This structure can be explained in terms of two effects:

1. For large Rabi frequencies ω_r , the open-channel wavefunction $|\Psi_{\text{op}}^{(F=2, N_0^{\text{op}}, \ell=0)}\rangle$ and the closed-channel wavefunction $|\Psi_{\text{cl}}^{(F=2, N_0^{\text{op}}-1, \ell=4)}\rangle$ both have non-vanishing components for all $-2 \leq M_F \leq 2$. For each $M_F \leq 1$, the open-channel component bearing the quantum numbers $(M_F, \ell = 0, N = N_0^{\text{op}} + M_F)$ resonates with the closed-channel component whose quantum numbers are $(M_F + 1, \ell = 4, m_\ell = -1, N = N_0^{\text{op}} + M_F)$. This accounts for four of the observed peaks.
2. The closed-channel state $|f_1 = f_2 = 1, F = 2, M_F = -1, \ell^{\text{cl}} = 4, m_\ell^{\text{cl}}, N = N_0^{\text{op}} - 2\rangle$ is also coupled, to first order in V_{ss} , to the d -wave open-channel state $|f_1 = f_2 = 1, F = 2, M_F = -2, \ell^{\text{op}} = 2, m_\ell^{\text{op}}, N = N_0^{\text{op}} - 2\rangle$. This coupling, and the corresponding ones for the dressed-state components along $M_F = -1, 0$, and $+1$, account for the remaining peaks observed on Fig. 11.15.

11.4.4. Differences between RF-induced and MW-induced Feshbach resonances.

We have shown that the RF-induced Feshbach resonances within the lower hyperfine manifold, presented in [20], cannot be due to the magnetic dipole coupling term alone (see Section 11.4.2). These resonances thus involve the weak spin-dependent interaction $V_{\text{ss}}(r)$. By contrast, the microwave-induced Feshbach resonances which we have described in Sections 11.1 and 11.2 do not involve $V_{\text{ss}}(r)$: they are due solely to the magnetic dipole interaction W between the two electron spins and the magnetic field.

This is the main difference between the work reported in [20] and the one we present in our published article [21]. Radio-frequency induced resonances can be seen as the oscillating-field equivalent of ‘narrow’ Feshbach resonances, whereas microwave-induced resonances, which do not involve V_{ss} , are analogous to ‘broad’ Feshbach resonances [1]. In this sense, microwave-induced Feshbach resonances are more closely related to optically-induced Feshbach resonances [17], where the incident two-atom state is coupled to an electronically-excited dimer state using a resonant oscillating electric field: these

latter resonances are due to the electric-dipole coupling and, like microwave-induced resonances, they do not rely on V_{ss} .

The couplings involved being different also has an impact on the partial waves taking part in the resonances. The isotropic magnetic dipole coupling W conserves the angular momentum ℓ , and the microwave-induced resonances we have described only involve s -wave Physics (see Section 10.2). On the other hand, the spin-dependent interaction $V_{\text{ss}}(r)$ is not isotropic, and it does not cause resonances between s -wave states; therefore, at least one of the two resonant states has a spatial angular momentum $\ell \geq 2$. We have identified the bound states causing the RF-induced resonances reported in [20] to be the s -wave level $|\nu = 15, \ell = 0, SI = (13), F = 2\rangle$ and the $\ell = 4$ level $|\nu = 14, \ell = 4, SI = (13), F = 2\rangle$, whose binding energies are $h \cdot 90$ MHz and $h \cdot 900$ MHz, respectively [48]. The s -wave level is resonant with the d -wave component of the incident scattering state, and the $\ell = 4$ level is resonant with both the s -wave and d -wave components of the incident scattering state.

Microwave-induced Feshbach resonances exploit a stronger coupling mechanism, therefore they allow for the use of weaker magnetic fields. We focus on the small magnetic field regime, where the Rabi frequency associated with the oscillating field amplitude B_{osc} is much smaller than the detuning δ of the frequency from the hyperfine transition frequency. In the specific case of Sodium, the microwave-induced resonance occurs for the detuning $\delta/2\pi = -200$ MHz, and the amplitude $B_{\text{osc}} = 1$ G, corresponding to a Rabi frequency of the order of 1 MHz, yields a resonance which is broad enough to be observed experimentally ($\Delta\omega/2\pi > 1$ kHz: see Table 11.2 and Section 11.3).

In this regime (Rabi frequency much smaller than detuning), the dressing of a single atom due to the microwave is negligible, and the dominant effect is the two-atom resonance between the incident scattering state and a well-defined bound state. Our weak microwave magnetic fields not affecting the single-atom Physics could turn out to be an important asset, for example in the context of experiments involving atomic clocks.

12. The numerical calculation of two-atom wavefunctions

This chapter describes the challenges presented by the numerical calculation of multi-channel scattering wavefunctions, and the approaches that we have used to meet them.

We have written our own, fully independent implementations of all of the programs described in this chapter. The data used as input (the large- r singlet and triplet electronic potentials, the corresponding scattering lengths, and the hyperfine atomic structure) are available¹ in the published literature (see [21] and references therein).

The difficulties associated with the calculation of two-atom wavefunctions can be summarised as follows:

1. The wavefunctions are solutions of a differential system involving boundary conditions at both ends of the integration interval.
2. The electronic potentials are not known with sufficient accuracy for small inter-atomic separations.
3. The physically acceptable solution is the one for which all closed-channel components asymptotically decay to zero, but other solutions of the same Schrödinger equation asymptotically involve growing exponentials.
4. The two-atom wavefunction may involve many coupled channels.
5. The two-atom wavefunction may be non-real.

We start with a precise statement of the differential system we wish to solve and of the boundary conditions involved (Section 12.1). Then, we introduce the accumulated-phase approach [31], which circumvents the need for accurate information on the inner parts of the electronic potentials (Section 12.2). Next, we present the two numerical approaches we have used to calculate two-atom wavefunctions. Our first approach, presented in Section 12.3, is based on the relaxation method. This approach addresses points 1, 2, and 3 above. This is the approach we have used to perform the calculations presented in the published article of Chapter 13. However, this method is not readily extended to address points 4 and 5. Our second approach, presented in Section 12.4, is based on the shooting method. This more elaborate approach addresses all five difficulties mentioned above.

¹We thank Prof. S. Kokkelmans for providing up-to-date electronic potentials for ⁸⁷Rb.

12.1. The multi-channel scattering state wavefunction

In this first section, we give a precise definition of the wavefunction we wish to calculate. This definition is similar to the one given in Section 11.2, but we now state it in more general terms to include the effects of inelastic collisions and of a static magnetic field \mathbf{B}_{stat} (in addition to the oscillating magnetic field \mathbf{B}_{osc}).

12.1.1. Hamiltonian

The scattering problem of interest is described by the radial Hamiltonian of Eq. (10.13):

$$H = \frac{p_r^2}{2m_r} \mathbb{1} + V_{\text{el}}(r) + V_{\text{hf}} + V_Z + \hbar\omega a^\dagger a + W \quad , \quad (10.13)$$

where we have restricted our analysis to s -wave scattering (no centrifugal term in the Hamiltonian), and we have allowed for both an oscillating magnetic field (magnetic dipole coupling term W) and a static magnetic field (Zeeman term V_Z).

The Hamiltonian H operates on an infinite-dimensional space of internal states. For bosonic alkali atoms, this internal-state space is spanned, for example, by the states $|\{f_1, m_1, f_2, m_2\}^+, N\rangle$, where f_j and m_j are the two hyperfine quantum numbers of atom j , the notation $\{\dots\}^+$ denotes bosonic symmetry, and the arbitrary integer N gives the number of photons. However, just like in Chapter 11, arguments stemming from the conservation of energy and angular momentum make it possible to restrict H to a finite-dimensional internal-state subspace², whose dimension we call N_{states} .

12.1.2. Dressed two-atom states

We define the dressed two-atom state basis \mathbf{e}_D in the same way as in Section 11.2.2. We introduce the total r -dependent potential part $V_{\text{tot}}(r)$ of the Hamiltonian H :

$$V_{\text{tot}}(r) = V_{\text{el}}(r) + V_{\text{hf}} + V_Z + \hbar\omega a^\dagger a + W \quad . \quad (12.1)$$

This operator asymptotically reduces to an r -independent operator V_∞ :

$$V_\infty = V_{\text{tot}}(r \rightarrow \infty) = V_{\text{hf}} + V_Z + \hbar\omega a^\dagger a + W \quad , \quad (12.2)$$

which is a real and symmetric $N_{\text{states}} \times N_{\text{states}}$ matrix. Its N_{states} eigenstates make up the dressed two-atom state basis

$$\mathbf{e}_D = \{|D_1\rangle, \dots, |D_{N_{\text{states}}}\rangle\} \quad , \quad (12.3)$$

ordered such that the corresponding eigenvalues satisfy $\varepsilon_1^D \leq \dots \leq \varepsilon_{N_{\text{states}}}^D$.

²This finite-dimensional subspace depends on the incident state of the two atoms and on the polarisation of the oscillating magnetic field \mathbf{B}_{osc} .

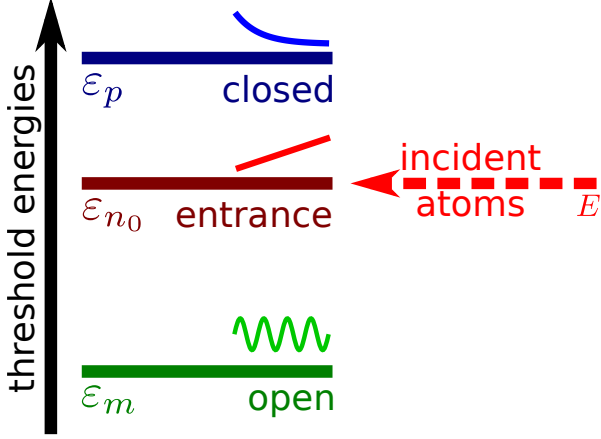


Figure 12.1. Threshold energies of the open ($\varepsilon_m < E$), entrance ($\varepsilon_{n_0} = E$) and closed ($\varepsilon_p > E$) channels. For large r , the radial wavefunction oscillates in all open channels, behaves like $(r - a)$ in the entrance channel, and decays exponentially in all closed channels.

12.1.3. Schrödinger equation and boundary conditions

We wish to calculate the scattering length $a = a_{n_0}$ characterising the collision between two atoms whose incident internal state is a given microwave-dressed two-atom state $|D_{n_0}\rangle$. The scattering length can be extracted from the asymptotic behaviour of the outgoing stationary scattering state [37] of H for the energy $E = \varepsilon_{n_0}^D$. This scattering state $|\Psi_{n_0}\rangle$, which is an N_{states} -component wavefunction, is defined by the Schrödinger equation:

$$H|\Psi_{n_0}\rangle = \varepsilon_{n_0}^D|\Psi_{n_0}\rangle \quad , \quad (12.4)$$

along with the large- r boundary conditions

$$\langle D_m | \Psi_{n_0}(r) \rangle = B_m \frac{1}{r} \exp(ik_m r) \quad \text{for } m < n_0 \text{ (open channel)} \quad (12.5a)$$

$$\langle D_{n_0} | \Psi_{n_0}(r) \rangle = \frac{r - a_{n_0}}{r} \quad \text{(entrance channel)} \quad (12.5b)$$

$$\langle D_p | \Psi_{n_0}(r) \rangle = A_p \frac{1}{r} \exp(-\kappa_p r) \quad \text{for } p > n_0 \text{ (closed channel)} \quad (12.5c)$$

where $\hbar k_m = (2m_r(\varepsilon_{n_0} - \varepsilon_m))^{1/2}$ for all open channels $m < n_0$ ($\varepsilon_m < \varepsilon_{n_0}$) and $\hbar \kappa_p = (2m_r(\varepsilon_p - \varepsilon_{n_0}))^{1/2}$ for all closed channels $p > n_0$ ($\varepsilon_p > \varepsilon_{n_0}$). In Eqs. (12.5), the (complex) coefficients A_p and B_m , as well as the (complex) scattering length a_{n_0} , are not known *a priori*; they can be extracted from the asymptotic behaviour of $\Psi_{n_0}(r)$ after it has been calculated. In other words, for large interatomic separations, the radial wavefunction $r|\Psi_{n_0}(r)\rangle$ reduces to a pure outgoing wave in all open channels, has the usual linear form in the entrance channel, and decays exponentially in all closed channels. The definitions of the open, entrance, and closed channels, as well as the asymptotic behaviours of the radial wavefunction components in these channels, are illustrated on Fig. 12.1.

Note that our choice of the incident state of the atom pair as an eigenstate of V_∞ implies that the microwave dressing of the internal states and the AC Zeeman shift on their energies are taken into account in our calculations. Also note the absence of kinetic energy in the channel $|D_{n_0}\rangle$ for large values of r , which causes the boundary conditions (12.5) to be spherically symmetric and thus ensures compatibility with our assumption of pure s -wave scattering.

12. The numerical calculation of two-atom wavefunctions

The Schrödinger equation (12.4) is a system of N_{states} coupled differential equations. In order for its solution to be uniquely determined, N_{states} conditions have to be applied in addition to Eqs. (12.5). These conditions have already been stated in Section 11.2.2; they enforce that the radial solution be regular [25] at $r = 0$:

$$\lim_{r \rightarrow 0} (r \Psi(r)) = \mathbf{0} \quad . \quad ((11.19))$$

12.1.4. In terms of radial wavefunctions

Exploiting the rotational symmetry in real space, we introduce the s -wave radial wavefunction $|\mathbf{U}\rangle$ defined, as in Eqs. (11.11), by [25]:

$$\Psi_{n_0}(r) = \frac{Y_0^0}{r} \mathbf{U}_{n_0}(r) \quad , \quad (12.6)$$

where $Y_0^0 = 1/\sqrt{4\pi}$ is the spherical harmonic for $l = m = 0$. In terms of $|\mathbf{U}_{n_0}\rangle$, the Schrödinger equation (12.4) reduces to a standard system of N_{states} coupled second-order differential equations:

$$\frac{d^2}{dr^2} \mathbf{U}_{n_0} = \frac{2m_r}{\hbar^2} (V_{\text{tot}}(r) - \varepsilon_{n_0}) \mathbf{U}_{n_0} \quad . \quad (12.7)$$

The large- r boundary conditions (12.5) become:

$$\langle D_m | \mathbf{U}_{n_0}(r) \rangle = \sqrt{4\pi} B_m \exp(ik_m r) \quad \text{for } m < n_0 \text{ (open channel)} \quad (12.8a)$$

$$\langle D_{n_0} | \mathbf{U}_{n_0}(r) \rangle = \sqrt{4\pi} (r - a_{n_0}) \quad \text{(entrance channel)} \quad (12.8b)$$

$$\langle D_p | \mathbf{U}_{n_0}(r) \rangle = \sqrt{4\pi} A_p \exp(-\kappa_p r) \quad \text{for } p > n_0 \text{ (closed channel),} \quad (12.8c)$$

and the regularity condition reads:

$$\mathbf{U}_{n_0}(r = 0) = \mathbf{0} \quad . \quad (12.9)$$

12.1.5. Real and non-real scattering lengths

An imaginary part $\text{Im}(a_{n_0}) \neq 0$ in the scattering length a_{n_0} is the signature of the presence of inelastic processes [33]. If the incident internal state of the atom pair is the lowest-energy internal state $|D_1\rangle$, the conservation of energy forbids inelastic processes, therefore a_1 is a real number. On the other hand, if the incident internal state is a higher-energy dressed state $|D_{n_0}\rangle$ ($n_0 > 1$), the atoms may undergo an inelastic decay into lower-energy channels (the conservation of energy being ensured by an increase in their kinetic energy): thus, a_{n_0} is not real.

From a mathematical point of view, the potential term $V_{\text{tot}}(r)$ appearing in the differential system (12.7) is real. Any solution of this system which is specified by real boundary conditions will be real; if the boundary conditions are not real, the solution may no longer be real. If the incident two-atom state is $|D_1\rangle$, the only open channel is

the entrance channel, and Eqs. (12.4) show that all boundary conditions involve only real numbers: this leads to a real wavefunction $|\Psi_1\rangle$ and, hence, to a real scattering length a_1 . If the incident two–atom state is $|D_{n_0}\rangle$ with $n_0 > 1$, other open channels are present besides the entrance channel; the wavefunction asymptotically behaves as an outgoing spherical wave in each of these channels: such spherical waves have non–zero imaginary parts, therefore the wavefunction $|\Psi_{n_0}\rangle$ is not real, which leads to a scattering length a_{n_0} which is not real.

12.2. The Accumulated–Phase approach

12.2.1. Description of the electronic interaction potentials

The only r –dependent term in the two–atom Hamiltonian (10.13) is the electronic interaction operator $V_{el}(r)$, expressed by Eq. (10.14) in terms of the singlet and triplet potentials V_S and V_T . These latter potentials can, in turn, be written in terms of a ‘dispersive’ part V_{disp} and an ‘exchange’ part V_{exch} [31]:

$$V_{S,T}(r) = V_{disp}(r) \mp V_{exch}(r) \quad , \quad (12.10)$$

The dispersive part is a power series in $1/r^2$ whose leading term is the van–der–Waals interaction $-C_6/r^6$:

$$V_{disp}(r) = - \left(\frac{C_6}{r^6} + \frac{C_8}{r^8} + \frac{C_{10}}{r^{10}} + \dots \right) \quad . \quad (12.11)$$

An analytical description of the exchange term is available only for large values of r ($r \gtrsim 20 a_0$) [49]:

$$V_{exch} = \frac{1}{2} J r^{[7/(2\alpha a_0)-1]} \exp(-2\alpha r) \quad , \quad (12.12)$$

where α is related to the atomic ionisation energy E_I by $E_I = E_h \cdot (\alpha a_0)^2$ [39] and $E_h = 4.36 \cdot 10^{-18}$ J is the Hartree energy.

Equations (12.11) and (12.12) show that, for $r \gtrsim 20 a_0$, the electronic potentials V_S and V_T are characterised by a small number of parameters (the dispersion coefficients C_j , the energy J , and the coefficient α). These few parameters can readily be extracted from the available experimental high–precision measurements and are thus known with very good accuracy. The description of the electronic potentials for smaller interatomic distances is more involved and less accurate. However, the scattering properties of these potentials are very sensitive to their short–range details.

Our two–atom wavefunction calculations have been performed using the Accumulated Phase approach, developed by Verhaar and coworkers [31, 50]. This approach encapsulates all of the short–range Physics into a boundary condition applied at a minimum non–zero radius r_0 , of the order of $20 a_0$. This boundary condition is formulated in terms of four parameters which can be tuned to reproduce available results, such as the values of the singlet and triplet scattering lengths a_S and a_T .

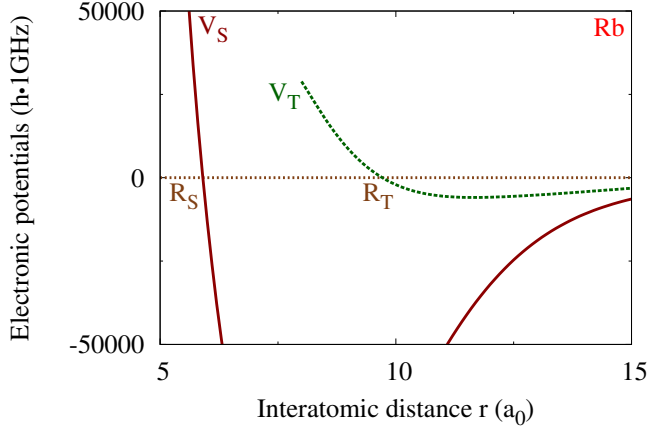


Figure 12.2. Zero-energy turning points R_S and R_T for the Singlet and Triplet electronic potentials of ^{87}Rb .

We describe this approach in the next two sections: we first focus on the single-channel case, and then describe our implementation of the approach in the context of a multi-channel problem.

12.2.2. Single-channel wavefunction

We start with the single-channel case, and we consider a radial wavefunction $u(r)$ which is a solution of the following Schrödinger equation:

$$\frac{d^2}{dr^2} u(r) = \frac{2m_r}{\hbar^2} (V(r) - E) u(r) \quad , \quad (12.13)$$

where $V(r)$ one of the two electronic potentials $V_S(r)$ or $V_T(r)$. The energy E can be zero, positive, or negative, as long as it remains small compared to the depth of the potential V ($E \sim \pm$ a few $a_{\text{hf}} \sim \pm$ a few tens of GHz).

We define the turning point $R(E)$ by the condition:

$$V(R(E)) = E \quad . \quad (12.14)$$

This definition is illustrated in Fig. 12.2 on the particular case of the electronic potentials for ^{87}Rb , for $E = 0$.

For $r_0 > R(E)$, the WKB approach [33] yields the following form for the radial wavefunction $u(r_0)$:

$$u(r_0) = A \frac{\sin \Phi(E, r_0)}{\sqrt{k(r_0)}} \quad , \quad (12.15)$$

where $\hbar k(r_0) = [2m_r (E - V(r_0))]^{1/2}$ is the local momentum at r_0 and

$$\Phi(E, r_0) = \int_{R(E)}^{r_0} dr k(r) + \text{constant} \quad (12.16)$$

is the accumulated phase up to r_0 , the constant being chosen to ensure the regularity condition $u(r = 0) = 0$. The range of relevant energies near the threshold $E = 0$ being

small, we use a linear approximation to the accumulated phase at r_0 :

$$\Phi(E, r_0) = \Phi_0 + E \Phi_0^E + \dots \quad , \quad (12.17)$$

where $\Phi_0 = \Phi(E = 0, r_0)$ and $\Phi_0^E = \left. \frac{\partial \Phi}{\partial E} \right|_{E=0, r_0}$.

Choosing $r_0 > R$ to be as small as possible (in our calculations, r_0 ranges from $10 a_0$ to $20 a_0$), while maintaining the validity of the WKB approach, Eqs. (12.15) and (12.17) yield a boundary condition on the logarithmic derivative of u , which is applied at the non-zero minimal radius r_0 but still enforces the regularity condition at $r = 0$:

$$\frac{u'(r_0)}{u(r_0)} = \frac{1}{\hbar} \frac{[2m_r(E - V(r_0))]^{1/2}}{\tan(\Phi_0 + E \Phi_0^E)} + \frac{1}{4} \frac{V'(r_0)}{E - V(r_0)} \quad , \quad (12.18)$$

where the prime denotes derivation with respect to r .

Calculating the accumulated-phase parameters

For each electronic potential V_S or V_T , the boundary condition defined by Eq. (12.18) encapsulates all of the short-range Physics into the two real numbers Φ_0 and Φ_0^E .

The parameter Φ_0 is the accumulated phase for $E = 0$. We adjust it such that the zero-energy scattering state wavefunction, which behaves like $u(r) = \sqrt{4\pi}(r - a)$ for large values of r , has the correct scattering length $a = a_S$ or a_T .

The coefficient Φ_0^E has a simple integral expression in terms of the potential $V(r)$ for $R < r < r_0$. First, we note that both electronic potentials V_S and V_T are very steep for energies close to the dissociation threshold (see Fig. 12.2): R_T and R_S only vary significantly on a scale of a few hundreds of GHz, whereas the energies relevant to us are of the order of tens of GHz. Therefore we take $R(E) \approx R(E = 0)$, both for the singlet for the triplet potentials. Now, the energy-derivative of Eq. (12.16) yields [51]:

$$\Phi_0^E = \hbar m_r \int_{R(E=0)}^{r_0} \frac{dr}{[2m_r(E - V(r))]^{1/2}} \quad , \quad (12.19)$$

The denominator of the integrand being the local momentum $\hbar k(r)$. An approximation for Φ_0^E can be calculated from Eq. (12.19) using the ‘inner parts’ of the electronic potentials. For all of the atoms we have considered, this approximation has been sufficiently accurate to reproduce the positions of known static-field Feshbach resonances.

12.2.3. Multiple channels

We now move on to the implementation of the accumulated-phase approach in the multiple-channel case.

The scattering problems we are interested in are described by the two-atom Hamiltonian H and involve multiple scattering channels which are coupled to each other (see Fig. 10.5 for a block-matrix representation of H which illustrates the channel couplings in the ‘molecular’ basis \mathbf{e}_M). There is no basis in which these channels uncouple for all values of r .

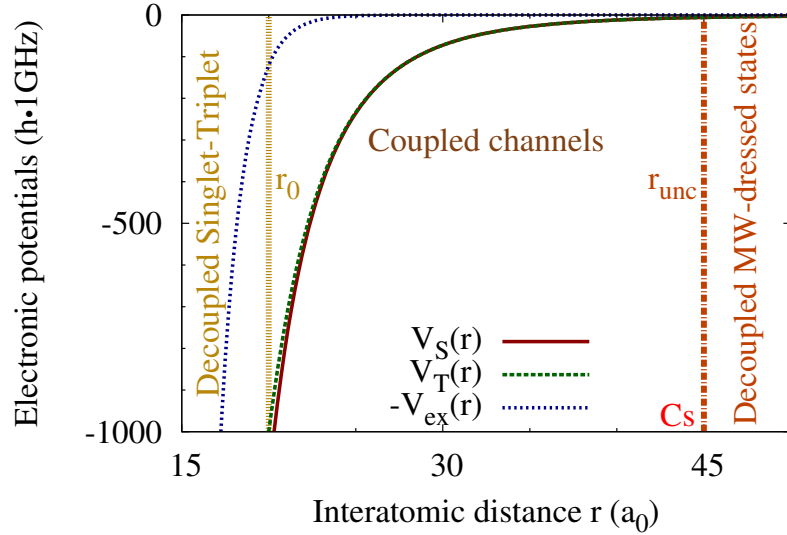


Figure 12.3. Three ranges of values of r leading to different coupling schemes, illustrated on the case of the ^{133}Cs potentials. For $r < r_0$, the exchange interaction dominates ($V_{\text{exch}}(r) \gg V_{\text{hf}}$) and the basis states in ϵ_{M} are uncoupled. For $r > r_{\text{unc}}$, the hyperfine interaction dominates ($V_{\text{exch}}(r) \ll V_{\text{hf}}$) and the mw-dressed states in ϵ_{D} are uncoupled. For $r_0 < r < r_{\text{unc}}$, no decoupling occurs and coupled-channel calculations are required.

However, as already mentioned in the context of spin recoupling (Section 10.2.5), a decoupling does occur for small interatomic separations. As shown on Fig. 12.3 in the case of ^{133}Cs , the exchange interaction V_{exch} is much larger than the hyperfine interaction V_{hf} for $r \lesssim 20 a_0$. The Zeeman term V_{Z} and the magnetic dipole term W are themselves much smaller than the hyperfine interaction³, therefore the exchange interaction yields the dominant contribution for small r . This term is diagonal in any basis whose states have definite two-electron spins S . In particular, all of the internal states in the ‘molecular’ basis ϵ_{M} are decoupled for $r \lesssim 20 a_0$.

Therefore, if the minimum radius r_0 (chosen to be the same in all scattering channels) is small enough to be in the range for which this decoupling occurs, the accumulated-phase boundary condition can be applied separately to each wavefunction component in the basis ϵ_{M} . For example, in the particular case of ^{133}Cs , $r_0 = 20 a_0$ leads to $V_{\text{exch}}(r_0) = 50 a_{\text{hf}}$ (where a_{hf} is the coefficient appearing in Eq. (10.10) which determines the hyperfine energy splitting), which is sufficient to ensure the singlet-triplet decoupling for $r \leq r_0$.

³For instance, the magnetic field amplitude $B_{\text{osc}} = 10 \text{ G}$ leads to $\mu_B B_{\text{osc}} = h \cdot 14 \text{ MHz}$, whereas a_{hf} is of the order of tens of GHz.

The adiabatic accumulated phase approach

The accuracy of the accumulated–phase approach can be improved [31] by accounting for the ‘adiabatic’ mixing between states in \mathfrak{e}_M caused by the hyperfine term for r smaller than, but close to, r_0 .

For that purpose, we apply the accumulated–phase approach, not in the basis \mathfrak{e}_M , but in the basis $\widetilde{\mathfrak{e}}_M$ which diagonalises $\widetilde{V}_{\text{tot}}(r_0) = (V_{\text{tot}}(r_0) - V_S(r_0)\mathbb{1})$, keeping in mind that all terms in this matrix other than the exchange interaction $V_{\text{exch}}(r_0) = (V_T(r_0) - V_S(r_0))$ are small corrections. In particular, this matrix contains V_{hf} , therefore the use of a basis in which it is diagonal accounts for the contamination due to V_{hf} . The ‘adiabatic’ approximation resides in the fact that, although the basis states in $\widetilde{\mathfrak{e}}_M$ no longer have definite values of the quantum number S , we still assume that the corresponding spatial components are pure singlet and triplet waves.

In order to identify the ‘singlet’ and ‘triplet’ channels in $\widetilde{\mathfrak{e}}_M$, we note that $\widetilde{V}_{\text{tot}}(r_0)$ acting on an electronic–triplet state contains $V_{\text{exch}}(r_0) > 0$, whereas $\widetilde{V}_{\text{tot}}(r_0)$ acting on an electronic–singlet state does not. Furthermore, we recall that $V_{\text{exch}}(r_0)$ is the dominant contribution to $\widetilde{V}_{\text{tot}}(r_0)$. Therefore, introducing N_{states}^S , the number of accessible internal states which are electronic–singlet, we approximate the spatial parts corresponding to the N_S lowest–energy eigenstates of $\widetilde{\mathfrak{e}}_M$ to pure singlet waves, and the spatial parts corresponding to the remaining $(N - N_S)$ eigenstates to pure triplet waves.

12.3. The relaxation method

In this section and the next one, we present the two numerical approaches we have used to calculate two–atom wavefunctions.

As mentioned in the introduction of this chapter, the differential system to be solved is a two–point boundary–value problem, as it involves boundary conditions at both ends of the integration interval. Two types of approaches are available for the numerical solution of such problems [52]: (i) relaxation methods and (ii) shooting methods. We have experimented with both approaches. We first briefly present an approach based on the relaxation method.

12.3.1. From a second–order differential system to a first–order one

The Schrödinger equation (12.7) is a system of N_{states} coupled *second–order* differential equations. Our first step is to rewrite it as a system of $2N_{\text{states}}$ coupled *first–order* differential equations:

$$\mathbf{Y}'(r) = \begin{pmatrix} 0 & \mathbb{1} \\ \frac{2m_r}{\hbar^2}(V_{\text{tot}}(r) - \varepsilon_{n_0}) & 0 \end{pmatrix} \mathbf{Y}(r) = \mathbf{G}(r, \mathbf{Y}(r)) \quad \text{with} \quad \mathbf{Y}(r) = \begin{pmatrix} \mathbf{U}_{n_0}(r) \\ \mathbf{U}'_{n_0}(r) \end{pmatrix}, \quad (12.20)$$

where the vectors $\mathbf{Y}(r)$ and $\mathbf{G}(r, \mathbf{Y}(r))$ have $2N_{\text{states}}$ –components, and the prime denotes derivation with respect to the variable r .

12.3.2. Discretisation of the differential system

We choose the integration interval to be $[r_0, r_{\max}]$. The lower bound $r_0 > 0$ is the radius at which the accumulated phase boundary condition is applied: we choose $r_0 = 10 a_0$ for ${}^7\text{Li}$, $r_0 = 16 a_0$ for ${}^{23}\text{Na}$, ${}^{41}\text{K}$, and ${}^{87}\text{Rb}$, and $r_0 = 20 a_0$ for ${}^{133}\text{Cs}$. The upper bound r_{\max} is chosen to be sufficiently large for the total potential matrix $V_{\text{tot}}(r_{\max})$ (Eq. (12.1)) to have reached its asymptotic value V_∞ , given by Eq. (12.2): we choose $r_{\max} = 1000 a_0$ for all considered atoms.

The relaxation method is based on the use of a mesh representing the integration interval. Following [52], we use an evenly-spaced mesh. The density of mesh points must be sufficiently large to accommodate for the oscillating behaviour of the wavefunction for small values of r (see Figs. 11.5): our implementation uses $M_{\text{points}} = 4 \cdot 10^5$ mesh points evenly spaced from r_0 to r_{\max} . The sought solution $\mathbf{Y}(r)$ is represented by $(2N_{\text{states}}M_{\text{points}})$ numbers, giving the values of the $2N_{\text{states}}$ components $Y_j(r_k)$ at each of the M_{points} mesh points r_k ($0 \leq k \leq M_{\text{points}} - 1$).

The relaxation method replaces the $2N_{\text{states}}$ coupled equations (12.20) by finite-difference equations at each mesh point. The finite-difference at the mesh point x_k ($1 \leq k \leq M-1$) reads:

$$\mathbf{Y}_k - \mathbf{Y}_{k-1} - (r_k - r_{k-1}) \mathbf{G} \left(\frac{r_{k-1} + r_k}{2}, \frac{\mathbf{Y}_{k-1} + \mathbf{Y}_k}{2} \right) = 0 \quad , \quad (12.21)$$

where the vectors \mathbf{Y}_{k-1} and \mathbf{Y}_k have $2N_{\text{states}}$ components and give the numerical values for the $2N_{\text{states}}$ coupled waves at the mesh points r_{k-1} and r_k . There are $2N_{\text{states}}(M_{\text{points}} - 1)$ such finite-difference equations; the boundary conditions provide $2N_{\text{states}}$ additional equations. Therefore, the discretisation process leads to $2N_{\text{states}}M_{\text{points}}$ coupled equations for an equal number of unknowns.

We solve these coupled equations using an iterative ‘relaxation’ procedure based on the multidimensional Newton method [52], exploiting the strong sparsity and the specific block structure of the linear systems involved.

12.3.3. Stability of the relaxation method

This first approach is the approach we have used for all of the numerical results presented in the published article of Chapter 13. Our choice of this method was due to the following remark (point 3 in the introduction of this chapter). The solutions of the Schrödinger equation (12.7) may asymptotically involve both growing exponentials $\exp(+\kappa_p r)$ or decaying exponentials $\exp(-\kappa_p r)$, in all closed channels $p > n_0$. The only physically-acceptable solution is the one which can be normalised, *i.e.* the one which involves only decaying exponentials. However, the existence of the unacceptable ‘growing’ solutions may contaminate the numerical calculation of the ‘decaying’ one. The use of relaxation methods helps to avoid such a contamination, because of its enforcing conditions at each mesh point (rather than only at the two ends of the integration interval).

12.3.4. Limitations of our implementation

The use of an evenly-spaced mesh, in conjunction with the oscillatory nature of the wavefunction components for small values of r , causes our implementation to require a large number of mesh points. Most of these mesh points are located in the large- r region, where a comparable accuracy could be obtained with a much smaller mesh point density. This issue could be solved by using a mesh with variable step sizes.

The present implementation (using evenly-spaced meshes) leads to long relaxation times. For example, each graph represented on Fig. 11.12, which results from calculations involving 8 coupled internal states (see Section 11.2), took several days to obtain. Such a slow convergence prohibits the use of this method for problems involving larger numbers of coupled internal states, such as the static-field resonances of Chapter 14 (up to 14 coupled states) or the microwave-induced resonances involving the ($M_F = 0$) subspace presented in Chapter 15 (48 coupled states).

Finally, this approach does not make use of the uncoupling which occurs for relatively large r : as shown on Fig. 12.3 for ^{133}Cs , the exchange interaction is negligible compared to the hyperfine energy term for distances greater than $r_{\text{unc}} \approx 45 a_0$ (in the case of ^{133}Cs , the choice of $r_{\text{unc}} = 45 a_0$ yields $V_{\text{exch}}(r_{\text{max}}) = 10^{-8} a_{\text{hf}}$). Therefore, even though the electronic potentials have not yet completely vanished, the electronic term V_{el} is diagonal in any basis, and the channels all decouple in the dressed-state basis ϵ_{D} .

Our second approach, described in the next section, is not affected by any of these limitations.

12.4. An approach based on the shooting method

In this last section, we describe the second approach we have used for the numerical calculation of two-atom wavefunctions. This second approach has been implemented to circumvent the limitations of the relaxation method described in Section 12.3: it does not use a mesh with a fixed step, it exploits the linearity of the differential system defined by Eq. (12.20) and the uncoupling that occurs for $r > r_{\text{unc}}$, and it runs considerably faster than our relaxation codes.

For this second approach, we abandon the ‘relaxation’ method of Section 12.3 and turn towards a ‘shooting’ scheme. We also relinquish the first-order differential system of Eq. (12.20), and go back to the original radial Schrödinger equation (12.7).

We operate on the integration interval $[r_0, r_{\text{max}}]$, defined in Section 12.3.2. We do not manually discretise this interval.

12.4.1. Two standard ‘shooting’ methods

We first briefly describe two standard methods involving ‘shooting’: the basic ‘shooting’ method and ‘shooting towards a fitting point’ [52].

In its basic implementation, the ‘shooting’ method consists in choosing ‘guess’ values for the N_{states} components of the wavefunction $\mathbf{U}(r_0)$ and those of its derivative $\mathbf{U}'(r_0)$ such that the boundary conditions at the lower bound r_0 are satisfied. The solution

is then ‘propagated’, using any *initial-value* differential equation solver, through the integration interval towards the upper bound r_{\max} . This ‘shot’ is successful if the components of $\mathbf{U}(r_{\max})$ and $\mathbf{U}'(r_{\max})$ satisfy the boundary conditions at r_{\max} . If the ‘shot’ is not successful, the initial ‘guess’ values are improved (for example, using Newton’s method for finding the zeros of a multi-variable function), and the whole procedure is iterated until a successful ‘shot’ is fired.

A more elaborate approach, called ‘shooting towards a fitting point’, involves the choice of an intermediate ‘fitting point’ r_{fit} within the integration interval $[r_0, r_{\max}]$. ‘Guesses’ are made for the wavefunction components and derivatives at the lower bound r_0 , chosen such that the boundary conditions at r_0 are satisfied; the solution is ‘propagated’, in the increasing- r direction, up to r_{fit} . Similarly, ‘guesses’ are made for the wavefunction components at r_{\max} satisfying the boundary conditions at that point; the solution is ‘propagated’, in the decreasing- r direction, down to r_{fit} . The ‘double-shot’ is successful if the wavefunction components and derivatives obtained at r_{fit} through the forward and backward propagations are equal. If it is not successful, the ‘guess’ values at r_0 and r_{\max} are improved, and the whole procedure is iterated until the backward- and forward-propagated solutions match at r_{fit} .

12.4.2. Shooting and fitting for a linear problem

The ‘shooting’ approach implemented in our program is a variant of ‘shooting towards a fitting point’, which we have adapted to the case of a linear problem in order to circumvent the need for iterations.

The radial Schrödinger equation (12.7) is a system of N_{states} coupled second-order Schrödinger equations. We call \mathcal{E}_{n_0} its set of solutions, which is a $2N_{\text{states}}$ -dimensional vector space.

Calculating basis solutions

As in the standard ‘shooting to a fitting point’ method, we introduce a ‘fitting radius’ r_{fit} within the integration interval $[r_0, r_{\max}]$. The choice of the value of r_{fit} will be discussed in Section 12.4.3.

The N_{states} accumulated-phase boundary conditions applied at r_0 (see Section 12.2) define an N_{states} -dimensional subspace of \mathcal{E}_{n_0} . We calculate a basis of N_{states} independent functions ($\mathbf{X}_i(r)$), each of which satisfies the N_{states} accumulated-phase boundary conditions. These functions are determined, for $r_0 \leq r \leq r_{\text{fit}}$, by integrating in the increasing- r direction starting from initial values at r_0 .

We now turn to the boundary conditions at the upper bound r_{\max} . The number of open channels (including the zero-energy entrance channel) is n_0 ; we call $N_{\text{cl}} = N_{\text{states}} - n_0$ the number of closed channels. We first focus on the closed-channel components. The

large- r boundary condition:

$$\langle D_m | \mathbf{Y}(r) \rangle = 0 \quad \text{for } m < n_0 \text{ (open channel)} \quad (12.22a)$$

$$\langle D_{n_0} | \mathbf{Y}(r) \rangle = 0 \quad \text{(entrance channel)} \quad (12.22b)$$

$$\langle D_p | \mathbf{Y}(r) \rangle = \sqrt{4\pi} A_p \exp(-\kappa_p r) \quad \text{for } p > n_0 \text{ (closed channel),} \quad (12.22c)$$

where the (A_p) 's are arbitrary numbers and the (κ_p) 's are defined as in Section 12.1.3, define an N_{cl} -dimensional subspace of \mathcal{E}_{n_0} , for which we calculate a basis $(\mathbf{Y}_j(r))_{1 \leq j \leq N_{\text{cl}}}$.

Next, we focus on the open-channel components (including the zero-energy entrance channel n_0). The large- r boundary conditions

$$\langle D_m | \mathbf{Z}(r) \rangle = \sqrt{4\pi} B_m \exp(ik_m r) \quad \text{for } m < n_0 \text{ (open channel)} \quad (12.23a)$$

$$\langle D_{n_0} | \mathbf{Z}(r) \rangle = \sqrt{4\pi} B_{n_0} \quad \text{(entrance channel)} \quad (12.23b)$$

$$\langle D_p | \mathbf{Z}(r) \rangle = 0 \quad \text{for } p > n_0 \text{ (closed channel),} \quad (12.23c)$$

where the (B_m) 's are arbitrary numbers and the (k_m) 's are defined as in Section 12.1.3, define an n_0 -dimensional subspace of \mathcal{E}_{n_0} , for which we calculate a basis $(\mathbf{Z}_l(r))_{1 \leq l \leq N_{\text{cl}}}$.

Finally, we calculate the single function $\mathbf{T}(r)$, defined by the large- r boundary condition:

$$\langle D_m | \mathbf{T}(r) \rangle = 0 \quad \text{for } m < n_0 \text{ (open channel)} \quad (12.24a)$$

$$\langle D_{n_0} | \mathbf{T}(r) \rangle = \sqrt{4\pi} r \quad \text{(entrance channel)} \quad (12.24b)$$

$$\langle D_p | \mathbf{T}(r) \rangle = 0 \quad \text{for } p > n_0 \text{ (closed channel).} \quad (12.24c)$$

The functions $(\mathbf{Y}_j(r))$, $(\mathbf{Z}_l(r))$ and $\mathbf{T}(r)$ are determined, for $r_{\text{fit}} \leq r \leq r_{\text{max}}$, by integrating in the decreasing- r direction starting from initial values at r_{max} .

Note that the numerical calculation of the functions (\mathbf{X}_i) , (\mathbf{Y}_j) , (\mathbf{Z}_l) , and \mathbf{T} only involves boundary conditions *at one end* of the integration interval (*i.e.* they are *not* two-point boundary value problems). Therefore, it can be performed using any of the standard numerical solvers for differential equations. We use an algorithm, based on Stoermer's rule [52], which is optimised for second-order systems of the form $\mathbf{y}'' = \mathbf{f}(r, \mathbf{y})$ (where the first-order derivative \mathbf{y}' does not appear). Our implementation includes adaptive stepsize control: the discretisation of the intervals $[r_0, r_{\text{fit}}]$ and $[r_{\text{fit}}, r_{\text{max}}]$ is done automatically, with an r -dependent step size that is chosen to improve accuracy and efficiency.

Calculating the physical wavefunction

The 'physical' wavefunction $\mathbf{U}(r)$, defined for $r_0 \leq r \leq r_{\text{max}}$, is the function in \mathcal{E}_{n_0} which satisfies both the accumulated-phase boundary conditions of Section 12.2 and the large- r behaviour of Eqs. (12.8). For values of r smaller than r_{fit} , it is a linear combination of the (\mathbf{X}_i) 's:

$$\mathbf{U}(r) = \sum_{i=1}^{N_{\text{states}}} x_i \mathbf{X}_i(r) \quad \text{for } r_0 \leq r \leq r_{\text{fit}}. \quad (12.25)$$

12. The numerical calculation of two-atom wavefunctions

For $r \geq r_{\text{fit}}$, it can be expressed in terms of the (\mathbf{Y}_j) 's, (\mathbf{Z}_l) 's and \mathbf{T} :

$$\mathbf{U}(r) = \sum_{j=1}^{N_{\text{cl}}} y_j \mathbf{Y}_j(r) + \sum_{k=1}^{n_0} z_k \mathbf{Z}_k(r) + \mathbf{T}(r) \quad \text{for } r_0 \geq r \geq r_{\text{fit}}. \quad (12.26)$$

The requirement that both $\mathbf{U}(r)$ and $\mathbf{U}'(r)$ be continuous at the fitting point $r = r_{\text{fit}}$ yields a linear system of $2N_{\text{states}}$ equations which determines the $2N_{\text{states}}$ complex coefficients $(x_i)_{1 \leq i \leq N_{\text{states}}}$, $(y_j)_{1 \leq j \leq N_{\text{cl}}}$, and $(z_k)_{1 \leq k \leq n_0}$.

12.4.3. Exploiting the large- r uncoupling of the dressed two-atom states

We have already mentioned (see Section 12.3.4) that the fast decay of the exchange interaction $V_{\text{exch}}(r)$ (see Eq. (12.12)) and Fig. 12.3) causes the electronic interaction term $V_{\text{el}}(r)$ to become spin-independent for $r \geq r_{\text{unc}}$, where r_{unc} is of the order of a few tens of a_0 (we take $r_{\text{unc}} = 45 a_0$ for ^{133}Cs). This causes the channels defined by the dressed two-atom states ($|D_n\rangle$) to become uncoupled for $r \geq r_{\text{unc}}$.

In order to take advantage of this uncoupling, we choose the fitting point r_{fit} to be equal to the uncoupling radius r_{unc} . Suitable choices of the values at r_{max} for the functions (\mathbf{Y}_j) , (\mathbf{Z}_l) , \mathbf{T} , and their derivatives, thus reduces their calculation, for $r_{\text{fit}} \leq r \leq r_{\text{max}}$, to single-channel calculations. The large- r boundary conditions for \mathbf{T} are specified by Eqs. (12.24). We choose the following values at r_{max} for the functions $(\mathbf{Y}_j)_{1 \leq j \leq N_{\text{cl}}}$ and $(\mathbf{Z}_l)_{1 \leq l \leq n_0}$:

$$\langle D_n | \mathbf{Y}_j(r_{\text{max}}) \rangle = \delta_{n,(n_0+j)} \quad \text{and} \quad \langle D_n | \mathbf{Y}'_j(r_{\text{max}}) \rangle = -\kappa_{(n_0+j)} \delta_{n,(n_0+j)} \quad (12.27a)$$

$$\langle D_n | \mathbf{Z}_l(r_{\text{max}}) \rangle = \delta_{n,l} \quad \text{and} \quad \langle D_n | \mathbf{Z}'_l(r_{\text{max}}) \rangle = ik_l \delta_{n,l} \quad (12.27b)$$

In Equation (12.27b), we use the convention $k_{n_0} = 0$ for the entrance channel, so that $|\mathbf{Y}_{n_0}(r)\rangle$ is asymptotically equal to $|\Delta_{n_0}\rangle$ for large values of r . The scattering length a is directly related to the corresponding (complex) coefficient z_{n_0} :

$$z_{n_0} = -\sqrt{4\pi} a \quad , \quad (12.28)$$

as can be obtained from the asymptotic behaviour of Eq. (12.26).

12.4.4. Accounting for the fast exponential decay in closed channels

When projected in the dressed-state basis, the closed channel components asymptotically behave like decaying exponentials $\exp(-\kappa_p r)$ (see for instance Eqs. (12.22)). If κ_p is large (*i.e.* if the channel energy ε_p is large), the integration in the decreasing- r direction starting from the boundary condition of Eq. (12.27a) will quickly yield very large numerical values for $\mathbf{Y}_j(r)$, which may cause numerical instabilities. We now explain how to avoid these instabilities.

We focus on a closed channel $|D_p\rangle$ with a large channel energy ε_p . More specifically, we assume that

$$V_{S,T}(r_{\text{fit}}) + \varepsilon_p > \varepsilon_{n_0} \quad . \quad (12.29)$$

We consider the function $\mathbf{Y}_j(r)$, defined for $r_{\text{fit}} \leq r \leq r_{\text{max}}$ by the boundary condition of Eq. (12.27a) and the single-channel Schrödinger equation:

$$Y_j''(r) = \frac{2m_r}{\hbar^2} (V_{\text{tot}}^p(r) - \varepsilon_{n_0}) Y_j(r) \quad , \quad (12.30)$$

where $j = p - n_0$, $Y_j(r) = \langle D_p | \mathbf{Y}_j(r) \rangle$, and $V_{\text{tot}}^p(r) = \langle D_p | V_{\text{tot}}(r) | D_p \rangle$. The condition (12.29) ensures that the potential term $(V_{\text{tot}}^p(r) - \varepsilon_{n_0})$ appearing in Eq. (12.30) never goes to zero. It is then readily seen⁴ that $Y_j(r)$ never goes to 0 for $r_{\text{fit}} \leq r \leq r_{\text{max}}$. Therefore, we introduce the logarithmic derivative $W_j(r)$ of the function $Y_j(r)$, defined by:

$$W_j(r) = \frac{Y_j'(r)}{Y_j(r)} \quad . \quad (12.31)$$

The Schrödinger equation (12.30) translates onto $W_j(r)$ as the following first-order equation:

$$W_j'(r) + W_j^2(r) = (V_{\text{tot}}^p(r) - \varepsilon_{n_0}) \quad , \quad (12.32)$$

and the boundary condition at r_{max} (Eq. 12.27a) reduces to $W_j(r_{\text{max}}) = -\kappa_p$. The function $W_j(r)$, being related to the logarithm of $Y_j(r)$, is no longer very large for values of r close to r_{fit} .

When solving the linear system of Section 12.4.2 giving the values of the coefficients (x_i) , (y_j) , and (z_k) , the values of $Y_j(r_{\text{fit}})$ and $Y_j'(r_{\text{fit}})$ can be replaced by 1 and $W_j(r_{\text{fit}})$, respectively: this amounts to changing the boundary conditions (12.27a) to include the additional condition $Y_j(r_{\text{fit}}) = 1$.

12.4.5. Calculating complex wavefunctions using real basis functions

We have already pointed out in Section 12.1.5 that the ‘physical’ wavefunction $\mathbf{U}(r)$ is real in the absence of inelastic processes, but that it becomes non-real as soon as inelastic processes are present, *i.e.* as soon one of open the open channels $|D_m\rangle$ satisfies $\varepsilon_m < E$, where E is the energy of the colliding atom pair.

We now show that such a complex wavefunction may be calculated from functions $(\mathbf{X}_i(r))$, $(\mathbf{Y}_j(r))$, $\mathbf{T}(r)$, and functions related to the $(\mathbf{Z}_l(r))$ which are all real.

We recall that the total potential operator $V_{\text{tot}}(r)$ is a real matrix for all values of r . Additionally, the boundary conditions (12.24) and (12.27a), respectively defining $\mathbf{T}(r)$ and the functions $(\mathbf{Y}_j(r))$, are real, therefore the functions $\mathbf{T}(r)$ and $(\mathbf{Y}_j(r))$ are real for

⁴The value $Y_j(r_{\text{max}}) > 0$. Integrating from r_{max} back towards r_{fit} , Eq. (12.30) shows that, as long as $Y_j(r)$ does not change signs, its second derivative $Y_j''(r)$ is positive. This entails that $Y_j'(r) < 0$ and, hence, that the function goes farther away from zero when r decreases towards r_{fit} .

12. The numerical calculation of two-atom wavefunctions

$r_{\text{fit}} \leq r \leq r_{\text{max}}$. Similarly, the boundary conditions at r_0 defining the functions ($\mathbf{X}_i(r)$) can be chosen to be real, which leads to the ($\mathbf{X}_i(r)$)'s being real for $r_0 \leq r \leq r_{\text{max}}$.

The boundary condition (12.27b), defining the functions ($\mathbf{Z}_l(r)$) for $1 \leq l < n_0$, are non-real, and thus lead to non-real solutions. However, each of the complex ($\mathbf{Z}_l(r)$)'s is a linear combination of two *real* functions in \mathcal{E}_{n_0} :

$$\text{For } 1 \leq l < n_0, \quad \mathbf{Z}_l(r) = \mathbf{Z}_l^c(r) + i \mathbf{Z}_l^s(r) \quad , \quad (12.33)$$

where $\mathbf{Z}_l^c(r)$ and $\mathbf{Z}_l^s(r)$ are defined by the following real boundary conditions at r_{max} :

$$\langle D_n | \mathbf{Z}_l^c(r_{\text{max}}) \rangle = \cos(k_l r_{\text{max}}) \delta_{n,l} \quad \text{and} \quad \langle D_n | \mathbf{Z}_l^{c'}(r_{\text{max}}) \rangle = -\sin(k_l r_{\text{max}}) \delta_{n,l} \quad , \quad (12.34a)$$

$$\langle D_n | \mathbf{Z}_l^s(r_{\text{max}}) \rangle = \sin(k_l r_{\text{max}}) \delta_{n,l} \quad \text{and} \quad \langle D_n | \mathbf{Z}_l^{s'}(r_{\text{max}}) \rangle = \cos(k_l r_{\text{max}}) \delta_{n,l} \quad . \quad (12.34b)$$

This remark allows the calculation of the $(n_0 - 1)$ complex functions (\mathbf{Z}_l) $_{1 \leq l < n_0}$ in terms of the $2(n_0 - 1)$ real functions (\mathbf{Z}_l^c) $_{1 \leq l < n_0}$ and (\mathbf{Z}_l^s) $_{1 \leq l < n_0}$.

12.5. Summary

In this chapter, we have presented the two approaches we have used for the numerical calculation of two-atom wavefunctions. Both of them use the accumulated-phase approach (Section 12.2) to encapsulate the short-range physics into a boundary condition applied at a non-zero radius r_0 for which the singlet and triplet potentials are well known.

Our first approach (Section 12.3) is based on the relaxation method for the solution of two-point boundary-value problems (first challenge mentioned in the Introduction). This method is stable and accurate, but it requires a very fine mesh to accommodate for the short-range oscillations of the wavefunction. It is thus ill-suited for problems involving many coupled channels, such as the ones involved in Chapters 14 and 15.

Our second approach (Section 12.4) is based on the shooting method. It is much faster than our relaxation approach. It exploits the linearity of the Schrödinger equation as well as the large- r uncoupling of the dressed two-atom states. It allows for the description of inelastic processes through the calculation of complex wavefunctions. It yields an accurate evaluation of the exponentially-decaying closed-channel components. It requires no iteration: the physical wavefunction is determined as a linear combination of $(N_{\text{states}} + N_{\text{cl}} + 2n_0)$ real solutions of the Schrödinger equation, among which $(N_{\text{cl}} + 2n_0)$ involve a single channel.

Our first method has been used for all numerical calculations presented in the published paper of Chapter 13. These calculations involved at most eight coupled channels.

Chapter 14 is devoted to the characterisation of Feshbach resonances in ^{133}Cs induced by small *static* magnetic fields: this characterisation requires coupled-channel calculations involving up to fourteen coupled channels. Chapter 15 focuses on *microwave*-induced Feshbach resonances involving two ^{133}Cs atoms whose incident state asymptotically belongs to the ($M_F = 0$) subspace. These resonances involve inelastic processes

(and hence non-real wavefunctions), and the corresponding calculations include up to forty-eight coupled channels. Our second method has been used for all numerical calculations presented in both of these chapters.

13. Article 2: Microwave–Induced Fano–Feshbach resonances

Microwave-induced Fano-Feshbach resonances

D. J. Papoular,^{1,*} G. V. Shlyapnikov,^{1,2} and J. Dalibard³

¹Laboratoire de Physique Théorique et Modèles Statistiques, CNRS, Université Paris-Sud, F-91405, Orsay, France

²Van der Waals-Zeeman Institute, University of Amsterdam, Valckenierstraat 65/67, NL-1018 XE Amsterdam, The Netherlands

³Laboratoire Kastler Brossel, CNRS, UPMC, Ecole Normale Supérieure, 24 rue Lhomond, F-75231, Paris, France

(Received 2 October 2009; published 15 April 2010)

We investigate the possibility to control the s -wave scattering length for the interaction between cold bosonic atoms by using a microwave field. Our scheme applies to any atomic species with a ground state that is split by hyperfine interaction. We discuss more specifically the case of alkali-metal atoms and calculate the change in the scattering length for ^7Li , ^{23}Na , ^{41}K , ^{87}Rb , and ^{133}Cs . Our results yield optimistic prospects for experiments with the four latter species.

DOI: [10.1103/PhysRevA.81.041603](https://doi.org/10.1103/PhysRevA.81.041603)

PACS number(s): 03.75.Nt, 37.10.Vz

Cold atomic gases constitute model systems to investigate a wealth of collective quantum phenomena, ranging from few-body physics [1,2] to condensed matter problems [3,4]. In particular one can control the strength of the interparticle interactions using scattering resonances that occur in a collision between two atoms with low energy. These so-called Fano-Feshbach resonances (FFR's) arise when the entrance collision channel, with an energy threshold E_{th} , is coupled to another channel that supports a molecular bound state b at an energy E_b close to E_{th} [1,5–7]. The scattering length that characterizes the s -wave scattering between the two atoms has a dispersive variation with $E_{\text{th}} - E_b$, and can, in principle, be tuned to a value with arbitrary sign and magnitude.

In practice, FFR's are generally obtained by adjusting the external magnetic field. One takes advantage of the degenerate structure of the lowest electronic energy level of the atoms. In the case of alkali-metal atoms that are widely used in cold atom experiments, the degeneracy emerges from the spins of the valence electron and of the nucleus. If the magnetic moment of the bound level b is different from that of the entrance channel, the energy difference $E_{\text{th}} - E_b$ can be tuned by scanning the external field. This leads to a resonant variation of the scattering length, with a width that depends on the coupling between the two channels and hence on the details of the interaction between the colliding atoms. For some atomic species, such as Li, K, or Cs, these magnetic FFR's have been an invaluable tool for many studies related to atom-atom interactions [1–4]. However, the absence of external control on the width of magnetic FFR's and their occurrence only for fixed values of the magnetic field may constitute a serious drawback. For Na atoms (^{23}Na), for example, the identified resonances are in the 1000 G region with a width around 1 G or less [8,9]. Similar values are found for polarized Rb atoms (^{87}Rb) [10]. These large field values and narrow widths severely limit the use of FFR's for these species.

In this Rapid Communication we study an alternative to magnetic FFR's, where the entrance channel is resonantly coupled by a microwave (mw) field to a bound state in another collision channel. All relevant states correspond to the electronic ground level of the atoms, and the resonance

is reached by adjusting the frequency of the mw. The width of the resonance is related to the strength of the magnetic dipole coupling between the two channels and is proportional to the mw intensity. Our scheme is reminiscent of optical FFR's, as proposed in [11] and experimentally demonstrated in [12,13]. There, the bound state b was an electronically excited dimer. Although optical FFR's, which rely on electric rather than magnetic dipole coupling, allow, in principle, stronger resonances, their practical use is limited by the unavoidable losses due to spontaneous emission processes. One can also use a pair of laser beams to coherently couple two states from the ground electronic level [14]. However, for a given change of the scattering length this method leads to a similar spontaneous emission rate as in the case of a single-photon excitation [15]. So far the lifetimes of atomic samples submitted to optical FFR were limited to tens of milliseconds, which is likely to be too short to reach a many-body equilibrium state. By contrast mw-FFR's do not suffer from any spontaneous emission process and the associated loss rates should be comparable to those observed with magnetic FFR's.

So far the use of mw or rf fields has been discussed in relation to manipulating existing FFR's [16–18]. Zhang *et al.* [17] proposed considering magnetic FFR's for atomic states dressed by a two-color Raman process or by an rf field. The idea was to provide an independent control of different scattering lengths in multicomponent gases. The rf coupling of several magnetic FFR's has been studied experimentally and theoretically in [18]. The analysis showed that the main role of rf is to couple the bound states that give rise to these resonances. Our idea of inducing new FFR's by using mw fields brings in a novel physical context. We focus on the case of zero static magnetic field, which is presently put forward in the studies of ground-state properties and quantum phase transitions in spinor Bose gases. Such experiments require extremely low magnetic fields (<10 mG), and the manipulation of the interatomic interactions becomes crucial for the observation of quantum transitions and their dynamics. Our scheme is also different from [16] where a resonant oscillating magnetic field was used to enhance the production of diatomic molecules near an existing FFR. In our case the bound state that is coupled to the entrance channel is only virtually populated, and no molecule is produced in the collision.

*david.papoular@lptms.u-psud.fr

zero. Therefore, W cannot induce any resonance between these two subspaces.

We now consider a resonance between the $M_F = 2i - 1$ subspace (dimension five) and the $M_F = 2i$ subspace. For the bare open-channel wave function we choose the $M_F = 2i - 1$ threshold-energy scattering state $|\Psi_{k=0}^{(2i-1)}\rangle$, in the presence of N photons. For large interatomic separations, this state corresponds to the two-particle state $|f_- f_-, F = 2i - 1, M_F = 2i - 1\rangle$ in which both atoms have $f = m_f = i - 1/2$ (see Fig. 1). The bare closed-channel wave function is chosen in the form $|\Psi_0^{(2i)}\rangle = |\varphi_T, \eta_1\rangle$, where $\varphi_T(r)$ is a bound state of H_T and $|\eta_1\rangle$ is defined previously (see Fig. 1).

The single-resonance two-channel model leads to the usual behavior for the scattering length as a function of the frequency ω close to an FFR resonance

$$a(\omega) = a_{\text{bg}} \left(1 + \frac{\Delta\omega}{\omega - \omega_{\text{res}}} \right). \quad (3)$$

The background scattering length a_{bg} corresponds to a collision in the absence of mw, between two atoms in the state $|f = i - 1/2, m_f = i - 1/2\rangle$. The resonance position is given by $\hbar\omega_{\text{res}} \approx \Delta E_{\text{hf}} - |E_T| + \alpha B_0^2$, where αB_0^2 is a small shift due to the coupling between the open and closed channels [1]. The width $\Delta\omega$ of the mw FFR is

$$\hbar\Delta\omega = \frac{1}{2\pi} \frac{\mu}{a_{\text{bg}}\hbar^2} (\mu_B B_0)^2 |\langle \Psi_0^{(2i)} | S^+ | \Psi_{k=0}^{(2i-1)} \rangle|^2. \quad (4)$$

It is proportional to the mw intensity B_0^2 and to the spin-flip Franck-Condon factor $|\langle \Psi_0^{(2i)} | S^+ | \Psi_{k=0}^{(2i-1)} \rangle|^2$.

For a given atomic species, method (i) requires the calculation of $\Psi_{k=0}^{(2i-1)}(r)$ and $\varphi_T(r)$. We account for the spin-recoupling phenomenon [1] through the coupled-channel method [21], encode the short-range physics in the accumulated-phase boundary condition [19,22], and use the relaxation method [23] to solve the resulting two-point boundary-value differential systems.⁴

We performed calculations for ${}^7\text{Li}$, ${}^{23}\text{Na}$, ${}^{41}\text{K}$, ${}^{87}\text{Rb}$, and ${}^{133}\text{Cs}$. We use the hyperfine splittings reported in [24] and the singlet and triplet potentials from [10,25–34]. The accumulated-phase boundary condition is applied at the radii $r_0 = 10 a_0$ for ${}^7\text{Li}$, $r_0 = 16 a_0$ for ${}^{23}\text{Na}$, ${}^{41}\text{K}$ and ${}^{87}\text{Rb}$, and $r_0 = 20 a_0$ for ${}^{133}\text{Cs}$. We calculate the initial phases of the zero-energy scattering wave functions at r_0 through back-integration using the singlet and triplet scattering lengths [10,27–29,32,35]. The energy derivatives of these phases are taken from [19,28] for ${}^{87}\text{Rb}$ and ${}^{23}\text{Na}$, and are calculated for the other species using the triplet and singlet potentials. Our results are given in Table I. In practice we find that the broadest resonance widths $\Delta\omega$, as given by Eq. (4) are obtained by choosing $\varphi_T(r)$ as the highest bound state of the triplet potential. For all considered atomic species except ${}^{133}\text{Cs}$, this is the resonance we report in Table I. However, in the case of ${}^{133}\text{Cs}$, the highest-energy bound state is so weakly bound ($|E_T| = h5 \text{ kHz}$) that the hyperbolic behavior of a [Eq. (3)] is not valid for $B_0 \gtrsim 1 \text{ mG}$, and we therefore

TABLE I. Characteristics of the mw-FFR in ${}^7\text{Li}$, ${}^{23}\text{Na}$, ${}^{41}\text{K}$, ${}^{87}\text{Rb}$, and ${}^{133}\text{Cs}$ involving the triplet bound states with energies E_T . The width $\Delta\omega$ scales as B_0^2 and is given for $B_0 = 1 \text{ G}$.

	${}^7\text{Li}$	${}^{23}\text{Na}$	${}^{41}\text{K}$	${}^{87}\text{Rb}$	${}^{133}\text{Cs}$
$ E_T /h$ (MHz)	12,000	200	140	25	110
$\omega_{\text{res}}/2\pi$ (GHz)	12	1.6	0.12	6.8	9.1
α (kHz/G ²)	0.33	6.8	21	120	30
$\Delta\omega/2\pi$ (Hz)	6	1400	350	60	–4500

report the resonance obtained with the second-highest bound state of V_T ($|E_T| = h110 \text{ MHz}$).

The largest resonance width is obtained for ${}^{133}\text{Cs}$ (-4500 Hz for $B_0 = 1 \text{ G}$). Relatively large widths are also obtained for ${}^{23}\text{Na}$ and ${}^{41}\text{K}$. In the case of ${}^{87}\text{Rb}$, the singlet and triplet scattering lengths differ by less than 10% [10]. Hence, the near-threshold properties of the singlet and triplet Hamiltonians are similar. The open- and closed-channel wave functions are thus nearly orthogonal, which leads to a reduction of their overlap and to a narrower resonance. For ${}^7\text{Li}$ the triplet scattering length is negative [35] and H_T does not support weakly bound molecular states [1]. The last bound state has a small spatial extent, which leads to an even narrower resonance.

We now turn to method (ii), where we take into account that colliding atoms are asymptotically in dressed atomic states. This method can be used for larger Rabi frequencies, such that $\mu_B B_0 \gtrsim \Delta$. We restrict the full Hamiltonian H to the eight-dimensional subspace spanned by all internal states in the $M_F = 2i + 1$, $2i$, and $2i - 1$ subspaces. For given values of B_0 and ω , we calculate the eight-component scattering state $|\Psi_{B_0,\omega}\rangle$ of H corresponding, for large interatomic separations, to dressed-state atoms with zero kinetic energy. The scattering length $a(B_0, \omega)$ is extracted from the asymptotic behavior of this wave function. For a given $\mu_B B_0 \ll |E_T|$, we checked that we recover the hyperbolic behavior of Eq. (3). We also evaluated the coefficient α giving the shift of the resonance position ω_{res} (see Table I).

Method (ii) allows us to investigate the mw-FFR in ${}^{133}\text{Cs}$ involving the highest bound state of V_T , where Eq. (3) is not applicable for $B_0 \gtrsim 1 \text{ mG}$. To avoid inelastic processes we assume that the atoms are asymptotically in the lowest atomic dressed state. For large $\delta < 0$, this state corresponds to the two-particle state $|f_- f_-, F = 2i - 1, M_F = 2i - 1\rangle$, and therefore $a = a_{\text{bg}} = -2500 a_0$. For large $\delta > 0$ it corresponds to $|f_+ f_+, F = 2i + 1, M_F = 2i + 1\rangle$, with $a_T = 2400 a_0$. For $B_0 \lesssim 1 \text{ mG}$ the resonance is hyperbolic, as predicted by method (i) [see Eq. (3)]. For larger B_0 the scattering length becomes very large for $\hbar\omega \approx \Delta E_{\text{hf}}$, but $a(\omega)$ no longer satisfies Eq. (3). Figure 2 shows how the dependence $a(\omega)$ evolves when B_0 increases from 0.1 mG to 1 G. In the $\delta > 0$ region, collisions between atoms in the “stretched” state $f_+ = m_f = i + 1/2 = 4$ occur with a large inelastic rate because of dipole-dipole interactions [36]. Therefore, one should operate in the $\delta < 0$ region, where the contamination of the collision state by the stretched state is small. A detailed modeling of the large- B_0 FFR’s will be presented elsewhere.

⁴The same approaches were used for method (ii).

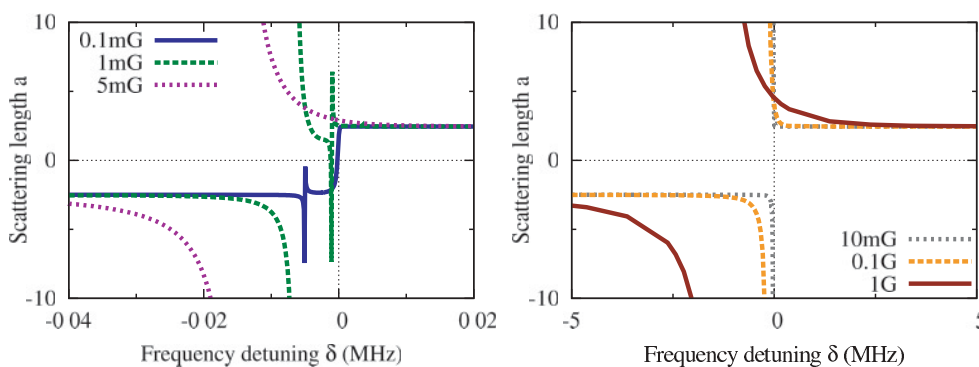


FIG. 2. (Color online) Resonance in ^{133}Cs involving the bound state with energy $|E_T| = h5 \text{ kHz} = \mu_B 4 \text{ mG}$, for B_0 ranging from 0.1 mG to 1 G, calculated using method (ii). The scattering length a is expressed in units of $1000 a_0$.

Our results draw optimistic prospects for modifying the scattering length in atomic gases using a mw field. Using small resonant transmitting loop antennas in the near-field regime, it is possible to reach mw magnetic field amplitudes $B_0 \sim 10 \text{ G}$ in the desired frequency range, while keeping a reasonable incident electromagnetic power (below 10 W). The resonance widths obtained for the hyperbolic resonances in all atomic species except ^7Li are then well above 1 mG, and thus notably exceed typical magnetic field fluctuations in setups with an efficient magnetic shielding. The nonhyperbolic resonance obtained with ^{133}Cs has a width of the order of 1 G for $B_0 = 1 \text{ G}$. Our scheme can be readily transposed to fermionic atoms, multicomponent gases, and heteronuclear

mixtures, and it can allow for a fine tuning of interspecies interactions in all three cases.

We thank M. Köhl, S. Kokkelmans, F. Gerbier, and Z. Hadzibabic for helpful discussions. We are grateful to S. Kokkelmans for providing us with the singlet and triplet electronic potential curves for Rubidium. This work is supported by Région Ile de France IFRAF, by ANR (Grant No. ANR-08-BLAN-65 BOFL), by the EU project SCALA, and by the Dutch Foundation FOM. LPTMS is a mixed research unit No. 8626 of CNRS and Université Paris Sud. LKB is a mixed research unit No. 8552 of CNRS, ENS, and Université Pierre et Marie Curie.

- [1] T. Köhler *et al.*, *Rev. Mod. Phys.* **78**, 1311 (2006).
- [2] E. Braaten and H.-W. Hammer, *Phys. Rep.* **428**, 259 (2006).
- [3] I. Bloch *et al.*, *Rev. Mod. Phys.* **80**, 885 (2008).
- [4] S. Giorgini *et al.*, *Rev. Mod. Phys.* **80**, 1215 (2008).
- [5] C. Chin, R. Grimm, P. Julienne, and E. Tiesinga, *Rev. Mod. Phys.* (to be published), e-print [arXiv:0812.1496](https://arxiv.org/abs/0812.1496).
- [6] A. J. Moerdijk, B. J. Verhaar, and A. Axelsson, *Phys. Rev. A* **51**, 4852 (1995).
- [7] E. Tiesinga, B. J. Verhaar, and H. T. C. Stoof, *Phys. Rev. A* **47**, 4114 (1993).
- [8] S. Inouye *et al.*, *Nature (London)* **392**, 151 (1998).
- [9] J. Stenger *et al.*, *Phys. Rev. Lett.* **82**, 2422 (1999).
- [10] A. Marte *et al.*, *Phys. Rev. Lett.* **89**, 283202 (2002).
- [11] P. O. Fedichev, Y. Kagan, G. V. Shlyapnikov, and J. T. M. Walraven, *Phys. Rev. Lett.* **77**, 2913 (1996).
- [12] M. Theis *et al.*, *Phys. Rev. Lett.* **93**, 123001 (2004).
- [13] K. Enomoto, K. Kasa, M. Kitagawa, and Y. Takahashi, *Phys. Rev. Lett.* **101**, 203201 (2008).
- [14] J. Bohn and P. S. Julienne, *Phys. Rev. A* **60**, 414 (1999).
- [15] G. Thalhammer, M. Theis, K. Winkler, R. Grimm, and J. H. Denschlag, *Phys. Rev. A* **71**, 033403 (2005).
- [16] S. T. Thompson, E. Hodby, and C. E. Wieman, *Phys. Rev. Lett.* **95**, 190404 (2005).
- [17] P. Zhang, P. Naidon, and M. Ueda, *Phys. Rev. Lett.* **103**, 133202 (2009).
- [18] A. Kaufman, R. P. Anderson, T. M. Hanna, E. Tiesinga, P. S. Julienne, and D. S. Hall, *Phys. Rev. A* **80**, 050701(R) (2009).
- [19] B. Verhaar, E. G. M. vanKempen, and S. J. J. M. F. Kokkelmans, *Phys. Rev. A* **79**, 032711 (2009).
- [20] C. Cohen-Tannoudji, J. Dupont-Roc, and G. Grynberg, *Atom-Photon Interactions: Basic Processes and Applications* (Wiley, New York, 1992).
- [21] H. T. Stoof, J. M. V. A. Koelman, and B. J. Verhaar, *Phys. Rev. B* **38**, 4688 (1988).
- [22] B. Verhaar, K. Gibble, and S. Chu, *Phys. Rev. A* **48**, R3429 (1993).
- [23] W. H. Press, S. A. Teukolsky, W. T. Vetterling, and B. P. Flannery, *Numerical Recipes, The Art of Scientific Computing*, 3rd ed. (Cambridge University Press, Cambridge, England, 2007).
- [24] E. Arimondo *et al.*, *Rev. Mod. Phys.* **49**, 31 (1977).
- [25] B. Barakat *et al.*, *Chem. Phys.* **102**, 215 (1986).
- [26] Z.-C. Yan, J. F. Babb, A. Dalgarno, and G. W. F. Drake, *Phys. Rev. A* **54**, 2824 (1996).
- [27] F. Colavecchia *et al.*, *J. Chem. Phys.* **118**, 5484 (2003).
- [28] F. A. van Abeelen and B. J. Verhaar, *Phys. Rev. A* **59**, 578 (1999).
- [29] S. Falke *et al.*, *Phys. Rev. A* **78**, 012503 (2008).
- [30] P. J. Leo, C. J. Williams, and P. S. Julienne, *Phys. Rev. Lett.* **85**, 2721 (2000).
- [31] C. Amiot and O. Dulieu, *J. Chem. Phys.* **117**, 5155 (2002).
- [32] C. Chin *et al.*, *Phys. Rev. A* **70**, 032701 (2004).
- [33] N. Vanhaecke *et al.*, *Eur. Phys. J. D* **28**, 351 (2004).
- [34] F. Xie *et al.*, *J. Chem. Phys.* **130**, 051102 (2009).
- [35] E. R. I. Abraham *et al.*, *Phys. Rev. A* **55**, R3299 (1997).
- [36] J. Söding, D. Guery-Odelin, P. Desbiolles, G. Ferrari, and J. Dalibard, *Phys. Rev. Lett.* **80**, 1869 (1998).

14. Static–Field Feshbach resonances

In this chapter, we temporarily steer away from microwave–induced Feshbach resonances (we will return to these in Chapter 15) and turn to resonances induced by *static* magnetic fields. These static–field Feshbach resonances have been extensively studied, both theoretically and experimentally, in the context of ultracold atomic systems [7, 53–55].

The first section is introductory: it recalls the structure of the Hamiltonian governing collisions in a static magnetic field, and the parameters characterising a static–field Feshbach resonances. In the second section, we focus on Feshbach resonances that have previously been studied, and we show that our numerical calculations recover the published parameters characterising these resonances. The third, and main section of this chapter is devoted to the theoretical description of Feshbach resonances that have been observed in Cesium for very small magnetic fields. To our knowledge, these observations had remained unexplained. Our numerical results show that these resonances are due to *s*–wave collisions and suggest that they involve the highest–energy bound state ($|E_T| = h \cdot 5 \text{ kHz}$) of the triplet electronic potential. This interpretation of the SYRTE measurements makes it possible to view them as experimental evidence for the existence of the very weakly bound triplet state in ^{133}Cs , which is involved in the resonances described in Section 11.2.4 and in Chapter 15.

14.1. Two atoms in a static magnetic field

We consider a collision between two bosonic alkali atoms in the presence of a *static* magnetic field \mathbf{B}_{stat} . *No oscillating magnetic field is added to the setup*: throughout this Chapter, we assume $B_{\text{osc}} = 0$. Consequently, the radial Hamiltonian (10.13) reduces to:

$$H = \frac{p_r^2}{2m_r} \mathbb{1} + V_{\text{el}}(r) + V_{\text{hf}} + V_Z \quad . \quad (14.1)$$

We call \mathbf{e}_z the direction of the static magnetic field: $\mathbf{B}_{\text{stat}} = B_{\text{stat}} \mathbf{e}_z$. As explained in Section 10.3.1, the Hamiltonian H of Eq. (14.1) commutes with F_z . Thus, two–atom internal–state subspaces corresponding to different values of the quantum number M_F are rigorously uncoupled. The Zeeman term V_Z does not commute with \mathbf{F}^2 , therefore, within each (M_F) subspace, the (F, M_F) sub–blocks are coupled to each other.

The uncoupling property of the previous paragraph can be read graphically off the block–matrix representation of the complete Hamiltonian (10.13) in the ‘molecular’ basis \mathbf{e}_M , shown on Fig. 10.5. The absence of an oscillating magnetic field ($B_{\text{osc}} = 0$) causes the blue blocks (corresponding to the magnetic dipole coupling W) to vanish; hence the black blocks, each corresponding to a given value of M_F , are uncoupled. Within each

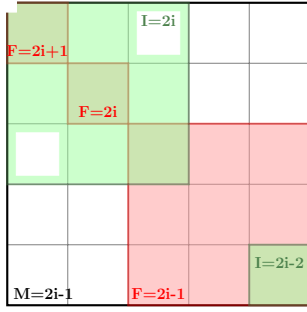


Figure 14.1. Block-matrix structure of the Hamiltonian describing the collision of two atoms in the presence of a static magnetic field B_{stat} , but *no oscillating field* ($B_{\text{osc}} = 0$). We assume that the atoms are initially in a ‘Zeeman-dressed’ two-atom state belonging to the $M_F = (2i - 1)$ subspace (5 coupled channels).

(black) (M_F) block, the (red) (F, M_F) sub-blocks are still coupled to each other by the green blocks, corresponding to the Zeeman term V_Z .

The coupling term V_Z may cause scattering resonances for specific values B_{res} of the static magnetic field. These resonances are the ‘standard’ static-field Fano-Feshbach resonances that have extensively been investigated in ultracold atomic systems, both theoretically and experimentally [7]. Neglecting inelastic collisions, the variation of the scattering length $a(B_{\text{stat}})$ exhibits a hyperbolic divergence for values of the static field B_{stat} close to the resonance position B_{res} :

$$a(B_{\text{stat}}) = a_{\text{bg}} \left(1 - \frac{\Delta B}{B_{\text{stat}} - B_{\text{res}}} \right), \quad (14.2)$$

where a_{bg} is the background scattering length and ΔB is the resonance width.

14.2. Recovering known Feshbach resonance results

Our coupled-channel programs allow us to recover the published parameters for previously studied (*s*-wave) static-field resonances. We illustrate this on the particular example of the resonances involving a pair of atoms which is asymptotically in the lowest-energy ‘Zeeman-dressed’ state, *i.e.* the one relating to both atoms having the quantum numbers $f = m_f = i - 1/2$ in the absence of the static magnetic field. Note that, throughout this chapter, the ‘*Zeeman dressing*’ of the two-atom states is due to the presence of the static magnetic field B_{stat} through the Zeeman term V_Z (in contrast to the *microwave dressing* of the two-atom states, due to the photon-energy and magnetic dipole terms ($\hbar\omega a^\dagger a + W$), encountered in Chapter 11).

The ‘bare’ two-atom state $|f^-, m_f = i - 1/2; f^-, m_f = i - 1/2\rangle$ belongs to the ($M_F = 2i - 1$) subspace. The uncoupling presented in Section 14.1 shows that the relevant scattering process is described by the restriction of H to this (stable) subspace. The block-matrix structure of the restricted Hamiltonian is shown on Fig. 14.1: it involves five coupled channels.

We have calculated the scattering length $a(B_{\text{stat}})$ numerically, using the coupled-channel method, for ${}^7\text{Li}$, ${}^{23}\text{Na}$, ${}^{41}\text{K}$, and ${}^{87}\text{Rb}$ (nuclear spin $i = 3/2$), and ${}^{133}\text{Cs}$ (nuclear spin $i = 7/2$). Our results, obtained with the ‘shooting’-based approach described in Section 12.4, are plotted on Figs. 14.2. These results are in good agreement with the resonance parameters B_{res} , ΔB , and a_{bg} , collected in [7] and reproduced in Table 14.1.

14.2. Recovering known Feshbach resonance results

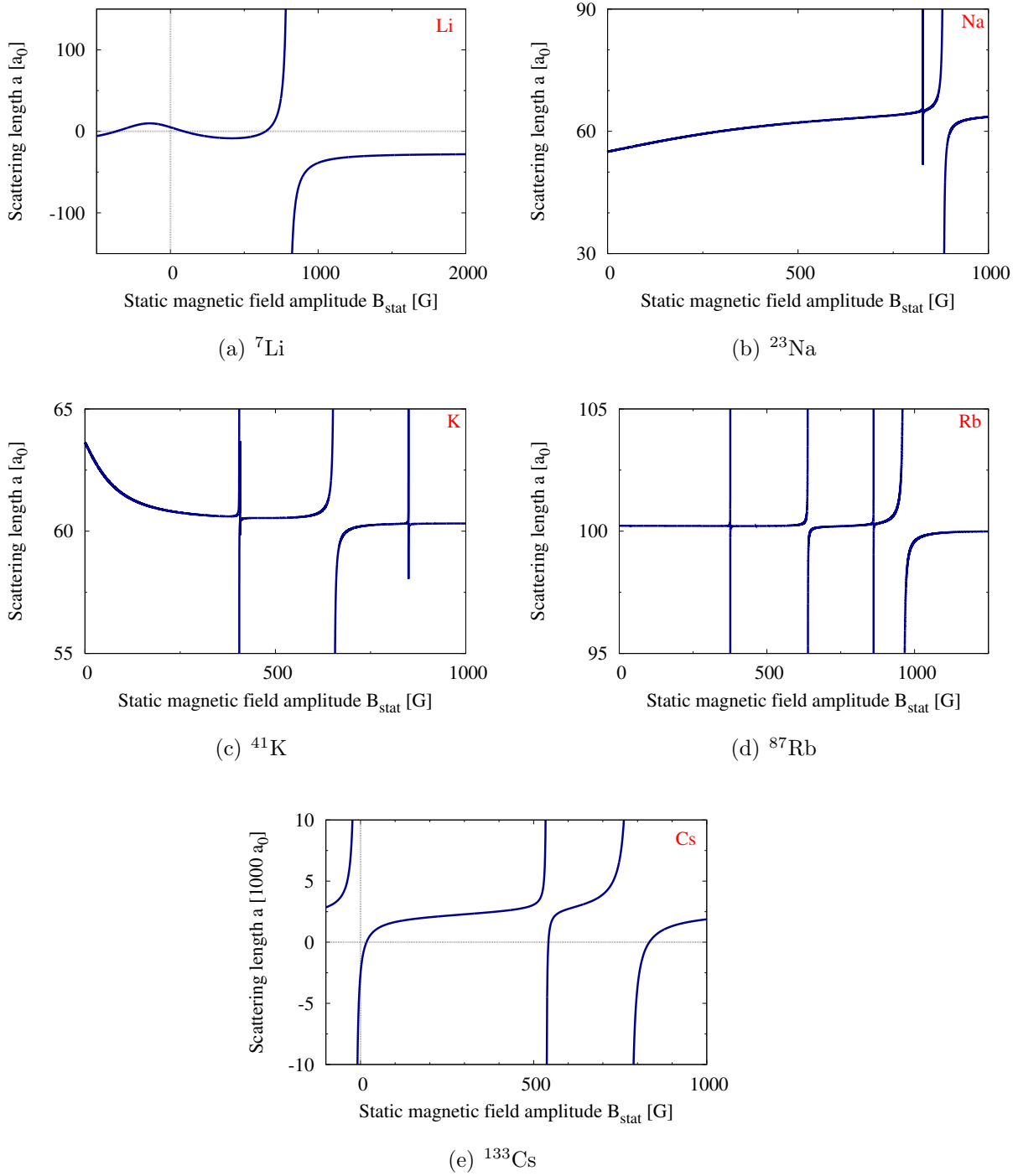


Figure 14.2. *Static-field Fano-Feshbach resonances in ${}^7\text{Li}$, ${}^{23}\text{Na}$, ${}^{41}\text{K}$, ${}^{87}\text{Rb}$, and ${}^{133}\text{Cs}$, as calculated with the ‘shooting’ approach. Our results are in good agreement with the published values in [7] and [56] (see Table 14.1).*

14. Static-Field Feshbach resonances

	B_{res} (G)	ΔB (G)	a_{bg} (a_0)
${}^7\text{Li}$	736.8	-192.3	-25
${}^{23}\text{Na}$	907 853	1 $2.5 \cdot 10^{-3}$	63 63
${}^{41}\text{K}$	856.8 661.2 409.6	$2 \cdot 10^{-3}$ 0.2212 $7.775 \cdot 10^{-3}$	(n/a) (n/a) (n/a)
${}^{87}\text{Rb}$	1007.4 911.7 685.4 406.2	0.21 $1.3 \cdot 10^{-3}$ $6 \cdot 10^{-3}$ $0.4 \cdot 10^{-3}$	100 100 100 100
${}^{133}\text{Cs}$	800 547 -11.7	87.5 7.5 28.7	1940 2500 1720

Table 14.1. Published values for the resonance parameters B_{res} , ΔB , and a_{bg} , for the s -wave resonances involving two atoms in the lowest-energy hyperfine-Zeeman state, relating to both atoms having $f^- = m_f = i - 1/2$ for $B_{\text{stat}} = 0$. (the resonance parameters for ${}^{41}\text{K}$ are reproduced from [56], those for the other atomic species are taken from [7]).

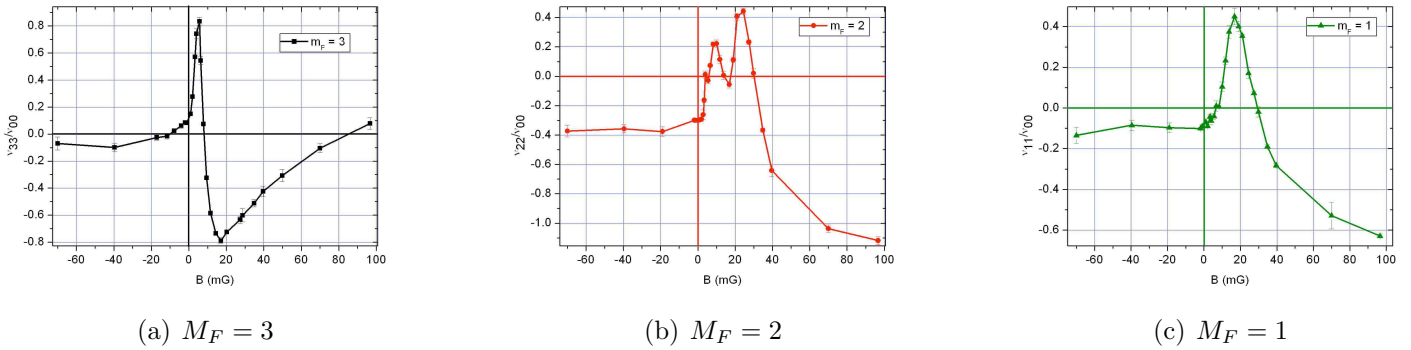


Figure 14.3. Low static-field resonances measured at SYRTE with ${}^{133}\text{Cs}$ atoms in the two hyperfine states $|f = 4, m_f = 0\rangle$ and $|f = 3, M\rangle$, with $M = 3, 2$, or 1 . For each value of M , the plot represents the measured clock shift as a function of the static magnetic field amplitude. (Reproduced from [57].)

14.3. Low static-field resonances in Cesium

The SYRTE group (Observatoire de Paris) has reported [57] the observation of Feshbach resonances in ${}^{133}\text{Cs}$ for small static magnetic fields ($B_{\text{stat}} \approx$ tens of mG), in systems containing atoms in two different hyperfine states: the clock state $|f = 4, m_f = 0\rangle$, and $|f = 3, m_f = M\rangle$ with $M = 3, 2$, or 1 . To the knowledge of the SYRTE researchers, these observations have remained unexplained.

We have reproduced these Feshbach resonances numerically. In this section, we present our numerical results and justify that the resonances observed at SYRTE are s -wave resonances involving the highest bound state of the triplet potential (binding energy $|E_T| = h \cdot 5$ kHz).

14.3.1. The relevant coupled channels

For a given value of M , the ‘bare’ two-atom state $|\{f^+, m_{f_1} = 0; f^-, m_{f_2} = M\}^+\rangle$ belongs to the $(M_F = M)$ subspace. Thanks to the decoupling described in Section 14.1, the scattering process which gives rise to the resonances of Figs. 14.3 is thus described by the restriction of the Hamiltonian (14.1) to the (stable) $(M_F = M)$. The block-matrix structure of the restricted Hamiltonian is represented on Figs. 14.4 for $M = 3, 2$, and 1. The $(M_F = 3)$ subspace contains 10 channels coupled by V_Z , the $(M_F = 2)$ subspace contains 13 coupled channels, and the $(M_F = 1)$ subspace contains 14 channels.

14.3.2. Choice of the incident ‘Zeeman-dressed’ two-atom state

For the sake of clarity, we focus in this section on the resonances involving the $(M_F = 3)$ subspace, but the argument we present is also directly applicable to resonances involving the $(M_F = 2)$ and $(M_F = 1)$ subspaces.

As explained in Section 12.1.3, we choose the incident two-atom state to be a ‘Zeeman-dressed’ two-atom state, *i.e.* an eigenstate of the operator V_∞ defined by Eq. (12.2). In the absence of an oscillating magnetic field ($B_{\text{osc}} = 0$), the operator V_∞ reduces to:

$$V_\infty = V_{\text{tot}}(r \rightarrow \infty) = V_{\text{hf}} + V_Z \quad . \quad (14.3)$$

We order the Zeeman-dressed states¹ $\{|D_1^{M_F=3}\rangle, \dots, |D_{10}^{M_F=3}\rangle\}$ by increasing energies $\varepsilon_1^{M_F=3} \leq \dots \leq \varepsilon_{10}^{M_F=3}$. We seek the Zeeman-dressed state $|D_n^{M_F=3}\rangle$ which relates, in the absence of any magnetic field, to the ‘bare’ two-atom state $|\{f^+, m_1 = 0; f^-, m_2 = 3\}^+\rangle$.

Our numerical calculations are performed using the exact Zeeman-dressed states and energies obtained through the diagonalisation of V_∞ within the subspace $(M_F = 3)$. In order to relate these Zeeman-dressed states to the separated-atom states $|\{f_1, m_1; f_2, m_2\}^+\rangle$, we now sketch a perturbative approach, considering V_Z as a small coupling term².

The bare two-atom internal states $|\{f_1, m_1; f_2, m_2\}^+\rangle$ belonging to the $(M_F = 3)$ subspace can be grouped in three categories:

- 3 states have both atoms in the hyperfine state f^+ (f^+f^+);
- 5 states have one atom in f^+ and the other in f^- (f^+f^-);
- 2 states have both atoms in the hyperfine state f^- (f^-f^-).

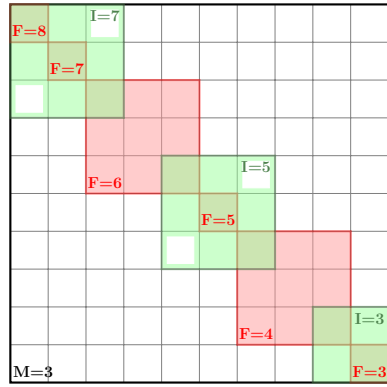
In the absence of any magnetic field, all states within each of these three groups are degenerate, and their energies are related to the hyperfine energy ΔE_{hf} :

$$E_{f^+f^+} = E_{f^+f^-} + \Delta E_{\text{hf}} = E_{f^-f^-} + 2\Delta E_{\text{hf}} \quad . \quad (14.4)$$

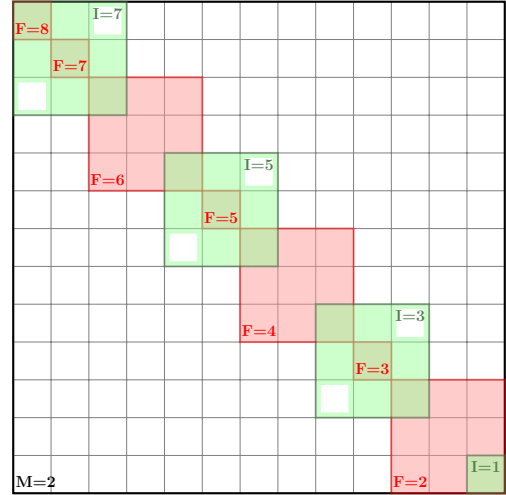
¹The Zeeman-dressed states $|D_j^{M_F}\rangle$, and the corresponding energies $\varepsilon_j^{M_F}$, depend both on the total spin projection M_F and on the magnetic field amplitude B_{stat} .

²The perturbative approach is licit, as the Zeeman term is of the order of $\mu_B \cdot 10 \text{ mG} \approx h \cdot 10 \text{ kHz}$, whereas the hyperfine term is of the order of $a_{\text{hf}} \approx h \cdot 10 \text{ GHz}$.

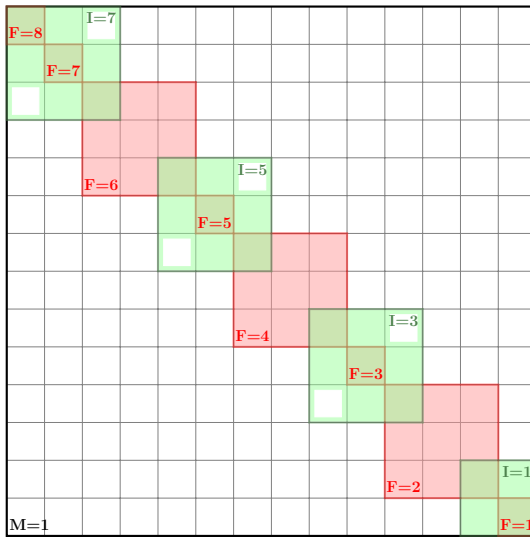
14. Static-Field Feshbach resonances



(a) $M_F = 3$



(b) $M_F = 2$



(c) $M_F = 1$

Figure 14.4. Block matrix structure of the Hamiltonians describing the collision of two atoms in the presence of a static magnetic field B_{stat} , but *no oscillating magnetic field* ($B_{\text{osc}} = 0$). We assume that the atoms are initially in a ‘Zeeman-dressed’ two-atom state belonging to a given (M_F) subspace, with M_F respectively equal to 3 (10 coupled channels), 2 (13 coupled channels), and 1 (14 coupled channels).

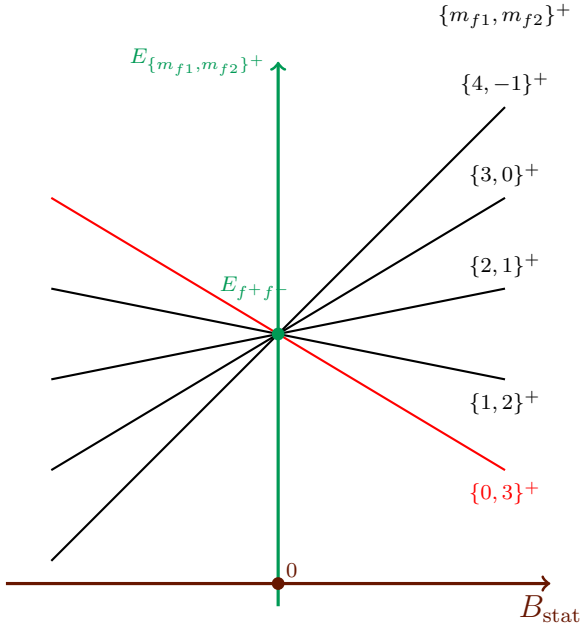


Figure 14.5. Degeneracy lifting, by the Zeeman term V_Z , between the states $|\{f^+, m_{f1}; f^-, m_{f2}\}^+\rangle$ of the subspace ($M_F = 3$), for small static magnetic fields B_{stat} . The incident state $|\{f^+, m_{f1} = 0; f^-, m_{f2} = 3\}^+\rangle$ is represented in red.

For the range of magnetic field amplitudes considered here ($B_{\text{stat}} \approx 10$ mG), the Zeeman term V_Z is always much smaller than the hyperfine energy ΔE_{hf} , therefore the three hyperfine groups ($f^+ f^+$), ($f^+ f^-$), and ($f^- f^-$) are not mixed by V_Z .

The ‘bare’ incident two-atom state $|\{f^+, m = 0; f^-, m = 3\}^+\rangle$ belongs to the ($f^+ f^-$) group. We are thus interested in the leading-order degeneracy lifting of the five ($f^+ f^-$) states due to $V_Z = 2\mu_B B_{\text{stat}} S_z$. Recalling that the operator S_z conserves the quantum number M_F , a direct calculation shows that the restriction of V_Z to the ($f^+ f^-$) group is diagonal:

$$\langle \{f^+, m_1; f^-, m_2\}^+ | V_Z | \{f^+, m'_1; f^-, m'_2\}^+ \rangle = \delta_{m_1, m'_1} \delta_{m_2, m'_2} (2\mu_B B_{\text{stat}}) \frac{m_1 - m_2}{2i + 1}, \quad (14.5)$$

where $i = 7/2$ is the nuclear spin of a single ^{133}Cs atom. Standard perturbation theory [25] applied to the degenerate energy levels in the ($f^+ f^-$) group shows that, to leading order in B_{stat} , the sought Zeeman-dressed states are the separated-atom states $|\{f^+, m_1; f^-, m_2\}^+\rangle$, and that the dependence of the Zeeman-dressed energies on B_{stat} is given by:

$$E_{\{f^+, m_1; f^-, m_2\}^+} = E_{f^+ f^-} + (2\mu_B B_{\text{stat}}) \frac{m_1 - m_2}{2i + 1}. \quad (14.6)$$

The degeneracy lifting of the ($f^+ f^-$) states due to V_Z is illustrated on Fig. 14.5. This figure shows that the Zeeman-dressed state relating to the ‘bare’ incident state $|\{f^+, m_1 = 0; f^-, m_2 = 3\}^+\rangle$ depends on the sign of the static magnetic field B_{stat} : for $B_{\text{stat}} > 0$, it is the lowest-energy Zeeman-dressed state in the ($f^+ f^-$) group, which is³ $|D_3^{M_F=3}\rangle$, whereas for $B_{\text{stat}} < 0$, it is the highest-energy Zeeman-dressed state in the ($f^+ f^-$) group, which is $|D_7^{M_F=7}\rangle$.

³The two lowest-energy dressed states relate to the two bare states in the ($f^- f^-$) group.

14. Static-Field Feshbach resonances

Similar arguments allow us to identify the incident states $|\{f^+, m = 0; f^-, m = M\}^+\rangle$, $M = 2$ or 1 , with the relevant Zeeman-dressed states $|D_j^{M_F}\rangle$ in the ($M_F = 2$) subspace and the ($M_F = 1$) subspace. For all three considered values of M , the relevant Zeeman-dressed state depends on the sign of B_{stat} . Furthermore, the incident Zeeman-dressed state never is the lowest-energy dressed state, as the Zeeman-dressed states relating to the ($f^- f^-$) group have lower energies: therefore, the atom pair may undergo inelastic decay into lower-energy channels.

14.3.3. Numerical results and interpretation

The magnetic-field dependence of the scattering lengths characterising the collisions defined above ($M = 3, 2$, or 1), obtained numerically using our ‘shooting’-based coupled-channel program (Section 12.4), is represented on Figs. 14.6. These graphs reveal the presence of Feshbach resonances, whose calculated positions are compared to the positions measured by SYRTE [57] in Table 14.2. In all three cases, our predictions for the positions of the widest resonances are in good agreement with the measured positions. Our results reveal the existence of additional, as yet unobserved, narrow resonances.

Resonance positions B_{res} [mG]					
$M_F = 1$		$M_F = 2$		$M_F = 3$	
measured	calculated	measured	calculated	measured	calculated
	-11 ± 5				
	2.7		4.0		3.0
	5.1	8	7.2		4.2
18 ± 3	16.5	25	22	5 ± 1	5.5

Table 14.2. Comparison between the resonance positions measured by SYRTE and those calculated using our coupled-channel code. Our numerical results show four resonances in the $M_F = 1$ subspace, three in the $M_F = 2$ subspace, and three in the $M_F = 3$ subspace, in agreement with the expected number of resonances in each subspace (see text).

The Hamiltonian (14.1), used in our coupled-channel calculations, conserves the total angular momentum ℓ^2 (see Section 10.2.3). It does not contain any centrifugal term and thus corresponds to s -wave collisions ($\ell = 0$). Our numerical results reproduce the observed resonances, which proves that the latter are due to s -wave collisions.

The scattering lengths $a(B_{\text{stat}})$ plotted on Figs. 14.6 are non-real. Furthermore, the calculated resonances do not yield hyperbolic divergences of a , but rather a smooth, dispersive variation. Both of these features are signatures of the occurrence of inelastic collisions. These inelastic processes were expected to take place (see Section 14.3.2) because of the presence of the lower-energy Zeeman-dressed states relating to the ($f^- f^-$) group.

Within a given (M_F) subspace, the closed channels yielding the observed small-field resonances are likely to be the states $|\varphi_T\rangle|\{f^+ f^-\}^+, F, M_F\rangle$, F odd, where $|\varphi_T\rangle$

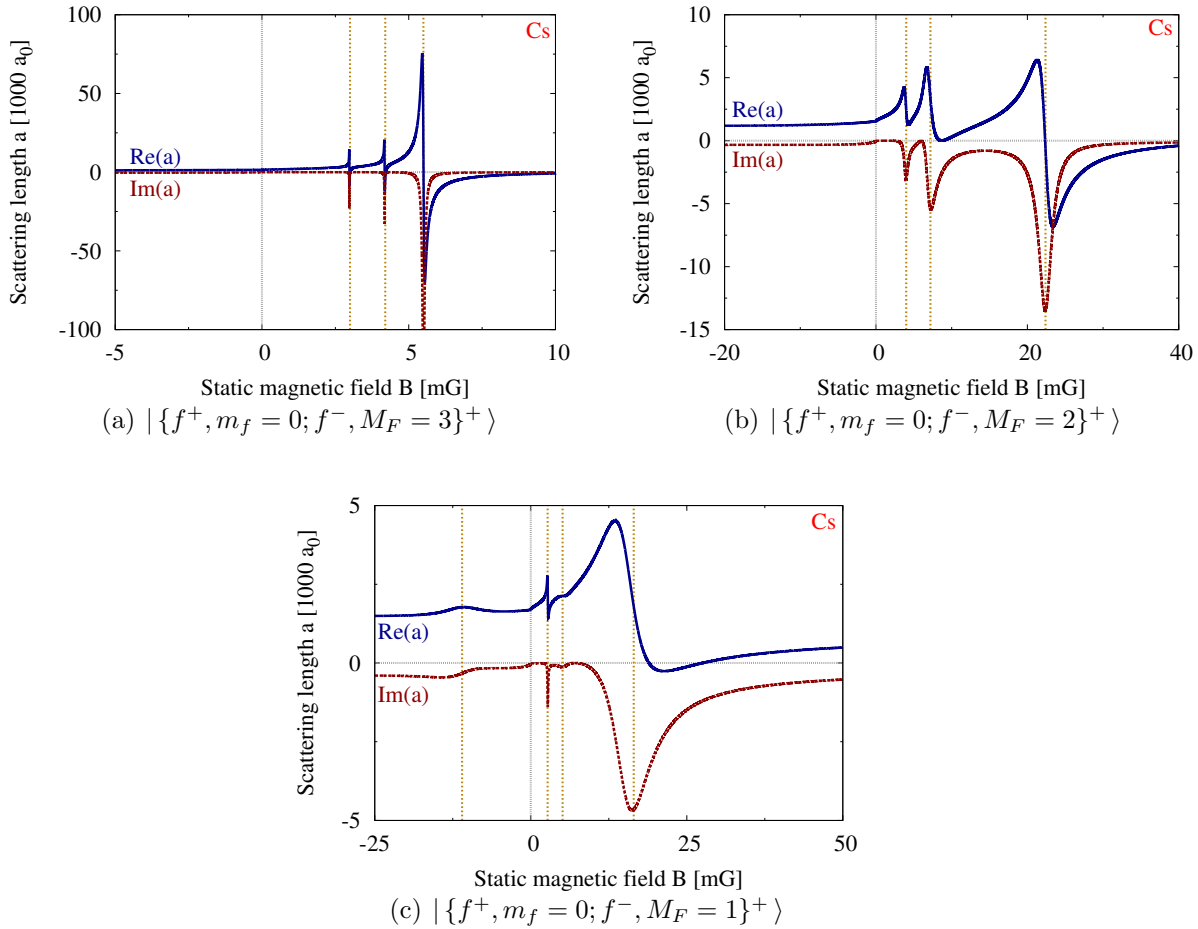


Figure 14.6. Feshbach resonances in Cesium in low static magnetic fields. The incident atoms are asymptotically in the two-atom Zeeman-dressed states relating to $|f^+, m_{f1} = 0\rangle$ and $|f^-, m_{f2}\rangle$, with $m_{f2} = 3, 2$, or 1 , corresponding to the three Hamiltonians whose block-matrix representations are shown in Figs. 14.4. The resonance positions are highlighted by golden dashed lines.

14. Static-Field Feshbach resonances

is the spatial wavefunction of the highest-energy triplet bound state (binding energy $|E_T| = h \cdot 5 \text{ kHz}$) and the internal-state ket describes a two-atom state which is purely electronic-triplet (see Section 10.3.3). This statement is supported by the following two observations:

- Our calculations show no similar resonances in ^{87}Rb , which does not have a very weakly-bound triplet state (for ^{87}Rb , the binding energy of the highest triplet bound state is $|E_T| = h \cdot 25 \text{ MHz}$ [58]);
- The observed resonance positions are of the order of $|E_T|/\mu_B = 4 \text{ mG}$.

For a given value of M_F , there are as many resonances as there are different internal states of the form $|\{f^+, f^-\}^+, F, M_F\rangle$, F odd. The total spin F results from the coupling of two atomic spins \mathbf{f}_1 and \mathbf{f}_2 having the quantum numbers $f^+ = i + 1/2 = 4$ and $f^- = i - 1/2 = 3$ respectively, and it must therefore satisfy $M_F \leq F \leq 2i = 7$. Furthermore, F must be odd in order to ensure the bosonic symmetry of the two-atom internal states. Consequently, four resonances are expected for $M_F = 1$ ($F = 7, 5, 3, 1$), whereas there are only three resonances for $M_F = 2$ and $M_F = 3$ ($F = 7, 5, 3$). The variation $a(B_{\text{stat}})$ of the scattering length a as a function of the magnetic field B_{stat} , shown on Figs. 14.6, exhibits the expected number of resonances in all three M_F subspaces.

15. Towards an experimental observation of our predictions

The microwave-induced resonances characterised in Chapter 11 are those whose theoretical description is the simplest: they can be modelled in terms of a small number of coupled channels, and they do not involve inelastic processes. However, these are not the resonances which are the most readily accessible experimentally.

An experimental study of the microwave-induced resonances in ^{133}Cs is likely to be performed soon using the Cesium fountain clocks set up at SYRTE—Observatoire de Paris. The experimental parameters in these fountain clocks differ from the conditions considered in Chapter 11 in three respects:

1. A small homogeneous static magnetic field is present in the experimental setup;
2. The microwave source is π -polarised (rather than circularly polarised);
3. The atoms are most easily prepared in the lowest-energy hyperfine state having zero spin projection along the axis defined by the static field.

In this chapter, we characterise the microwave-induced resonances occurring in ^{133}Cs due to the very weakly-bound triplet dimer state in the experimental conditions listed above. The description of these resonances requires a larger number of coupled channels, and inelastic processes must be accounted for.

We start by recalling the dependence of the magnetic dipole coupling on the polarisation of the oscillating magnetic field. Then, assuming that no static magnetic field is present, we determine the microwave-dressed two-atom state which relates to the bare two-atom state mentioned above. We present a plot of the dependence of the (complex) scattering length $a(\omega)$ in the frequency range for which the weakly-bound triplet state is expected to be resonant, and we qualitatively explain many of the features of this plot. Finally, we include the effect of an additional small static magnetic field along the quantisation axis, and we show that this static field only has a small qualitative impact on the microwave-induced resonances.

15.1. Two atoms in a linearly-polarised magnetic field

Up to Chapter 13, we had only considered microwave-induced resonances caused by circularly-polarised magnetic fields. In the present chapter, we abandon circularly-polarised fields and turn to a linearly-polarised magnetic field, whose direction is par-

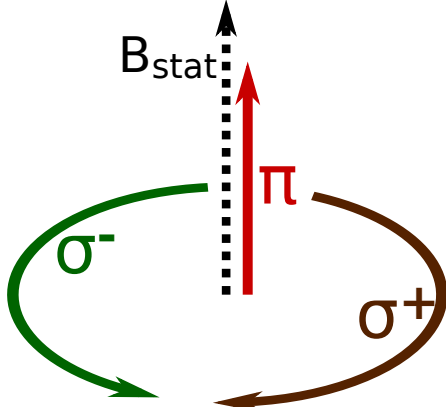


Figure 15.1. The three basis polarisations for the oscillating magnetic field in the presence of a static field component $\mathbf{B}_{\text{stat}} = B_{\text{stat}}\mathbf{e}_z$. The π polarisation is linear and parallel to \mathbf{B}_{stat} . The σ^+ and σ^- polarisations are circular and correspond to fields that rotate counter-clockwise and clockwise about \mathbf{B}_{stat} , respectively.

allel to the ambient static magnetic field. In this section, we describe the Hamiltonian modelling an ultracold collision between two atoms in this magnetic field configuration.

15.1.1. Magnetic field polarisation and magnetic dipole coupling

We choose the unit vector \mathbf{e}_z to be along the quantisation axis. In the absence of a static magnetic field, as was the case in Chapter 11, the choice of the quantisation axis is arbitrary. However, in this chapter, we will consider non-zero static field components \mathbf{B}_{stat} , and we choose the quantisation axis to be (positively) parallel to the static magnetic field: $\mathbf{e}_z = \mathbf{B}_{\text{stat}}/B_{\text{stat}}$.

The magnetic dipole coupling W term depends on the polarisation $\boldsymbol{\varepsilon}$ of the magnetic field \mathbf{B}_{osc} . In the general case, $\boldsymbol{\varepsilon}$ is a three-component unit vector with complex coefficients, which can be expressed in the polarisation basis $(\boldsymbol{\varepsilon}_{\sigma^+}, \boldsymbol{\varepsilon}_{\sigma^-}, \boldsymbol{\varepsilon}_{\pi})$, where the three (complex) unit basis vectors are defined by:

$$\boldsymbol{\varepsilon}_{\sigma^+} = (\mathbf{e}_x + i\mathbf{e}_y)/\sqrt{2} \quad (\sigma^+ \text{ circular polarisation}) \quad (15.1a)$$

$$\boldsymbol{\varepsilon}_{\sigma^-} = (\mathbf{e}_x - i\mathbf{e}_y)/\sqrt{2} \quad (\sigma^- \text{ circular polarisation}) \quad (15.1b)$$

$$\boldsymbol{\varepsilon}_{\pi} = \mathbf{e}_z \quad (\pi \text{ linear polarisation}). \quad (15.1c)$$

The three basis polarisations of Eqs. (15.1) are illustrated on Fig. 15.1: the polarisations $\boldsymbol{\varepsilon}_{\sigma^+}$ and $\boldsymbol{\varepsilon}_{\sigma^-}$ are circular polarisations about the quantisation axis \mathbf{e}_z , whereas the polarisation $\boldsymbol{\varepsilon}_{\pi}$ is linear and parallel to \mathbf{e}_z .

The magnetic dipole coupling terms W corresponding to the basis polarisations of Eqs. (15.1) read [59]:

$$W_{\sigma^+} = w_1 (S^+a + S^-a^\dagger) \quad (15.2a)$$

$$W_{\sigma^-} = w_1 (S^-a + S^+a^\dagger) \quad (15.2b)$$

$$W_{\pi} = \sqrt{2} w_1 S_z (a + a^\dagger) \quad (15.2c)$$

The coupling term used in chapters 11 and 13 is W_{σ^+} , which expresses that the atom pair may *absorb* one photon, in which case the total spin projection M_F *increases* by one unit, or *emit* a photon, in which case the total spin projection *decreases* by one

unit. These processes enforce the conservation of angular momentum, as σ^+ -polarised photons carry one unit of angular momentum along \mathbf{e}_z .

In this chapter, we focus on the π -polarised case: the coupling term W_π expresses that the atom pair may *absorb* or *emit* a photon, and that *neither of these processes causes a change in the total spin projection*. These two latter processes are also compatible with the conservation of angular momentum, as π -polarised photons carry no angular momentum.

15.1.2. Hamiltonian and relevant coupled channels

The Hamiltonian describing two atoms in the presence of a π -polarised magnetic field is similar to Eq. (10.9), where the coupling operator W is replaced by W_π . In its radial s -wave form, it reads:

$$H = \frac{p_r^2}{2m_r} \mathbb{1} + V_{\text{el}}(r) + V_{\text{hf}} + V_Z + \hbar\omega a^\dagger a + W_\pi \quad . \quad (15.3)$$

We assume that the two incident atoms are in the (dressed state relating to the) ‘bare’ two-atom state $|f^-, m_f = 0; f^-, m_f = 0\rangle$, in the presence of N photons whose frequency is close to the hyperfine energy ΔE_{hf} . This ‘bare’ incident state belongs to the $(M_F = 0, N \text{ photons})$ subspace. Being in their lowest-energy hyperfine state f^- , each of the two atoms may absorb one photon, but neither may emit a photon. Hence, the coupling term W connects the ‘incident’ subspace $(M_F = 0, N \text{ photons})$ subspace to the $(M_F = 0, N - 1 \text{ photons})$ and $(M_F = 0, N - 2 \text{ photons})$ subspaces, through the absorption of a single photon, and of a photon by each atom, respectively. The block-matrix structure, in the ‘molecular’ basis \mathbf{e}_M , of the restriction of the Hamiltonian to these three subspaces is represented on Fig. 15.2. The $(M_F = 0)$ blocks corresponding to different photon numbers are distinct, therefore the restricted Hamiltonian operates on $N_{\text{states}} = 3 \times 16 = 48$ coupled channels.

15.2. In the absence of a static magnetic field

In this section, we assume that the magnetic field has no static component ($B_{\text{stat}} = 0$). The effect of an additional static component will be presented in Section 15.3.

In the absence of a static magnetic field, the quantisation axis \mathbf{e}_z is defined by the direction of the linearly-polarised oscillating magnetic field \mathbf{B}_{osc} .

15.2.1. Choice of the incident dressed two-atom state

As explained in Section 12.1.3, we choose the incident state of the two atoms, in the presence of the magnetic field, to be a ‘dressed’ two-atom state, *i.e.* one of the $N_{\text{states}} = 48$ eigenstates of the symmetric matrix V_∞ , defined by Eq. (12.2):

$$V_\infty = V_{\text{tot}}(r \rightarrow \infty) = V_{\text{hf}} + V_Z + \hbar\omega a^\dagger a + W_\pi \quad . \quad (12.2)$$

15. Towards an experimental observation of our predictions

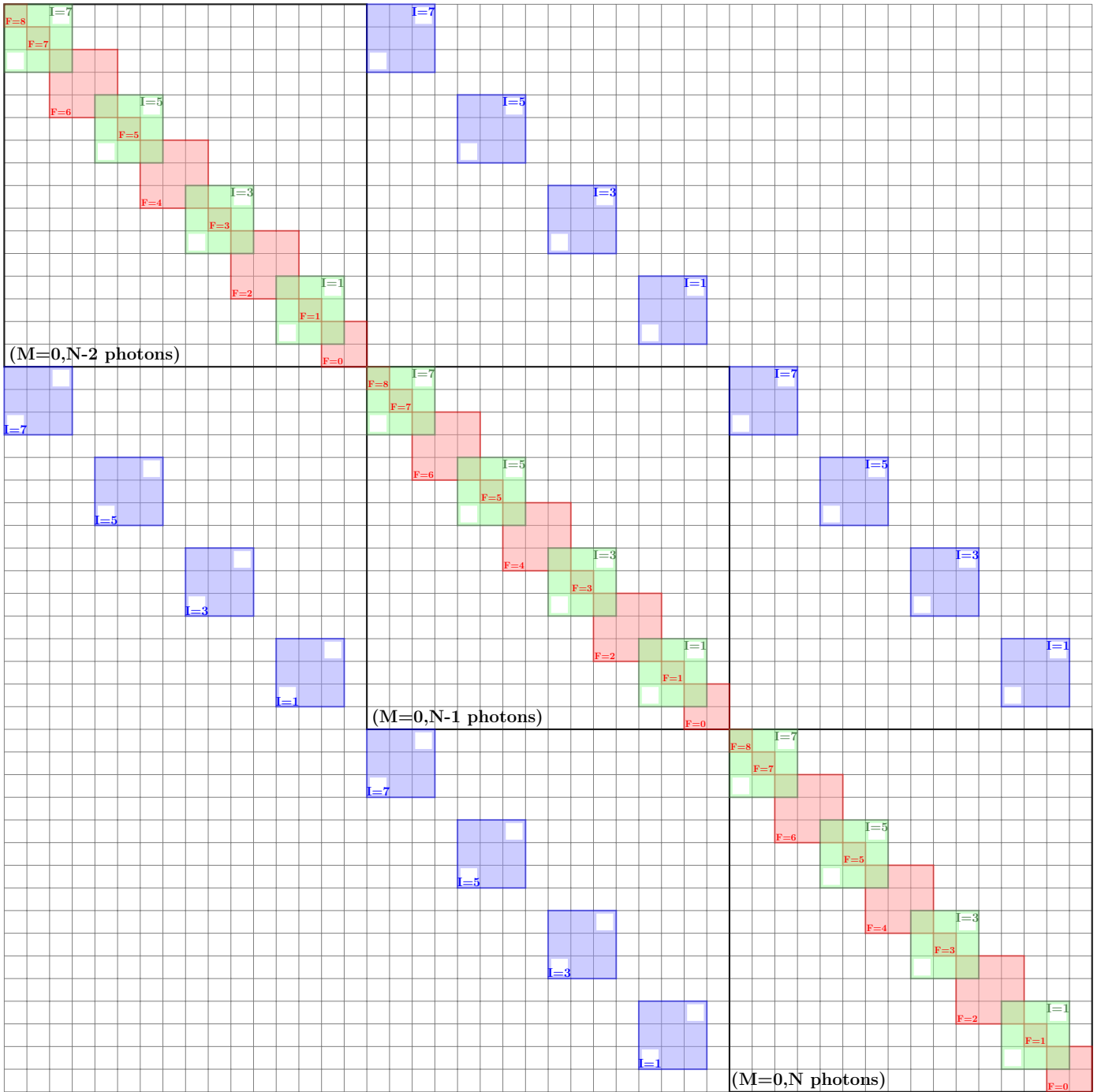


Figure 15.2. Block-matrix structure, in the molecular basis ϵ_M , of the Hamiltonian describing a collision between two atoms in the presence of a static magnetic field B_{osc} (contributing the green V_Z blocks) and a π -polarised magnetic field B_{osc} (contributing the blue W blocks), restricted to the $(M_F = 0, N \text{ photons})$, $(M_F = 0, N - 1 \text{ photons})$, and $(M_F = 0, N - 2 \text{ photons})$ subspaces ($N_{\text{states}} = 48$ coupled channels). In the absence of a static magnetic field ($B_{\text{stat}} = 0$), the green V_Z blocks vanish, but the three distinct $(M_F = 0)$ blocks are still coupled by the blue W blocks.

The choice of the incident state n_0 among these N_{states} states is dictated by the internal state of the atoms before the microwave field is turned on in the actual experiment: we assume that the experiment is performed with atoms that are all in the same state $|f^-, m_f = 0\rangle$ in the absence of the microwave field. Therefore, we are looking for the dressed two-atom state $|D_{n_0}\rangle$ which has the largest overlap with the ‘bare’ two-atom state $|f^-, m_1 = 0; f^-, m_2 = 0\rangle$, in the presence of N photons.

In the case of the static-field Feshbach resonances, we have used a perturbative analytical approach to determine the relevant ‘dressed’ two-atom state (see Section 14.3.2). In the present case, the situation is slightly more intricate as two parameters are involved: the magnetic field amplitude B_{osc} and the detuning δ , defined by $\hbar\delta = \hbar\omega - \Delta E_{\text{hf}}$ (there was only one parameter in the static-field case: the magnetic field amplitude B_{stat}). Hence, we replace the analytical approach of Section 14.3.2 with a closely related numerical approach which we now describe.

The left-hand part of Fig. 15.3 shows a plot of the ‘bare’ energies of the two atoms in the presence of the microwave field (*i.e.* neglecting the couplings due to V_Z and W : the plotted energies are the eigenvalues of $V_{\infty}^{(0)} = V_{\text{hf}} + \hbar\omega a^\dagger a$) as a function of the detuning δ . We assume that $\hbar|\delta|$ is large enough compared to $\mu_B B_{\text{osc}}$ for the microwave dressing not to mix the bare states too strongly away from their bare-state asymptotes plotted in Fig. 15.3(left).

The index n_0 of the relevant ‘dressed’ state is determined as follows from Fig. 15.3(left). We start from the quantum numbers describing the ‘bare’ two-atom state: the quantum numbers $\{f^-, f^-\}$ indicate that we should look at the lower group of three lines, and the photon number N points towards the horizontal line in this group. The degeneracies (given by the small integers on the left part of the plot) then imply that, for negative detunings close to $\delta = 0$: (*i*) there are four such bare states, and (*ii*) there are $4 + 4 + 7 = 15$ states that have lower energies. Thus, the relevant dressed two-atom states are¹ $|D_{16}\rangle$, $|D_{17}\rangle$, $|D_{18}\rangle$, and $|D_{19}\rangle$. Subsequently, a plot of the overlaps of these four dressed states with the bare two-atom state $|f^-, m_1 = 0; f^-, m_2 = 0\rangle$ for $B_{\text{stat}} = 0$, $B_{\text{osc}} = 1$ mG, and detunings $\delta/2\pi \approx -5$ kHz (which is the detuning expected to cause a coupling to the weakest-bound triplet bound state of two ^{133}Cs atoms), shown on the right-hand side of Fig. 15.3, reveals that the sought dressed state is $|D_{16}\rangle$.

Note that the choice of $|D_{16}\rangle$ as the dressed state relating to the ‘bare’ state specified above is valid only for a given range of the parameters δ and B_{osc} around the values given above. For example, for positive detunings (and the same magnetic field amplitudes), the dressed state relating to $|f^-, m_f = 0; f^-, m_f = 0\rangle$ is $|D_{31}\rangle$ (see the $\delta > 0$ half of Fig. 15.3).

15.2.2. Inelastic processes

The dressed state we have selected ($n_0 = 16$) is not the lowest-energy dressed state. Consequently, the two atoms can undergo inelastic collisions which bring them to states with lower energy than the incoming state.

¹The two-atom dressed states $|D_j\rangle$ are ordered by increasing energies: see Section 12.1.2.

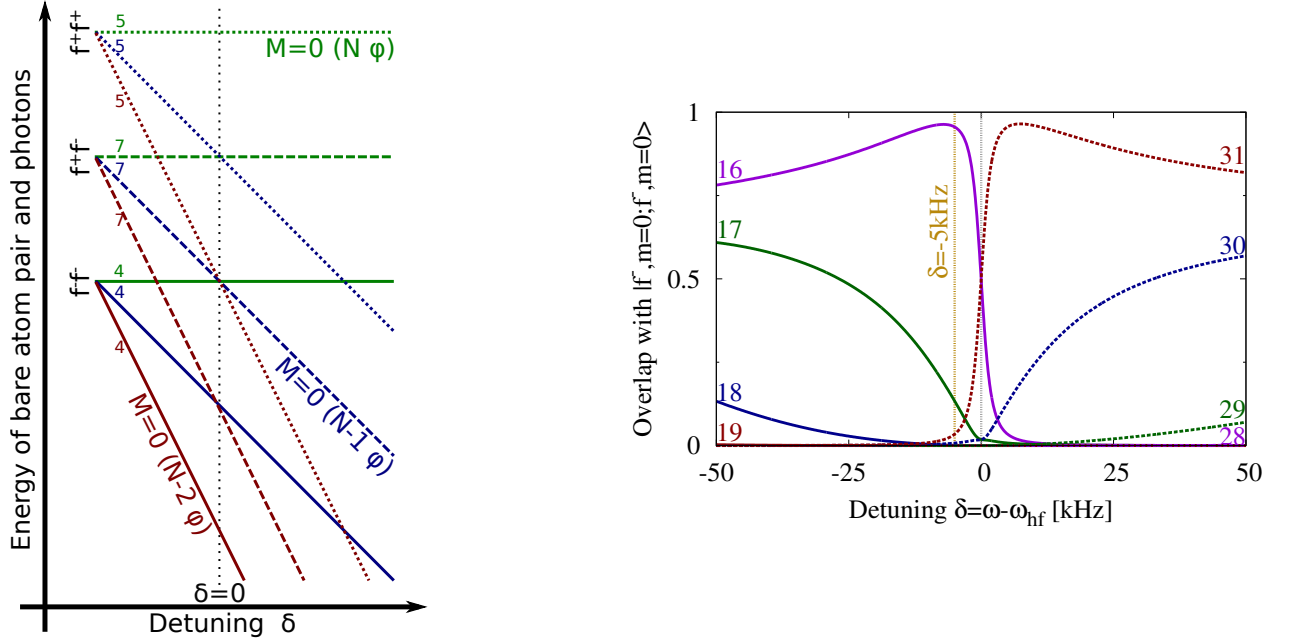


Figure 15.3. Left: ‘Bare’ energies of the two atoms in the presence of the microwave field, as given by the Hamiltonian $V_\infty^{(0)}$. The green lines correspond to $M_F = 0$ (N photons), the blue lines to $M_F = 1$ ($N - 1$ photons), and the red lines to $M_F = 2$ ($N - 2$ photons). The solid lines represent states belonging to the $\{f^- f^-\}$ group, the dashed lines to $\{f^+ f^-\}$ and the dotted lines to $\{f^+ f^+\}$. For given values of the quantum numbers $\{f_1, f_2\}^\pm, F, M_F$, all of the states $|\{f_1, f_2\}^\pm, F, M_F\rangle$ are degenerate: the corresponding degeneracies are given by the small integers on the left-hand part of the plot.

Right: Overlaps between the mw-dressed states $|D_n\rangle$ and the ‘bare’ state $|f^-, m_1 = 0; f^-, m_2 = 0, N\rangle$ (N is the photon number), calculated for $B_{\text{stat}} = 0$ and $B_{\text{osc}} = 1$ mG. Only the dressed states yielding the largest overlaps are represented: $D_{13}, D_{14}, D_{15}, D_{16}$ for $\delta < 0$, and $D_{28}, D_{29}, D_{30}, D_{31}$ for $\delta > 0$.

The microwave-dressed two-atom states $|D_j\rangle$ are ordered by increasing energies. Therefore, there are fifteen states whose energies are lower than $|D_{16}\rangle$. The left part of Fig. 15.3 shows that, for negative and small detunings δ , among these fifteen states,

- 4 belong to the $(\{f^-, f^-\}, M = 0, N - 2 \text{ photons})$ group (energy $-2\Delta E_{\text{hf}}$ lower than the incident state);
- 4 belong to the $(\{f^-, f^-\}, M = 0, N - 1 \text{ photons})$ group (energy $-\Delta E_{\text{hf}}$ lower than the incident state);
- 7 belong to the $(\{f^+, f^-\}, M = 0, N \text{ photons})$ group (energy $-\Delta E_{\text{hf}}$ lower than the incident state);

The inelastic processes cause the scattering length a_{n_0} to acquire an imaginary component; in $\text{Re}(a(\omega))$, the hyperbolic divergence predicted by the two-channel model in the absence of inelastic collisions is replaced by a dispersive dependence on ω which does not diverge at the resonance frequency (see Fig. 15.4).

Note that the only inelastic processes taken into account in our calculations are those due to the interaction with the magnetic field through the coupling term² W_π . In particular, the weak anisotropic spin-spin interaction V_{ss} (see Section 11.4.3 and [39]) are not accounted for.

15.2.3. MW-induced resonances involving the dressed state D_{16}

We have used our ‘shooting’-based coupled-channel program (see Section 12.4) to calculate the scattering length $a(\omega)$ associated with the dressed two-atom state $|D_{16}\rangle$, for $B_{\text{stat}} = 0$ (no static magnetic field) and the magnetic field amplitude³ $B_{\text{osc}} = 1 \text{ mG}$. The dependence $a(\omega)$ is represented on Fig. 15.4, for a range of detunings around $\delta = 0$ and of the order of $|E_T| = h \cdot 5 \text{ kHz}$, where $|E_T|$ is the binding energy of the weakest bound state of the triplet potential for ^{133}Cs . For the range of detunings explored on this figure, the dressed state $|D_{16}\rangle$ relates to the bare state $|f^-, m_{f1} = 0; f^-, m_{f2} = 0\rangle$ for $\delta < 0$, and to $|f^+, m_{f1} = 0; f^+, m_{f2} = 0\rangle$ for $\delta > 0$.

The main microwave-induced resonance

The main resonance due to the weakest bound state in the Triplet potential is expected to occur for detunings δ close to $\hbar\delta_{\text{res}}^0 \approx -|E_T| = h \cdot (-5 \text{ kHz})$ (see Eq. (11.8)). Indeed, Fig. 15.4 exhibits a multi-peaked resonance for $\delta/2\pi \approx -5 \text{ kHz}$.

²In the presence of a static magnetic field, the Zeeman coupling term V_Z may also cause inelastic processes. These are absent in this Section as $B_{\text{stat}} = 0$, but will be present in Section 15.3, where $B_{\text{stat}} \neq 0$.

³We work with small magnetic field amplitudes ($B_{\text{osc}} < |E_T|/\mu_B \approx 4 \text{ mG}$, where $|E_T| = h \cdot 5 \text{ kHz}$ is the energy of the weakest-bound triplet bound state of two ^{133}Cs atoms) in order to avoid an interplay between the two-atom resonance that we describe here and single-atom dressed-state effects near the hyperfine transition frequency: see Section 11.2.4.

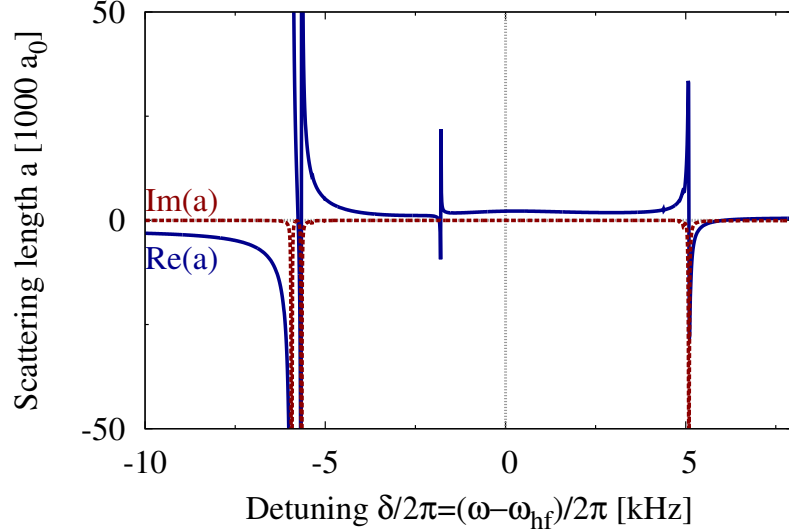


Figure 15.4. Frequency dependence $a(\omega)$ of the (complex) scattering length $a(\omega)$ associated with the dressed two-atom state $|D_{16}\rangle$, calculated for $B_{\text{osc}} = 1 \text{ mG}$, $B_{\text{stat}} = 0$, and $-10 \text{ kHz} \leq \frac{\delta}{2\pi} \leq 6 \text{ kHz}$. The dressed state relates to $|f^-, m_{f1} = 0; f^-, m_{f2} = 0\rangle$ for $\delta < 0$ and to $|f^+, m_{f1} = 0; f^+, m_{f2} = 0\rangle$ for $\delta > 0$.

This resonance is analogous to the one that we have identified with ^{133}Cs atoms that are asymptotically all in the state $|f^-, m_f = i - 1/2\rangle$ (see Chapter 11: it is analogous to the resonance due to the intersection *A* on Fig. 11.11). The present resonance differs from the previous one in two respects:

1. Because of inelastic processes, $a(\omega)$ has a non-zero imaginary part which becomes important near the resonance;
2. The multi-peaked structure is a signature of the presence of multiple resonant closed-channel states.

These features are new in the context of microwave-induced resonance, but they have already been encountered in our analysis of the small static-field Feshbach resonances measured at SYRTE (see Chapter 14).

Let us focus on the second new feature. The choice of $|D_{16}\rangle$ as the incident two-atom ‘dressed’ state determines the open-channel block to be $(M_F = 0, N \text{ photons})$. The absorption of a single π -polarised photon connects this block to the $(M_F = 0, N - 1 \text{ photons})$ block, which therefore contains the closed channels. The resonance we are discussing occurs for $\hbar\delta \approx -|E_T|$ and is therefore due to the triplet bound states in $(M_F = 0, N - 1 \text{ photons})$ which have odd F : $F = 7, 5, 3, 1$. These multiple closed-channel states yield the multi-peaked structure observed on Fig. 15.2.

The second-order resonance occurring for negative detunings

The resonance occurring at $\delta/2\pi \approx -\frac{1}{2} 5 \text{ kHz}$ is a two-photon resonance involving the ($M_F = 0, N$ photons) and ($M_F = 0, N - 2$ photons) blocks. It is analogous to the second-order mw-FFR resonance involving the $M_F = 2i - 1$ (open) and $M_F = 2i + 1$ (closed) subspaces which we have previously encountered (see Section 11.2.4 and the intersection B on Fig. 11.11).

Its single-peak character can be understood in terms of an energy-conservation argument. The incident atoms are in a (dressed) state which relates to a bare two-atom state belonging to the $\{f^- f^-\}$ group within the ($M_F = 0, N$ photons) block. The absorption of two photons, each of which has a frequency tuned close to the hyperfine transition energy, will therefore lead to a state belonging to the $\{f^+ f^+\}$ group (conservation of energy) within the ($M_F = 0, N - 2$ photons) block. There is only one purely triplet state which satisfies these two conditions, namely $|\{f^+ f^+\}, F = 2i + 1 = 8, M_F = 0, N - 2 \text{ photons}\rangle$. Therefore, the two-photon resonance involving the $M_F = 0$ (open) and $M_F = 2$ (closed) subspaces should only have one peak.

No second-order resonance occurs at⁴ $\delta/2\pi \approx +\frac{1}{2} 5 \text{ kHz}$. This is due to the absence of a triplet two-atom state satisfying the required energy-conservation condition. Indeed, on the $\delta > 0$ side of the anticrossing, the incident two-atom state belongs to the ($\{f^+, f^+\}, M_F = 0, N - 2$ photons) block. The emission of two photons would connect the incident state with one in the ($\{f^-, f^-\}, M_F = 0, N$ photons) block, which contains no triplet internal state, and thus does not support a weakly-bound state whose binding energy would be $\approx h \cdot 5 \text{ kHz}$.

A narrower first-order resonance for positive detunings

Figure 15.4 shows that a resonance occurs for detunings $\delta/2\pi \approx +5 \text{ kHz}$. This is a first-order resonance involving the ($M_F = 0, N - 2$ photons) block (open subspace) and the ($M_F = 0, N - 1$ photons) block (which contains the closed triplet channels).

This first-order resonance corresponds to the intersection C on Fig. 11.11. Unlike in Section 11.2.3, this resonance is not suppressed. Indeed, in the present situation, the incident two-atom internal state for $\delta > 0$ has non-zero components along the states $|\{f^+, f^+\}, F, M_F = 0\rangle$ with $F = 6, 4, 2$, and 0 : these four internal states are not purely electronic-triplet and may thus take part in resonances involving triplet closed channels.

However, this first-order resonance on the $\delta > 0$ side of the graph is much narrower than its $\delta < 0$ counterpart, as $|D_{16}\rangle$ has a large overlap with the purely-triplet state⁵ $|\{f^+, f^+\}, F = 8, M_F = 0\rangle$.

⁴The resonance corresponding to the intersection D on Fig. 11.11 is not suppressed, but it occurs for detunings $h\delta \approx +\frac{1}{2} |E_b|$, where $|E_b|$ is the binding energy of a bound state supported by an (F even, M_F) block and is expected to be of the order of a few tens of MHz.

⁵For $\delta > 0$, the incident dressed two-atom state is close to the bare state $|f^+, m_f = 0; f^+, m_f = 0\rangle$, whose squared overlap with $|\{f^+, f^+\}, F = 8, M_F = 0\rangle$ is 0.38. Only the $F = 6, 4, 2$, and 0 components cause a resonance; their total squared overlap with the incident state is only ≈ 0.62 , which explains the narrowness of the calculated resonance.

15. Towards an experimental observation of our predictions

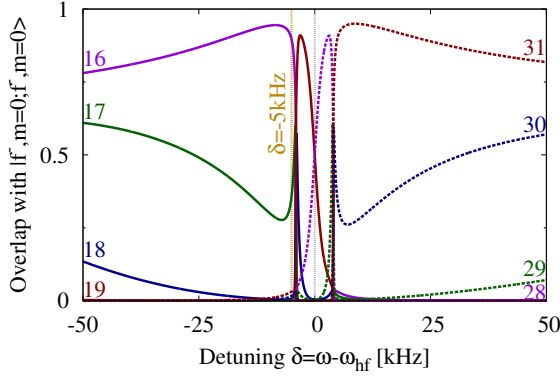


Figure 15.5. Overlaps between the dressed states $|D_n\rangle$ and the ‘bare’ state $|f^-, m_1 = 0; f^-, m_2 = 0, N\rangle$ (N is the photon number), calculated for $B_{\text{osc}} = 1$ mG and $B_{\text{stat}} = 1.6$ mG. Only the dressed states yielding the largest overlaps are represented: $|D_{16}\rangle, |D_{17}\rangle, |D_{18}\rangle, |D_{19}\rangle$ for $\delta < 0$, and $|D_{28}\rangle, |D_{29}\rangle, |D_{30}\rangle, |D_{31}\rangle$ for $\delta > 0$ (this graph is the analog, for the $B_{\text{stat}} \neq 0$ case, of Fig. 15.3(right)).

15.3. In the presence of a static magnetic field

We now describe the effect of an additional *static* magnetic field \mathbf{B}_{stat} along the quantisation axis \mathbf{e}_z . We choose the amplitude $B_{\text{stat}} = 1.6$ mG, which is the typical static magnetic field amplitude in a Cesium fountain clock experiment [60]. The amplitude of the oscillating magnetic field is $B_{\text{osc}} = 1$ mG, as in Section 15.2. We find that the additional static field only has a small effect on the microwave-induced resonances described in the previous Section.

The argument concerning the choice of the entrance channel, presented in Section 15.2.1, relies only on the degeneracies of the bare two-atom states and on the assumption that both components of the magnetic field (static and oscillatory) are small enough for the dressed-state energies not to lie too far away from their bare-state asymptotes (see the left part of Fig. 15.3). Therefore, this argument is still applicable, and shows that the relevant dressed states for negative detunings ($\delta/2\pi \approx -5$ kHz) are $|D_{16}\rangle, |D_{17}\rangle, |D_{18}\rangle$, and $|D_{19}\rangle$.

A plot of the overlaps of these four states with $|f^-, m = 0; f^-, m = 0\rangle$, calculated for the magnetic field amplitudes $B_{\text{osc}} = 1$ mG, $B_{\text{stat}} = 1.6$ mG, and detunings $\delta/2\pi \approx -5$ kHz, represented on Fig. 15.5, shows that the sought dressed state is $|D_{16}\rangle$. Note, however, that the dressed states $|D_j\rangle$ depend on all magnetic field parameters, and in particular on B_{stat} ; hence, the dressed state $|D_{16}\rangle$ discussed here is not the same as the one discussed in Section 15.2.1.

The scattering length $a(\omega)$ associated with the incident dressed state $|D_{16}\rangle$ is represented on Fig. 15.6. The $\delta < 0$ part of this figure exhibits a wide double-peaked resonance which is very similar to the one obtained in the absence of a static magnetic field (see Fig. 15.5). On the $\delta > 0$ part of the graph, the effect of the static magnetic is to split the narrow first-order resonance at $\delta \approx 5$ kHz, which has a single main peak for $B_{\text{stat}} = 0$, into separate components. This multiple-peaked structure is due to the presence of multiple triplet states in the $(M_F = 0, N - 1 \text{ photons})$ subspace. Indeed, the states $|\{f^+, f^-\}^+, F, M_F = 0\rangle$, with $F = 1, 3, 5$, and 7 , are all purely triplet and thus each support a weakly-bound state whose binding energy is $|E_T| = h \cdot 5$ kHz and which may contribute a peak to the resonance at $\delta/2\pi \approx +5$ kHz.

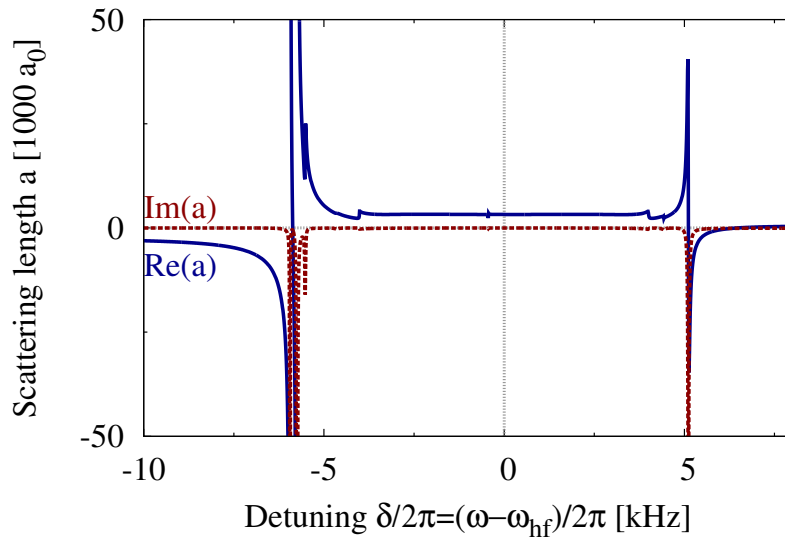


Figure 15.6. Frequency dependence $a(\omega)$ of the (complex) scattering length $a(\omega)$ associated with the dressed two-atom state $|D_{16}\rangle$, calculated for $B_{\text{osc}} = 1 \text{ mG}$, $B_{\text{stat}} = 1.6 \text{ mG}$, and $-10 \text{ kHz} \leq \delta/2\pi \leq 6 \text{ kHz}$. The dressed state relates to $|f^-, m_{f_1} = 0; f^-, m_{f_2} = 0\rangle$ for $\delta < 0$ and to $|f^+, m_{f_1} = 0; f^+, m_{f_2} = 0\rangle$ for $\delta > 0$.

16. Conclusion and outlook

The object of the work presented in the second part of this manuscript has been to describe a new type of scattering resonance occurring in ultracold atomic systems: the microwave-induced Fano–Feshbach resonances. Scattering resonances occur when a low-energy scattering state of a pair of colliding atoms, in given internal states, is coupled to a bound state of the two atoms in a different two-atom internal state. In the case of the “standard” Feshbach resonances, the coupling between the scattering state and the resonant bound state is obtained using a static magnetic field. Microwave-induced Feshbach resonances are caused by couplings generated by oscillating magnetic fields whose frequencies are tuned close to the atomic hyperfine splitting.

Just like their static-field counterparts, microwave-induced Feshbach resonances cause a hyperbolic divergence in the scattering length (see Eq. (11.1)). Therefore, they can be used to set the value of the scattering length to any desired value and sign, and thus to tailor the nature (attractive or repulsive) and strength (strongly-interacting regime, ideal gas, . . .) of the interactions within the ultracold atomic sample. They also allow the scattering length to be adiabatically scanned through the resonance (*e.g.*, in view of an experimental study of a BEC–BCS crossover): such a scan can be performed, for example, by working at a fixed magnetic field amplitude and slowly ramping the magnetic field frequency from one side of the resonance to the next.

Despite their kinship, microwave-induced Feshbach resonances differ from static-field resonances in quite a few respects. Microwave-induced Feshbach resonances occur even in the absence of any static magnetic field. The resonance frequencies and widths of microwave-induced resonances are not directly related to the characteristics of static-field resonances. Furthermore, the widths of microwave-induced resonances are proportional to the squared amplitude of the magnetic field, and these resonances can therefore be made very broad if a powerful microwave source is available.

We have focused on the case of bosonic alkali atoms, although neither of these two assumptions is essential. We have characterised the microwave-induced resonances occurring in ${}^7\text{Li}$, ${}^{23}\text{Na}$, ${}^{41}\text{K}$, ${}^{87}\text{Rb}$, and ${}^{133}\text{Cs}$ using three different approaches: (*i*) the two-square-well approach (Section 9.2), (*ii*) the two-channel approach (Section 11.1), and (*iii*) the coupled-channel approach (Section 11.2). The first approach involves a simple model from which orders of magnitude for the resonance positions, widths, and shifts can be extracted without resorting to elaborate numerical methods. The second approach yields simple scaling laws for the resonance width and the shift on the resonance position due to the interchannel coupling. The third approach is the most

16. Conclusion and outlook

accurate and general: it remains applicable in the presence of larger oscillating fields (Section 11.2.4), it accounts for inelastic processes, and for the presence of both static and oscillating fields (Chapter 15). The results of all three approaches (Tables 9.2, 11.1, and 11.2) are in good agreement with each other.

Our numerical results for the resonance widths lead to optimistic experimental prospects with all atoms except ${}^7\text{Li}$ (for the oscillating field amplitude $B_{\text{osc}} = 10\text{ G}$, all predicted resonance widths are much larger than 1 kHz, except for ${}^7\text{Li}$; see the discussion in Section 11.3). In the case of ${}^7\text{Li}$, the absence of a microwave-induced resonance is not a hindrance, as a very broad static-field Feshbach resonance is already available [22].

The divergence associated with a microwave-induced resonance is actually hyperbolic only for magnetic field amplitudes that are small enough. For all atoms except ${}^{133}\text{Cs}$, the resonance remains hyperbolic for magnetic field amplitudes of the order of 10 G (see Fig. 11.9). In the specific case of ${}^{133}\text{Cs}$, the resonance involving the weakly bound triplet dimer state (binding energy $|E_T| = h \cdot 5\text{ kHz}$) becomes non-hyperbolic for magnetic fields as small as 5 mG (see Fig. 11.12). We have analysed the large-field behaviour of this resonance in terms of a competition between the two-atom resonance and single-atom dressed-state effects (Section 11.2.4).

Small static-field resonances have been observed in Cesium fountain clocks at SYRTE-Observatoire de Paris [57]. To our knowledge, these resonances had since remained unexplained. We have shown (Section 14.3) that they are s -wave resonances involving the same weakly bound dimer state discussed in the previous paragraph.

Finally, we have characterised microwave-induced Feshbach resonances in Cesium involving experimental parameters that are relevant for a prospective observation in a Cesium fountain clock experiment (Chapter 15). The description of the resonances occurring in these situations involves numerous coupled channels; inelastic collisions, as well as the effect of a small additional static magnetic field, have been accounted for.

All of the numerical calculations presented in this manuscript have been performed with our own implementations of the coupled-channel method, using the accumulated phase approach. These implementations are described in Chapter 14.

Throughout the present part of this manuscript, we have characterised the collisional properties of ultracold atoms using scattering lengths only. Scattering lengths are zero-temperature quantities; in most cases, the scattering properties at non-zero, albeit small, temperatures may be deduced from the zero-temperature case [1]. However, in the particular case of Cesium, the very large value of the triplet scattering length ($a_T = 2500 a_0$) causes atomic interactions to be strongly affected by thermal effects [61]. An experiment performed in a Cesium fountain clock will be sensitive to these thermal effects, even for

temperatures as low as $T = 1 \mu\text{K}$. We are currently working on the inclusion of these thermal effects in our theoretical description.

Our method can be extended to the case of heteronuclear mixtures. Microwave-induced resonances may thus be used to tune the interaction in such systems (*e.g.* in experiments related to the work presented in the first part of this manuscript) in situations where static-field Feshbach resonances are not easily accessible.

Microwave-induced Feshbach resonances are present even in the absence of a static magnetic field. This situation is actively studied in the context of spinor Bose gases. Microwave-induced resonances could be used to tune the sign of the interaction between various hyperfine states, possibly leading to novel accessible quantum states.

Bibliography

- [1] Thorsten Köhler, Krzysztof Góral, and Paul S. Julienne. “Production of cold molecules via magnetically tunable Feshbach resonances”. In: *Rev. Mod. Phys.* 78.4 (Dec. 2006), pp. 1311–1361. DOI: 10.1103/RevModPhys.78.1311.
- [2] Stefano Giorgini, Lev P. Pitaevskii, and Sandro Stringari. “Theory of ultracold atomic Fermi gases”. In: *Rev. Mod. Phys.* 80.4 (Oct. 2008), pp. 1215–1274. DOI: 10.1103/RevModPhys.80.1215.
- [3] L. Pitaevskii and S. Stringari. *Bose-Einstein condensation*. Clarendon Press, 2003. ISBN: 0198507194.
- [4] Franco Dalfovo et al. “Theory of Bose-Einstein condensation in trapped gases”. In: *Rev. Mod. Phys.* 71.3 (Apr. 1999), pp. 463–512. DOI: 10.1103/RevModPhys.71.463.
- [5] M. H. Anderson et al. “Observation of Bose-Einstein Condensation in a Dilute Atomic Vapor”. In: *Science* 269.5221 (1995), pp. 198–201. DOI: 10.1126/science.269.5221.198.
- [6] E.A. Donley et al. “Dynamics of collapsing and exploding Bose-Einstein condensates”. In: *Nature* 412.6844 (2001), pp. 295–299. ISSN: 0028-0836. DOI: doi:10.1038/35085500.
- [7] Cheng Chin et al. “Feshbach resonances in ultracold gases”. In: *Rev. Mod. Phys.* 82.2 (Apr. 2010), pp. 1225–1286. DOI: 10.1103/RevModPhys.82.1225.
- [8] T. Bourdel et al. “Experimental Study of the BEC-BCS Crossover Region in Lithium 6”. In: *Phys. Rev. Lett.* 93.5 (July 2004), p. 050401. DOI: 10.1103/PhysRevLett.93.050401.
- [9] Immanuel Bloch, Jean Dalibard, and Wilhelm Zwerger. “Many-body physics with ultracold gases”. In: *Rev. Mod. Phys.* 80.3 (July 2008), pp. 885–964. DOI: 10.1103/RevModPhys.80.885.
- [10] Jocelyne Guéna et al. “Evaluation of Doppler Shifts to Improve the Accuracy of Primary Atomic Fountain Clocks”. In: *Phys. Rev. Lett.* 106.13 (Apr. 2011), p. 130801. DOI: 10.1103/PhysRevLett.106.130801.
- [11] Kurt Gibble. “Decoherence and Collisional Frequency Shifts of Trapped Bosons and Fermions”. In: *Phys. Rev. Lett.* 103.11 (Sept. 2009), p. 113202. DOI: 10.1103/PhysRevLett.103.113202.
- [12] H Marion. “Contrôle des collisions froides du Césium 133. Tests de la variation de la constante de structure fine à l’aide d’une fontaine atomique double Rubidium-Césium”. PhD thesis. Université Paris VI, 2005.

Bibliography

- [13] C. Pethick and H. Smith. *Bose-Einstein condensation in dilute gases*. Cambridge University Press, 2002. ISBN: 0521665809.
- [14] J. Stenger et al. “Strongly Enhanced Inelastic Collisions in a Bose-Einstein Condensate near Feshbach Resonances”. In: *Phys. Rev. Lett.* 82.12 (Mar. 1999), pp. 2422–2425. DOI: 10.1103/PhysRevLett.82.2422.
- [15] A. Marte et al. “Feshbach Resonances in Rubidium 87: Precision Measurement and Analysis”. In: *Phys. Rev. Lett.* 89.28 (Dec. 2002), p. 283202. DOI: 10.1103/PhysRevLett.89.283202.
- [16] M. Marinescu and L. You. “Controlling Atom-Atom Interaction at Ultralow Temperatures by dc Electric Fields”. In: *Phys. Rev. Lett.* 81.21 (Nov. 1998), pp. 4596–4599. DOI: 10.1103/PhysRevLett.81.4596.
- [17] P. O. Fedichev et al. “Influence of Nearly Resonant Light on the Scattering Length in Low-Temperature Atomic Gases”. In: *Phys. Rev. Lett.* 77.14 (Sept. 1996), pp. 2913–2916. DOI: 10.1103/PhysRevLett.77.2913.
- [18] M. Theis et al. “Tuning the Scattering Length with an Optically Induced Feshbach Resonance”. In: *Phys. Rev. Lett.* 93.12 (Sept. 2004), p. 123001. DOI: 10.1103/PhysRevLett.93.123001.
- [19] K. Enomoto et al. “Optical Feshbach Resonance Using the Intercombination Transition”. In: *Phys. Rev. Lett.* 101.20 (Nov. 2008), p. 203201. DOI: 10.1103/PhysRevLett.101.203201.
- [20] A. J. Moerdijk, B. J. Verhaar, and T. M. Nagtegaal. “Collisions of dressed ground-state atoms”. In: *Phys. Rev. A* 53.6 (June 1996), pp. 4343–4351. DOI: 10.1103/PhysRevA.53.4343.
- [21] D. J. Papoular, G. V. Shlyapnikov, and J. Dalibard. “Microwave-induced Fano-Feshbach resonances”. In: *Phys. Rev. A* 81.4 (Apr. 2010), p. 041603. DOI: 10.1103/PhysRevA.81.041603.
- [22] K.E. Strecker et al. “Formation and propagation of matter-wave soliton trains”. In: *Nature* 417.6885 (2002), pp. 150–153. ISSN: 0028-0836. DOI: 10.1038/nature747.
- [23] G. Herzberg. *Molecular Spectra and Molecular Structure. I. Spectra of Diatomic Molecules*. D. Van Nostrand, 1950.
- [24] Kevin M. Jones et al. “Ultracold photoassociation spectroscopy: Long-range molecules and atomic scattering”. In: *Rev. Mod. Phys.* 78.2 (May 2006), pp. 483–535. DOI: 10.1103/RevModPhys.78.483.
- [25] C. Cohen-Tannoudji et al. *Quantum Mechanics. Vols. 1 and 2*. Wiley Interscience, 1977.
- [26] J. Dalibard. “Collisional dynamics of ultracold atomic gases”. In: *Proceedings of the International School of Physics Enrico Fermi, Course CXL: Bose – Einstein condensation in gases*. Societa Italiana di Fisica, 1998. Chap. Collisional dynamics of ultracold atomic gases.

- [27] G. F. Gribakin and V. V. Flambaum. “Calculation of the scattering length in atomic collisions using the semiclassical approximation”. In: *Phys. Rev. A* 48.1 (July 1993), pp. 546–553. DOI: 10.1103/PhysRevA.48.546.
- [28] GV Shlyapnikov, J.T.M. Walraven, and E.L. Surkov. “Antihydrogen at sub-Kelvin temperatures”. In: *Hyperfine Interactions* 76.1 (1993), pp. 31–46. ISSN: 0304-3843. DOI: 10.1007/BF02316704.
- [29] A. D. Lange et al. “Determination of atomic scattering lengths from measurements of molecular binding energies near Feshbach resonances”. In: *Phys. Rev. A* 79.1 (Jan. 2009), p. 013622. DOI: 10.1103/PhysRevA.79.013622.
- [30] C. Cohen-Tannoudji, J. Dupont-Roc, and G. Grynberg. *Atom-Photon Interactions: Basic Processes and Applications*. Wiley, 1998.
- [31] B. J. Verhaar, E. G. M. van Kempen, and S. J. J. M. F. Kokkelmans. “Predicting scattering properties of ultracold atoms: Adiabatic accumulated phase method and mass scaling”. In: *Phys. Rev. A* 79.3 (Mar. 2009), p. 032711. DOI: 10.1103/PhysRevA.79.032711.
- [32] E. Arimondo, M. Inguscio, and P. Violino. “Experimental determinations of the hyperfine structure in the alkali atoms”. In: *Rev. Mod. Phys.* 49.1 (Jan. 1977), pp. 31–75. DOI: 10.1103/RevModPhys.49.31.
- [33] L.D. Landau and L.M. Lifshitz. *Quantum Mechanics: Non-Relativistic Theory*. 3rd ed. Butterworth-Heinemann, 2003.
- [34] H. T. C. Stoof, J. M. V. A. Koelman, and B. J. Verhaar. “Spin-exchange and dipole relaxation rates in atomic hydrogen: Rigorous and simplified calculations”. In: *Phys. Rev. B* 38.7 (Sept. 1988), pp. 4688–4697. DOI: 10.1103/PhysRevB.38.4688.
- [35] F. H. Mies et al. “Estimating Bounds on Collisional Relaxation Rates of Spin-Polarized 87Rb Atoms at Ultracold Temperatures”. In: *J. Res. Natl. Inst. Stand. Technol.* 101 (July 1996), pp. 521–535. URL: <http://nvl.nist.gov/pub/nistpubs/jres/101/4/cnt101-4.htm>.
- [36] A. J. Moerdijk, B. J. Verhaar, and A. Axelsson. “Resonances in ultracold collisions of ${}^6\text{Li}$, ${}^7\text{Li}$, and ${}^{23}\text{Na}$ ”. In: *Phys. Rev. A* 51.6 (June 1995), pp. 4852–4861. DOI: 10.1103/PhysRevA.51.4852.
- [37] A. Messiah. *Quantum Mechanics*. Vol. II. North Holland Publishing Company, 1966.
- [38] F. D. Colavecchia et al. “The potential energy surface for spin-aligned $\text{Li}_3(1^4A')$ and the potential energy curve for spin-aligned $\text{Li}_2(a^3\Sigma_u^+)$ ”. In: *The Journal of Chemical Physics* 118.12 (2003), pp. 5484–5495. DOI: 10.1063/1.1555124.
- [39] E. G. M. van Kempen et al. “Interisotope Determination of Ultracold Rubidium Interactions from Three High-Precision Experiments”. In: *Phys. Rev. Lett.* 88.9 (Feb. 2002), p. 093201. DOI: 10.1103/PhysRevLett.88.093201.
- [40] S. Bize. “Tests fondamentaux à l’aide d’horloges à atomes froids de rubidium et de césium”. PhD thesis. Université Pierre et Marie Curie, 2001.

Bibliography

- [41] M. Köhl. private communication. 2009.
- [42] *Magnetic loop antenna calculator*. URL: http://www.66pacific.com/calculators/small_tx_loop_calc.aspx.
- [43] I. Spielman. private communication. 2009.
- [44] L. Turner. private communication. 2010.
- [45] Kendall B. Davis et al. “Evaporative Cooling of Sodium Atoms”. In: *Phys. Rev. Lett.* 74.26 (June 1995), pp. 5202–5205. DOI: 10.1103/PhysRevLett.74.5202.
- [46] Tin-Lun Ho. “Spinor Bose Condensates in Optical Traps”. In: *Phys. Rev. Lett.* 81.4 (July 1998), pp. 742–745. DOI: 10.1103/PhysRevLett.81.742.
- [47] E. G. M. van Kempen. “Feshbach Resonances in Cold Atomic Gases”. PhD thesis. Technische Universiteit Eindhoven, 2001.
- [48] A. J. Moerdijk and B. J. Verhaar. “Laser cooling and the highest bound states of the Na diatom system”. In: *Phys. Rev. A* 51.6 (June 1995), R4333–R4336. DOI: 10.1103/PhysRevA.51.R4333.
- [49] B.M. Smirnov and M.I. Chibisov. “Electron exchange and changes in the hyperfine state of colliding alkaline earth atoms”. In: *Soviet Physics JETP* 21 (1965), p. 624.
- [50] Boudewijn Verhaar, Kurt Gibble, and Steven Chu. “Cold-collision properties derived from frequency shifts in a cesium fountain”. In: *Phys. Rev. A* 48.5 (Nov. 1993), R3429–R3432. DOI: 10.1103/PhysRevA.48.R3429.
- [51] J. M. Vogels et al. “Coupled singlet-triplet analysis of two-color cold-atom photoassociation spectra”. In: *Phys. Rev. A* 61.4 (Mar. 2000), p. 043407. DOI: 10.1103/PhysRevA.61.043407.
- [52] W.H. Press et al. *Numerical Recipes: the Art of Scientific Programming*. 3rd ed. Cambridge University Press, 2007.
- [53] E. Tiesinga et al. “Conditions for Bose-Einstein condensation in magnetically trapped atomic cesium”. In: *Phys. Rev. A* 46.3 (Aug. 1992), R1167–R1170. DOI: 10.1103/PhysRevA.46.R1167.
- [54] E. Tiesinga, B. J. Verhaar, and H. T. C. Stoof. “Threshold and resonance phenomena in ultracold ground-state collisions”. In: *Phys. Rev. A* 47.5 (May 1993), pp. 4114–4122. DOI: 10.1103/PhysRevA.47.4114.
- [55] S. Inouye et al. “Observation of Feshbach resonances in a Bose-Einstein condensate”. In: *Nature* 392.6672 (1998), pp. 151–154. ISSN: 0028-0836. DOI: 10.1038/32354.
- [56] Chiara D’Errico et al. “Feshbach resonances in ultracold 39 K”. In: *New Journal of Physics* 9.7 (2007), p. 223. URL: <http://stacks.iop.org/1367-2630/9/i=7/a=223>.
- [57] S. Bize et al. *Feshbach resonances at very low magnetic field in a Cesium 133 fountain and other results*. Presentation at ICAP 2004.

- [58] R. S. Freeland. “Photoassociation Spectroscopy of Ultracold and Bose-condensed Atomic Gases”. PhD thesis. The University of Texas at Austin, 2001.
- [59] S. Haroche. “Etude théorique et expérimentale des propriétés d’atomes habillés par des photons de radiofréquence”. PhD thesis. LKB - Université Paris VI, 1971.
- [60] P. Rosenbusch. private communication. 2011.
- [61] Paul J. Leo et al. “Collisional Frequency Shifts in ^{133}Cs Fountain Clocks”. In: *Phys. Rev. Lett.* 86.17 (Apr. 2001), pp. 3743–3746. DOI: 10.1103/PhysRevLett.86.3743.

Acknowledgements

This memoir describes the research work I have performed towards the preparation of my Ph.D. at Laboratoire de Physique Théorique et Modèles Statistiques (CNRS — Université Paris–Sud) from 2007 to 2011. I am very grateful to Profs. S. Ouvry and M. Mézard, who directed LPTMS during that time, for their very warm welcome.

My Ph.D. work has been supervised by Prof. G. Shlyapnikov. Every encounter with Gora has been inspirational. His drive for research and his benevolence seem to have no bounds. It has been a great privilege to benefit from his clear explanations and his well–thought–out advice. Gora’s interests extend far beyond Physics, his sense of humour is outstanding, and it has been a great pleasure to learn a little about Russian history and culture from him. I would like to convey my very sincere thanks to him for all of his help and involvement in this work.

I am hugely indebted to Prof. J. Dalibard (LKB, ENS–Paris) for his luminous explanations and his constant optimism. I am very grateful for his availability and his willingness to help. I have also learnt a lot about pedagogy from him.

I am very much beholden to Profs. S. Stringari (Univ. Trento) and J. Walraven (Univ. Amsterdam) for the interest they have shown for this work, and for readily accepting to act as Referees for my defence. My special thanks also go to Profs. O. Dulieu (LAC), R. Kaiser (INLN), and E. Trizac for accepting to take part in the Jury.

Many thanks are due to Drs. P. Rosenbusch and S. Bize (SYRTE–Observatoire de Paris), who have patiently explained the experimental issues associated with atomic clocks. The interest they have expressed for our work on microwave–induced resonances has been instrumental in seeing it through. I warmly thank S. Bize for inviting me to give a seminar at SYRTE.

Dr. D. Petrov has kindly guided my first steps at LPTMS. I thank him for his help and explanations concerning our theoretical work on composite bosons.

I wish to thank Prof. C. Salomon (LKB, ENS–Paris) for his enthusiastic presentation of the experimental challenges of the study of heteronuclear Fermi mixtures.

I am very grateful to Prof. M. Leduc (LKB, ENS–Paris and IFRAF), who, along with J. Dalibard, suggested that I contact G. Shlyapnikov in the first place. Moreover, IFRAF’s generous financial support has enabled me to attend ICAP 2010 in Australia.

Acknowledgements

I thank Profs. J. Robert, P. Mendels, N. Pavloff, and Dr. F. Caetano for giving me the chance to take part in the teaching effort at Univ. Paris–Sud, and for sharing their invaluable experience. I am very much obliged towards Dr. L. Capéran (Lycée Louis–le–Grand), who has transmitted his enthusiasm for teaching Physics to me, and who provided me with early teaching opportunities.

I am happy to acknowledge help from two friends and colleagues. Dr. P. Cladé (LKB Jussieu) has proofread the greater part of this manuscript. Dr. E. Lepage (Univ. Paris VI) has explained away many mathematical mysteries, in amazingly clear and simple terms. I thank them both for very fruitful discussions.

Last but not least, I am extremely grateful to all my family for their unfailing support. I thank my grandparents for their wisdom, my younger sister for her constant good humour, my mother for her infinite patience, and my father, who first showed me how rewarding scientific research can be.